Population based evaluation of actin cytoskeletal morphometric descriptors as characterisation of stem cell differentiation

Asad Dodhy

Submitted in partial fulfilment of the

requirements of the Degree of

Doctor of Philosophy

School of Engineering and Materials Science,

Queen Mary University of London

London, United Kingdom

Statement of originality

I, Asad Dodhy, confirm that the research included within this thesis is my own work or that where it has been carried out in collaboration with, or supported by others, that this is duly acknowledged below, and my contribution indicated. Previously published material is also acknowledged below.

I attest that I have exercised reasonable care to ensure that the work is original and does not to the best of my knowledge break any UK law, infringe any third party's copyright or other Intellectual Property Right, or contain any confidential material.

I accept that the College has the right to use plagiarism detection software to check the electronic version of the thesis.

I confirm that this thesis has not been previously submitted for the award of a degree by this or any other university.

Asad Dodhy

Date: 29/03/2018

“Do or do not, there is no try.”

- Yoda

Dedicated to my father Hameed and my mother Samina

Acknowledgements

It is often used as a cliché, but in this case it would not be over stated to say that without the help of certain people this thesis would not have been possible.

Firstly, I would like to thank my supervisor Dr Nuria Gavara for giving me the opportunity to embark upon this journey with her. Her support and advise not only in academic but also personal matters have been invaluable. Particularly, I would like to acknowledge my appreciation for her understanding, support and constant encouragement through some difficult times.

I would also like to thank Prof Julia Shelton and Prof Dan Badar, who during my undergraduate years provided a lot of support and inspired me to follow this path.

Furthermore, I am grateful to Dr Stephen Thorpe for providing guidance and sharing his knowledge. I also appreciate having such a patient and collaborative colleague as Luis Rafael Pereira Do Carmo Flores. It was always a pleasure having him around, especially while working in the labs over the weekends.

I would also like to thank Sabrina and Awais for being awesome friends.

To my family, particularly my parents, thank you for everything you have done for me, for working tirelessly to give me the opportunities you never had, and thank you for always believing in me. Without you, I wouldn't be the person I am today.

Above all, I would like to thank my amazing wife Kathrin for her love and non-stop care, it really kept me sane during these last few months. Thank you for being my proof-reader, editor and grammar checker, but most importantly being my best friend. I owe you so much that I cannot put into words.

Abstract

Stem cells have yet to contribute to their full potential in the field of regenerative medicine and further understanding of the underlying kinetics of cell differentiation could be the step forward. Various methods have been used to characterise stem cell lineage commitment. However, most of these techniques are end-point assays and provide very little information about the changes occurring in the early stages of the differentiation process.

This project aims to explore if the structural and geometrical specificity of the cytoskeletal components (actin in particular) encode information regarding cell lineage. Adipogenic and osteogenic differentiation lineages were selected, as they have been extensively studied over the past few decades. We have developed a novel approach to describe cells by defining their cytoskeletal and nuclear morphology in terms of 19 geometric measurements. This set of parameters has a range of complexity, extending from one dimensional (e.g. fibre length, fibre thickness) to compound geometrical readings (e.g. chirality and fibre alignment), while some estimate morphological and mechanical properties of the nucleus i.e. Poisson ratio and chromatin condensation. A proprietary image analysis algorithm is used to analyse fluorescent images of cells biochemically and mechanically stimulated to differentiate for a period of up to 10 days. Our analysis pipeline is currently optimised for images acquired at x20 magnification using epi-fluorescence but can be further adapted for high throughput live cell imaging.

Factorial analysis of the measured features showed that some parameters change markedly in the early stages of differentiation. More interestingly we observed these changes to be non-linear and non-monotonic. This analysis, in light with previously published literature on the subject has allowed us to more intricately hypothesise probable mechanisms involved with mechanotransduction which direct the lineage commitments. As our technique quantifies the morphology of individual cells, we used our extracted feature data to characterise each cell using a multivariate predictive model (LDA).

Table of Contents

List of Abbreviations

Reappearing abbreviations and symbols are defined below, abbreviations which are less frequently used are defined within the text itself.

AD	Adipogenic differentiat (-ion, ed)
ADM	Adipogenic differentiation media
AFM	Atomic force microscopy
APS	Ammonium persulfate
BSA	Bovine serum albumin
CSK	Cytoskeleton
DMEM	Dulbecco's modified eagle's medium
DMSO	Dimethyl sulfoxide
DNA	Deoxyribonucleic acid
FA	Focal adhesion
FBS	Fetal bovine serum
FGF	Fibroblast growth factor
FITC	Fluorescein isothiocyanate
hMSCs	Human mescenchymal stem cells
LDA	Linear discriminant analysis
MDS	Multidimensional scaling
mRNA	Messenger ribonucleic acid
OD	Osteogenic differentiat (-ion, ed)
ODM	Osteogenic differentiation media
PAA	Polyacrylic acid
PBS	Phosphate buffered saline
PCA	Principal component analysis
PCR	Polymerase chain reaction
PFA	Paraformaldehyde
RT	Room temperature
SC	Stem cells
SVM	Support vector machine
TEMED	Tetramethylethylenediamine
UPW	Ultra-pure water
xPan	Expansion media

List of Figures

List of Tables

Chapter 1 | Introduction

Stem cells are undifferentiated cells with the capacity to mature into several specialist cell types (Spradling, Drummond-Barbosa, & Kai, 2001). Their unique ability to replenish their reserves themselves and high plasticity make them extremely desirable for a wide range of applications (Li & Xie, 2005). In the last few decades they have held the prime interest for modelling diseases, drug development and cell-based therapies (Maciel et al., 2014). Stem cell therapy is continually being developed experimentally and clinically in the field of veterinary medicine (Fortier & Travis, 2011), yet, there is still a lot that we don't understand. It is widely accepted that mechanotransduction is the key mechanism by which stem cells determine their functional output. Whilst, it has also been reported that cells look visibly different when differentiated. Hence, it would not be farfetched to suggest that cells adopt morphologies that complement their function requirements, which would in turn require specific CSK and FA organisation.

The aim of this project is to investigate if the structural and geometrical specificity of the cytoskeletal components (actin in particular) encode information regarding cell lineage. We used a proprietary image analysis algorithm to extract a combination of existing and new morphometric features from cytoskeletal and nuclear images. Statistical analyses of these features were also conducted to describe and relate these features to known biological processes, as well as to evaluate their (group) effectiveness and (individual) influence in the multivariate classification of SC, AD and OD cells.

For this, the objectives of this thesis were segmented as follows:

1. Design an experimental protocol to acquire single cell images of differentiating hMSCs.
2. Optimise starting parameters for the differentiation to ensure the single cell sparsity for the longest possible duration.
3. Optimise the image acquisition protocol to maximise consistency of controlled factors.
4. Process cell images to quantify fluorescent signals from actin fibres and nucleus.
5. Define and calculate morphometric features.
6. Perform a feature assessment for machine learning.

The outline of this thesis is described in the following:

- *Chapter 1 – Introduction: This chapter includes an introduction on the thesis background, followed by the aims and objectives and an outline of the following chapters.*

- *Chapter 2 – Literature review: This chapter presents an introduction to the topics discussed in this thesis. Ranging from cell biology and stem cell differentiation to techniques used for the characterisation of stem cells.*

- *Chapter 3 – Methods and materials: This chapter gives an overview of the materials and methods used for the experimentation in this thesis.*

- *Chapter 4 – Optimum conditions for single cell image quantification of differentiating cells: This chapter includes pilot studies investigating optimum experimental conditions required for single cell image quantification of differentiating cells. Ideal starting cell densities and gel substrate stiffness were determined as well as morphometric features designed.*

- *Chapter 5 – Morphometric characterisation of stem cell differentiation: This chapter investigates how each of the 19 morphometric features evolves during differentiation glass substrates and how the aptness and influence of individual features can change the multivariate classification of our dataset.*

- *Chapter 6 – Effects of substrate stiffness on the morphometrics of cell differentiation: This chapter focuses on the influence of substrate stiffness on the 19 morphometric features during differentiation and compares the results to those obtained with glass substrates.*

- *Chapter 7 – Discussion and outlook: This chapter offers a general discussion on the findings presented in this thesis and provides an outlook for future work.*

Chapter 2 | Literature review

In the following chapter theory and state of the art for topics discussed in this thesis are given. The theory is separated into basic cell biology, mechanobiology and stem cell differentiation, followed by state of the art techniques used for stem cell characterisation including.

2.1 Cells

Eukaryotic cells are structural and functional constituent units of organisms. Although most of the cells in an organism are adapted to perform specific functions, a proportion of them are kept in a more adaptable state. This pool of compliant cells acts as a supply line for growth and repair throughout the life span of the organism. Eukaryotic cells have evolved to very elegantly segregate their essential operations and associate them to various membrane bound structures, known as cell organelles e.g. plasma membrane, DNA, cytoplasm ribosomes (Figure 2.1) (C. M. O'Connor & Adams, 2010).

In addition to this compartmentalisation of internal functions, they also have put in place a support and position system for these organelles called the cytoskeletal network. This docking system in turn heavily dictates the cell's geometric and mechanical architecture. This internal infrastructure contributes to its stiffness, mobility, as well as the transportation of cargo filled vesicles, individual molecules and cell organelles. The cytoskeletal network is highly dynamic and constantly going through remodelling to meet the instantaneous requirements of the cells (C. O'Connor, Adams, & Fairman, 2014).

The name cytoskeletal network derived from it not being a single component but rather a group of fibre types working together to perform various functions (C. O'Connor et al., 2014). Its functioning principles are identical to that of a tent, where a balance between opposing forces exerted by its elements stabilises its structure. Very similar to the musculoskeletal system in animals, cytoskeleton provides docking for cell organelles and allows the cell body to move about. Its dynamic in nature and can readily remodel itself in a completely new architectural configuration. This remodelling of CSK along with its integration with motor proteins enable cell mobility, e.g. the function of motile cilia is regulated by the interactions between cell membrane, cytoskeleton and its associated motor proteins (Alberts et al., 2008; Reece et al., 2013).

.

Cytoskeleton of a eukaryotic cell is characterised in three categories i.e. microtubules, microfilaments, and intermediate filaments. In comparison to other cytoskeletal structures, actin microfilaments will be discussed in more detail in the following (Section 2.1.3).

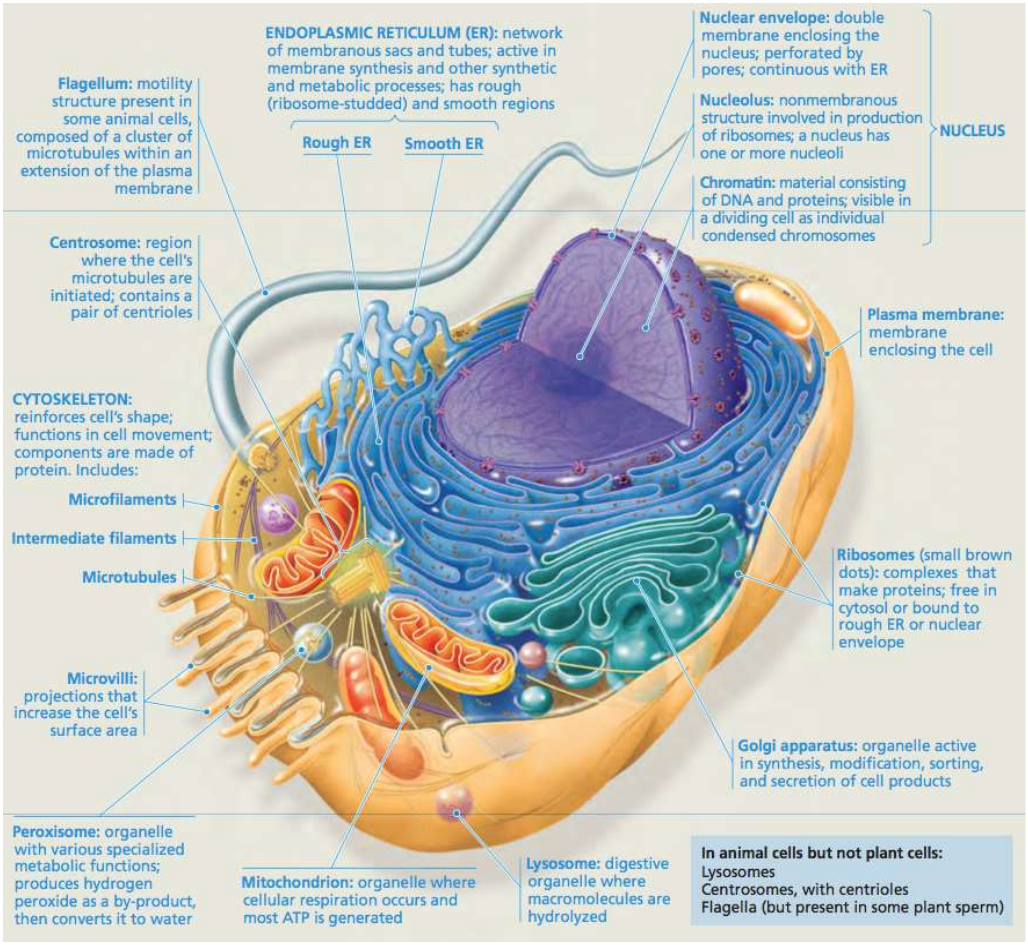

Figure 2.1 Eukaryotic Cell (cutaway view of generalised cell) (Reece et al., 2013)

2.1.1 Microtubules

Microtubules are hollow rods composed of tubulin globular proteins. A tubulin unit is a dimer, constituted by α-tubulin and a β-tubulin peptide. Microtubule filaments are a composite of subsequent dimers, about 25 nm in diameter. Along with providing support and shape to the cell, the most important function of microtubules is to assist with the transportation of organelles and secretory vesicles within the cell. The microtubules network serves as track for the associated motor proteins attached to cellular objects to be transported (Reece et al., 2013).

2.1.2 Intermediate filaments

A family of tension bearing fibres are categorised as intermediate filaments. All members of intermediate filaments have their diameter ranging from 8 to 12 nm; hence, as the name

suggest, diameters are smaller than microtubules and larger than microfilaments. Unlike microtubules and microfilaments, which are constantly remodelling, intermediate filaments are more permanent; they even remain intact after cell death, i.e. skin consists of dead cells containing keratin. Intermediate filaments specialise in resisting stretch to the cell's body. The fact that the nucleus is enclosed in a hutch of intermediate filaments, suggests that these fibres are also involved in fixing the positions of cell organelles (Reece et al., 2013).

2.1.3 Actin microfilaments

Actin microfilaments are globular actin proteins linearly joined up to form 7 nm wide actin fibres. Each microfilament is composed of two actin fibres twisted around each other. Microfilaments can also join side chains with the help of associated proteins to form networks architecture. These networks give cytoplasm a gel like consistency in contrast to the more fluidic consistency of cytosol. It is these actin filaments which, when working in conjunction with myosin motor proteins, enable cell mobility. Thousands of microfilaments and myosin fibres slide past each other allowing contractions required for a cell to move. It is also believed that actin-myosin contractions facilitate cytosol transportation by causing cytoplasmic streams (Alberts et al., 2008).

2.2 Actin

In cells, actin coexists as monomers and as filaments as show in Figure 2.2. A single monomer is composed of 375 amino acid peptides. These peptides aggregate to form dicotyledic-shaped structures, where each half is further compartmented into 2 substructures (Kabsch & Holmes, 1995; Sheterline & Sparrow, 1994). Enclosed between the two cotyledons is a nucleotide containing an adenosine triphosphate (ATP) or adenosine diphosphate (ADP) (Kabsch & Holmes, 1995).

These monomeric units bind together to construct a double strand, such that all the units are aligned directionally and each unit is bonding with 4 others. However, the strongest binding is along the length of the fibre (Dennis. Bray, 2001).

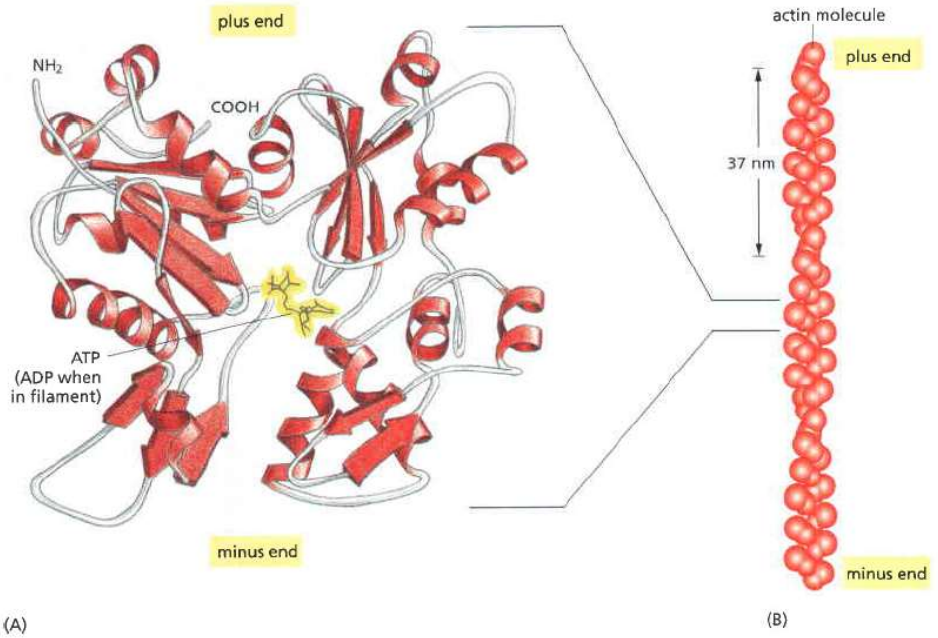

Figure 2.2 Illustration of an actin monomer and filament (A) actin monomer consisting of 375 amino acid peptides wrapped around histone with an ATP or ADP nucleotide (B) Organisation of actin monomers in the formation of a filament (Alberts et al., 2008)

2.2.1 Actin filament formation

Actin filaments can be polymerised in vitro in a suitable environment of ionic buffers. The process can be described in three stages, nucleation, elongation and steady state. Nucleation is a rather slow phase, during which, three monomers join to form a stable structure which acts as an initiation point for the rapid polymerisation phase i.e. elongation. Cells overcome this slower nucleation phase by producing proteins called actin nucleators. The Arp2/3 complex and formin family of proteins are well known for their role in the nucleation of actin filaments, whereas Spire is a protein whose role in this process has been more recently established. Unlike Arp2/3, Spire can initiate nucleation on its own and does not bind to the sides of the filaments which leads to branching (Schuldt, 2005).

In the elongation phase, actin monomers continually attach and detach at both ends of the fibre, which are called the barbed and pointed end. The rate of this polymerisation varies at both ends during elongation and eventually comes to an equilibrium referred to as the steady state. The concentration of the monomers at which polymerisation and depolymerisation reaches equilibrium is called the critical concentration C_c (Alberts et al., 2008; Sheterline & Sparrow, 1994). At C_c, the association and disassociation of actin monomers at the barbed and the pointed ends of the filament give rise to a phenomenon called tread milling, which in effect allows a fibre to move across the cytosol.

2.2.2 Actin structures and their associated function

Not only are actin filaments important components in the structural composition of cells, but they are even more crucial for a range of cellular processes, the most prominent of which are mitosis and motility. Its role in some processes is apparent across many cells types, while for some its more specific. Cell motility not only requires actin activities within the cell but also in the cell's surroundings. To be able to push themselves forward, cells are required to from focal adhesions with the substrate. To form these adhesions, actin filaments employ integrins, zyxin, paxillin, talin, vinculin and other proteins (Burridge & Connell, 1983).

2.2.2.1 Filopodia

Filopodia are protrusions of the cell membrane, which cells rely on to probe their environment (Figure 2.3). In a migrating cell they usually originate from the lamellipodia (Section 2.2.2.2) at the leading edge (Mattila & Lappalainen, 2008). A typical filopodial protrusion may contain a bundle of about 10-30 actin filaments held together by filament binding proteins, with a diameter ranging between 60-200 nm. In these bundles, barbed ends of the filaments face the protruding tip of the filopodium. The lengthening and the shortening of the filopodium is regulated by the balance of polymerisation and deplumation rates at the ends of the actin filaments (Mallavarapu & Mitchison, 1999). Moreover, the number of protrusions is influenced by the difference in stiffness of the cells and the substrate (Bastmeyer & Stuermer, 1993). Liou *et al.* (2014) showed that lung cancer cells grown on different stiffness substrates developed longer filopodia and appeared at higher densities on softer gels (Figure 2.3).

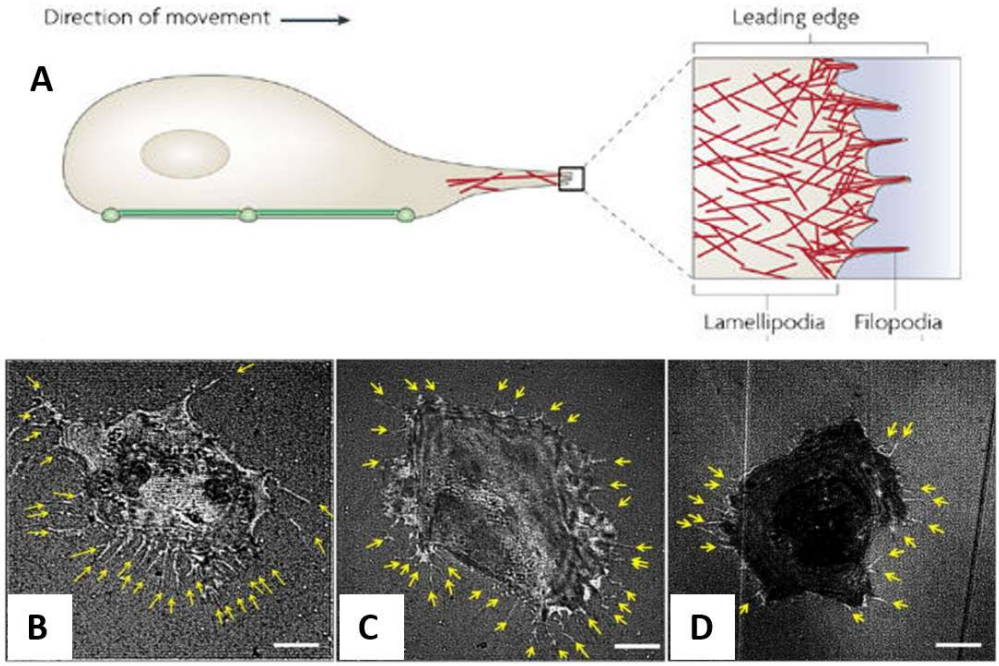

Figure 2.3 A) Illustration of filopodia at the leading edge, i.e. the protruding structures with barbed end facing the cell membrane (Mattila & Lappalainen, 2008) *(B) Images showing the influence of increasing (from left to right) substrate stiffness on the development of filopodia. The scale bar indicates 5 µm* (Liou et al., 2014)

2.2.2.2 Lamellipodia

Lamellipodia is formed at the leading edge when animal cells migrate on an adhesive substrate (Figure 2.4). It is a thin layer packed with a highly branched network of polarised actin filaments. Similar to the filopodia, barbed ends of the actin filaments are directed towards the membrane and the pointed end towards the centre of the cell (Small, Herzog, Häner, & Abei, 1994). Yang and Svitkina (2011) reported that most branching actin filaments in the lamellipodia form an angle of about 35° with the normal to membrane (Atilgan, Wirtz, & Sun, 2005). This orientation of the actin branches is the result of nucleation points on the existing filaments by Arp2/3 complexes (Mullins, Heuser, & Pollard, 1998). It is the collective force applied by actin filaments in this structure which stretches the cell membrane and allow the cells to spread and move forward (Ridley, 2011).

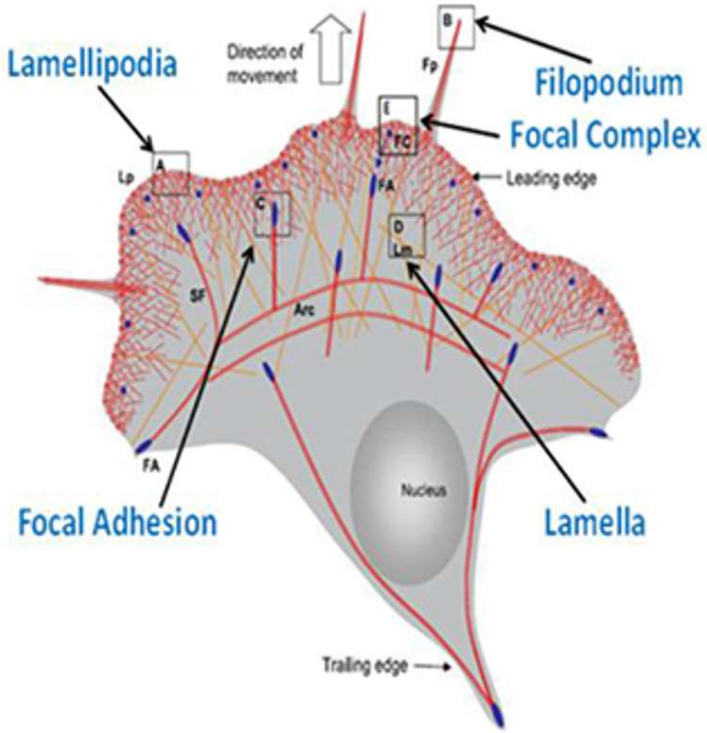

Figure 2.4 Illustration of lamellipodia at the leading edge, i.e. the meshwork of actin filament (red) with barbed ends facing the membrane (Alexandrescu, 2016)

2.2.2.3 Lamellum

Unlike filopodia and lamellipodia, lamellum consists of less dynamic but contractile F-actin bundles. The region where lamellipodia meets the lamellum, is where focal adhesions are formed with the substrate (Ponti, Machacek, Gupton, Waterman-Storer, & Danuser, 2004). These focal adhesions serve as 'molecular clutches' by preventing retrograde flow of the elongating acting filament bundles of the lamellipodia (Alexandrova et al., 2008; Giannone, Mège, & Thoumine, 2009). The reaction force provided by these clutches increase when focal adhesion complexes mature under stress over time, by slowing down the back flow of the actin bundles (Giannone et al., 2009). To prevent cells from being permanently anchored at one location, focal adhesions provide attachment points for the myosin powered stress fibres and transmit their contractions as traction forces against the substrate. This allows cells to move themselves forward whilst retracting their trailing edge pulling off any adhesions at that end (Jurado, Haserick, & Lee, 2004). Pushing of the membrane and pulling the cell body forward operate together to serve as cell motility function. This mechanism is illustrated in (Figure 2.5). In addition to the said functionality, focal adhesion complexes are also hypothesised to serve as mechanosensing elements. When stress fibres pull against the substrate via focal adhesions, they also sense its rigidity.

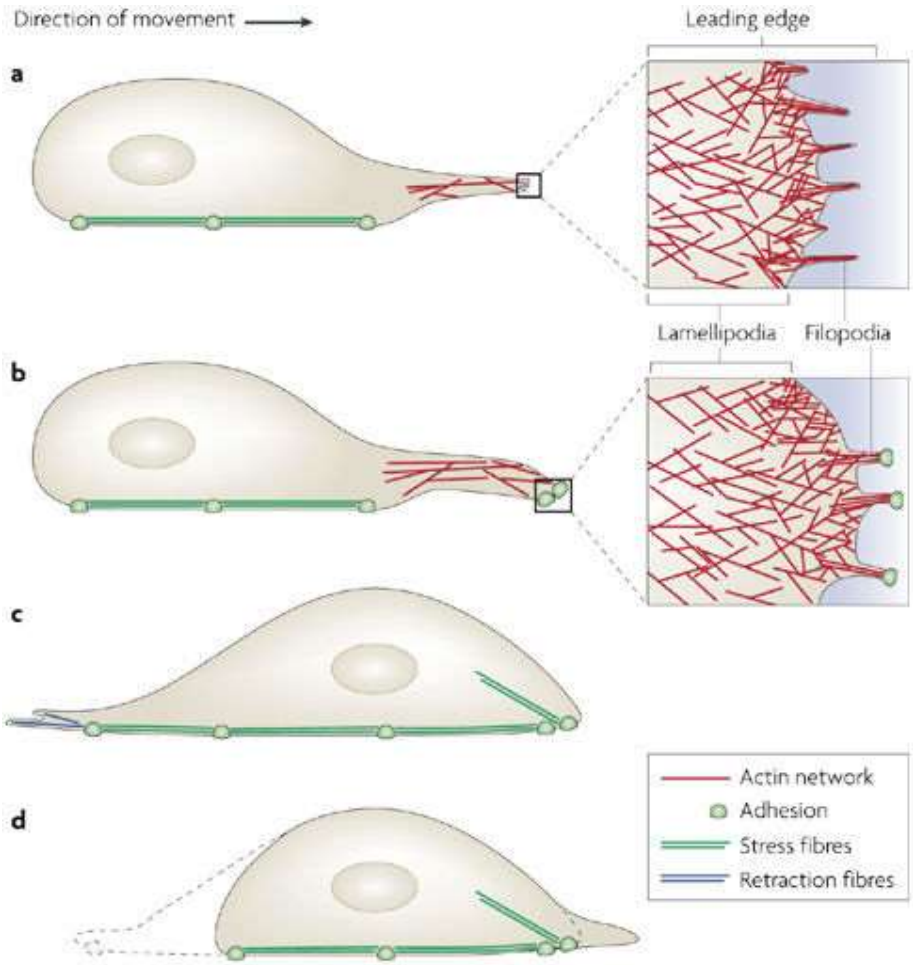

Figure 2.5 Illustration of steps in which lamellum enables cell mobility. a) The process is initiated with the formation of lamellipodia and filopodial protrustions at the leading edge (b) The extended region of the cell body forms new adhesions with the substrate (c) Contractions in the stress fibres connecting the newly formed focal adhesion would translocate the nucleas and the cell body forward (d) At the same time, stress fibre contraction in the rear of the cell body will promote focal adhesion disassociation from the substrate surfance and will call the trailing edge to retract (Mattila & Lappalainen, 2008)

2.2.2.4 Cell cortex

The cell cortex is a thin layer of actin filament stabilised by actin binding proteins and functionalised by myosin motor proteins (Figure 2.6) (D Bray & White, 1988). In addition to its crucial role during mitosis and cytokinesis, it is also contributing to the cell shape regulation and mechanical support to the cell membrane. On its own, the cell membrane is unable to resist shear stresses or apply traction forces to the surface of the substrate. The cell cortex is an integral component of the actin infrastructure responsible for cell motility (Hamill & Martinac, 2001).

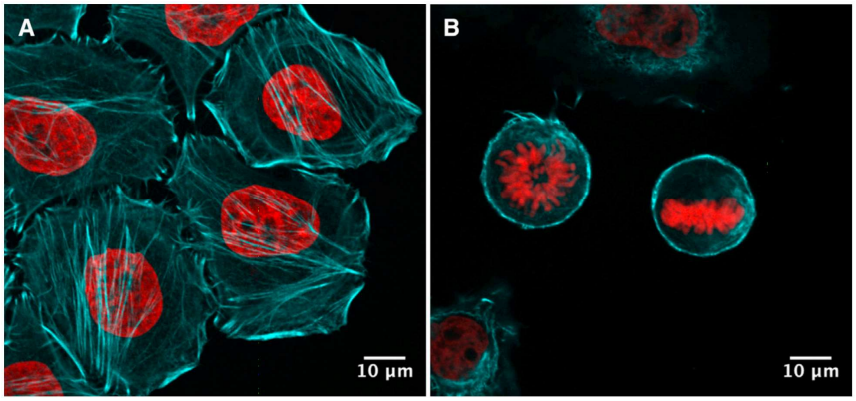

Figure 2.6 Illustration of the cell cortex for actin networks of HeLa cells. Staining was carried out with DAPI and Phalloidin, where red represents DNA and cyan represents F-actin. A) shows spread interphase cells, where actin is mostly present as stress fibres and B) shows mitotic round cells consisting of mostly cortical actin (Chalut & Paluch, 2016)

2.2.2.5 Stress fibres

As mentioned earlier, stress fibres are typically stretched from one end anchored at the focal adhesion and the other attached close to the cell nucleus (Figure 2.7). It is composed of actin filaments, myosin II motor proteins and α-actinin and is hypothesised by many experts to be serving as a mechanotransmitter between the nucleus and the cell's surroundings (Stricker, Falzone, & Gardel, 2010). The mechanical properties of the stress fibres themselves are highly influenced by the distribution of myosin II motor proteins along its length, and this distribution is maintained according to the mechanical needs of the cell (Lu, Oswald, Ngu, & Yin, 2008). Deguchi et al. in their 2006 study suggested that the strain regulated elastic modulus of stress fibres is a functional characteristic of their role as mechanosensors (Deguchi et al., 2006).

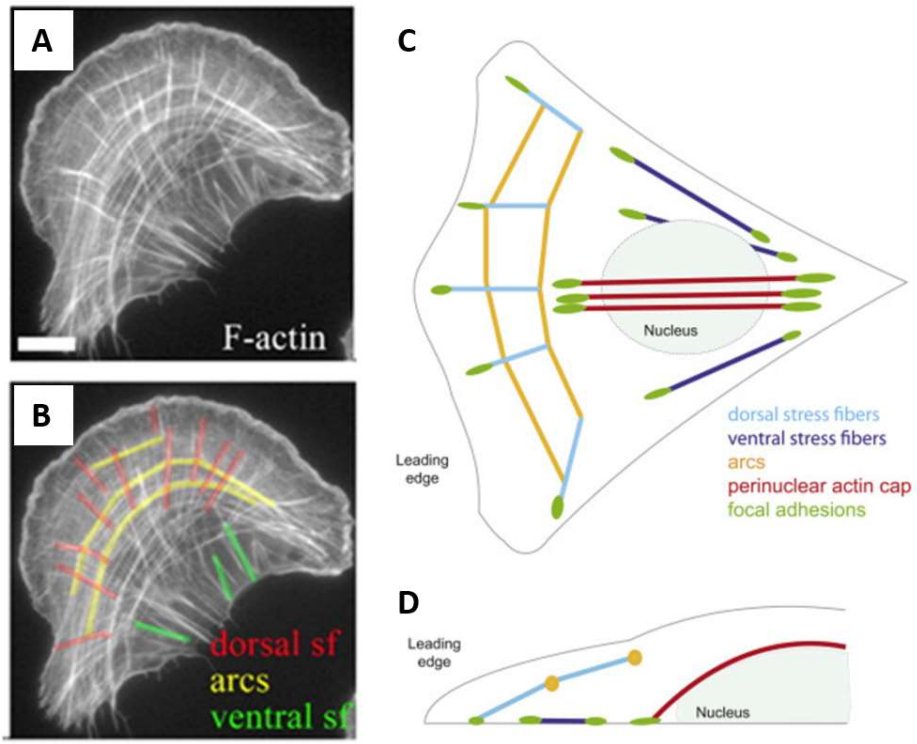

Figure 2.7 A) F-actin stained U2OS osteosarcoma cell and B) highlighting three different actin stress fibres: dorsal, arcs and ventral. (Pellegrin, Mellor, Barry, Andrews, & Jester, 2007) *Schematic of actin stress fibres in migrating cells from C) top and D) side view, showing dorsal, ventral, arcs and perinuclear actin cap* (Burridge & Guilluy, 2016). *The scale bar in (A) indicates 10 µm.*

2.3 Nucleus

Among all the cell organelles found in eukaryotic cells, the nucleus is the largest and stiffest. In mammalian cells its around 6 µm in diameter and is found in all cell types except for red blood cells. Its primary purpose is to store, protect and facilitate the transcription and replication of DNA. Along with associated proteins for nuclear processes, the DNA is enclosed in a bilipid layers called the nuclear envelop. Although the nuclear cavity is segregated from the cytoplasm by this membrane it stays functionally connected with the outside through nuclear pores by allowing selective transport of material e.g. RNA and water (Strambio-De-Castillia, Niepel, & Rout, 2010). The nuclear membrane is in turn capsulated by a mechanically supportive mesh of intermediate filaments known as nuclear lamina (Dechat et al., 2008).

The DNA molecule is around 2 m long in mammalian cells, and therefore requires extensive compaction to fit in a very small nuclear cavity. This is accomplished by an energy reliant process known as chromatic condensation. In this process, the entire length of DNA is wrapped around histones as nucleosomes to form an 11nm wide fibre, as shown in the Figure 2.8.. A nucleosome is the smallest chromatin substructure which is formed when a 147 base pair long section of DNA molecule makes 1.65 turns around a histone octamer (Luger, Dechassa, & Tremethick, 2012).

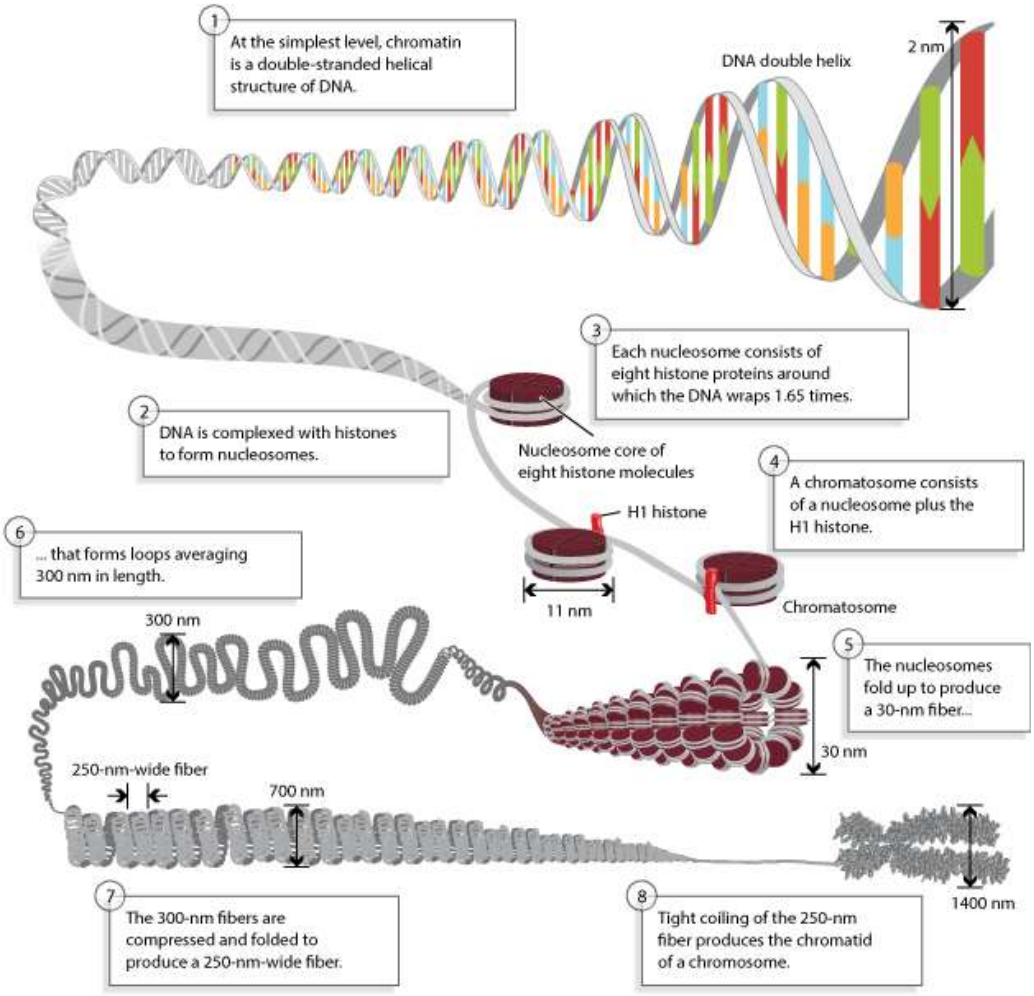

Figure 2.8. Schematic showing the packaging mechanism of DNA into chromosomes (C. O'Connor et al., 2014)

Each nucleosome is joined with the next nucleosome by a 20-80 base pair long string of DNA called the "Linker DNA". Histone beads interact with others across the entire length of the fibre to form a higher order 3D chromatin construct (Rui P. Martins, Finan, Farshid, & Lee, 2012), which is highly dynamic and can go under substantial reconfiguration in response to any mechanical (sliding, splitting) or chemical (histone modification) stimuli (Luger et al., 2012). Nevertheless, even the compaction gained with the primary and secondary folding of the DNA molecule is not enough to fit it completely inside the nuclear cavity, thus it further bends and folds onto itself to form a higher order chromatin structures.

2.3.1 Organising a genome

The primary function of the condensation process is to enable a very large molecule to fit in a very small space, however, this cannot be achieved at the cost of the cell's ability to regulate gene expression. DNA exists in regions of lightly (euchromatin) and highly (heterochromatin) condensed chromatin. In contrast to the heterochromatin, the loose packed region of

euchromatin is where the transcription process is carried out. The regulation of gene activation is further regulated by the assembly of chromatin into distinct chromosomes (Schardin, Cremer, Hager, & Lang, 1985). It has been reported in studies that transcriptionally active chromosomes are positioned closer to the centre of the nucleus and inactive chromosomes near the edges (Goetze et al., 2007). Furthermore, It is believed that mechanical forces applied to the cells can be transmitted to the nucleus via stress fibres and can alter the chromatin condensation and hence the gene expressions (Volpi et al., 2000). The process underlying this regulation of gene expression is when histones undergo chemical changes. Depending on the mechanism involved, these changes can result in the disengagement among nucleosomes as well as between nucleosomes and the higher chromatin structures (Kouzarides, 2007). Of all the modification mechanisms that have been studied, acetylation has the most effect on the de-condensation of chromatin.

2.4 Mechanobiology

2.4.1 Actin and associated components

In vivo, cells are subjected to a wide range of mechanical stimuli from their surroundings, i.e. compression, tension, shear or hydrostatic forces, and cells detect these cues through passive or active mechanosensing. In passive sensing, external forces, are for example transmitted via integrin to the stress fibres, and any increase or decrease in their tension triggers a signalling cascade. Whereas in active sensing, stress fibres can generate and exert pulling force to their extra cellular surroundings via integrin to detect its rigidity, surface topography or ligand density (Holle & Engler, 2011). The active mechanosensing requires cells to organise their cytoskeleton, as well as form adhesions in a suitable arrangement. Researchers have reported that mechanosensing plays an essential role in the development of an organised tissue repair, as well as in regulating the immune response to many diseases, especially those involving changes in the normal pathology of the tissue.

As discussed in section 2.2.2, the actin cytoskeleton is physically connected to the cell's surrounding via adhesion complexes. These focal adhesions are regularly receiving and transmitting forces in both directions of the membrane. These stimuli often bring about an overall response from the cells in the form of a change in their shape, mobility or both (Gillespie & Walker, 2001). The involvement of adhesions cannot be understated during the cell's motility, during which they are constantly sensing their substrate's characteristics (stiffness, topography etc), as well as being formed and disintegrated based on the functional requirements, across the cell's body (Vogel, 2006). What distinguishes actin stress fibres from other types of actin filaments is their association with myosin II motor proteins, which

enables them to actively contract. Though regardless of their function the modulus of the F-actin network stays independent. It is believed that this stress fibre and adhesion complex plays an important role in the regulation of cell polarity and consequently its fate (McBeath, Pirone, Nelson, Bhadriraju, & Chen, 2004; Svitkina, Verkhovsky, McQuade, & Borisy, 1997).

2.4.2 Nuclear mechanics

The size and shape of the nucleus not only varies between cell type and the organism but also during the cell cycle itself (Maeshima, Iino, Hihara, & Imamoto, 2011). This variation in size of nucleus is owed predominantly to the level of compaction as well as the amount of DNA packed in it. Nuclear mechanical properties are strongly influenced by the state of its constituent components i.e. nuclear envelop, chromatin organisation and nuclear lamina (Webster, Witkin, & Cohen-Fix, 2009). As mentioned in section 2.3.1, the organisation of chromatin can be altered mechanically, and since the actin network maintains a stable architecture physically linking the nucleus to the adhesion sites, the mechanical environment of the cell subsequently has a significant impact on gene expression and consequently on its fate (Dahl, Ribeiro, & Lammerding, 2008; Wang, Tytell, & Ingber, 2009). It has been reported in the literature that cells seem to maintain certain nucleus to cell body ratio (Jorgensen et al., 2007). It is hypothesised that this ratio is crucial for the transcriptional activities inside the nucleus. It has also been observed that a change in nuclear size correlates with the regulation of certain gene expressions (Wu, Rolfe, Gifford, & Fink, 2010). The mechanism by which the nuclear size is regulated can be envisioned as the effect of changing resulting forces acting upon a flexible enclosure (nuclear membrane). Predominant forces being the outward pull applied by the actin network and the inward pull by condensation of chromatin. Under such forces, the nuclear membrane is supported by the nuclear lamina which is also responsible for the overall nuclear stiffness. Stem cells in the absence of a constituent component of nuclear lamina (Lamins A), have much softer nuclei and are therefore easily deformed by the application of internal or external forces (Schäpe, Prauße, Radmacher, & Stick, 2009). It has been reported that with the expression of Lamins A during differentiation, the cell nucleus becomes stiffer and resists deformation (Pajerowski, Dahl, Zhong, Sammak, & Discher, 2007). The more easily expandable nuclear cavity also allows stem cells to have more of the DNA as euchromatin than specialised cells, which is needed for their higher plasticity towards various specialist lineages. Moreover, the cell nucleus has been reported to be about 3-10 times stiffer than the surrounding cytoplasm (Dahl & Kalinowski, 2011).

2.4.3 Mechanotransduction

It refers to the process by which mechanical stimuli to biomolecules is translated into the expression of chemical signals. This happens when the application of forces on certain proteins exposes active sites to enable and initiate the binding of other protein; the process which can trigger biochemical signalling. One of the well-studied mechanosignalling cascades involves the enrolment of vinculin at the adhesion complex when talin is stretched (del Rio et al., 2009). This initiates further signalling that leads to the cytoskeletal remodelling, gene expression, as well as changes in nuclear and cellular shape. Mechanotransductions have shown to accomplish the job often quicker than chemical signalling alone. This concept is well illustrated in the Figure 2.9, when external force is applied to the focal adhesion, it is projected on to the nucleus (via stress fibres) which can deform chromatin structures to expose previous hidden sites (shows as euchromatin). In many cases mechanical and chemical signalling work in coordination; where an application of external force or active contractions produced by the stress fibre network can initiate a biochemical response and vice versa. At macro level, mechanotransduction becomes more complex and effective, where a stimulus received at a tissue level is transported to distant target nuclei almost instantaneously and simultaneously (Wang et al., 2009). When undisturbed, cell components are held in a stasis by force balance, which when perturbed, often inflict deformation of their nuclei, resulting in chromatin alteration and ultimately gene expression (Mazumder & Shivashankar, 2007).

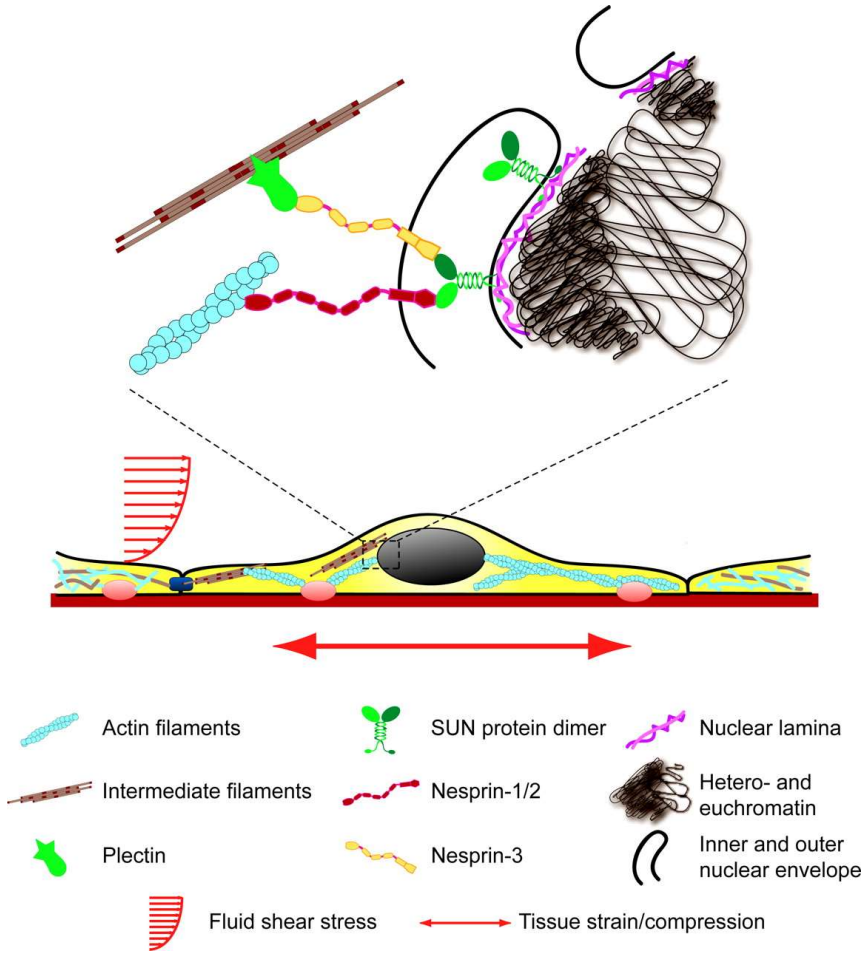

Figure 2.9 Detailed schematic displaying pathway of physical transmission of external forces (Fluid shear stress or Tissue strain) via cytoskeleton to the nucleus; which may pull against the chromatin compaction to expose previous inaccessible genes (Dahl et al., 2008)

2.5 Stem cells

Stem cells are undifferentiated cells with the potency to be matured to many specialist lineages (Spradling et al., 2001). They can further be classed as totipotent, pluripotent, multipotent, and unipotent, thought it could be argued that unipotent cells are instead the progenitor of stem cells with differentiation options limited to only one cell type (Slack, 2000). Stem cells can (theoretically) divide an infinite number of times into cells that are identical to the parent cell. This attribute is responsible for regulating their population in vivo during the life span of the organism (van der Kooy & Weiss, 2000). This unique ability to replenish their reserves themselves and high plasticity is extremely desirable for a wide range of applications (Li & Xie, 2005).

In the last few decades they have held the prime interest for modelling diseases, drug development and cell-based therapies (Maciel et al., 2014). Stem cell therapy is continually being developed experimentally and clinically in the field of veterinary medicine (Fortier &

Travis, 2011). Moreover, their remarkable attribute to attract low levels of immune response from host organisms even allows them to be used for allogenic implantation (Lanza, 2009).

Where stem cells are harvested from dictates their characteristic features i.e. potency, stemness etc. The two of the most commonly studied type of stem cells are embryonic and adult stem cells.

Embryonic stem cells are pluripotent at conception, though continually become less divergent through the course of foetal development. Organisms, however, require a consistent pool of stem cells supplied to recover from damage caused by injuries or routine wear and tear. It is proposed that these pools are virtually located in most adult tissues and supply somatic stem cells throughout the lifespan of an organism (Chamberlain, Fox, Ashton, & Middleton, 2007). Somatic stem cells inherit some of the fundamental features of their earlier forms (embryonic stem cells) i.e. the ability to go through infinite self-renewal cycles (theoretically) and the potency to differentiate into more than one cell type (Schofield, 1978; Tumbar & Fuchs, 2009). Within tissues, stem cells are stored in a specialised microenvironment called the "niche". Cells are sensitive to extracellular cues from the environment, which influences their function. Mechanical parameters of the niche along with the methylation of the encrypted genetic material, keeps stem cells dormant until they are required following an injury or for natural growth of the tissue (Li & Xie, 2005; Morrison & Spradling, 2008).

Mesenchymal stem cells (MSCs) are for example non-hematopoietic adult stem cells that participate in the development and regeneration of connective tissues and can differentiate into bone, cartilage, muscle, ligament, tendon, and adipose cells (Li & Xie, 2005). It is vital to comprehend how stem cells are influenced by their niche in order to sustain or modify their characteristics (Tumbar & Fuchs, 2009).

Furthermore, despite having different functional characteristics, it is proposed that at a molecular level all kinds of stem cells share many similarities at nuclear transcription level; similarities that are termed as stemness by some (section 2.5.2). This proposal is backed by the similarities in the transcription profiling of various stem cells found in many research studies.

2.5.1 Isolation

MSCs have been extracted (with considerable purity), proliferated and studied across various species including mice, rats, cats, dogs, rabbits, pigs, and baboons (Javazon, Beggs, & Flake, 2004). Stem cells have been extracted from adipose tissue, amniotic fluid, periosteum, and foetal tissues (Campagnoli et al., 2001; in `t Anker et al., 2003; Nakahara et al., 1991; Zuk et

al., 2002); bone marrow, however, is the preferred site of extraction for research purposes. Although bone marrow tissue contains a very small percentage of stem cells (i.e. ratio of 1 to 10^4 of the total nucleated cells), they can be expanded in vitro to achieve a required number, while preserving their stemness (Chamberlain et al., 2007; Javazon et al., 2004).

Any culture of MSCs with 70-80 % confluency may contain a morphologically variant population of narrow spindle shaped to more spread polygonal shaped cells (Javazon et al., 2004). It is of importance to know that even though phenotypic biomarkers for stem cells are well established, they are not unique to mesenchymal stem cells. Therefore, we can accurately identify stem cells within a population, but we cannot have 100 % certainty of their mesenchyme origin (versus i.e. a hematopoietic origin), for these reasons, MSCs are most conveniently/reliably characterised by their tri-differentiation potency.

2.5.2 Stemness

Theoretically, embryonic stem cells can differentiate into any type of specialised cell. With age, they lose their plasticity, giving rise subtypes, which based on their tissue of origin will have dissimilar lineage restrictions (Spivakov & Fisher, 2007). Mechanical and soluble cues from their niche not only dictates their fate but also the extent of self-renewal. Many soluble signalling molecules are known to influence this process i.e. hh, Wnts, BMPs, FGFs, Notch, SCF, Ang- 1, and LIF or Upd through the JAK-Stat pathway. In many species, BMPs and Wnts are known to contribute in maintaining stemness and by consequence the differentiation as well. Some of the above mentioned growth factors/cytokines are effective in regulating one particular characteristic across stem cell types, whilst others are effective on stem cells across various species (Li & Xie, 2005).

As stem cells mature their actin network develops, their nuclear membrane stiffens and their chromatin reorganises to be specialised at expressing a precisely defined level of certain proteins, in a process known as differentiation. As of now, this process is understood to be one way, at least for all practical purposes. Once a stem cell is transformed into a specialised cell type, the reconfiguration of chromatin compaction ensures that it keeps on expressing the type and levels of genes required to functionally assimilate with the other cells of the tissue (Rui Pires Martins, Ostermeier, & Krawetz, 2004).

2.5.3 Applications

It has been shown that when MSCs were introduced in circulatory systems of the host organism, they were able to locate injury sites and differentiate in response to the local cues (Gojo et al., 2003). Whilst another approach is to differentiate (allogeneic) stem cells in vitro culture before introducing them to the treatment site (Mobasheri, Kalamegam, Musumeci,

& Batt, 2014; Tuan, Boland, & Tuli, 2003). In an application of the later approach, Guilak *et al.* (2009) integrated biomaterial constructs with traditional cell culture techniques, with the aim to better prepare stem cells for later implantation into the treatment site by simulating that environment in vitro. Guilak *et al.* (2009) integrated biomaterial constructs with traditional cell culture techniques, with the aim to better prepare stem cells for later implantation into the treatment site by simulating that environment in vitro.

2.5.4 In vitro culture

Different types of stem cells require different in vitro culture conditions to sustain and proliferate. MSCs are one of the most commonly studied stem cell type with well-developed in vitro culture conditions (Spradling et al., 2001). Maciel et al., in their 2014 study recognised 6 distinct shapes MCSs display on high stiffness substrates. Some of these 6 shapes were variations of spindle geometry and some were more spread out cell bodies. Spindle shaped cells had a higher aspect ratio, nucleus located closer to the centre and relatively much less cytoplasmic volume in comparison to more spread out cells. Spindle shaped cells either had a cytoplasmic process on each end of its length (Figure 2.10 A), three of these processes forming a Y-shape (Figure 2.10 B) or had most of its mass on one end with a narrow projection trailing in the other direction (Figure 2.10 C). More spread-out cells on the other hand, appeared in rectangular (Figure 2.10 D) and rounder shape (Figure 2.10 E), some with low cytoplasmic basophil (Figure 2.10 F) (Maciel et al., 2014).

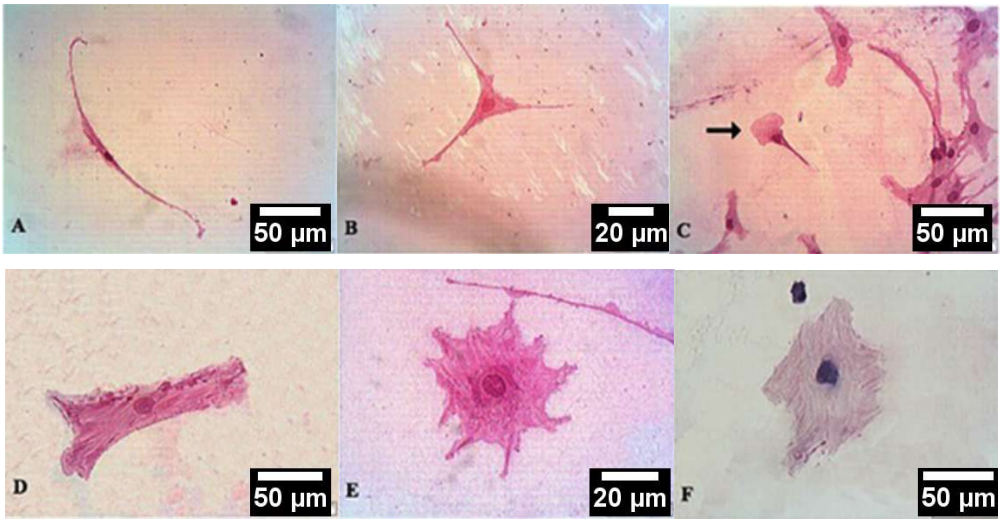

Figure 2.10 Representative images of different spindle-shaped (A, B and C) and widespread cells (D, E and F) taken with a phase contrast microscope with Wright's stain (Maciel et al., 2014)

2.5.5 Differentiation

A large amount of research has been focused on differentiating stem cells in vitro, with the idea of later delivering the differentiated cells into the damaged tissue. Biochemical differentiation has been extensively used for the past few decades. Only recently the importance of mechanical stimulus has been discovered, and several studies have used various mechanical cues to drive differentiation.

2.5.5.1 Signalling pathways

It has been reported that stem cells commit to AD and OD lineage in response to blobbed and stretched architecture (respectively), which were in turn regulated by the expression of negative RhoA and active RhoA, respectively. It was found, that this RhoA-ROCK commitment signal required actin-myosin-generated tension (McBeath et al., 2004). Similarly, the condition of musculoskeletal tissue during morphogenesis is mediated by a number of growth factors/cytokines i.e. hedgehog proteins (Hhgs), Wnt proteins, Notch ligands, members of TGF-β superfamily of growth factors, or FGFs. TGF-β1 is recognised as one of the earliest growth factors to influence chondrogenesis. It has shown to regulate the production of fibronectin and N-CAM (Han et al., 2007). BMPs have also shown to contribute to the development of bone and cartilage by guiding the lineage determination of stem cells (Han et al., 2007; Potian, Aviv, Ponzio, Harrison, & Rameshwar, 2003).

2.5.5.2 Biochemically induced differentiation

Biochemical differentiation has been extensively used for the past few decades. Only recently the importance of mechanical stimulus has been discovered, and several studies have used various mechanical cues to drive differentiation.

A classic method of differentiating MSCs in vitro is by incubating cells under appropriate culture conditions with soluble induction factors. Over the last few decades numerous studies have attempted to differentiation MSCs into mesenchymal cell lineages i.e. osteocytes, adipocytes, chondrocytes, tenocytes, skeletal myocytes, neurons, and endothelial cells (Pittenger, 1999; Reyes et al., 2001; Wakitani, Saito, & Caplan, 1995; Woodbury, Schwarz, Prockop, & Black, 2000). Some of these differentiation protocols have not been optimised yet and despite of expressing biomarkers associated to a certain cell type, these cells may lack some essential functional features. For instance, in contrast to the findings presented in 2000 by Woodbury *et al.* on neurogenic differentiated cells, Hofstetter *et al.* highlighted in 2002 the lack of ion channels required for voltage induction in those neurons. Among the entire above-mentioned set of cell lineages that could be induced through soluble factors in MSCs, osteogenic, adipogenic and chondrogenic differentiation

protocols are some of the most developed and extensively tested. These three techniques are briefly described below.

OD can be induced in MSCs by incubating the cells for about two to three weeks with ascorbic acid, B-glycerophosphate and dexamethasone in specific concentrations. Over time, the cell culture will accumulate alkaline phosphatase and calcium deposits (Pittenger, 1999), which would be tested by staining the sample with alizarin red and von Kossa techniques (Chamberlain et al., 2007).

For AD, cells are cultured in a typical MSCs culture media with the addition of dexamethasone, insulin, isobutylmethylxanthine (IBMX) and indomethacin. With the progression of differentiation, lipid filled vacuoles will appear in the cells and can be assessed for identification with oil red O staining (Pittenger, 1999).

To lead MSCs into chondrogenic differentiation, cells must first be allowed to lump together (i.e. pellet formation through centrifugation), the pellet can then be cultured for 2-3 weeks in a culture media prepared with Insulin-Transferrin-Selenium-G Supplement, Linoleic acid, L-ascorbic acid, Dexamethasone, TGF-β3, L-proline, Bovine serum albumin (BSA), Sodium pyruvate solution and DMEM (High Glucose, GlutaMAX) (Mackay et al., 1998). Successfully differentiated cell culture can be positively assessed with toluidine blue by verifying the presence of glycosaminoglycan (Kopen, Prockop, & Phinney, 1999). Differentiation culture conditions, however, are unlikely to reflect the physiological signals MSCs receive in vivo. There have been some recent reports investigating the role of mechanical stimuli on MSCs in culture (Chamberlain et al., 2007).

2.5.5.3 Stiffness induced differentiation

Some of the very first studies to investigate the effects of mechanical cues on stem cells used substrate modulus as their independently variable parameter. Ingber suggested in 2004 that the cytoskeletal bears self-induced tension as it applies contractile force on the surface of the substrate through integrin adhesions. Through this mechanism, cells are able to detect the stiffness of their surrounding tissue and hence are able to direct their differentiation response. Researchers have examined this by culturing cells on substrates of varying elasticity and monitoring their lineage commitments. Engler *et al.* reported in 2006 that cells when grown on pulposus material (simulating brain tissue stiffness) differentiated to neurons; whereas cells adapted myogenic and osteogenic lineages when cultured on material of intermediate and higher stiffness, respectively. Manipulating the cross-linking concentration of polyacrylamide gels can produce substrates with a multitude of elastic properties. AFM measurements deduced that stiffer substrates give rise to stiffer

phenotypes. Another study was carried out on neural cell cultures grown on gels of moduli ranging from 10 to 10000 Pa. Cells responded poorly to softer material (10 Pa) by showing reduced spreading, proliferation and differentiation. Whereas cells on material with moduli approximating brain tissue (i.e. 100 Pa) responded best by expressing the highest levels of neural biomarker i.e. β-tubulin III. However, substrates with Young's modulus higher than 1000 Pa derived cells towards glial differentiation (Saha et al., 2008). Similarly, in 2009 Winer *et al.* were able to show that MSCs when grown on substrate with moduli matching that of bone marrow tissue kept cells in a dormant state. The elasticity of cell culture substrate is now considered to be integrant in guiding stem cell fate in vivo and in vitro (D E Ingber, 2004; Saha et al., 2008).

A caveat to such methods of differentiation is the fact that many cell niches have similar elastic properties, which may make it extremely difficult to achieve multiple cell lineages with similar mechanical loadings. This indicates to the complexity of the processes regulating the cell stem cell population and lineage determination in vivo, and hence calls for the development of more sophisticated differentiation protocols (Watt & Hogan, 2000).

2.5.5.4 Shape induced differentiation

Cell shape is known to regulate stem cell differentiation during embryonic development (Hofstetter et al., 2002) and, just as for the matrix stiffness, effects of cell shape have also been of interest to researcher. In 1972, Manasek *et al.* associated cell shape as a fundamental parameter to myocardial development in vivo. In most studies of this nature, variable cell shapes have been achieved through interactions with bioengineered scaffolds. When embedded in a 3D construction of culture environment, cells adopt relatively spheroidal geometry which has shown to influence cells differently as to when cells are cultured in 2D on a flat surface. In a study published by Holtzer *et al.* in 1960, chondrocytes when cultured on flat surface, lost their chondrogenic phenotype to a more fibroblastic phenotype. Rounded cell morphology could also be achieved by the reorganisation of actin cytoskeleton with soluble factors. In the 1980's Newman and Watt (1988) as well as Zanetti and Solursh (1984) investigated the effects of this method on lineage commitment and their results showed considerable presence of chondrogenic molecular markers. Various other studies reaffirmed the chondrocytic fate of stem cells when cultured in 3D construction, either as cell pellet or embedded in bio-scaffolds (Guilak et al., 2009). In 2008, McBride and Knothe Tate were able to show a positive correlation between increasingly rounder cell shapes to higher expression of biomarkers associated with chondrogenesis. With the use of

more adherent bio constructs (i.e. fibrin or gelatin), Cheng *et al.* (2009) were able to achieve more spread cells, which differentiated into a fibro chondro-phenotypic lineage.

To further explore this concept, researchers indirectly controlled cell shape by manipulating the area available for cells to adhere on the substrate. This approach known as 'micro patterning', finely imprints adhesive proteins on the surface of a substrate. On smaller patterns, cells took on a puffed-up shape in comparison to a more flattened morphology on larger protein islands. These changes in shape are a result of the actin cytoskeleton reorientation and selective integrin attachments. This shape controlling approach pushed rounder cells (on small islands) towards AD and flattened cells were derived towards an OD phenotype (McBeath et al., 2004). Figure 2.11 represents the findings of the investigation.

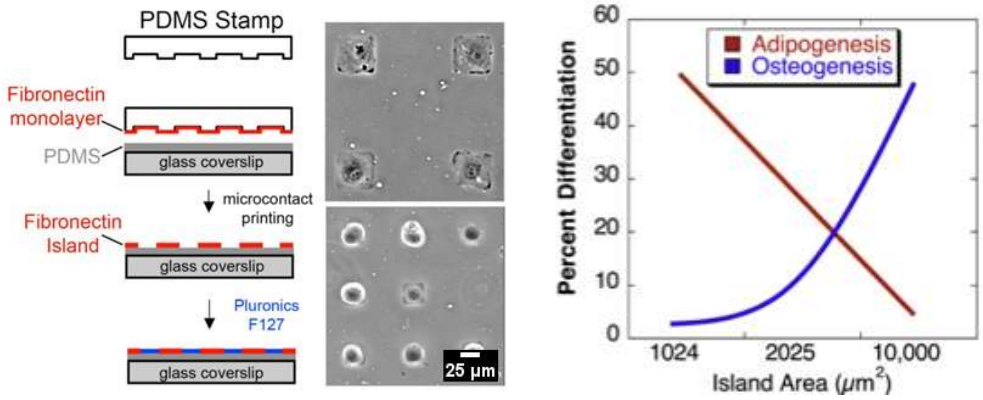

Figure 2.11 Control of cell shape through micro contact printing regulates differentiation of MSCs (Guilak et al., 2009) *(scale added)*

Interestingly, blocking Rho/ROCK signalling did not yield the same differentiation products, confirming that changes were brought on by Rho/ROCK mediated reorganisation of filamentous actin cytoskeleton. This was also backed up by studies presenting continuous variation in the cytoskeleton architecture (Sonowal, Kumar, Bhattacharyya, Gogoi, & Jaganathan, 2013) and mechanical integrity of the cell during the differentiation into osteocyte or chondrocyte (Bongiorno et al., 2014; Kwon et al., 2011).

Claiming that a variable cell shape was the only affecting parameter in determining cell fate in these studies could be questioned as the consequent effect of change in localized stress and osmotic variation was not addressed. Though some of these studies show that the effects of cell shape are exclusive to cellular signalling consequential to adhesion mechanics and other physical influences (Meyers, Craig, & Odde, 2006; Neves et al., 2008).

2.5.5.5 Nano-topography induced differentiation

We previously discussed the ability of cells to detect geometrical characteristics of their environment. Cells however are shown to be sensitive to even nanoscale geometry of their

surroundings i.e. surface topography, fibre thickness and density. Adult rat progenitor cells from the hippocampus grown on a laminin modified polystyrene pattern (grooves of 13 µm wide and 4 µm high) were realigned in the direction of the grooves (Recknor, Sakaguchi, & Mallapragada, 2006). In a similar study by Yim *et al.* (2007), Yim *et al.* (2007), cytoskeletal and nuclear alignment with grooves was observed. In both studies elevated levels of molecular biomarker, i.e. microtubules- associated proteins, were detected. Christopherson et al. (2009) seeded cells on the laminin covered electrospun fibres, with sizes ranging from 283 nm to 1452 nm. On finer fibres, cells were observed to spread well in all directions and cell aggregation was discouraged, whereas elongated cell shapes were adapted on thicker fibres.

Earlier discussed studies indicate that variation in the nano-geometry of the adhesion surface may mediate the distribution of focal adhesions and hence the cytoskeletal architecture of the cell (Figure 2.12 A). As surface nano-topography has shown to affect stem cell proliferation and differentiation and considering its effect on the cytoskeletal architecture, it is highly likely that Rho/ROCK mechanisms are involved (Arnold et al., 2004). This idea is also supported by Gerecht *et al.* (2007), who reported that varying nano-topography affected F-actin, vimentin, γ-tubulin, and the α-tubulin skeletal structure. They also mentioned that using actin-depolymerising factors prohibited the effects of varying surface nano-architecture on the proliferation and differentiation of stem cells. Though the effects of nano-graphic features (i.e. size and height) could also be due to the effective stiffness of the material perceived by the cell (Figure 2.12 B) (Discher, Janmey, & Wang, 2005; Saha et al., 2008).

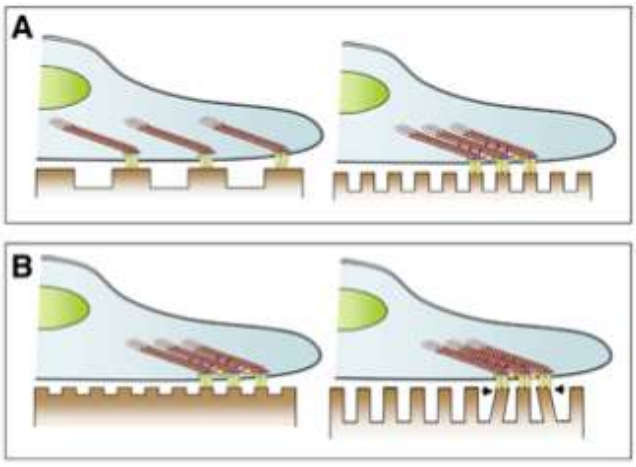

Figure 2.12 Variations in focal adhesions to different (A) nano-geometry and (B) mechanical properties of the ECM (Guilak et al., 2009)

2.5.5.6 Mechanical loading

Cells are constantly subjected to mechanical perturbation throughout the life of an organism. These mechanical interactions are suggested to modulate tissue growth and repair by directing the proliferation and lineage commitment of stem cells (Donald E Ingber, 2003). Recently, many scientific investigators have exhibited interest in studying consequences of in vitro mechanical cues on stem cells embodied in 3D constructs. A critical barrier in such studies poses the difficulty in isolating the effect of individual mechanical signals in any physical interaction. In most of these cases, the influence of a secondary mechanical signal is inevitable e.g. tension applied in the plan of the cell body will cause compression in the perpendicular axis. The majority of physical interactions are a complex of time-varying stress, strain, fluid flow, and pressure and, potentially, other biophysical changes such as osmotic pressure (Guilak et al., 2009).

As discussed in previous sections, cells often respond to extrinsic factors by remodelling their cytoskeleton and hence adjust to an appropriate mechanical state. These mechanical changes are believed to regulate signalling cascades and being responsible for stem cell differentiation and expression of associated proteins (Engler et al., 2006; McBeath et al., 2004).

For example, smooth muscle actin (SMA) was observed in reaction to myogenic differentiation, when MSCs cultured on protein coated flexible substrate were subjected to 5 % - 10 % uniaxial stretch (Gong & Niklason, 2008; Hamilton, Maul, & Vorp, n.d.; Park et al., 2004; Y. Yang, Beqaj, Kemp, Ariel, & Schuger, 2000). Additionally, Yang *et al.,* (2000) Yang *et al.,* (2000) demonstrated the importance of specificity in the mechanical stimuli, as their study showed a lack of SMA expression with 1 % and 15 % strain. Along with strain magnitude, surface adhesion was also proposed to be a limiting factor in the mechanotransduction of stem cells (Gong & Niklason, 2008). Stem cells originating from different tissues are influenced differently by the same mechanical strain. i.e. with 10 % stretch (1 Hz for 7 days) on adipose derived cells demonstrated reduced expression of myocyte associated biomarkers (Lee, Maul, Vorp, Rubin, & Marra, 2007).

The application of biaxial loading appear to direct MSCs towards osteocytic lineage, as was indicated by the expression of Runx2, osterix, alkaline phosphatase, and calcium deposition (Sen et al., 2008; Simmons et al., 2003; Thomas & El Haj, 1996; Yoshikawa, Peel, Gladstone, & Davies, 1997). Moreover, pulsating fluid perfusions have also shown to push MSCs towards OD; provided, these cells were pre-stimulated by osteogenic induction media (Knippenberg et al., 2005). Similarly, incremental hydrostatic pressure on pre-treated MSCs (chondrogenic

induction media) produced increased levels of chondrogenic markers (collagen and proteoglycan) in comparison to the unloaded cells (Angele et al., 2003).

In summary of the above discussion, it can be concluded that physical signals, in part, regulate lineage commitment processes but also that the resultant phenotype is determined by a multitude of factors including, but not limited to, origin of stem cells (tissue of extraction), differentiating state of the cell (pre-treated), substrate properties, soluble growth factors/cytokines and frequency and magnitude of mechanical loading. For instance, in an experiment carried out by Terraciano *et al.* (2007), the same physical environment yielded contrasting results for two different cell phenotypes. MSCs and embryonic stem cells embedded in hydrogel scaffolds, when subjected to compression, expressed increase and decrease, respectively, in Sox-9, type II collagen and aggrecan (chondrogenic markers). Terraciano *et al.* (2007), the same physical environment yielded contrasting results for two different cell phenotypes. MSCs and embryonic stem cells embedded in hydrogel scaffolds, when subjected to compression, expressed increase and decrease, respectively, in Sox-9, type II collagen and aggrecan (chondrogenic markers).

2.6 Stem cell characterisation

As described previously, stem cells have the potency to differentiate into various cell types both, in vivo and in vitro. Assaying their plasticity has become a convenient method for their identification.

Various methods have been developed for the characterisation of lineage specificity of stem cells. Some of the well-established procedures include, but are not limited to, histochemical, immunohistochemical and gene expression assays. Essentially, these techniques can be broadly grouped into staining and non-staining methods. Since robust protocols have been established for in vitro osteogenic and adipogenic differentiation of hMSCs, these two lineages are ideal for developing and validating any new approach (Krause, Seckinger, & Gregory, 2011).

In the past decade, a number of new characterisation techniques based on indirect measurements i.e. mechanical and visual features, have been the subject of many studies. One of the main factors contributing to this interest in such methods is their tendency to preserve information on the population heterogeneity, which has been possible as measurements are taken at a single cell level. Another very influential reason for their promise is that most of these techniques are also suitable for live cell analysis and would thus allow for detailed longitudinal evolution of the differentiation process.

2.6.1 Classification techniques for osteogenic differentiation

Osteocytes when cultured in vitro produce alkaline phosphatase (ALP), aggrecan, and extracellular deposition of calcium phosphate. Histological staining is one of the earliest diagnostic methods to verify the presence of oestrogenic ECM, though certain limitations in this process initiated the need for more efficient assays. Histological techniques are heavily depended on the objectivity of the investigator and they require considerably high levels of detectable secretion of molecular cues. Such levels of ECM are achieved only at rather late stages of the differentiation process and could consume up to 30 days of experimentation time. Real time PCR is a more appropriate and robust approach for early diagnostics of differentiation and could validate differentiation as early as 7 days after the exposure to induction media (S. E. Boucher, 2011). RT-PCR is therefore a popular method for validating OD at present, as it is more sensitive and quantitative. However, the expression of osteogenic genetic markers may not essentially confirm a cell's functionality as the activity of secreted proteins can be regulated at numerous stages by posttranslational modifications. Constraints in mRNA assays have revived improved versions traditional validation techniques (i.e. histological staining). More recently there has been an emergence of new characterisation techniques that utilise non cytochemical analysis, i.e. visual and mechanical cues.

2.6.1.1 Semi-quantification of mineralisation by Alizarin Red S staining and recovery

Results from an experiment conducted on samples with variant levels of osteogenic differentiation are plotted below. Figure 2.13 A shows the cells without any treatment from ODM, while Figure 2.13 B and C display cells with moderate and prolonged exposure to ODM. The red dots on the line graph (Figure 2.13 left) represent the absorbance acquired from the relative concentration of Alizarin Red S (ARS) and confirms the linearity of the assay (Vemuri, Chase, & Rao, 2011).

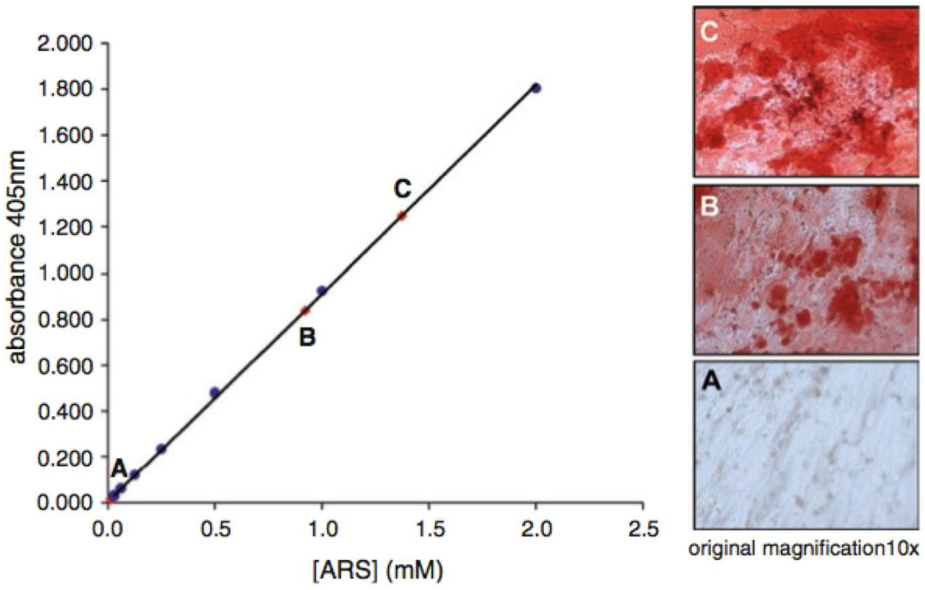

Figure 2.13 Typical semi-quantitative result of an Alizarin Red S staining. (A) cell culture not exposed to ODM, (B) cell culture with moderate exposure to ODM, (C) cell culture with prolonged exposure to ODM (Vemuri et al., 2011)

2.6.1.2 Quantification of mineralisation by acid mediated recovery and Arsenazo III assay

The Arsenazo III assay is a direct quantification of calcium ions released by hMSCs in ODM. It is based on the extent of colour change when Arsenazo III dye bonds with calcium ions (Bauer, 1981; Leary, Pembroke, & Duggan, 1992). The method is lengthy in comparison to other approaches, though very sensitive and does not require any specialised equipment. A major upside to Arsenazo III over the ARS assay is the possibility to use it in 3D cell culture systems in addition to traditional cell cultures on flat substrates.

2.6.1.3 Quantification of ALP activity by kinetics of PNPP to nitrophenolate conversion

MSCs when differentiated to osteocytes produce ECM i.e. hydroxyapatite (HA). Phosphate, a constituent component of HA must first be synthesised, the production of which is initiated by alkaline phosphatase (ALP) (Anderson, 2003; Poole, Matsui, Hinek, & Lee, 1989). The activity of ALP can be rapidly determined by following the conversion of *p*-nitrophenylphosphate (PNPP) to *p*-nitrophenolate (Bessey, Lowry, & Brock, 1946). This conversion can be verified easily as a colour change from colourless to deep yellow occurs, which can be confirmed by absorbance at 405 nm. An automated plate reader can be used to detect the rate of conversion of *p*-nitrophenolate by adding PNPP directly to the osteogenic cell culture. It is advised to normalise results by the cell number, as protein content can inconsistently be produced in cell cultures. Figure 2.14 A shows a representative kinetic profile of an ALP assay demonstrating accumulation of the yellow p-nitrophenolate product over time. Note that the reactions can exhibit a slight lag phase in the initial seconds of the assay and a plateau as the substrate becomes depleted. The slope of the linear section

of the curve (indicated by grey rectangle) should be used for the calculation of ALP activity (Krause et al., 2011). Figure 2.14 B shows a data plot from three different specimens, where the gradient of the line is directly proportional to the level of ALP activity; and ALP activity is in turn directly proportional to the degree of differentiation.

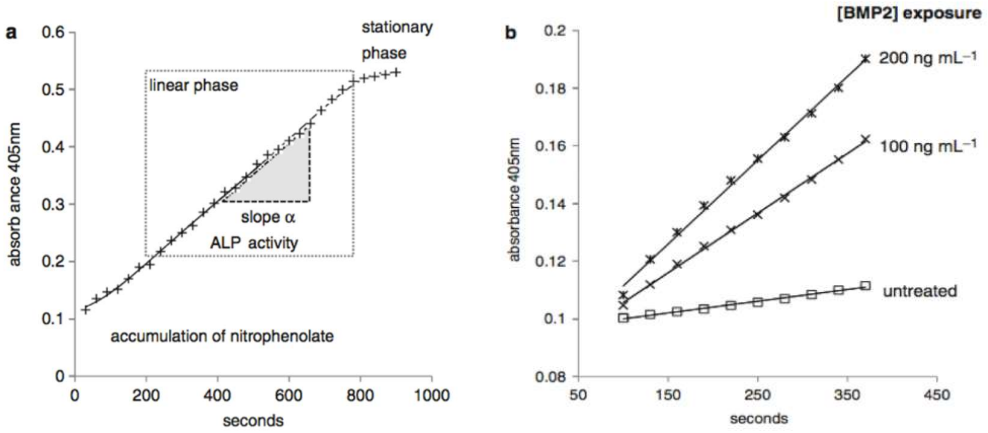

Figure 2.14 Example of ALP activity measurements on hMSCs monolayers treated with osteogenic supplements and two concentrations of bone-morphogenic protein 2 (BMP2). Higher gradients correspond to a higher ALP activity (Vemuri et al., 2011)

2.6.1.4 Quantification of OPG secretion by enzyme linked immunosorbent assay (ELISA)

Osteoprotegerin (OPG) synthesis in ODM exposed media can serve as an early indicator of OD. Its secretion peaks very early in the process, and extenuates as the differentiation progresses, as can be seen in Figure 2.15 (Vemuri et al., 2011).

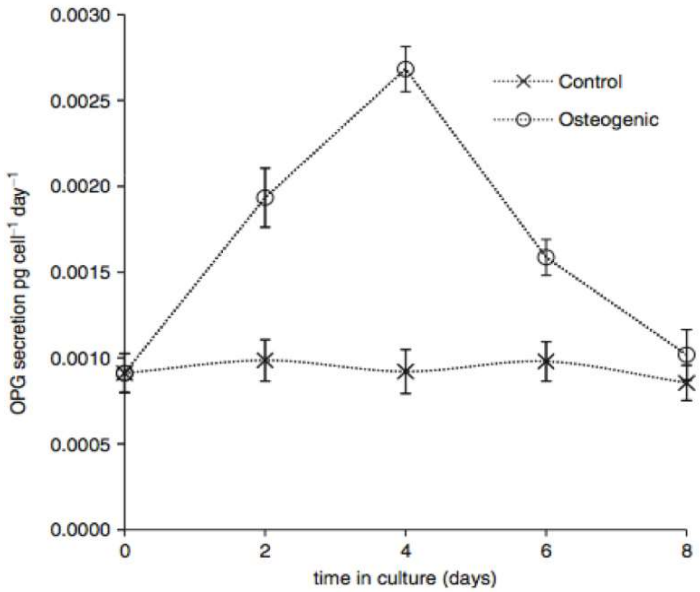

Figure 2.15 Time course of OPG secretion by hMSCs after treatment with osteogenic supplements. Note that OPG levels rise dramatically over the initial 4–7 days of exposure, then decline as ALP activity increases. In some cases, OPG secretion can return to control levels (Vemuri et al., 2011)

2.6.1.5 Gene expressions

mRNA can be extracted from differentiating cell populations and amplified to analyse the expression of genes related to osteoblasts. Typical of these are alkaline phosphatase, collagen type I, Runnx2, osteocalcin and osteopontin (Mori et al., 2011). Additionally, gene expression can also be assessed and (semi) quantified with immunoblotting. Typical markers analysed by immunoblotting include pERK1/2, pFAK, pSTAT5a, βcatenin, pJNK and pAkt (Shih, Tseng, Lai, Lin, & Lee, 2011).

2.6.2 Characterisation techniques for adipogenic differentiation

Like OD, MSCs exposed to ADM produce intracellular build-up of lipid filled vacuoles. They also express adipocyte specific marker proteins. These cells could therefore be characterised by histochemical assays or through transcriptional analysis (Fink & Zachar, 2011).

2.6.2.1 Histochemical analysis with BODIPY and Hoechst Stain

The presence of lipid droplets can be detected by staining cells with oil red O reagent. Although it is one of the most commonly used verification techniques of adipogenesis, it is not suitable for high magnification imaging. Moreover, oil red O staining is only suitable to use after 7 days of exposure to ADM (Figure 2.16 A). Adipogenic differentiation is sometimes also verified by another staining technique where cell culture is treated by BODIPY and Hoechst 33342 fluorescent dyes, which is suitable for high resolution microscopy (Figure 2.16 B) (Fink & Zachar, 2011).

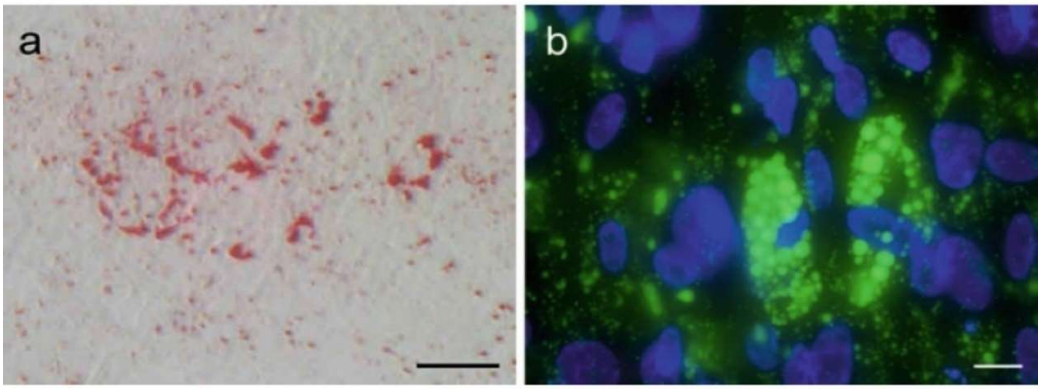

Figure 2.16 Human adipose tissue-derived mesenchymal cells were induced into adipogenesis by dexamethasone, isobutyl methylxanthine, insulin, indomethacin, and rosiglitazone. (a) After 7 days, the lipid droplets were stained with oil red O, and bright-field microscopy was used to capture the image. The scale bar indicates 200 µm. (b) After 14 days, the lipid inclusions and nuclei were stained with the fluorescent dyes BODIPY and Hoechst 33342, respectively. The scale bar indicates 20 µm.(Fink & Zachar, 2011)

The degree of differentiation can also be estimated by semi quantification techniques. In a study conducted by Aldridge *et al.* (2013) a grading method was used, initially developed by English *et al.* (2007), to score the amount of fat in individual cells. Cells from 4 different

batches i.e. fibroblast (Fib), bone marrow donor 1 (BM1), bone marrow donor 2 (BM2) and bone marrow donor 3 (BM3) were differentiated with ADM for up to 21 days and scored for grading. The grading was based on the proportion of cell area occupied by fat lipids, representative images of cells from each grade are shown in Figure 2.17 A. Figure 2.17 B displays bar charts showing the percentage of cells belonging to grade 1 or grade 2+3+4. These results demonstrate that biochemical differentiation media can affect bone marrow derived stem cells from different donors in different ways.

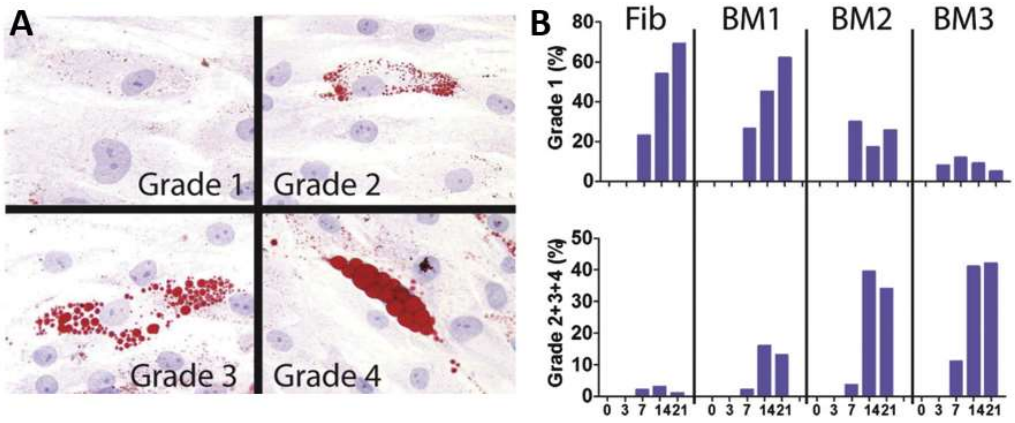

Figure 2.17 Representation of a grading method for scoring the amount of fat in individual cells. A) oil red O stained cells scored in 4 different grades according to their lipid content and B) bar charts displaying the grading distribution of 4 different cell batches (Fib=fibroblasts, BM1=bone marrow donor 1, BM2=bone marrow donor 2 and BM3=bone marrow donor3) over time in days (Aldridge et al., 2013). Imaged at magnification of 400x.

2.6.2.2 Gene expression

Similar to osteoblast associated gene expression analysis, RT-PCR can be used to detect known adipocyte biomarkers i.e. peroxisome proliferator activated receptor-g (PPARγ), fatty acid binding protein 4 (FABP4) and CCAAT enhancer binding protein (C/EBPβ and C/EBPα) (S. Boucher, Lakshmipathy, & Vemuri, 2009). Expression of PPARγ has been shown to strictly relate to AD and follows a nonlinear change in its level over the period of 14 days from, as can be seen in Figure 2.18 (Qian et al., 2010).

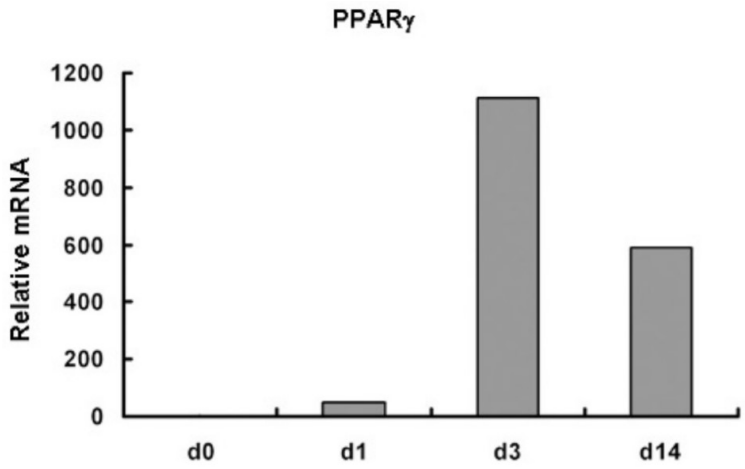

Figure 2.18 Expression of PPARγ plotted over time in days, relative amounts were detected by real-time PCR (Qian et al., 2010)

In the same study, Qian et al. (2010) detected relatively consistent expression for C/EBPβ during most of the differentiation process, though with a decrease after 14 days. On the other hand, C/EBPα showed an almost identical trend to PPARγ, reaching its maximum by day 3 followed by a decrease by day 14 (Figure 2.19).

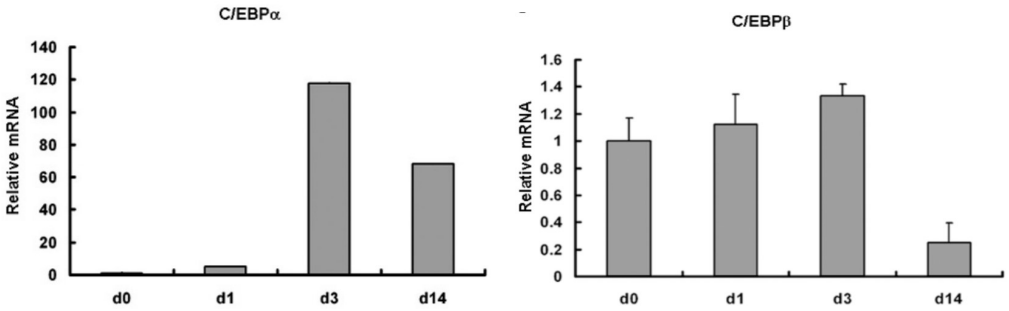

Figure 2.19 Expression of C/EBPBα (left) and C/EBPβ (right) over time in days, , relative amounts were detected by real-time PCR (Qian et al., 2010)

Despite these well-established characterisation techniques, more understanding into the cell response to differentiation is highly desirable, not least for the cases in which adipogenically differentiated cells have shown to accumulated lipid deposits without expressing any transcriptional markers (Fink et al., 2004).

2.6.3 Single cell analysis

Population based analysis inherently adopts an unsubstantiated assumption that cell populations of the same type and in the same environment are homogeneous and respond synchronously. Population based analysis misses out on the important information of the detailed composition of the subject population. These reasons alone are sufficient to explore population characterisation techniques based on a single cell assessment.

The concept of asynchronous differentiation is well illustrated by Bongiorno *et al.* (2014) illustrated in Figure 2.20 and is also supported by the fact that not all cells produce ECM at the same time (Figure 2.21). Considering these findings, it may be assumed that the difference in function also causes a difference in appearance, which could allow prediction of their function.

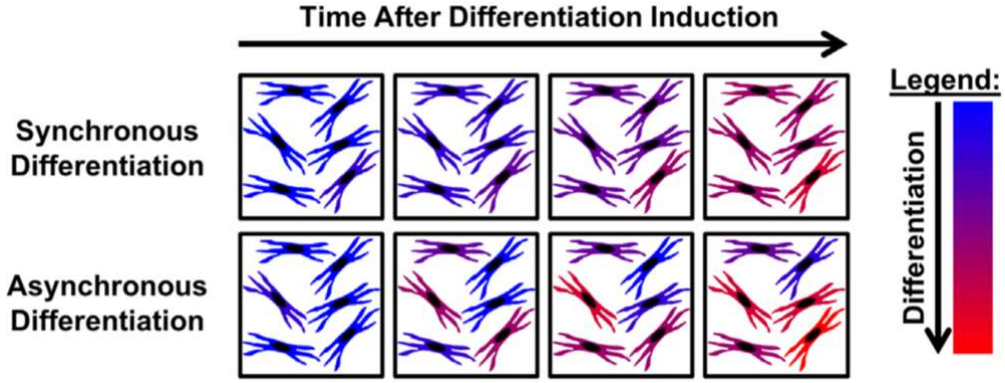

Figure 2.20 Schematic shwowing the difference of synchronous and asynchronous differentiation over time illustrating the need for single cell analysis techniques due to population inhomogeneity (Bongiorno et al., 2014)

The single cell approach is not completely new, as was mentioned earlier in section 2.6.2, Aldridge et al. (2013) performed semi quantification of oil lipid formation at single cells. However, the technique is limited to the characterisation of adipogenic differentiation and can be used only much later in the differentiation as it requires the formation of oil lipids which are formed much later in the process (Figure 2.21).

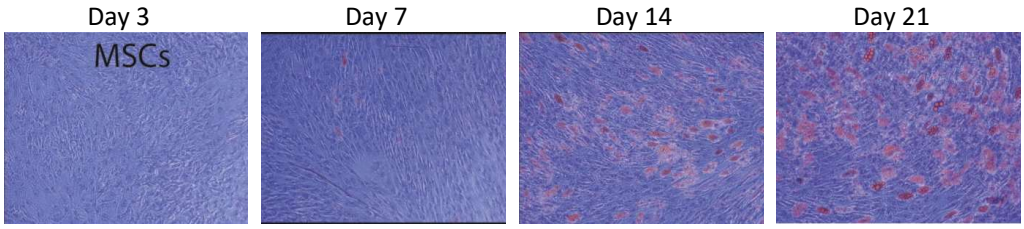

Figure 2.21 Microscopy images showing the adipogenesis of bone marrow MSCs over the course of 21 days (Aldridge et al., 2013). *Imaged at magnification 100x*

Most attempts of single cell characterisation studies have been based on the bio-physiological measurements i.e. visual and mechanical (Bongiorno et al., 2014; Sonowal et al., 2013), instead of the usual biochemical markers. Considering the results published by previous studies, it seems worthwhile to develop a more sophisticated quantification technique measuring physiological features at single cell level. These studies have also suggested a link between the physiology cells adopt and their assigned function (Bongiorno et al., 2014).

2.6.3.1 Mechanical measurements

A study by Kwon *et al.* (2011) reported a "good correlation" between the stiffness of the cell cortex and the level of differentiation. The stiffness was measured using AFM and the level of differentiation assessed by oil red O staining. AFM can be used to measure the elastic modulus of living cells at nanoscale resolution. Interestingly, they reported that along with significant variation in the amount of oil lipid cells, there were also noticeable morphological differences among the cells within a population.

Another study carried out by Bongiorno *et al.* in 2014 considered the relationship between the changes in cell mechanics during osteogenic differentiation to that of previously established molecular biomarkers. They found that not only the variation in cell mechanics was backed by the trends in the levels of relevant molecular expressions but was also more closely correlated with the progress of differentiation over time.

Other studies have used micropipette aspiration to measure the elastic modulus of differentiating stem cells. In one such study (Yu et al., 2010) nonlinear change in the stiffness of cells induced with ADM over the period of 21 days was reported. On the other hand, osteogenesis seemed to display a gradual increase in the actin cortex stiffness (Figure 2.22).

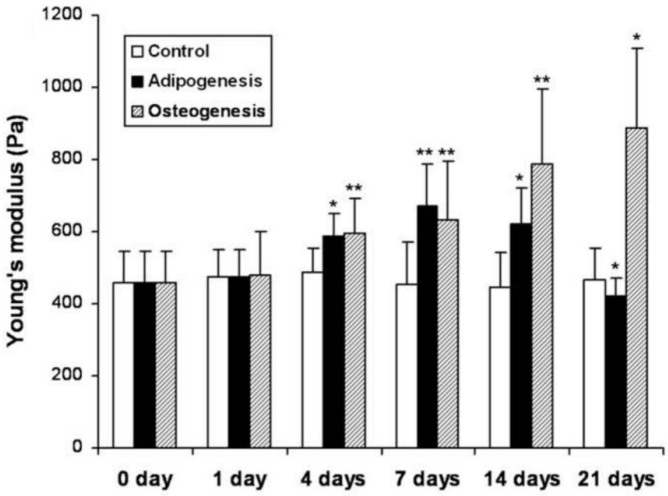

Figure 2.22 Young's modulus for hMSCs during adipogenic, osteogenic and no differentation over the course of 21 days. Stars above the error bars indicate significance (Yu et al., 2010)

2.6.3.2 Visual quantitative analysis

More recently, researchers have started to investigate if changes in a cell's morphology hold any clues to the cell's lineage. Dalbay *et al.* (2015) studied the effect of differentiation on the length of primary cilia. They found that primary cilia of the cells elongate over the period of a 7 day treatment with adipogenic differentiation media. The cilia elongation was detected within the first 2 days and was attributed to differentiation by the detection of increased levels of PPARγ.

Similarly, (Sonowal et al., 2013) quantified changes in the amount of actin in MSCs over a 14 day period of osteogenic and adipogenic differentiation. Cells were analysed by flow cytometry at timepoints 0, 1, 3, 7, and 14 days. Their results showed a statistically significant change in the levels of F-Actin expression (Figure 2.23) and they argued that this reorganisation of F-actin network is a prerequisite for the differentiation process.

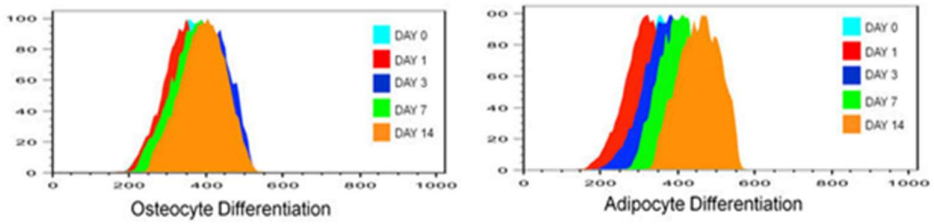

Figure 2.23 Histograms displaying the cell size of osteogenic and adipogenic differentiated MSCs determined by flow cytometry for days 0, 1, 3, 7 and 14 after differentiation was induced (Sonowal et al., 2013)

2.6.3.3 Geometric measurements

In addition to the amount of F-Actin, cell differentiation also showed visual differences in the structure of actin network (Figure 2.24) (Sonowal et al., 2013). Their investigation also studied the effects of differentiation on size and shape of the cells. They found that adipogenesis increase the cells area whereas osteogenesis has no to little effect. Moreover, they also reported that by day 14, cells had adopted globular, polygonal and spindle shapes in adipogenic, osteogenic and cell expansion media, respectively.

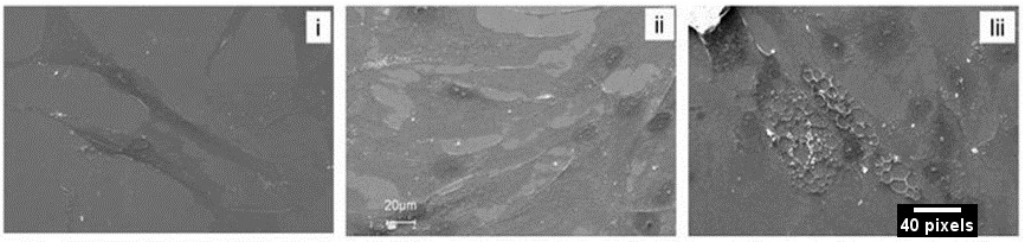

Figure 2.24 SEM micrographs of differentiated MSCs before induction (i) or after 14 days of inducing osteogenesis (ii) or adipogenesis (iii) (Sonowal et al., 2013) *(scale Bar added)*

Another interesting aspect is the effect of modulating cell area and shape on the organisation of actin cytoskeleton and on the lineage commitment. Kilian *et al.* (2010) and later Mathieu and Loboa (2012) showed that cells inclined towards adipogenic lineage when they are constrained to a round or small shape on a micropatterned adhesive area, suggesting that certain cytoskeletal configurations promote specific cell functions.

A study by Kilian *et al.* (2010) characteristically described the cytoskeletal organisation in MSCs on differently shaped micropatterns. Cells were cultured on a star or flower shaped island of adherable surface for 6 hours. Cells were then fixed and stained for actin and vinculin, followed by an assessment of the configuration of actin network and adhesion sites in relation to the geometrical requirements (Figure 2.25).

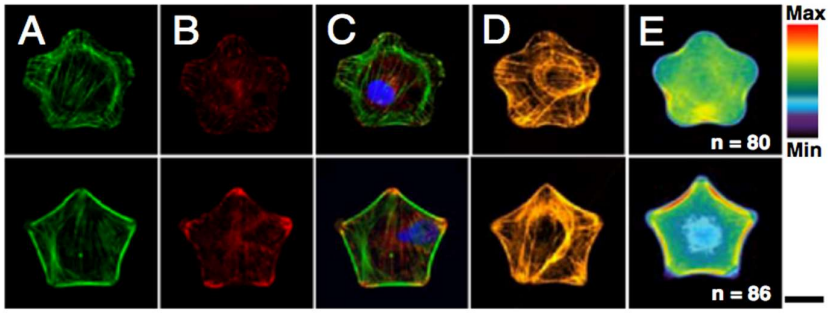

Figure 2.25 (A)-(C) Immunofluorescent images of cells in flower and star shapes stained for F-Actin (green), vinculin (red) and nuclei (blue). (D) Immunofluorescent images of cells in flower and star shapes stained for myosin IIa. (E) Fluorescent heatmap of > 80 cells stained for myosin IIa as a quantitative measure of contractility (scale bar, 20 µm) (Kilian et al., 2010)

Considering the findings of above-mentioned studies, it is not farfetched to suggest that cells require distinct CSK and FA organisation to stabilise their morphology and that cells adopt a certain morphology to complement their assigned function.

2.6.3.4 Actin organisation

To get a better understanding of why a cell's morphology needs to be adjusted to its evolving function, the components responsible for those changes must be investigated. Actin cytoskeleton is not only the result of bio-functional needs of the cell but it also influences the very same functions it is regulated by (Sonowal et al., 2013). Stem cells generally have a spindle shape with stress fibres running along their length as shown in Figure 2.26. They become polygonal in shape with thicker stress fibres if differentiated to osteoblasts or rounder with thinner fibres if differentiated towards adipocytes. Linking back to what has been discussed in section 2.6.3.3, if the cell area increases with adipogenesis then the actin network must reorganise to accommodate for the thinning of the actin fibres (Sonowal et al., 2013).

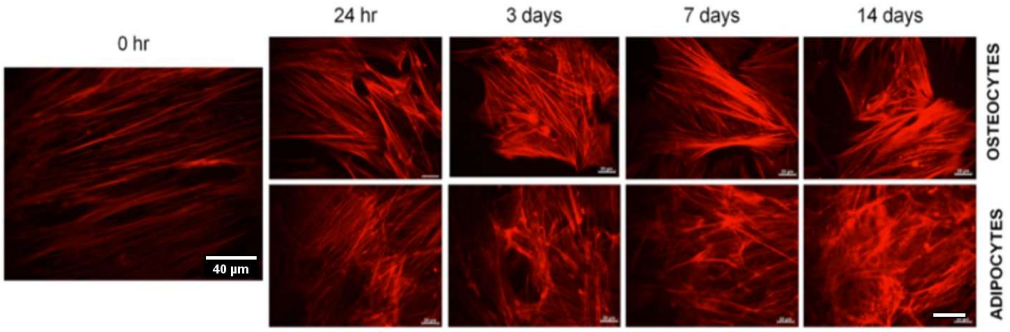

Figure 2.26 Images of the F-actin network in MSCs over the course of osteogenic and adipogenic differentiation. Cells were stained with phalloidin (Sonowal et al., 2013). *Scale bar indicates 40 µm*

Another similar study backed these observations and reported that upon differentiation to osteogenesis, thin parallel stress fibres of hMSCs reorganised into a mesh of thicker fibres,

as can be seen in Figure 2.27 (Yourek, Hussain, & Mao, 2007). It was also observed that focal adhesions were noticeably larger after 10 days of osteogenesis (Born et al., 2009).

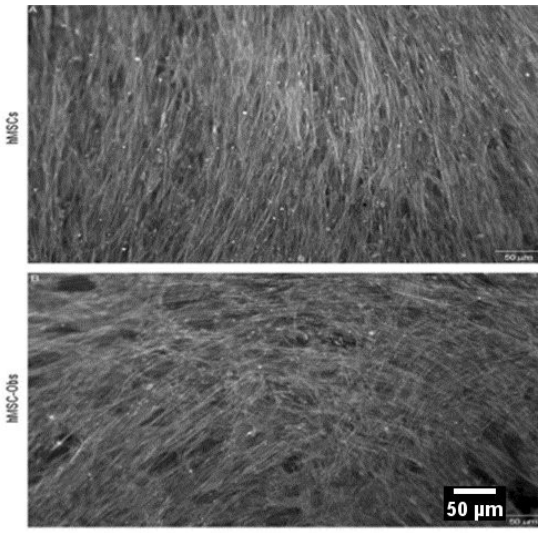

Figure 2.27 Undifferentiated hMSCs (top) and osteogenic hMSCs (bottom) displaying the altered organisation of stress fibres of the F-actin network. Cells were stained with phalloidin and images converted into grayscale, where actin is white (Yourek et al., 2007) *(Scale bar is added)*

2.6.3.5 Morphometrics

As discussed in earlier sections, changes to cell shape and by extension to the cytoskeletal configuration, go hand in hand with the differentiation process. Based on this, the identification of cytoskeletal features may explain details of the underlying processes involved, especially in response to mechanical stimuli. A reasonable assumption would be that, if distinct cytoskeletal configurations can be observed visually, then they can also be measured using computer vision technologies. For this, fluorescent images of the cells could be used to quantify cytoskeletal geometry and organisation.

The high variation of fluorescent intensity and the sharpness of signal within and among images of cells pose many practical challenges in the extraction of reliable quantification data (Zemel, Rehfeldt, Brown, Discher, & Safran, 2010). Some examples of such variations can be observed in images shown in Figure 2.28 (Eltzner, Wollnik, Gottschlich, Huckemann, & Rehfeldt, 2015).

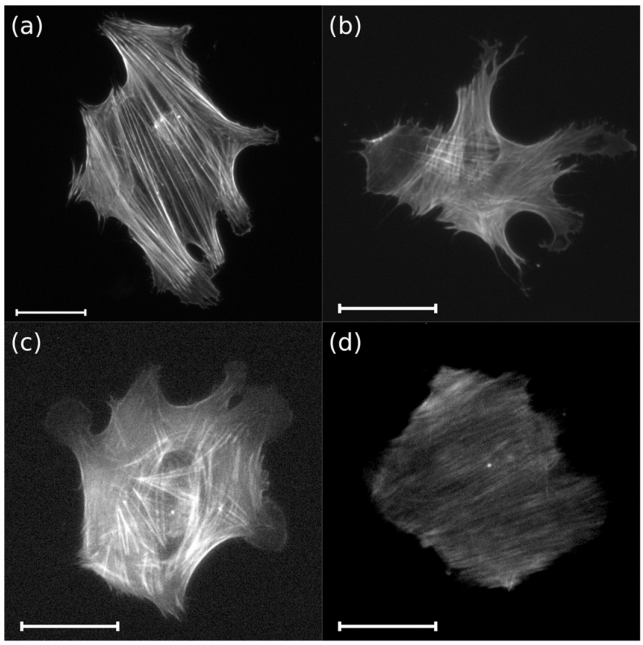

Figure 2.28 Demonstration of variability in image quality of stress fibres in hMSCs for immunostained and fixed cells (a and b) and for live cells (c and d) (Eltzner et al., 2015). *Scale bars are 100 µm.*

Once quantified, suitable statistical techniques are required to use this vast pool of data. Along with more typical analysis of descriptive statistics, more advance multivariate analysis and machine learning classification would be ideal for such data sets.

The potential of this approach is well exhibited in a study published in 2010 by Treiser *et al.*, where "numerous quantitative features of actin fluororeporter shapes, intensities, texture, and spatial distribution" were captured and analysed with Support Vector Machine (SVM) classifier. SVM reduced data from 43 features down to 3 components, where each component represents nonlinear combination of all those 43 features. This method was able to correctly classify AD from OD with an accuracy of up to 0.95 within 24 hours of being induced with ADM and ODM. It is important to note that their results showed a difference in their algorithm's accuracy for cells from different donors, as can be seen in the comparison of ACC values in Figure 2.29.

Once quantified, suitable statistical techniques are required to use this vast pool of data. Along with more typical analysis of descriptive statistics, more advance multivariate analysis and machine learning classification would be ideal for such data sets.

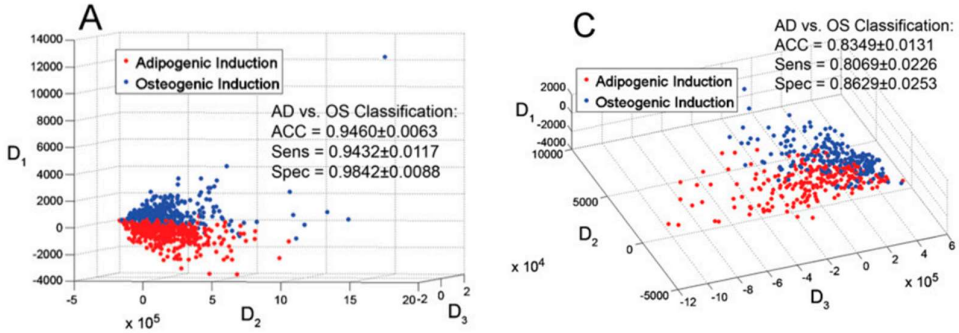

Figure 2.29 Multivariate classification (SVM and MDS) of adipogenic and osteogenic differntiation for two different donors A and C presented in 3D scatter plots (Treiser et al., 2010)

Chapter 3 | Methods and materials

The following chapter includes materials and methods used for the experimentation of this thesis. Firstly, the equipment used for imaging and mechanical testing are discussed followed by the preparation of human mesenchymal stem cell culture and polyacrylamide gels. Lastly the different staining techniques and data acquisition are explained.

3.1 Equipment

3.1.1 Epifluorescence microscopy

Images were acquired with a Leica DMI4000B inverted microscope, equipped with A4, L5 and N3 filter cubes. The microscope also features an internal filter wheel with motorised excitation manager and FIM (Fluorescence Intensity Manager), enabling excitation of fluorochromes in less than 20 ms. The FIM can regulate light intensity at five fixed levels and remembers the setting for each filter cube. For special diagnostics requirements, primary antibodies were selected in consideration to their affinity for target human antigens. Whereas selection for secondary antibody relied on their suitability for the filter sets available on the Epifluorescent DMI4000 microscope and their compatibility with the primary antibody. To exemplify, FITC (fluorescein isothiocyanate) has its excitation peak at around 475 nm and emission at 540 nm, which is in line with the L5 filter set, as shown in Table 3.1 and Figure 3.1.

Table 3.1 Specifications of Epifluorescence microscope and filter sets ("Chroma Spectra Viewer | Chroma Technology")

Filter cube	Dichromatic [nm]	Excitation [nm]	Emission [nm]	Fluorophore
A4	400	360/40	470/40	**DAPI**, Hoechst dye no. 33258, Hoechst dye no. 33342
L5	505	480/40	527/30	Alexa 488, Astrazone Orange R, BCECF, BODIPY FL, Calcium Green, Carboxyfluorescein diacetate C-FDA, FDA (fluorescein diacetate), **FITC (fluorescein isothiocyanate),** FITC (selective), FITC/ethidium bromide, Fluo 3, Oregon Green (488, 500, 514), Rhodamine 123
N3	565	546/12	600/40	Acridine red, Alexa 532, Aminoactinomycin D-AAD, Nuclear Fast Red, Phycoerythrin (PE), TRITC (selective), **TRITC (tetramethyl rhodamin isothiocyanate)**, XRITC

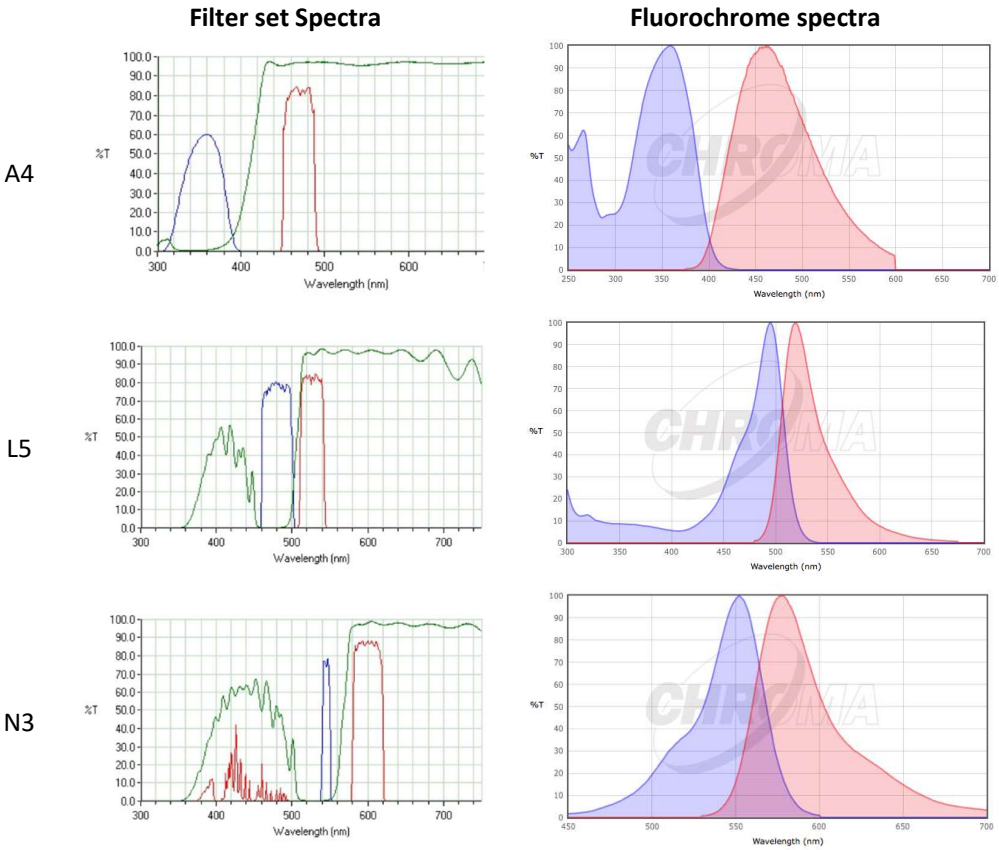

Figure 3.1 Filter set spectra (left) and Fluorochrome spectra (right) for different filter cubes (A4, L5 and N3) in the Epifluorescence microscope ("Chroma Spectra Viewer | Chroma Technology")

3.1.2 Mechanical testing machine

Mechanical testing of the gel substrates was carried out with a MTS BIONIX 100 using a 50 N load cell. Gel samples were indented with 20 % compressive strain at 0.05 mm/s by a circular flat head of 3 mm diameter. Each sample was indented at several locations to normalise for any systemic variation.

3.2 Cell culture

3.2.1 hMSCs

Human mesenchymal stem cells (hMSCs) were purchased commercially from Stem cell Technologies (lot # 982281048). As per vendor's description, primary human stromal cells were derived from bone marrow (BM) mononuclear cells (MNCs) of a 24 year old male donor. BM was collected by using heparin as an anticoagulant and in accordance with the approved protocols from the Institutional Review Board (IRB). The purity of stromal cells was reported at ≥ 90 % for CD73, CD90, CD105 and < 5 % for CD14, CD34, CD45 by flow cytometry. Cells were expanded for 2 weeks before being cryopreserved in vials of ~350k cells. Before each

experiment, cells were thawed and expanded for 10 days and were used at Passage 4 or Passage 5.

Prior to the thawing of cells, expansion media (xPan) was prepared via the following composition:

Table 3.2 Components and their final concentrations in expansion media (xPan)

Item	Storage temperature	Final concentration
Dulbecco's Modified Eagle Media (DMEM) with low Glucose (1g/mL) and Sodium Pyruvate (Sigma 11885084)	4 °C	90 %
Penicillin-Streptomycin (Pen-Strep) solution stabilised, with 10,000 units of penicillin and 10 mg streptomycin/mL, (Pen-Strep) (SIGMA P4333)	-20 °C	100 U/mL pen. 100 µg/mL strep.
Foetal bovine serum (FBS) (Sigma F7524)	-20 °C	10 %
Amphotericin B solution 250 µg/mL in UPW (Sigma A294)	-20 °C	2.5 µg/mL
Recombinant Human FGF-basic from E.Coli (PeproTech 100-18B)	-20 °C	10 ng/mL
HEPES solution, 1 M, pH 7.0-7.6 (Sigma H0887-100ML)	RT	10 mM

As stem cells are known to be very sensitive to environmental changes, a consistent thawing protocol to discourage systemic variability was required. After removing the cell vial from the cryobank it was placed in a 37 °C water bath. Once thawed, the vial content was transferred to a 15 mL falcon tube under sterile conditions. Previously prepared xPan was added dropwise to the tube while gently swirling the cell suspension. xPan was continually added, until a final volume of 13 mL was reached. The resulting suspension was centrifuged for 10 min at 1300 rpm to form a cell pellet at the bottom of the tube. The supernatant was removed while ensuring the cell pellet remained unharmed. The cell pellet was then gently flushed with 1 mL of xPan using a pipet until the pellet had resuspended. More xPan was added and the cell suspension was moved to a T25 flask. Cells were allowed to stabilise and proliferate for up to 10 days, while xPan was replaced every 2-3 days.

3.2.2 Cell seeding

Cells were allowed to proliferate (for approximately 7-10 days) in culture until they covered the flask area evenly at around 70 % confluency. It is crucial, that the cells do not reach full confluency as this would promote adipogenic differentiation. Before detaching the cells from

the flask, coverslips were placed in a 24-well plate, submerged with 500 µL of 10 % DMEM solution and incubated for approximately 3 h. Meanwhile, 5-7 images at 5x magnification were taken randomly across the T25 flask. These images were used to estimate the cell numbers in the flask using the method described in section 4.1.3.

After calculating cell numbers, xPan media was removed and the flask was rinsed twice with PBS. Approximately 0.5 mL of Accutase suspension (Table 3.3) was added to the flask while it was swirled gently to spread it over the surface. Subsequently, the flask was placed into a 37 °C, 5 % CO_2 incubator for 3-5 minutes and cell detachment was checked after 3 min and then every min after that, using the light microscope. Once most of the cells appeared to have detached, approximately 5 mL of xPan was added and the cell suspension was gently flushed a few times, using a pipette, to collect most cells. The cell suspension was transferred to an appropriately sized container. Based on the cell count, the appropriate volume of cell suspension was taken and resuspended in the required volume of xPan to achieve a final concentration of ~1000 cells/mL. 1 mL of the final cell suspension was then added to each well of the previously prepared 24-well plate containing coverslips.

Table 3.3 Reagents used for cell passaging and their storage conditions

Item	**Storage temperature**
Dulbecco's Phosphate Buffered Saline (PBS) Modified, without calcium chloride and magnesium chloride, powder, suitable for cell culture (Sigma D5652)	RT
Accutase Cell dissociation reagent (StemPro A111050)	-20 °C

3.2.3 Differentiation media

Osteogenic differentiation media (ODM) and adipogenic differentiation media (ADM) were prepared by adding differentiation supplements to xPan (without FGF), as previously reported by (Dalbay et al., 2015). The supplements were added to xPan to achieve the final concentrations as listed in Table 3.4 and Table 3.5 below.

Table 3.4 Components and their final concentrations as used for osteogenic differentiation media (ODM)

Item	**Storage temperature**	**Stock concentration**	**Final concentration**
xPan (without FGF)	4 °C	-	-
Dexamethasone - water soluble (Sigma D2915) (DEX)	4 °C	100 µM	100 nM
β-Glycerophosphate disodium salt hydrate ≥99.0% (titration) (Sigma G9422) (BGP)	-20 °C	1 M	10 mM

L-ascorbic acid, Dexamethasone-water soluble (Sigma D2915) (L-Asc)	-20 °C	50 mM	50 µM

Table 3.5 Components and their final concentrations as used for adipogenic differentiation media (ADM)

Item	Storage temperature	Stock concentration	Final concentration
xPan (without FGF)	4 °C	-	-
Dexamethasone - water soluble (Sigma D2915) (DEX)	4 °C	1 mM	1 µM
3-Isobutyl-1-methylxanthine (IBMX) ≥99% (Sigma I5879)	-20 °C	500 mM	500 µM
Indomethacin; ≥99% (Sigma I7378) (INDO)	-20 °C	100 mM	100 µM
Insulin human; recombinant, expressed in yeast (Sigma I2643) (INS)	-20 °C	10 mg/mL	10 µg/mL

Due to the -20 °C storage requirements for some of the components, both ODM and ADM were prepared freshly before each use and replaced every 2-3 days in the cell culture.

3.3 Polyacrylamide gel preparation

Reagents required for the preparation of polyacrylamide gels are listed in Table 3.6 below.

Table 3.6 Components used during the preparation of polyacrylamide gels

Item	Storage conditions	Stock concentration
3-(Trimethoxysilyl) propyl methacrylate (Sigma-Aldrich 440159)	4 °C, in dark, sealed with rubber bunk	98 %
Toluene anhydrous (Sigma-Aldrich 244511-1L)	RT, in dark, sealed with rubber bunk	99.8 %
Acrylamide solution (Bio-Rad 1610140)	4 °C, in dark	40 %
Bis solution (Bio-Rad 1610142)	4 °C, in dark	2 %
Ammonium Persulfate (APS) (Bio-Rad 1610700)	-20 °C	10 %
TEMED (Bio-Rad 1610800)	4 °C, in dark	99 %
Sulfo-SANPAH (Thermo Scientific 22589)	-80 °C, in dark	50 mg/mL
Fibronectin (Santa Cruz sc-29011)	-80 °C	250 µg/mL

Prior to the preparation of the gels, coverslips were activated as described by Trappmann et al. (2012). In brief, coverslips were rinsed and sonicated for 10 min in ethanol. Once dried,

the coverslips were placed with no overlap on a tray for the Zepto low pressure plasma system (Diener electronic, Ebhausen, Germany). Coverslips were oxidised for 10 min and the coverslips were transferred to a glass petri dish, while ensuring the exposed side of the coverslip stayed upwards with no overlap between the coverslips. Then, the coverslips were submerged in the activation solution, this was performed in a 15 mm petri dish with 15 mL Toluene anhydrous and 45 µL of 3-(Trimethoxysilyl)propylmethacrylate. The petri dish was covered with aluminium foil and left to stand in the fume hood overnight. The following morning, the activation solution was removed, and the coverslips were washed three times with UPW and once with ethanol via sonication. Subsequently, the coverslips were left to dry in an incubator in a dust-free environment. The constituent composition of the Acrylamide/Bis-acrylamide pre-mix is given in Table 3.7 below.

Table 3.7 Composition of Acrylamide/Bis-acrylamide pre-mix for different degrees of gel stiffness

Stiffness	40 % Acrylamide	2 % Bis-acrylamide	UPW	Total Volume
~2 kPa	1.875 mL	0.145 mL	7.980 mL	10 mL
~3 kPa	1.875 mL	0.190 mL	7.935 mL	10 mL
~5 kPa	1.875 mL	0.330 mL	7.795 mL	10 mL
~10 kPa	1.875 mL	0.610 mL	7.515 mL	10 mL
~35 kPa	1.875 mL	1.850 mL	6.275 mL	10 mL

The Acrylamide/Bis-acrylamide pre-mix solution was stored at 4 °C and used up within a few weeks. Before each use, the pre-mix solution was degassed with N_2 or Ar gas for approximately 20 min to reduce the oxygen content in the solution, as the presence of oxygen can prevent PPA from polymerising.

3.3.1 PAA polymerisation and fibronectin coating

3.3.1.1 Method A

Hydrophobic glass slides were prepared by wiping each side of the glass slides with filter paper soaked in SigmaCote. Once dried, glass slides were rinsed gently with UPW and dried with a dust-free tissue paper. Hydrophobic glass slides were prepared fresh on the day to be used.

10 % (w/v) ammonium solution (0.1 g per 1 mL) previously prepared and stored at -20 °C, was thawed and mixed thoroughly with a pipette. 500 µL of Acrylamide/Bis-acrylamide pre-mix solution was moved to an Eppendorf tube and 5 µL of APS as well as 0.75 µL of TEMED was added. The aliquot was then well mixed by pipetting up and down 3-5 times, taking care not to introduce any air bubbles. 10 µL drops of the gel precursor solution were pipetted onto the hydrophobic glass slides, and a coverslip was placed face down with the activated

side on top of each droplet. By this, the gel solution spread out and covered the entire coverslip. Completion of the polymerisation process was assessed via the shrinkage of the gels edges as well as by inverting the remaining aliquot solution to confirm the formation of a gel. As soon as the polymerisation was verified, the coverslips were removed from the glass slides by dragging them off the edge with a tweezer. Once removed, gels were moved to a petri dish and submerged in PBS to keep them hydrated.

Heterobifunctional cross-linker Sulfo-SANPAH was used to covalently attach fibronectin to the surface. Stock solution was prepared by mixing 50 mg of Sulfo-SANPAH in 1 mL of DMSO and was stored at -80 °C in 12 µL aliquots. Once hydrated, Sulfo-SANPAH has a very short half live at room temperature, which required all other components to be ready before thawing Sulfo-SANPAH. PBS was removed from the petri dish and any excess PBS on the surface of the gels was absorbed with a dust-free tissue paper, taking care not to touch the gels. 12 µL of Sulfo-SANPAH was then dissolved in 1 mL of PBS and 50 µL of the final solution was pipetted on the surface of each gel. This step was carried out under low lighting conditions, once all gels were covered with Sulfo-SANPAH solution, they were exposed to UV light (300-460 nm lamp) for 5-10 min. Subsequently, gels were washed 5 times with PBS, for 3 min at each washing step. The gels were then moved to a 24-well plate and incubated in 300 µL (per well) of 25 µg/mL fibronectin solution overnight. Gels were washed 5 times and kept in 10 % FBS media in the incubator for 3 h prior to cell seeding.

3.3.1.2 Method B

Fibronectin solution with a stock concentration of 25 µg/mL in PBS was used to pipette two 100 µL drops on a piece of parafilm. Subsequently, a glass slide was placed on the fibronectin solution drops and was left at RT for 30 min. Glass slides were then rinsed with PBS and left to dry in air. 10 % (w/v) ammonium solution (0.1 g per 1 mL) previously prepared and stored at -20 °C, was thawed and mixed thoroughly with a pipette. 500 µL of Acrylamide/Bis-acrylamide pre-mix solution was moved to an Eppendorf tube and 5 µL of APS as well as 0.75 µL of TEMED was added. 10 µL drops of the gel precursor solution were pipetted onto the treated side of the glass slides, and a coverslip was placed face down with the activated side on top of each droplet. By this, the gel solution spread out and covered the entire coverslip. Completion of the polymerisation process was assessed via the shrinkage of the gels edges as well as by inverting the remaining aliquot solution to confirm the formation of a gel. As soon as the polymerisation was verified, the coverslips containing the gels were carefully removed from the glass slide with the help of a tweezer and placed in 24-well plates. Gels were submerged in 10 % FBS media and kept in the incubator for 3 h prior to cell seeding.

3.3.2 Gel preparation for mechanical testing

PAA solutions for the 5 different stiffnesses (Table 3.7) were prepared and degassed with N_2 gas. 500 µL from each of the 5 PAA solutions was transferred to a separate 1 mL vial (Ø10 mm) and polymerised as described in section 3.3.1.1. Gels were then extracted from the vials and cut across their (circular) cross section into cylindrical constructs. Attention was given to ensure the cut surfaces were uniform and construct thickness was as consistent as possible. Once cut, gels were stored submerged in UPW to keep them hydrated.

3.4 Staining

Reagents used in the staining process are listed in Table 3.8 below.

Table 3.8 Reagents used for staining

Item	Stock Concentration
Paraformaldehyde (PFA) (252549 Sigma)	3.7 %
Bovine Serum Albumin (BSA) (A9418 Sigma)	1 %
Saponin (47036 Sigma)	2.5 %
Phalloidin-Tetramethylrhodamine B isothiocyanate (Sigma P1951)	2500 µg/mL
Triton X-100 (Sigma T8787)	0.25 %
Goat Serum (Sigma G9023)	10 % & 1.5 %
Goat IgG-FITC - anti-mouse (sc-2010)	400 µg/mL
Pan-Cytokeratin Antibody (C11) (sc-8018)	200 µg/ml
Vimentin Antibody (RV202) (sc-32322)	200 µg/ml
α Tubulin Antibody (TU-02) (sc-8035)	200 µg/ml
Anti-Myosin IIA, non-muscle antibody produced in rabbit	1000 µg/ml
Goat IgG-FITC - Anti-rabbit (Sigma F0382)	1000 µg/ml
ProLong® Gold Antifade Reagent with DAPI (P36935)	N/A
Oil Red O (Sigma O0625) in 99% isopropanol	0.3 % w/v
Alizarin Red S (Sigma A5533) in UPW	1 % w/v

3.4.1 Immersion fixation

Prior to staining, fixation of the cells was required, for this, the culture media was removed from the wells and each well was rinsed with PBS 3 times. A cross linking fixative, i.e. PFA, was added to each well, ensuring full coverage of the coverslip surface (approximately 0.5 mL). The specimens were left in PFA for about 10 min before being washed with PBS 3 times. In case the staining was not initiated immediately after fixation, specimens were kept hydrated in PBS (approximately 1 mL per well). From this step onwards, any further procedures were carried out outside of a sterile hood.

3.4.2 Phalloidin staining

400 µL of DMSO was added to 1 mg of phalloidin powder and the mixture was swirled around for a few min. Aliquots of 20 µL were prepared and the stock batch was stored at -20 °C. Before the staining process, BSA buffer was prepared by diluting a 2.5 % saponin solution in PBS by a factor of 100, followed by the addition of BSA powder in 0.001 w/v ratio. Phalloidin stock solution was diluted with the BSA buffer in 0.002 volume ratio, e.g. for 1 µL of phalloidin stock solution, 500 µL of BSA buffer was added. 300 µL of this final solution was then added to each well, ensuring complete submergence of the coverslips. The 24-well plates were covered with aluminium foil to avoid photobleaching and left on a shaker for about 1 h. After 1 h of incubation, the diluted phalloidin solution was removed from the wells and each well was washed with PBS 3 times, leaving the PBS in for about 3-5 min at each washing step. The samples were then submerged in PBS and stored.

3.4.3 Immunostaining

Immunostaining was carried out in 2 steps, where the cytoskeleton of interest was firstly tagged with a primary antibody, whereupon the primary antibody was tagged with a fluorescent secondary antibody (FITC).

Permeabilisation of the plasma membrane is required for the antibodies to pass through. This was fulfilled by treating the cells in each well with 0.5 mL of 0.25 % Triton X-100 for 4-5 min. Triton X-100 was then removed and each well was washed with PBS 3 times. Prior to the antibody staining, cells in each well were incubated with 300 µL of blocking buffer (10 % goat serum) at RT for 45 min. Blocking buffer was then removed and each well was washed with PBS 3 times. Cells were then incubated overnight in the refrigerator with 300 µL (per well) of the primary antibody solution. The primary antibody solution was removed the next day and samples were washed with PBS 3 times, followed by 300 µL (per well) of the secondary antibody solution for 45 min. To avoid photo bleaching, well plates were covered with aluminium foil. Samples were then washed 3 times with PBS under low lighting (to prevent photobleaching) before being mounted on glass slides for imaging. Working solutions of the primary and secondary antibody were prepared by adding the relevant antibody in 1.5 % goat serum.

3.4.4 Mounting

A drop of mounting medium (ProLong® Gold Antifade Reagent with DAPI) was pipetted on a clean glass slide, preventing any air bubbles. Coverslips were then removed from the wells and excess PBS was soaked up with a dust-free tissue paper, avoiding touching the surface

of the gels on the coverslips. The coverslips were then placed on the drop of mounting media with the cell side sandwiched between glass slide and coverslip. This step was carried out under low lighting conditions to prevent photobleaching.

3.4.5 Histochemical staining

Cells were stained with oil red O to investigate adipogenic differentiation, as it stains any oil lipids produced by the cells. Oil red O stock solution was prepared by adding oil red O to 99 % isopropanol at 0.3 % w/v. Working solution was then prepared by diluting the stock solution by a factor of 1 ⅔ (e.g. 4 mL of UPW were added to 6 mL stock solution) and filtering it after 10 min of incubation at RT. It was ensured, that the working solution was used within 2 h of preparation. For the staining process, samples were gently washed with PBS and fixed with 3.7 % PFA solution (as mentioned in section 3.4.1). PFA solution was then removed and each well was washed with PBS, followed by incubation for 5 min with 60 % isopropanol at RT. Oil red O working solution was gently added via the side of the well to avoid washing away any lipids and incubated for 5 min at RT. The solution was then removed from the wells and samples were rinsed off clear and submerged in tap water. If possible, cells were imaged using the phase contrast mode on the day of staining or otherwise stored at 4 °C.

Cells were stained with Alizarin Red S to investigate osteogenic differentiation. 1 % w/v of Alizarin Red S was prepared with UPW and the pH was adjusted to 4.1 using 0.1 % ammonium hydroxide (NH_4OH) or concentrated Hydrochloric acid (HCl). Once adjusted, the solution was filtered using Whatman filter paper and kept in the dark. As the pH is critical for the staining process, working solution was prepared fresh for every use. Care was taken to treat the samples gently throughout the whole process as the mineral deposits can cause the cell monolayer to be brittle and prone to detachment thus posing the risk of being washed away. For the staining process, cells were first fixed with PFA solution (as mentioned in section 3.4.1). PFA solution was then removed and each well was washed with PBS, followed by incubation in Alizarin Red S solution for 30 min at RT. Wells were then washed 3-5 times with UPW by gentle shaking. If possible, cells were imaged using the phase contrast or bright field on the day of staining or otherwise stored at 4 °C.

3.5 Data acquisition

3.5.1 Imaging acquisition and pre-processing

To be as consistent as possible, all samples from an experiment were stained and mounted in the same session. These samples were imaged within 4-5 weeks form the point of being stained and were stored in 4 to 8 °C for this duration. To minimise the effects of photo-

bleaching, cells were imaged by first focusing on the nucleus in the DAPI channel and then momentarily switching to TRITC channel to image CSK.

Images of the actin cytoskeleton and the corresponding nuclei of each cell were captured without moving the stage. Samples were also covered with a black card and the room light was kept off during the imaging sessions. It was always attempted to acquire images of cells across the area of a specimen to ensure imaged cells were representative of the whole population.

As individual cell imaging was not always possible, especially at later time points in the differentiation, images were later cropped to separate each cell due to working requirements of the developed algorithm (single cell images). During the process of cropping, images were also converted to grayscale. An exemplary image containing multiple cells can be seen in Figure 3.2.

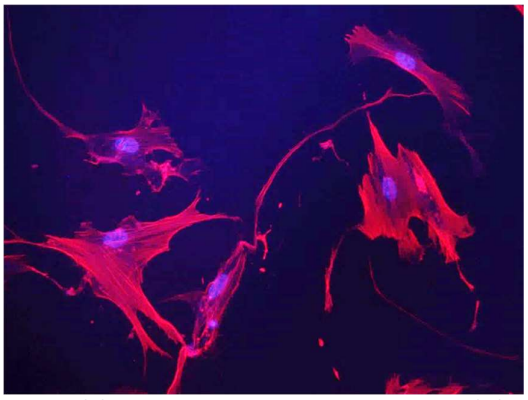

Figure 3.2 Exemplary image acquired during an imaging session containing mutliple cells instead of individual cells (brightness increased for better visibility). Superimposed image to show nucleus (DAPI - blue) and actin cytoskeleton (phalloidin - red) simultaneously. Imaged at maginification 20x

Even after individual cell separation via image cropping, some cells exhibited protruding extensions far out of the cell body which were in contact with similar extensions of neighbouring cells. Thus, before applying countrification macro, single cells were 'lassoed' to indicate their boundaries. This process ensured a more accurate definition of each cell's boundaries and helped exclude areas in the image not belonging to the cell from fibre identification, which substantially sped up the overall process time.

3.5.2 Image quantification

Image quantification was conducted in the following 5 steps:

1. Cell boundary identification
2. Cytoskeleton segmentation
3. Fibre refinement
4. Background subtraction

5. Parameter calculations

3.5.2.1 Cell boundary identification

The cell boundary is detected by the ensemble of grayscale thresholding of any contour dilation. The contour is defined by drawing a lasso around the cell shape with a mouse pointer, as can be seen in Figure 3.3.

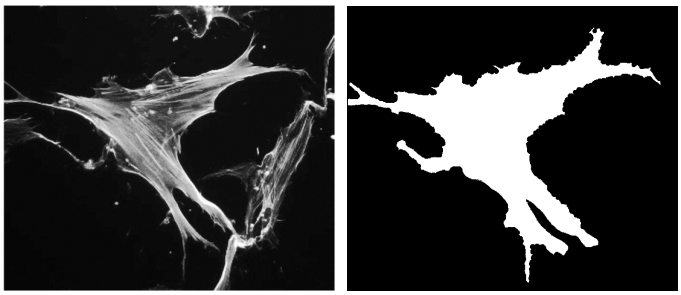

Figure 3.3 Original image showing two cells after image cropping (left - brightness was increased for better visibility) and binary map of cell boundary (right) for an individual cell after defining the contour with a lasso tool

3.5.2.2 Cytoskeleton segmentation

Once the cell boundary is identified, images are rotated to fit the smallest possible image area to reduce computation time. Following the boundary detection, segmentation of fibres is performed using the convolution of the original image with a series of elongated Laplace of Gaussian (eLoG) kernels i.e. a filter of 21 x 21 pixels, as used by (Zemel et al., 2010). This filter is applied at each pixel within the boundary detected in the previous step. At each location this filter is rotated by 30 increments of 6° each, and the angle at which a maximum signal is achieved is recorded for each pixel. Fibres are recognised by cross correlating images with the eLoG kernels. Following this process one map of signal intensity and another of angular orientation for each pixel belonging to the fibres are created (Figure 3.4). Unlike reported by Zemel et al. (2010), our algorithm does not subtract bright spots at this stage, these artefacts are rectified during the following fibre refinement stage.

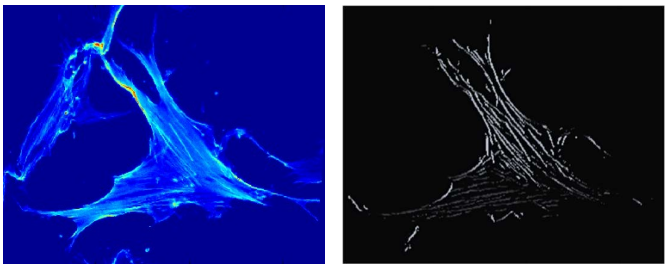

Figure 3.4 Original cropped image of a single cell after rotation to fit the smallest possible image area (left) and the corresponding fibre orientation map after cytoskeleton segmentation (right)

3.5.2.3 Fibre refinement

Fibre refinement is carried out using a coherence-enhancing diffusion (CEDF) filter. The binary image of the fibres is first enhanced by the algorithm as it extends and connects

interrupted fibres. CDEF filters are designed to enhance flow like structures e.g. fingerprints (Weickert, 1999). The underlying idea is to anisotropically diffuse along the flow lines to close any gaps (Weickert, 1999). Using the angular orientation map obtained in the previous step, the orientation of each newly added pixel (with CFDE) is compared to the average orientation of other pixels belonging to the same fibre within a [9 × 9] neighbourhood. If the average lies within 50 margins to the angle of the newly added pixel it is kept or otherwise discarded. These two steps (fibre enhancement followed by fibre trimming) are iterated until no further changes take place to the binary fibre map. The fibre refinement step ensures that interrupted lines are connected and that the effect of bright dots is removed.

3.5.2.4 Background subtraction

The last step involves the determination and removal of any background fluorescence due to the presence of unbound monomers of the insert fluorophore, which in this case is phalloidin. To create a background fluorescent map, the algorithm computes the median value of signal intensity within a [21 x 21] window at each pixel edging the fibres. The pixels belonging to fibres are not used in the computation of the background map. The result is a smoothly changing intensity map with fibre pixels replaced by the median of non-fibre pixels.

This background map is then subtracted from the original image and the pixels that obtained negative values belonging to a fibre map are removed and the process is iterated until convergence is reached. This process ensures that only pixels with a positive intensity value which belong to a fibre are included in the resulting fibre map (Figure 3.5).

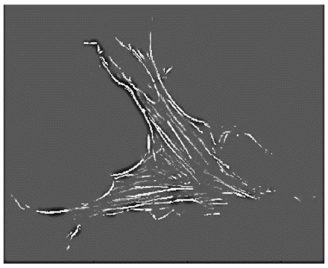

Figure 3.5 Exemplary fibre intensity map after background subtraction (brightness was increased for better visibility)

3.5.2.5 Parameter calculations

Following the above described image processing, 19 geometrical and structural features of the F-actin network and the nuclei were designed, which are as follows:

1. **Cell area:** Cell area is represented by the total area of all the pixels encompassed in the cell boundary defined in previous steps (section 3.5.2.1); where each pixel covers 0.1043 μm^2 of the actual area on the specimen.

2. **Cell aspect ratio:** When calculating the aspect ratio of a cell, any long and thin protrusions can lead to a misrepresentation. Figure 3.6 illustrates 4 possibilities of fitting the same cell in a bounding box, where Figure 3.6D represents a fit which calculates the aspect ratio of the cell body while excluding any long trailing protrusions.

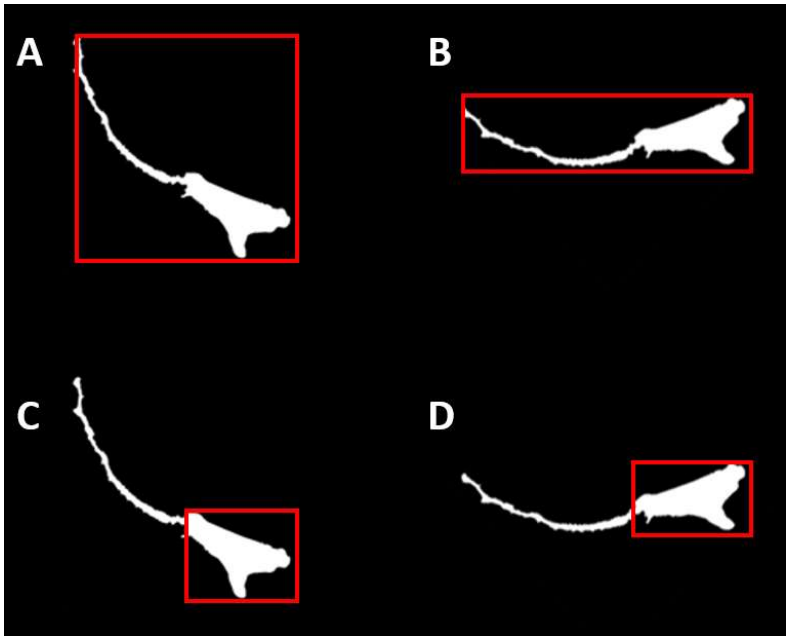

Figure 3.6 Illustration of different possibilities to fit the same cell in a bounding box for calculating the aspect ratio of the cell body

3. **F-actin:** Signal intensity of all the pixels belonging to cell's fibre map (described in section 3.5.2.2 and 3.5.2.3) is added up as a representative measure of the total F-actin, normalised by the 'gain' and 'exposure time' (i.e. normalised pixel intensity (NPI)).
4. **Actin fibre bundle thickness:** It is important to mention that this feature provides a representative value instead of the absolute thickness. Individual actin filaments are about (~ 7-8 nm) wide and form compact bundles in cells. Even the bundle thickness is much smaller than the dimensions covered by individual pixels at 20x magnification (i.e. 0.323 µm x 0.323 µm). "Actin fibre bundle thickness" is calculated by summing up the intensity signal of all pixels belonging to a fibre bundle (as defined in section 3.5.2.2 and 3.5.2.3) and normalising by its length. This process is repeated for each fibre bundle and a median value for the cell is recorded.
5. **Fibre thickness variability:** This feature describes the standard deviation (as a percentage of mean) among of fibre bundle thicknesses measured in the previous step.

6. **Fibre alignment:** This parameter provides a measure of the level of variation (standard deviation) among the angular orientation of all pixels belonging to fibre map. The values are bound between 0 to 0.4 and are measured in circular coordinates. The smaller this value is the more aligned (on average) fibre bundles are within a cell, i.e. more parallel they run to each other. Examples of varying level of fibre alignment in different cells can be seen in Figure 3.7. Fibre map (as defined in section 3.5.2.4) is rendered with 180^0 colour scale, starting from red at 0^0 and ending with blue at 180^0, whilst yellow/green in the middle at 90^0 from the positive x-axis.

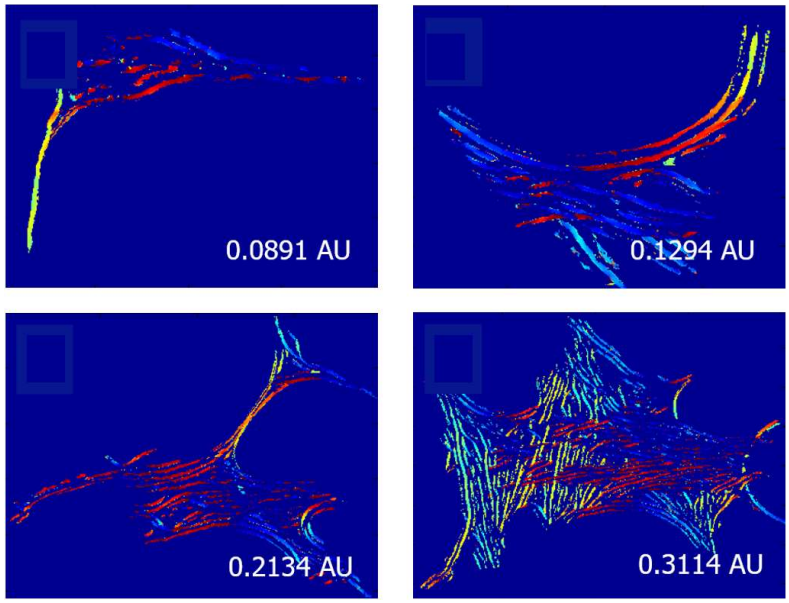

Figure 3.7 Exemplary fibre bundle alignments for different cells and their corresponding values

7. **Fibre curvature:** This feature provides an indication of the curvature of fibre bundles in relation to the centre of the cell. The measurements are bound between 0 and 0.4 and are measured in circular coordinates.
8. **Location of peak fibre intensity (LPFI):** This feature provides the position of peak actin fibre concentration along the cell radius. Signal intensities of all the pixels belonging to a 1-pixel wide path (geometrically similar to cell boundary) are summed. This is repeated for every concentric 1-pixel wide boundary-path between the cells boundary and its centre. The location of the concentric-path with the highest total intensity is recorded and normalised by radial length i.e. position 0 corresponds to the cell's centre and 1 to the cell's edge.
9. **Fibre spread variability**: Provides an indication of the distribution of actin fibres across the cell area. Figure 3.8 shows fluorescent heatmaps as an example of low dispersion of F-actin (A), as most of the fluorescent intensity is concentrated to the

edges (red) with very little at the centre of the cells (blue). Whereas Figure 3.8 B displays a example of cell which has a relatively uniform distribution of F-actin across its area (mostly green).

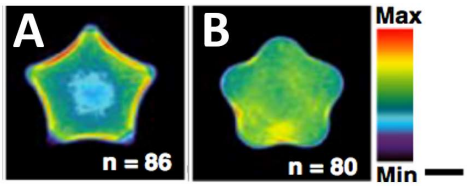

Figure 3.8 Fluorescent heatmaps of > 80 cells on a defined-shape micro-pattern and stained for myosin IIa. Fluorescent images of all cells were super imposed to create the heatmaps (scale bar, 20 µm) (Kilian et al., 2010).

10. **Stellate factor:** Stellate factor assess the relative likeness in the cell shape to that of a regular star polygon or circle on a scale of 0 to 1, with 0 being a circle. (Figure 3.9).

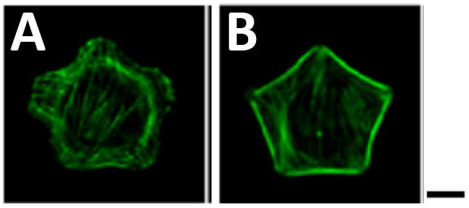

Figure 3.9 Exemplary images for cells grown in flower (A) or star (B) shape (scale bar, 20 µm) (Kilian et al., 2010)

11. **Fibre length:** is the average length of fibres (bundles) within a cell. A typical fibre bundle thickness corresponds to around 3 pixels and hence the fibre (bundle) length is calculated as 3rd of its area (in pixels). It is also weighted by its average pixel intensity.
12. **Fibre length variability:** It's the measure of variance among the fibre lengths within a cell, recorded as 'percentage standard deviation' from the mean.
13. **Fibre chirality:** Determines how fibre bundles in a cell are orientated in relation to their centre of mass, i.e. pointing towards or tangential to the centre. For every pixel of a fibre bundle, the angle formed between the line joining the pixel to the centre of the cell and its local orientation are calculated and averaged. This average value is then weighted by the average intensity of the same fibre bundle to get the final chirality score for each fibre. Median of these values is then used to represent overall chirality of the cell. Figure 3.10 displays exemplary images of cells, arranged (from A to C) in an order of increasing chirality. The measure is bound between 0 and 90^0.

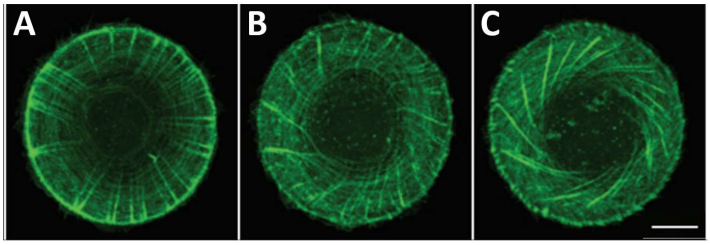

Figure 3.10 Exemplary images of different cell chirality and their corresponding chriality values (scale bar, 10 µm) (Tee et al., 2015)

14. **Fibre chirality variability**: It is the variance among the chirality measure of each fibre within a cell.
15. **Nuclear brightness**: Signal intensity of all the pixels enclosed within the nuclear boundary is added up as a representative measure of the total nuclear content, normalised by the 'gain' and 'exposure time' (i.e. normalised pixel intensity (NPI)).
16. **Chromatin condensation:** Is calculated by measuring of the local changes in fluorescent (DAPI) intensity of pixels in the cell nucleus. An increased number of speckles (brighter dots surrounded by regions of dimmer fluorescence intensity) reflects an increase in the condensation of the chromatin in the nucleus. The pixel intensity was also normalised by the 'gain' and 'exposure time' (i.e. normalised pixel intensity (NPI)).
17. **Nuclear volume**: To estimate the physiological and mechanical parameters of the nucleus, it was assumed that an undeformed nucleus forms a perfect spheroid. However, nucleus is thought to be under continuous forces with in the cell which cause it to take up ellipsoidal shape. Then to measure nucleus' volume, its dimensions in the x and y axis were taken directly from the (2D) images, whilst its z dimension was estimated by extrapolating the intensity gradient of the (2D) nuclear images as shown in Figure 3.11 "Averaged fluorescence intensity profile as a function of radial distance. Black squares correspond to fluorescence intensities recorded, and the imaged nucleus is taller than the depth of focus of the objective lens. Red line corresponds to the ellipse obtained when fitting the fluorescence intensity profile of the outermost pixels. Left axis shows the fluorescence intensity values from the analysed image, while right axis shows the height profile estimated using the calibration factor" (Keeling et al., 2017).Figure 3.11. The calculated volume was then normalised by the (estimated) volume of the isolated nucleus. This method of nuclear volume estimation from 2D images has also been used and explained in detail by Keeling *et al.* (2017).

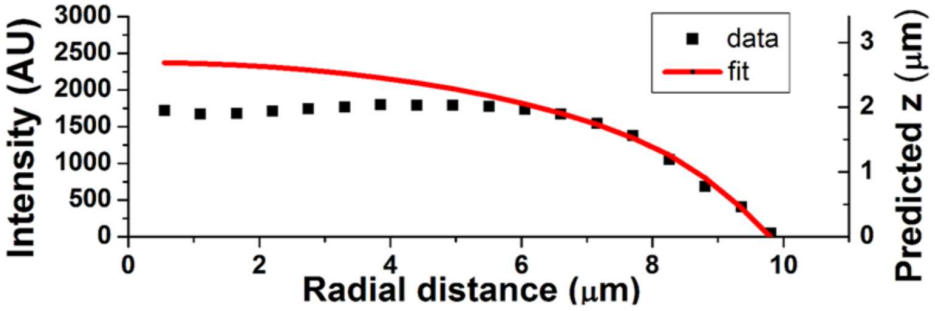

Figure 3.11 "Averaged fluorescence intensity profile as a function of radial distance. Black squares correspond to fluorescence intensities recorded, and the imaged nucleus is taller than the depth of focus of the objective lens. Red line corresponds to the ellipse obtained when fitting the fluorescence intensity profile of the outermost pixels. Left axis shows the fluorescence intensity values from the analysed image, while right axis shows the height profile estimated using the calibration factor" (Keeling et al., 2017).

18. **Poisson ratio:** As explained previously, an isolated nucleus is assumed to have a perfect spherical geometry. Poisson ratio is then deduced from the difference between the (estimated) volume of the deformed nucleus (as calculated in feature 17 above) to that of its isolated form.
19. **Nuclear stiffness:** It is a (apparent) measure of nuclear stiffness, as reflected by the amount of nuclear deformation (in 3D) induced by the cell's intracellular forces. To estimate nuclear stiffness, a slightly modified approach presented by Versaevel, Grevesse, & Gabriele, (2012) was used. Accordingly, it was assumed that a nucleus experiences compressive loads in two main directions: normal compression which makes the nucleus flatten in the z axis, and lateral compression, which causes the nuclei of very elongated cells to display an elongated shape in the x-y axis. Using this this model, elastic modulus (E) was computed. The process is explain in further details in the publication by (Keeling et al., 2017)

Algorithms used to extract the above mentioned features were developed within the group, by building upon work published by Gavara & Chadwick in 2016.

3.6 Data analysis

Once the above listed features were processed, SPSS was used to assess the normality or data distribution, first by calculating and evaluating their skewness and kurtosis against reference range published by (Kim, 2013). It was also supported by Shapiro-Wilks normality test and where these methods could not yield a conclusion, visual assessment of frequency distribution and Q-Q plots were employed to reach a decision. All of this was performed using the built-in functions of SPSS. Based on the outcome of distribution assessment, appropriate descriptive measurements (i.e. Mean for normally and Median for lognormally distributed data) were calculated MS Excel and plotted using Origin Pro. Outlier assessment was ask performed using the SPSS built-in function where data points with values outside

1.5 time and 3 times the interquartile range (IQR) were labelled with * and ** respectively. This gave an idea of the reliability of the descriptive statistical calculations. Additionally, Levene's test was also performed on all the data to calculate the homogeneity of variance (SPSS). Where the data was not normally distributed, it was converted to log scale before performing ANOVA (followed by Tukey corrections) to determine the differences among the data points (SPSS).

Following this, Linear Discriminant Analysis (LDA) was used to assess the performance of the 19 measured features in the classification of cells across (Osteogenic and Adipogenic) lineages and time points. LDA was trained and testing in in python by the code provided in section 9.4 of appendix. Then Principal Component Analysis (PCA) was used to assess the relative contributions of each parameter in the total variance segregating the classification domains. Principal components were calculated in Minitab. Lastly feature correlation analysis was performed using the built-in function of SPSS and the results were presented with the aid of colour scaling using MS Excel.

Chapter 4 | Optimum conditions for single cell image quantification of differentiating cells

Up to date, no research studies have been reported in which morphometric examination of hMSCs differentiation at a single cell level for the first week of differentiation has been attempted. Thus, based on the novelty of this thesis, experimental conditions were required to be optimised from bottom up. The following chapter entails details of preliminary investigations that were performed to define suitable experimental conditions for this study regarding cell density, substrate stiffness, feature analysis and imaging standards.

4.1 Standardisations

4.1.1 Aim

Cell proliferation, migration and spreading have an inverse effect on the length of duration for which most cells are likely to stay segregated from each other. Cell behaviour varies not only under different culture conditions but also between cell batches. This experimental research was carried out to define optimum starting conditions which would allow for single cell analysis over the longest possible differentiation period.

4.1.2 Doubling time

Firstly, the behaviour of the cell batch used in this thesis had to be investigated, for which their doubling time was studied. For this, a vial of 50k cells at P2 was thawed and grown in T25 flasks until ~70 % confluency was reached, at which point cells were split into 2 flasks allowing more space for further proliferation. During the splitting process, cells were counted using a haemocytometer. The process was repeated at every passage through to the 9^{th} passage. From the obtained cell counts, the doubling time at each passage was estimated and plotted in Figure 4.1.

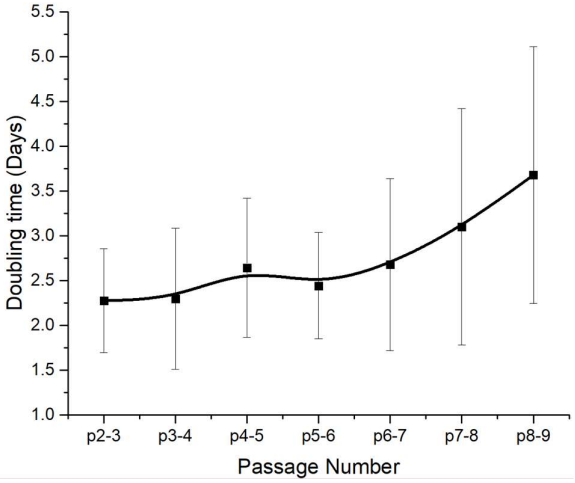

Figure 4.1 Doubling time of the cell batch used in this study over 9 passages

Doubling time remains relatively consistent until passage 6 from which onwards it starts to increase. Based on these findings, all experiments in this thesis were performed with cells between P4 and P6 for consistency.

4.1.3 Cell Counting

Research has shown that the cell density before differentiation is induced has a very strong influence on the extent of the differentiation process (McBeath et al., 2004). For this reason, cell cultures were prevented from reaching full confluency prior to being seeded on coverslips before differentiation. Cells were detached with 0.5 mL of Accutase solution at ~ 70 % confluency, 10 µL of which was used to estimate cell numbers with a haemocytometer. Based on the size of a typical hMSC, a fully confluent T25 flask can contain up to 0.7 million cells, while ~ 70 % confluency would result in around 0.5 million cells. When detached with 0.5 ml of Accutase solution, this would yield a suspension with a concentration of approximately 1 million cells/mL (~100 cells per 0.1 µL). At such low cell numbers, haemocytometer counts often return estimates with a very high standard deviation. Considering this lack of precision, a more suitable cell counting method was developed for this study, details of which are explained below.

After thawing, cells were seeded in a T25 flask. After reaching around 70 % to 90 % confluency, flasks were imaged at 5 - 7 random regions by phase contrast microscope. Cells were then detached, counted with a haemocytometer, re-suspended in 10 mL of xPan and split equally in 2 T25 flasks. Cells were then allowed to re-attach for about 6 h and the new flasks were imaged again by phase contrast microscope at 5 - 7 random regions of the flask. The whole process was repeated until passage 9. At every passage, the old flasks were also imaged at 5 - 7 random regions and those cells still attached were counted and logged, along

with cell counts from images of the new flasks. These cell counts were then averaged and used to estimate cell numbers at every passage. The equipment specific conditions and calculations are as follows:

- **Pixels size:** 6.45 µm x 6.45 µm
- **Image resolution:** 1344px x 1024px
- **Image size**

  @5x magnification: 1733.76 µm x 1320.96 µm

  @10x magnification: 866.88 µm x 660.48 µm
- **Area of the image**

  @5x magnification: 0.022902276 cm^2

  @10x magnification: 0.005725569 cm^2
- **Cells per T25 =** $\frac{\boldsymbol{Avg\ cell\ count\ per\ view\ field}}{\boldsymbol{Area\ of\ the\ view\ field}}$ x 25

This method can only be considered reliable if cells are uniformly distributed across the whole area of the flask.

Both cell counting methods were compared by calculating the percentage difference (PD) between the cell count estimates (CCE) from haemocytometry and post-split images to those of pre-split images. Figure 4.2 shows that the PD between CCE from pre- and post-split images was much more consistent than that between CCE from haemocytometry and pre-split images. The gradual increase in the PD between CCE from pre- and post-split images was supported by the observation that cells appeared to become more adhesive with increasing passage number as detachment time increased, similar to the number of cells remaining attached to the old flask.

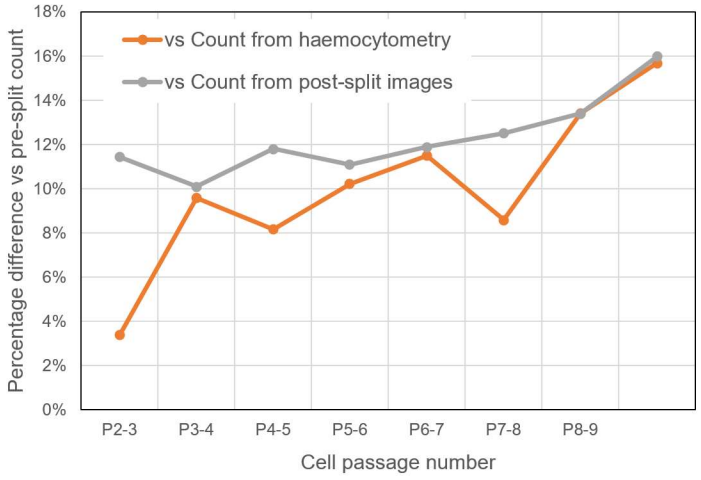

Figure 4.2 Percentage difference between the cell count estimates from haemocytometry and post-split images to those taken of pre-split images

Figure 4.3 displays the CCE from pre-split images versus post-split images with a slope of 0.8831, indicating a consistent difference of around 12 %.

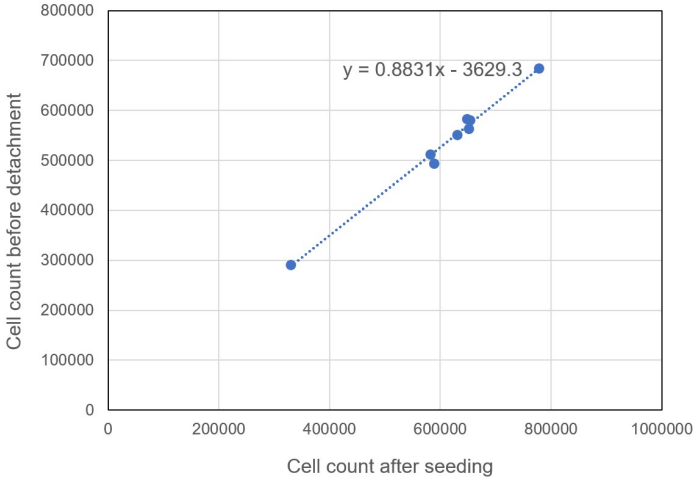

Figure 4.3 Cell count estimates from pre- against post-split images. Each point is from a separate passage number.

Based on these findings, it can be concluded that around 85 - 90 % of the hMSCs survive through passaging with Accutase solution. Hence, cell count estimates acquired with the above presented method were corrected for this difference by applying 15 % reduction.

4.1.4 Cell seeding

As mentioned earlier, cell density can not only influence the differentiation process but also complicate single cell imaging. Most cell densities reported in literature, for both osteogenic and adipogenic differentiation in 2D cultures, lie above 3000 cells per cm^2. Some representative studies are mentioned in Table 4.1 including differentiation type and cell densities used.

Table 4.1 Cells densities used in the literature for stem cells differentiation

Study	**Differentiation type**	**Cell density**
(Jaiswal et al., 2000)	Osteogenic	3.0×10^3 cells/cm^2
(Parhami et al., 1999)	Adipogenic	8.5×10^4 cells/cm^2
(Ignotz & Massagué, 1985)	Adipogenic	Fully confluent monolayer
(Dalbay et al., 2015)	Adipogenic Osteogenic	5.0×10^3 cells/cm^2
(Treiser et al., 2010)	Adipogenic Osteogenic	3.0×10^3 cells/cm^2
(Aldridge et al., 2013)	Adipogenic	4.0×10^4 cells/cm^2

	Osteogenic	

As can be seen in Figure 4.4, cells are in contact with each other at a cell density of 4.0×10^4 cells/cm^2.

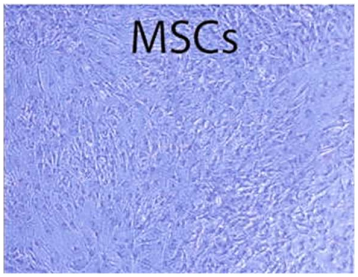

Figure 4.4 MSCs seeded at a cell density of 4.0 x 10^4 cells/cm^2 (Aldridge et al., 2013) *(brightness and contrast increased for better visibility). Imaged at magnification 100x*

Based on the aim of this project, starting conditions, which would enable single cell observations for the longest duration of osteogenic and adipogenic differentiation of hMSCs were investigated. While selecting a range of cell seeding densities, factors such as cell area, doubling time and the total area of the culture surface were also considered.

Cells were seeded in 9 of the 12 wells of a 12-well plate, with 3 wells used for each of the following cells densities i.e. 500, 1000 and 1500 cell/well. 1 well of each cell density was then treated with xPan, ODM and ADM for up to 21 days.

Throughout the process, cells were examined regularly during the 21 days to determine until which time point cells would stay separate to enable single cell imaging. It should be mentioned, that among the 3 culture media, cells proliferated the fastest in xPan and the slowest in ADM, as was also reported by Sekiya *et al.* (2003). Interestingly, opting for a too low starting cell number (500 cells/well) resulted in clustering of the cells, while 1000 cells/well was found to be the optimum starting cell density. At this density most cells remained separate until day 5-6 in xPan, day 6-7 in ODM and day 12 in ADM. Cells induced with ADM were observed to increase drastically in size which caused cells to establish physical contact with each other. This process was repeated on 5 different stiffnesses of PAA gels with fibronectin coating. Further information on this can be found in section 4.1.5.2. A general observation concerning the cell density was that no clear difference in the degree of differentiation was noticed between cultures at high or low cell densities.

As mentioned above, cell cultures in xPan and ODM reached a higher than desired confluency for single cell imaging by day 6 and 7, respectively. Since the aim of this study also included cell morphology observation for the longest possible time, other approaches were tested to increase the experimental duration. One of those was to differentiate cells in a 96-well plate

at high and low cell densities, followed by detachment on days 3, 5 and 7 with subsequent reseeding corresponding to ~ 1000 cells/well. Cells were allowed to resettle (attach and spread) for around 24 h after reseeding before resuming the day count. Here, it was observed that the longer cells were treated with ADM, the fewer cells reattached after reseeding, whereas cells treated with ODM exhibited no complications during reattachment.

It was also found that the second approach did not result in reliable analytics, as it could not return consistent cell estimates due to detachment and reseeding. The assessment of images highlighted that several cells were found to be damaged and folded-over on themselves (Figure 4.5).

Figure 4.5 Exemplary cell images for damaged cells and cells folded-over on themselves after detaching and reseeding (brightness increased for better visibility) taken at a magnification of 20x

It can be hypothesised that the damage and folding over of cells was due to the lack of adhesion after reseeding. Based on the above presented findings, the first approach with a starting cell density of 1000 cells per well was chosen and the experiment duration limited to 7 days.

4.1.5 Substrate optimisation

Most research in the field of substrate stiffness has reported values between 1 - 4 kPa for adipogenic and 20 - 35 kPa for osteogenic differentiation (Gefen & Benayahu, 2014; Hwang et al., 2015; Lv et al., 2015; Terraciano et al., 2007; Zhao et al., 2016). However, none of those studies were designed for single cell image analysis. Therefore, five gels of different stiffness of 2, 3, 5, 10 and 35 kPa were tested for their suitability for this thesis. Suitability assessment was based on factors such as cell spreading, proliferation rate, reproducibility of the stiffness and uniformity of coating.

4.1.5.1 Reproducibility

PAA gels of 5 different stiffnesses were produced as described in section 3.3. The chosen concentrations were estimated from data published by (Yeung et al., 2005). The PAA mixes were prepared as listed in Table 3.7 and degassed with N_2 gas for about 20 min. 500 µL of each mix was transferred to separate 1 ml Eppendorf tubes and polymerised. Polymerised

gels were then extracted from the vials and uniform cylinders were cut-out from the cross section. Subsequently, these cylinders were mechanically tested as explained in section 3.3.2. Figure 4.6 shows the stress/strain plots from the compression test of 2 kPa and 9 kPa PAA gels. Higher variance among the gradients of 2 kPa graphs (Avg 1.36 kPa, SD 21.03 %) (Figure 4.6 A) compared to the gradients 9 kPa graphs (Avg 8.14, SD 14.88 %) (Figure 4.6 B) suggests a lack of precision in reproducing lower stiffness gels. Though the variation during the mechanical testing of lower stiffness gels could also be due to systemic limitations, such as load cell sensitivity or an uneven cut surface of the construct.

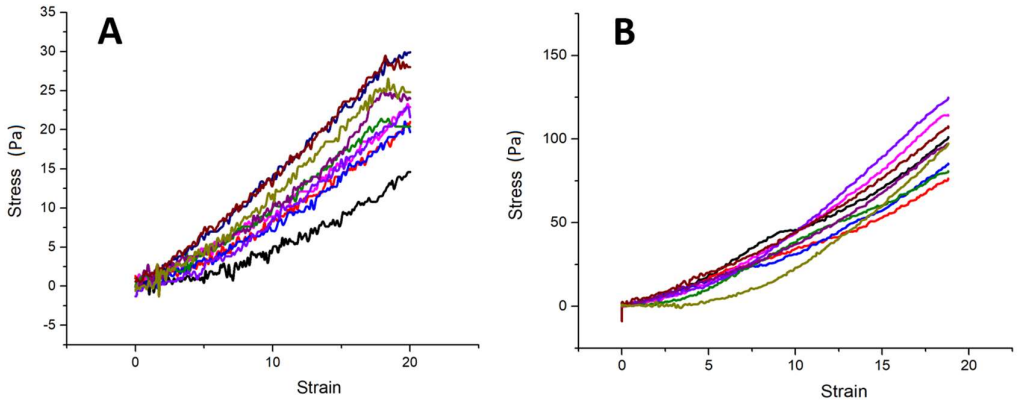

Figure 4.6 Stress vs strain plots for mechanical testing of PAA gels with different stiffness. A) 2 kPa and B) 9 kPa

4.1.5.2 Fibronectin coating

Different variations for coating PAA gels with fibronectin have been reported in the literature. Two of those methods have been tested for their suitability in this thesis.

In method A, fibronectin was attached to the PAA gel via a crosslinker (Sulfo-SANPAH) as explain in section 3.3.1.1. Cells were seeded at approximately 1000 cells per gel and were cultured for up to 10 days in xPan, ADM or ODM. It was observed that fewer cells attached on the gels as compared to cells seeded on glass at the same cell density, which was found to be most prominent for gels of 2 and 3 kPa, where only a few dozen cells attached. Most cells on 35 kPa gels appeared well spread, whereas cells on softer gels formed aggregates (Figure 4.7) which increased in size over time.

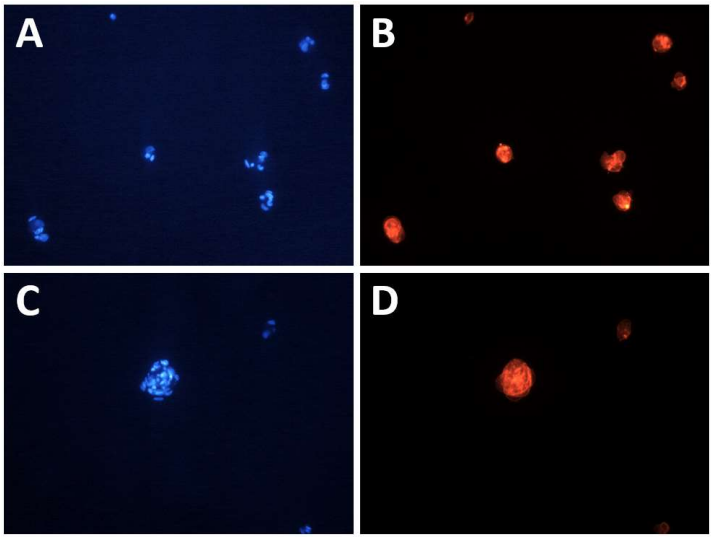

Figure 4.7 Epifluorescent images of the cell nucleus (A and C) stained with DAPI and the cytoskeleton (B and D) stained with phalloidin for cells grown on PAA gels with a stifness of 2 kPa (brightness increased for better visbility) taken at a magnification of 20x

In cases where cells were not aggregated they were usually too small for multi-feature image quantification. Figure 4.8 shows cells grown on low stiffness PAA gels being small and exhibiting closely packed actin fibres.

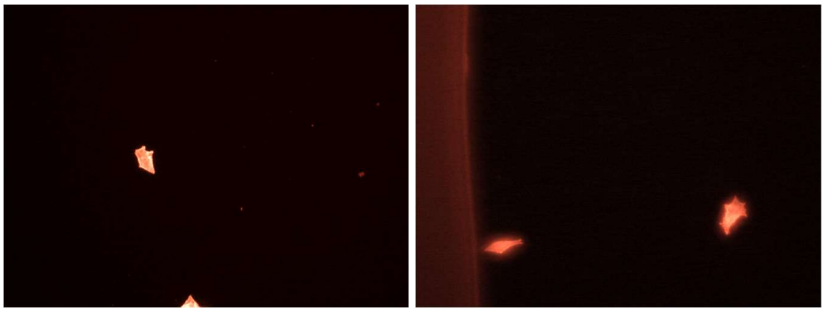

Figure 4.8 Epifluorescent images of the cell cytoskeleton stained with phalloidin for cells grown on PAA gels with a stiffness of 2 kPa (brightness increased for better visbility) taken at a magnification of 20x

These observations raised doubts over the reliability in identifying CSK fibres at the available image quality (sensor resolution). Imaging at higher resolution to overcome this reliability issue resulted in out-of-focus bright images at magnifications above 10x, due to cells growing much taller in the z-plane compared to the x- and y- plane on softer gels. Our observations on the effect of substrate stiffness on cell spreading was in agreement with reports by Hwang *et al.* (2015) as well as Caliari and Burdick (2016) (Figure 4.9).

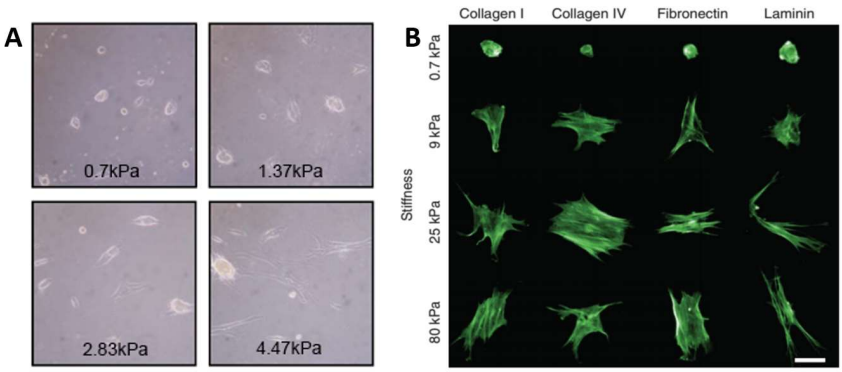

Figure 4.9 Exemplary images taken from studies A) (Hwang et al., 2015) *and B)* (Caliari & Burdick, 2016) *supporting observations on the effect of subsrate stiffness on cell spreading, Scale bar: 50 µm.*

Similar as on glass, cells multiplied the fastest in xPan and slowest in ADM. In addition to exhibiting a slower proliferation rate, less cells appeared to atta

ch on softer gels in comparison to stiffer ones. Based on an investigation performed by Gobaa *et al.* (2015), hMSCs exposed to ADM for 11 days on a substrate with 10 kPa stiffness resulted in a significantly higher expression of fat lipids in comparison to their counterparts differentiated on 30 or 50 kPa substrates. Although their cell seeding density was too high for single cell analysis, cell images presented by them showed visible stress fibres. Considering these findings, a stiffness of 10 kPa was chosen for adipogenic differentiation in our experiments.

Cell seeding optimisation (section 4.1.4) was repeated with gels of 10 kPa and 35 kPa stiffness for adipogenic and osteogenic differentiation, respectively. This resulted in 1500 and 1000 cells per well for AD and OD, respectively, which were considered as suitable starting cell densities.

Method B which involved embedding the fibronectin coating in the PAA gel at the time of polymerisation without any crosslinker yielded comparable results as method A. However, due to less steps involved, method B was chosen to be used for this thesis.

4.1.6 Feature development

Few studies have been reported in literature which attempted to extract visual/geometric measurements from cell images and correlate them with applied stimuli. Those investigations revealed interesting findings and have laid promising groundwork for further investigations. For example, Sonowal *et al.* (2013) showed that exposure to ADM or ODM produced measurable changes very early in the differentiation process i.e. changes in the amount of actin were recorded in the first 24 h (Figure 4.10).

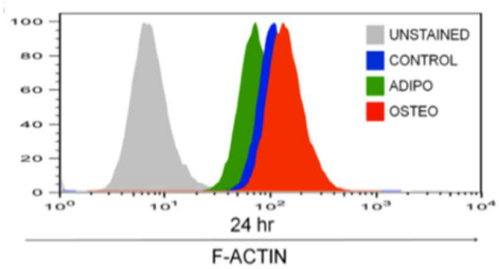

Figure 4.10 Changes recorded in the amount of actin in the first 24 h after adipogenic or osteogenic differentiation was induced (Sonowal et al., 2013)

Treiser *et al.* (2010) measured multiple geometric parameters over a period of 96 h and showed a clear classification of OD and AD precursors using multivariate analysis. Unlike Sonowal *et al.* (2013), Treiser *et al.* (2010) imaged cells in 2D configuration, which allowed them to visualise and quantify changes in cell morphology caused by differentiation.

For this research project, cells were differentiated for 7 days, fixed and stained for actin, nucleus and myosin. The samples were imaged and examined to identify geometric features of cell morphology. This was carried out for both osteogenesis and adipogenesis with specific attention given to any features distinguishing the cell types. Following the development of feature quantification algorithms, a batch of cells with distinct appearances was tested, such as for chirality and angular variability (exemplary images for this can be found in section 3.5.2.5). The algorithm's reliability was qualitatively assessed by comparing the output values against the visual appearance of the cells. Where necessary, the feature quantification algorithm was improved to yield more accurate representative values.

4.1.7 Optimisation of imaging protocol

The best options for imaging of cells for this thesis were the epifluorescent microscope, the confocal microscope and an IN Cell1000 analyser. One essential requirement for a reliable multivariate analysis is the need for large amounts of information. Thus, image acquisition could be considered the bottleneck in this process, which is why an IN Cell1000 analyser for high throughput imaging was tested. It was found that the IN Cell1000 was suitable for imagining in multi-well plates. Owing to the nature of our experimental setup where coverslips are mounted on glass slides for imaging, a guide rig was designed to assist with the precise mounting of the coverslips which arranged them similar to wells of a 24 well-plate. Images of this guide utensil can be seen in Figure 4.11.

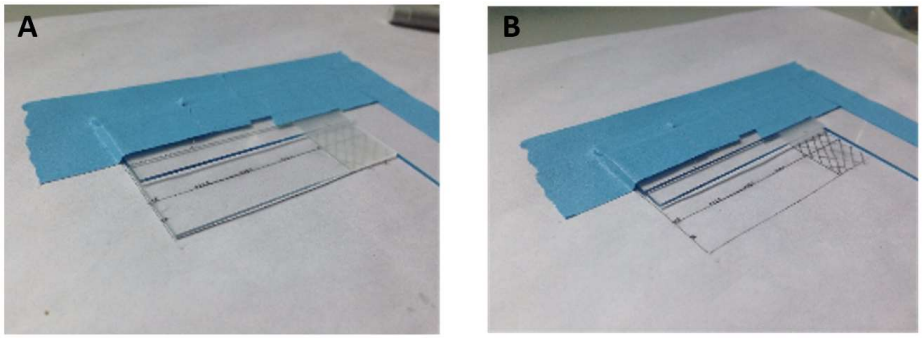

Figure 4.11 Images of a guide appliance for high throughput imaging of cells on coverslips with the IN Cell1000. A) is showing the setup with coverslips mounted on a glass slide in position, B) appliance without glass slide

The inability of the IN Cell analyser to refocus at every frame on the coverslip posed a limiting factor, which was due to the inconsistent spread of mounting media between the glass slide and coverslips. The attempt to even out the spread of mounting media by applying gentle force resulted in damage of the cells (an exemplary image of a damaged cell can be seen in Figure 4.5).

Imaging with a confocal microscope provides higher quality images, though at the cost of a fast acquisition time as well as algorithm processing time. Thus, prioritising quantity of data as well as time efficiency, a small amount of image detail was compromised, and images were acquired with an epifluorescent microscope.

Throughout the feature development process, it was observed that actin intensity varied considerably across different timepoints during the differentiation, which in some cases resulted in cells being under- or overexposed, if the exposure time and gain values were kept constant. In order to reduce systemic errors during the process, it was desirable to acquire images at similar settings, which is why the dye concentration was optimised to produce similar levels of signal intensities at all timepoints throughout the differentiation process. The volume ratios shown in Table 4.2 were determined as optimum conditions after testing a variety of different combinations.

Table 4.2 Optimum volume ratios for different staining protocols to ensure a similar level of signal intensity during imaging cells at different timepoints throughout the differentiation process

Staining	Volume ratio
Vimentin Antibody (primary) – mouse	1:4000
A Tubulin Antibody (primary – mouse	1:50
Myosin Antibody (primary) – rabbit	1:200
FITC – Anti-mouse	1:200
FITC – Anti-rabbit	1:200
Phalloidin - TRITC	1:1000

Although, with the optimisation of staining concentrations, it was possible to keep fluorescence relatively consistent across different CSKs in stem cells, changes in the CSK network itself during the differentiation still resulted in certain cells being imaged either too dim or too bright, especially at later timepoints. Thus, varying image settings, i.e. exposure time and gain, was required.

To accommodate these variations, the algorithm was modified to access metadata of each image for normalisation of their fluorescent signal by exposure time and gain. This function was then validated by analysing the output data from images of the same cells captured at different exposure times and gain settings.

4.2 Systemic variance

Though great care was taken when choosing experimental methods, especially in relation to control variables, certain systemic variances could not be excluded. In this section we will evaluate some of the identified variances that may be present in the data discussed in the Chapter 5 and 6

4.2.1 Substrate based variance

To evaluate any variance related to substrate properties, stem cells were cultured on three different substrates i.e. 35 kPa PAA gel with fibronectin coating, glass with FBS coating and glass with fibronectin coating. First the measurements of individual features were compared between conditions (appendix 9.1.1), followed by their multivariate analysis of variance ($p < 0.001$) (MANOVA appendix 9.1.2.1). ANOVA of individual features between the conditions showed significant difference in 13 out 19 features (appendix 9.1.2.2). These observations suggest that it is not only the stiffness of the substrate but also the coating which may have some influence on how cells react to differentiation stimuli. To further evaluate the extent of these influences, data from experiments on different stiffness but with the same coating should be repeated for comparison.

4.2.2 Donor based variance

In the same experiment, we also compared cells from 2 different donors cultured on the different substrates (35 kPa PAA gels with fibronectin coating, glass coated with FBS (gFBS) and fibronectin (gFibro). ANOVA of the individual feature analysis showed 11 out of 19 features with significant difference ($p < 0.001$) among donors on gFBS and gFibro (appendix 9.1.3.1). MANOVA on data from both glass substrates also showed significant ($p < 0.001$) overall difference (appendix 9.1.3.2). Based on these observations it can be proposed that cells from different donors show very different morphometrics. The extent to which cells

from different donors can vary in their morphology should be further investigated with a higher number of donors to supplement the findings of this study.

4.2.3 Variance of experimental repeats

Lastly, we assessed the variance between 3 repeats of the experiment discussed in chapter 5 (i.e. differentiation towards AD and OD on glass coverslips). It was found that there were significant (MANOVA $p < 0.001$) differences between corresponding data points (days 3 and 7) from the 3 repeats (section 9.1.4). Considering the differences between data retrieved from day 0, it was assumed that the stem cells might change during their time being cryogenically preserved. MANOVA of the feature data of control cells from 5 experiments spread over a 2 year period was performed, which also showed significant differences in a number of features. As our method is still in the developmental stage, longer periods between repeats were unavoidable. However, moving forward this time based variance should be taken into consideration when designing further studies such that it minimises the duration between attempts. One solution to reduce this could be to employ high throughput imaging.

4.3 Summary

In this chapter pilot studies were conducted to investigate the optimum experimental conditions required for single cell image quantification of differentiating cells.

For this, in addition to developing a unique cell count estimation method, we also determined the optimum starting cell density for adipogenic and osteogenic differentiation on glass. A cell density of 1000 cells per well was found to deliver adequate cell sparsity for single cell imaging until the 7^{th} day of differentiation.

Suitable stiffnesses of PAA gel substrates were also investigated, where 10 kPa for adipogenic and 35 kPa for osteogenic differentiation were found as optimum. This decision was based on a number of factors which are crucial for the successful completion of this research project. One of these was the limit on the lower end of cell size that can be processed by our algorithm, which is due to the smallest dimensions that eLoG kernels are still able to identify as a fibre. Cells were found to be small as well as form aggregates and exhibited attachment issues on lower stiffness PAA gels (below 4 kPa). Another influential factor in the selection of gel stiffness was the consistency in reproduction. Due to cell morphology greatly varying even with slight changes in substrate stiffness, reproducibility of gel stiffness with adequate precision was essential. Lower stiffness gels displayed a higher variation in Young's modulus,

which was assumed to be due to systemic limitations concerning sample preparation and testing.

Lastly, morphometric features were determined with specific attention given to any features which can characteristically distinguish cell types. Following on from that, feature quantification algorithms were developed and images of cells with appearances representing the defined features were tested. The accuracy of the algorithms was qualitatively assessed by comparing the output values against a visual assessment of the cells. Discrepancies were identified, and algorithms modified accordingly until satisfactory outputs were achieved.

Chapter 5 | Morphometric characterisation of stem cell differentiation

Differentiating stem cells adapt according to their prospective specialised role, which involves changes at the chemical as well as structural level. Various studies have reported changes in the mechanical properties of cells during differentiation and like any other mechanical structure, cell geometry (internal and external) must adapt to reflect its mechanical integrity. Osteogenic and adipogenic lineages were chosen for this study due to the excessive amount of research carried out on them, which can provide reliable references. As suggested in previous studies, mechanical properties of cells might reflect their underlying bio-functions (Gonzalez-Cruz, Fonseca, & Darling, 2012). Structural integrity regulating those mechanical properties could further help understand the underlying cellular processes.

In this chapter, we investigated how each of the 19 features evolved during differentiation and proposed probable explanations for any observed trends. We also assessed the aptness and influence of individual features on multivariate classification of our dataset.

5.1 Materials and methods

5.1.1 Experimental setup

hMSCs were seeded at 600 cells/cm^2 on Ø 13 mm glass coverslips (thickness of 0.17 mm) housed in 24-well plates. Figure 5.1 displays the experimental configuration in the multi-well plate.

Prior to cell seeding, glass coverslips were incubated with 10 % FBS in 24-well plates for 3-4 h. Cells were detached from T25 flasks using Accutase solution, in which they had been cultured for up to 10 days without reaching full confluency. Cells were then portioned and re-suspended in xPAN at a concentration of approximately 1000 cells/mL. For the timepoints 0.25, 0.50, 0.75, 1.00, 2.00, 3.00, 4.00 (days) 1 mL of the cell suspension was gently pipetted in each well (containing one coverslip), for the remaining timepoints (5.00, 7.00, 10.0 days) only 700 µL was used. The cell suspension was regularly stirred to prevent cells from settling down. The above mentioned timepoints were chosen such as to measure early changes in the differentiation process at a higher resolution.

	ADM (Glass)	ADM (Glass)	ODM (Glass)	ODM (Glass)
Day 0.25				
Day 0.50				
Day 0.75				
Day 1.00				
Day 2.00				
Day 3.00				

	ADM (Glass)	ADM (Glass)	ODM (Glass)	ODM (Glass)
Day 4.00				
Day 5.00				
Day 7.00				
Day 10.0				
xPan	Day 0	Day 1	Day 2	Day 3
	Day 5	Day 7	Day 10	Extra

Figure 5.1 Schematic of the configuration for experimental groups (adipogenic, osteogenic and control) at different timpoints

Once seeded, cells were allowed to settle and attach for about 24 h before being induced with differentiation media. At their specific timepoints, coverslips were transferred to another multi-well plate, washed 3 times with (37 °C) sterile PBS and fixed with 10 min incubation in 3.7 % formaldehyde. Coverslips were then washed with PBS and stored in a refrigerator submerged in PBS. Once all timepoints were completed and fixed, one coverslip from each condition was permeabilised with triton-X100 before staining for actin and mounting on glass slides (thickness 1 mm). The mounting media contained DAPI to stain the nucleus. Imaging was carried out immediately after the staining process was completed to avoid photo-bleaching. Imaging was performed as described in detail in section 3.5.1. Some additional coverslips were also treated with differentiation media in parallel to the main experiment (explained above). These cells were differentiated for up to 21 days and then stained with histochemical staining to confirm differentiation. Images of cells treated with ADM for 21 days and then stained with Oil Red O are showing in Figure 5.2.

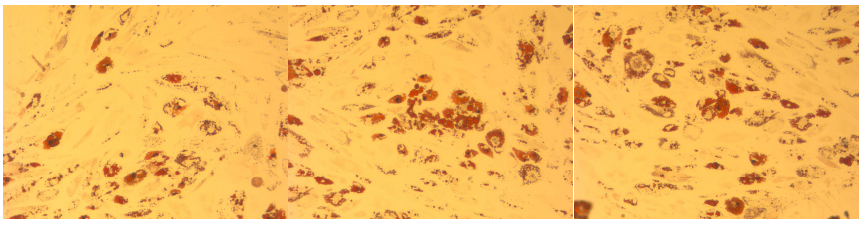

Figure 5.2 Images of cells treated with ADM for 21 days and then stained with Oil Red O take at 20x magnification

5.1.2 Statistical analysis

Data sets of 3 repeats were combined and population distributions were assessed. The assessment was based on the criteria listed in Table 5.1 (adopted from Kim, 2013). Populations matching these criteria were treated as normally distributed for further statistical analysis. Sections 9.2.1 and 9.2.2 (appendix) entail skewness and kurtosis values of the population distributions of each data point, along with their respective z-scores.

Table 5.1 Skewness and kurtosis values of the population distribution with respective z-scores (Kim, 2013)

Sample size	Criteria
n < 50	-1.96 < z-score < 1.96 (alpha of 0.05)
50 < n < 300	-3.29 < z-score < 3.29 (alpha of 0.05)
n > 300	Distribution was assessed qualitatively from their histograms and Q-Q plots, provided that absolute skewness and kurtosis values were smaller than 2 and 7, respectively

Furthermore, results were evaluated using the Shapiro-Wilks normality test. Shapiro-Wilks calculations did not always match with the assessed z-scores, in these cases visual inspection of the histograms and normal Q-Q plots were used to reach a decision. For hugely skewed data, outliers were assessed by thresholding data points to 3 times the Interquartile Range (IQR). Additionally, Levene's test was also performed on all the data to calculate the homogeneity of variance.

Analysis showed that data was log-normally distributed and therefore median values (with Q1 and Q3 as error bars) were plotted as line graphs with b-spline interpolation. 2-way ANOVA followed by TUKEY corrections on the logarithmic values of the dataset was also performed. The significance of differences was presented at 3 levels i.e. $p < 0.05$, $p < 0.01$ and $p < 0.001$, unless otherwise stated.

Another aim of this study was to assess the suitability of these morphometric features for machine learning characterisation. Dimensionality reduction techniques such as LDA and PCA were used to weigh what effect each feature might have on the classification of population.

5.2 Results

The number of cells processed for each timepoint are provided in Table 5.2. Most of the variables (sections 9.2.1 and 9.2.2) exhibited a highly skewed distribution, hence median values were used to plot line graphs.

Table 5.2 Number of cells processed at each timepoint for 3 experimental rounds and their total

Day	AD				OD			
	Exp1	Exp2	Exp3	Total	Exp1	Exp2	Exp3	Total
0.25	72	132	108	312	64	77	72	213
0.50	42	107	113	262	50	100	115	265
0.75	0	18	83	101	37	74	72	183
1.00	51	105	55	211	69	94	12	175
3.00	0	107	40	147	43	99	55	197
4.00	21	78	31	130	48	158	60	266
5.00	59	114	43	216	0	106	81	187
7.00	78	100	182	360	75	0	52	127
10.0	0	0	166	166	0	141	0	141

5.2.1 Univariate morphometric analysis

5.2.1.1 Cell level morphometric features

Cell area

Various studies have reported changes in hMSCs gross morphology during OD and AD. Figure 5.3 displays changes in the cell area over the course of differentiation for adipogenesis and osteogenesis. The cell area of cells directed towards AD lineage increase almost 4 fold over 10 days, whereas no insignificant change can be seen for OD. This observation is in agreement with a study published by Sonowal *et al.* in 2013.

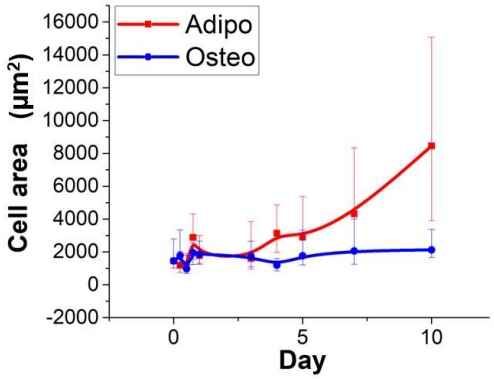

Figure 5.3 Cell area of adipogenic and osteogenic cells over a differentiation period of 10 days

Pairwise analysis of variance (between AD and OD) showed that cell area became significantly different ($p < 0.005$) after day 3. The analysis also showed that cell area of adipogenic cells became significantly different ($p < 0.005$) from the control group around the same time, whereas osteogenic cells showed no statistically significant difference from the control. This many fold increase in cell area of adipogenic cells can be related to its prospective function. It has been reported that larger adipogenic cells exhibit a higher fatty acid synthesis and lipoprotein activities, as well as a higher expression of leptin and GLUT4 protein. Researchers

also correlated the higher concentration of integrin/ERK detected in large AD cells to their increased size, as ERKs can modulate the expression of proteins important for adipose functions (Farnier et al., 2003).

Cell aspect ratio

Median cell aspect ratios for cells differentiated towards osteogenic and adipogenic lineages over a period of 10 days are shown in Figure 5.4. A consistent decrease in the polarity of cell shape can be seen over the 10-day period of differentiation. Although ANOVA returned no significant difference between the two differentiation lineages, changes in cell aspect ratio were significant ($p < 0.005$) within the first 6 h.

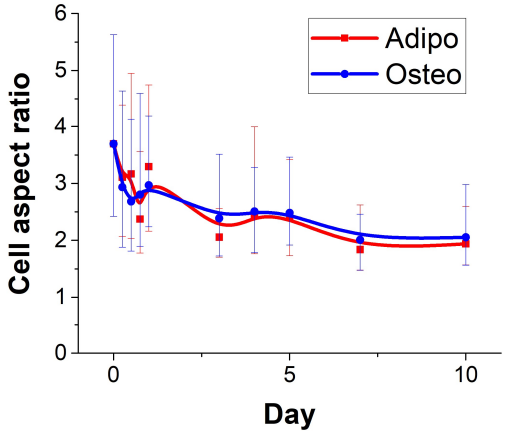

Figure 5.4 Cell aspect ratio of adipogenic and osteogenic cells over a differentiation period of 10 days

It is well established that both size and shape of the nucleus change during differentiation (Wu et al., 2010), which is predominantly owed to the organisation and level of chromatin condensation. As explained in section 2.3.1, chromatin organisation is regulated based on parts of the DNA required for transcription (Dahl et al., 2008; Wang et al., 2009). This is often achieved by direct application of mechanical forces on the nucleus by stress fibres. Based on our analysis, it can be hypothesised that CSK might need to be reorganised in a non-polar and stable architecture to enable multidirectional access to the nucleus.

Amount of F-actin

Figure 5.5 displays the amount of F-actin during AD and OD. An initial increase of F-actin can be seen for both lineages, as well as a peak around day 3 for OD and day 4 for AD, with levels returning to the initial values by day 5. This initial increase in the amount of F-actin is in accordance with observations by Sonowal *et al.* (2013), who noticed a slight increase of F-actin within the first 24 h after the induction with differentiation media. Interestingly, F-actin does not continue to increase throughout the differentiation process, but in fact appears to restore to pre-induction levels. This trend correlates well with the expression of OPG during

osteogenic differentiation (as explained in section 2.6.1.4). The increased expression of OPG has been linked to increased levels of RANK and integrin β3 in the early stages of differentiation, where integrin β3 has been known to enhance adhesion formations and subsequently F-actin polymerisation to form thick actin bundles (Havaki et al., 2007; Zhao et al., 2016). Moreover, in the later stages of differentiation, OPG has been shown to break down F-actin (Fu et al., 2013). It also poses the question if there could be any corresponding biochemical signal during AD that might regulate the amount of F-actin.

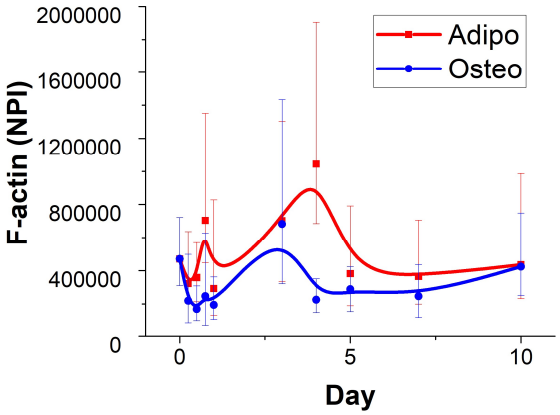

Figure 5.5 F-actin of adipogenic and osteogenic cells over a differentiation period of 10 days

Stellate factor

Figure 5.6 displays the stellate factor for AD and OD over a differentiation period of 10 days. While AD exhibited no significant variation at all, OD showed a slight decrease in stellate factor over time ($p < 0.005$). However, the slight drop at day 7 could be an anomaly.

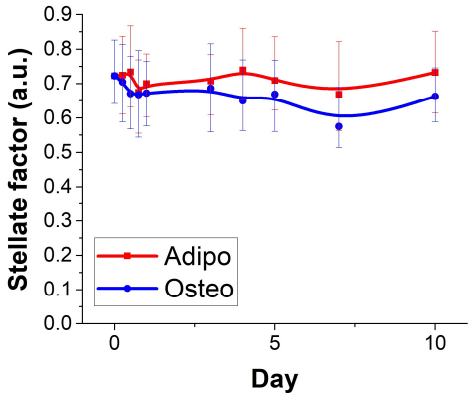

Figure 5.6 Stellate factor of adipogenic and osteogenic cells over a differentiation period of 10 days

5.2.1.2 Fibre level morphometrics features

Fibre length and thickness

Fibre length and thickness for AD and OD cells over a period of 10 days are shown in Figure 5.7. Almost no change can be observed in the median length of actin fibre during AD, whereas a significant ($p < 0.005$) decrease was seen during osteogenic differentiation by day 7. It can

be expected that any decrease in aspect ratio, while keeping the cell area the same, is likely to reduce the average length of actin fibres as cells would lose the long fibre bundles running across the spindle shaped stem cells. In the case of OD cells, this assumption holds true, as shown by the decrease of fibre length over time. Whereas adipogenic cells increase their cell size over time, counter acting to the decreasing aspect ratio and consequently maintaining the average fibre length.

Fibre thickness follows a similar trend as the amount of F-actin, exhibiting a peak for both cell lineages followed by levels decreasing to the initial values. As explained earlier, this could be explained by the increase in integrin complexes and subsequently in fibre bundle thickness.

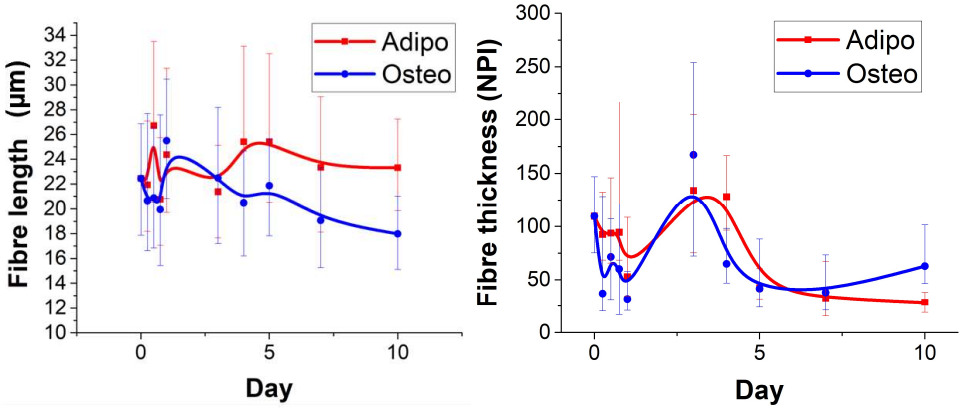

Figure 5.7 Fibre length and fibre thickness of adipogenic and osteogenic cells over a differentiation period of 10 days

Fibre orientation

This group of features measures how fibres orientate themselves against other reference points, including fibre alignment, fibre curvature, fibre chirality and location of peak intensity (

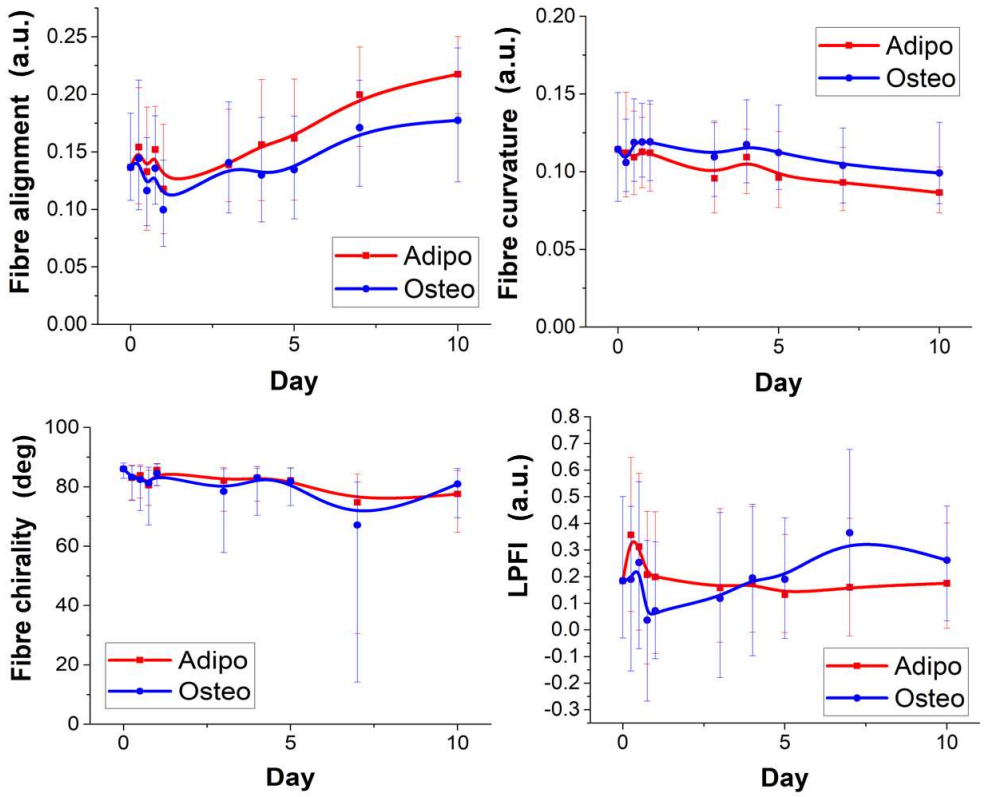

Figure 5.8). A steady ($p < 0.05$ by day 7) increase in fibre alignment can be seen for both lineages, whereas fibre curvature follows a steady decrease during the 10-day differentiation process. The decrease in fibre curvature (from t=0) was significant ($p < 0.05$) by day 5 and 7 for AD and OD, respectively. A significant difference was found in fibre alignment (by day 4) and in fibre curvature readings (by day 5) between OD and AD lineages. No apparent variation and trend could be observed in fibre chirality and location of peak fibre intensity, respectively.

As was discussed for the cell aspect ratio, adopting a high variance in fibre orientation could give cells multidirectional access to the nucleus for effective mechanotransduction. A loss in fibre curvature on the other hand, can be attributed to the tensing of stress fibres which are active in transducing mechanical signals.

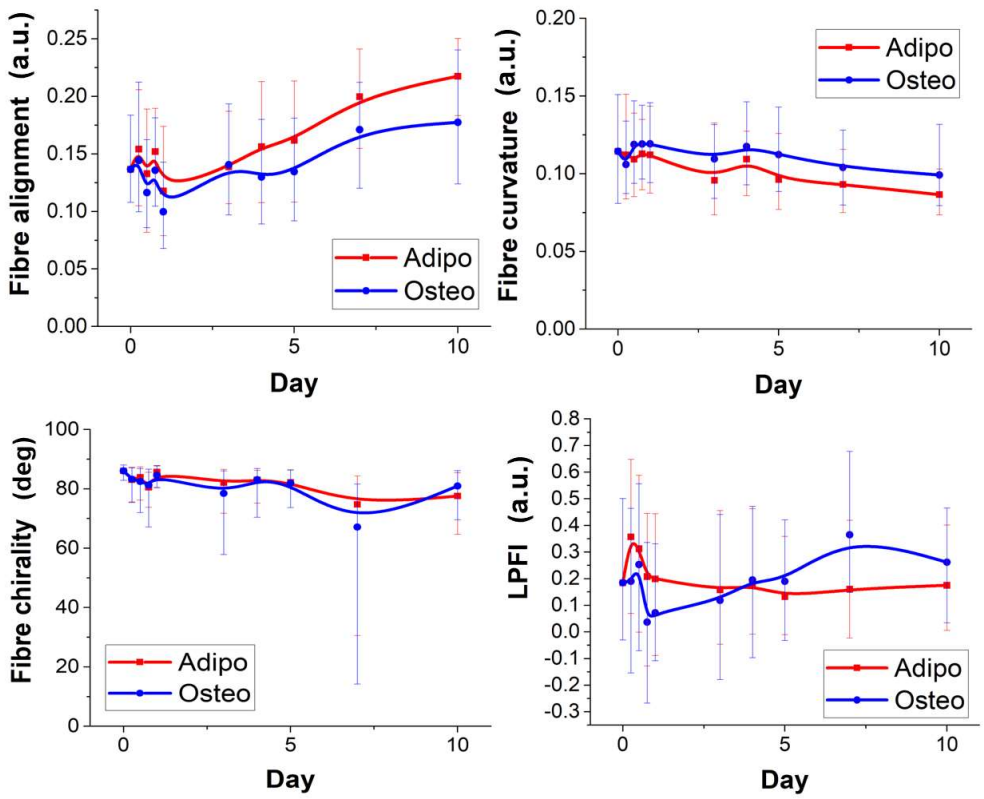

Figure 5.8 Fibre alignment, fibre curvature, fibre chirality and location of peak fibre intensity of adipogenic and osteogenic cells over a differentiation period of 10 days

5.2.1.3 Variance based features

In the previous sections, trends of the median values of geometric features were discussed. The variability of these features (fibre length, thickness and chirality) can be seen in Figure 5.9. Fibre length, for example, did not vary significantly during adipogenesis, however, its variance increased significantly ($p < 0.05$ by day 4) during the same period of time. On the other hand, variance in fibre length of OD followed a similar decline as fibre thickness itself, but only gaining a significant difference with $p < 0.05$ by day 10. Variance in fibre thickness increased during adipogenesis, while it remained unchanged for osteogenesis.

The variance in fibre chirality during both, osteogenesis and adipogenesis, almost doubled over 10 days and was significantly different form the starting point. Whereas, fibre spread variability showed no apparent trends over time.

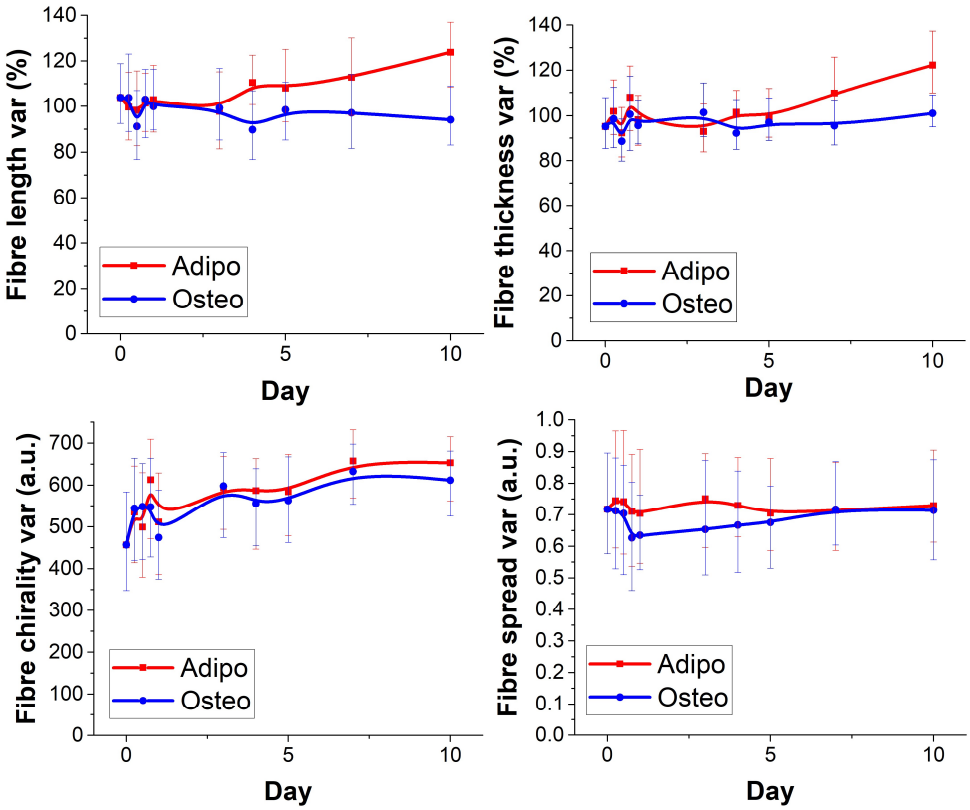

Figure 5.9 Variability of fibre length, fibre thickness and fibre chirality of adipogenic and osteogenic cells over a differentiation period of 10 days

5.2.1.4 Nuclear morphometrics

A number of features (Figure 5.10) were derived by extrapolation of 2D nuclear images. Nuclear brightness appears to be consistent throughout the differentiation process for both cell lineages, indicating that DNA quantity inside the nucleus is conserved. Whereas nuclear volume varied non-monotonically, possibly due to the influence of external forces and consequently the unfolding of chromatin. Interestingly, an almost linear increase in the (extrapolated) nuclear stiffness of the AD nucleus was observed, which appears to be closely related with the cell area and fibre thickness variability. It could be hypothesised, that in order to support a larger cell area, the actin CSK network reorganises into a mesh-like (high angular variability) structure which makes the cell body more rigid, and consequently causes a more compressed and stiffer nucleus. A sharp drop in chromatin condensation immediately after the induction with differentiation media can be seen, indicating the unfolding of DNA in order to access parts of the DNA needed for differentiation. Analysis of variances showed that the drop in chromatin condensation was significant ($p < 0.001$) within the first 6 h.

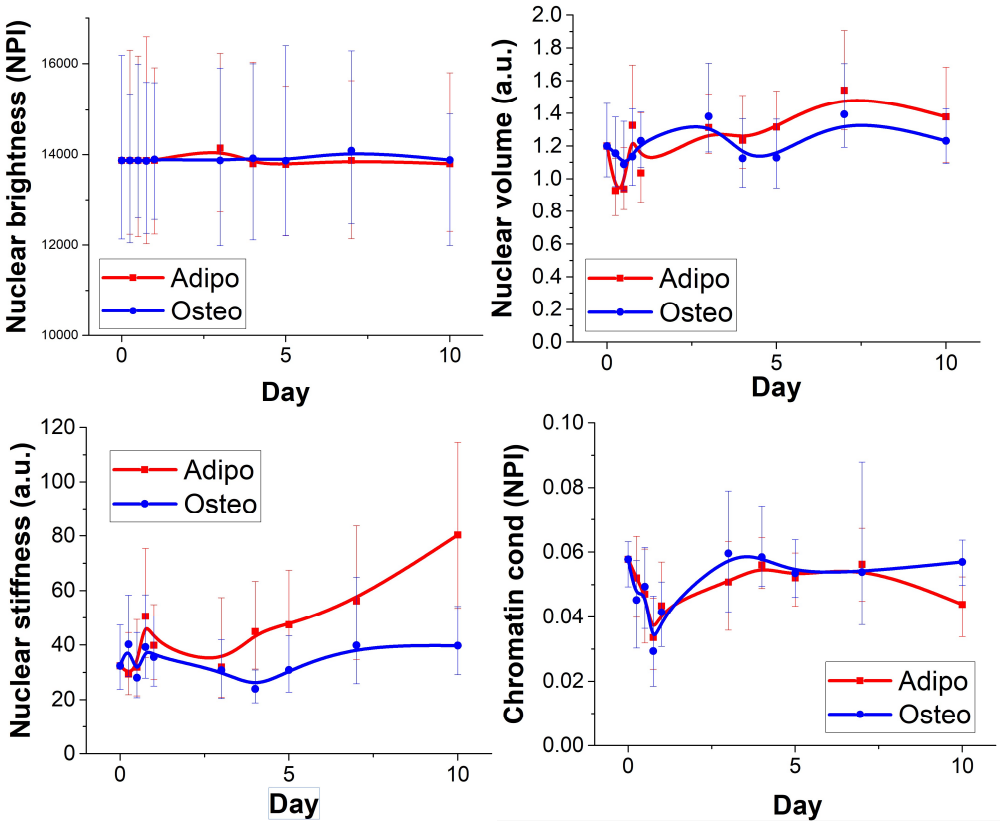

Figure 5.10 Nuclear brightness, nuclear volume, nuclear stiffness and chromatin condensation of adipogenic and osteogenic cells over a differentiation period of 10 days

Figure 5.11 shows the Poisson ratio over 10 days of adipogenic and osteogenic differentiation. Both, AD and OD, showed a consistent increase in the Poisson ratio from day 0 to day 5. After day 5, AD cells continued to follow the trend, whereas OD had a (out of path) fall in the Poisson ratio. Nevertheless, our calculations returned a negative Poisson ratio, which aligns with findings by Pagliara et al. (2014), who also reported auxetic properties of the cell nucleus.

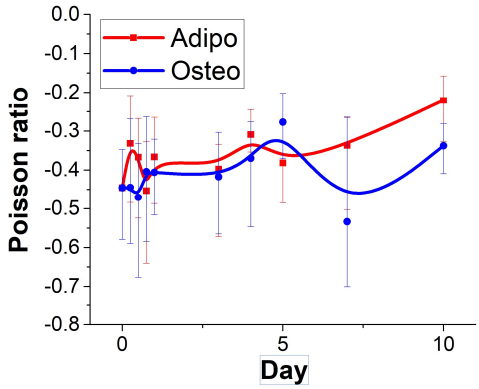

Figure 5.11 Poisson ratio of adipogenic and osteogenic cells over a differentiation period of 10 days

5.2.2 Multivariate assessment

In the previous section we evaluated the paths followed by each of the 19 features individually, as well as any underlying biological processes that might explain their behaviour. Certain features, like fibre alignment and fibre length variability, followed trends which were obvious and easily to interpret, while others, like F-actin and fibre thickness, were subtler and often non-monotonic. In the following section we will investigate the collective effect of these 19 features on the classification of differentiation treatments.

5.2.2.1 Pairwise classification of adipogenic and osteogenic differentiation

In the first step, the individual features were normalised internally by the following equation.

$$X_{norm} = \frac{X - X_{min}}{X_{ma} - X_{min}}$$

Morphometric data of each timepoint from OD, AD and control cells (SC) was fitted with a Linear Discriminant Analysis (LDA) model. The LDA fit was then scored against the original class labels. Figure 5.12 shows scatter plots of LDA fitting for different timepoints during the differentiation process, accompanied with 'correct prediction percentage' (CPP) (more timepoints can be found in appendix 9.2.3), which shows an overall increase in the class segregation over time.

Since control group data points formed an almost completely segregated cluster from AD and OD, the CPP between AD and OD was also calculated separately to assess the effectiveness of intra-lineage classification. Like the CPP of the (SC, OD, AD) data, the CPP of the (AD, OD) data also showed a general increase over the course of differentiation.

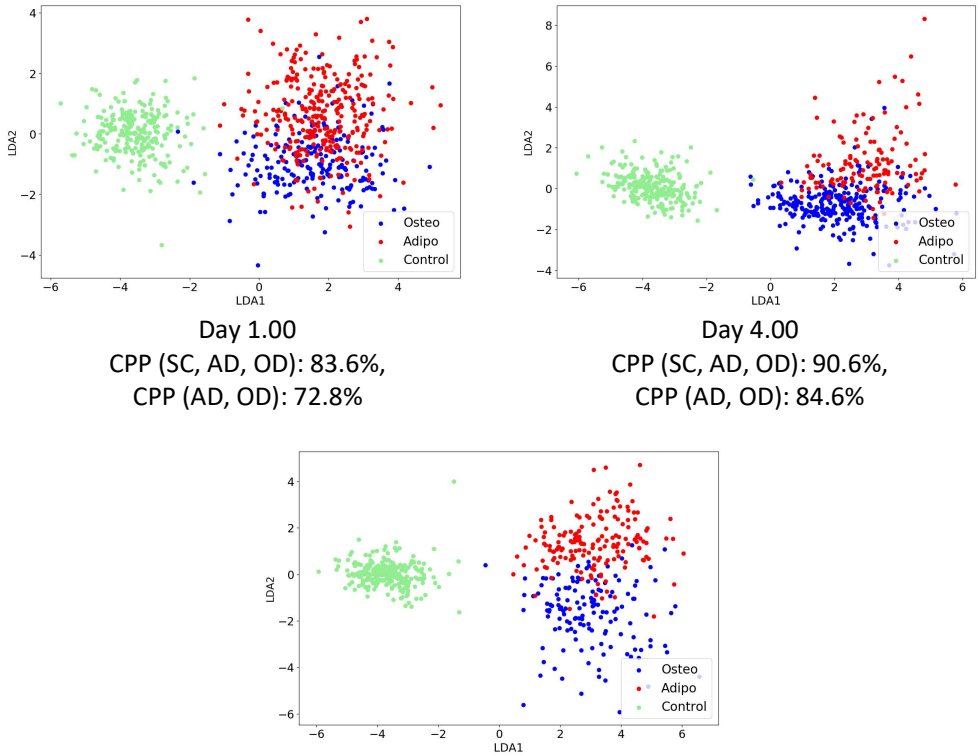

Day 1.00
CPP (SC, AD, OD): 83.6%,
CPP (AD, OD): 72.8%

Day 4.00
CPP (SC, AD, OD): 90.6%,
CPP (AD, OD): 84.6%

Day 10.0 - CPP (SC, AD, OD): 95%, CPP (AD, OD): 91%

Figure 5.12 Two component LDA fit representation of multivariate data from adipogenic, osteogenic and control cells (A) LDA clustering data from day 1 with a CPP of 0.836 (B) LDA clustering data from day 4 with a CPP of 0.906 (C) LDA clustering data from day 10 with a CPP of 0.950

5.2.2.2 Feature analysis

Considering the above mentioned observations, the influence of each feature in the multivariate classification was assessed by calculating the coefficients of Principal Components (PCA). This technique is used to reduce the dimensionality of data by redistributing the total variance (in the data) such that most of it is represented by the fewest components. PCA creates the same number of new components as the original number of variables. The Eigenvalue of a principal component specifies the number of original variables whose variance is captured by that component e.g. a component with Eigenvalue of 1 has the same variance as one of the original variables. Any component with an Eigenvalue smaller than 1 is usually discarded, but even then, we may often end up with more components than desired. Another way of selecting the number of components is by observing an abrupt change in the gradient on a scree plot. Scree plots constructed from the Eigenvalues of the 19 principal components at each timepoint of the (SC, AD, OD) datasets were created. An exemplary plot for day 3 is shown in Figure 5.13 (additional scree plots in section 9.2.4 appendix). For all plots, PC1 was found to capture most of the variance throughout the data.

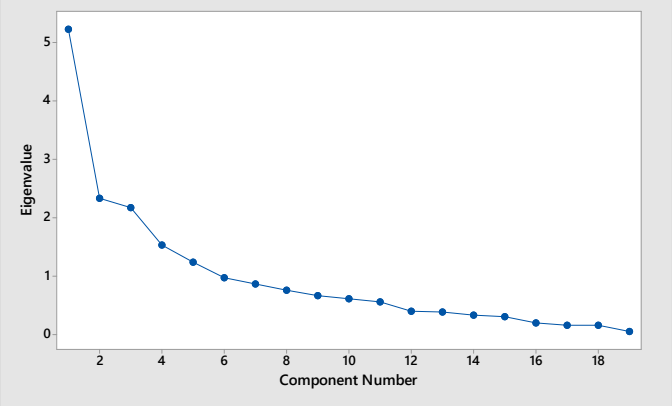

Figure 5.13 Exemplary scree plot for the (SC, AD, OD) dataset at day 3

The coefficient of the dominant principal components (PC1 and PC2) were calculated and their longitudinal contributions assessed. In Table 5.3 each cell is assigned a colour based on its value in relation to the maximum (9.4 % - bright red) and minimum (-8.8 % - deep blue) value in the table. Positive values correspond to undifferentiated cells while negative values correspond to adipogenic or osteogenic differentiated cells. Table 5.3 indicates that features such as cell area and fibre curvatures gained more influence, whereas cell aspect ratio, nuclear stiffness and fibre alignment decreased their influence on PC1 over time. The direction of this change suggests that cells from all three classes spread out more. Moreover, chromatin condensation also seems to become more influential in the class determination over time, while the highest weighed feature is the variance in fibre chirality.

Table 5.3: Coefficients of PC1 represented as a percentage contribution to the overall PCA transformation of (SC, AD, OD) dataset at each of the 9 timepoints

	Day 0.25	**Day 0.50**	**Day 0.75**	**Day 1.00**	**Day 3.00**	**Day 4.00**	**Day 5.00**	**Day 7.00**	**Day 10.0**
Cell area	6.6%	6.4%	7.1%	8.9%	6.6%	7.2%	8.0%	7.2%	7.5%
Cell aspect ratio	-8.5%	-8.6%	-7.6%	-7.7%	-7.7%	-7.3%	-6.8%	-7.8%	-6.8%
F-Actin	6.0%	6.8%	5.3%	6.5%	6.7%	7.6%	7.0%	6.0%	6.0%
Fibre thickness	3.8%	3.9%	5.3%	4.4%	6.1%	7.2%	4.5%	3.2%	2.8%
Fibre thickness var	6.4%	5.1%	6.2%	7.2%	5.4%	5.4%	5.8%	6.3%	7.4%
Fibre alignment	9.0%	8.6%	8.3%	7.3%	6.8%	7.2%	6.6%	8.3%	7.6%
Fibre curvature	-8.8%	-7.5%	-8.0%	-8.3%	-7.9%	-7.5%	-7.5%	-7.9%	-6.9%
LPFI	-0.1%	0.4%	-3.1%	-2.5%	-5.2%	-4.0%	-5.2%	-4.3%	-5.9%
Fibre spread var	6.5%	5.2%	5.9%	5.9%	6.4%	6.3%	6.7%	7.4%	7.1%
Stellate factor	5.7%	3.1%	4.5%	5.2%	6.0%	6.1%	6.3%	6.4%	6.6%
Fibre length	1.3%	-0.9%	1.6%	2.0%	3.9%	4.1%	4.9%	4.9%	5.3%
Fibre length var	-0.2%	-0.9%	-1.4%	0.2%	-0.8%	-0.3%	0.1%	0.8%	1.6%
Fibre chirality	-4.3%	-6.3%	-5.4%	-4.0%	-4.5%	-4.6%	-3.4%	-4.3%	-3.7%
Fibre chirality var	9.4%	9.3%	9.1%	8.7%	8.6%	8.3%	8.1%	8.5%	7.9%
Nuclear brightness	-1.2%	-1.1%	0.2%	-1.4%	-0.6%	-0.1%	-1.1%	-0.9%	-0.5%
Chromatin cond	6.3%	6.3%	6.5%	5.3%	6.8%	7.3%	7.5%	6.0%	6.7%
Nuclear volume	4.1%	6.2%	5.6%	5.0%	6.6%	5.6%	5.9%	6.9%	6.0%
Poisson ratio	-4.1%	-6.1%	-4.6%	-2.7%	-3.4%	-1.8%	-0.2%	-1.4%	2.1%
Nuclear stiffness	7.9%	8.4%	8.6%	9.2%	6.7%	6.7%	8.1%	6.2%	7.5%

Figure 5.14 displays an exemplary two component PCA representation of multivariate data from adipogenic, osteogenic and control cells from day 10.0. The control group data points are well segregated from those of AD and OD, PC1 and PC2 coefficients were calculated without SC data points.

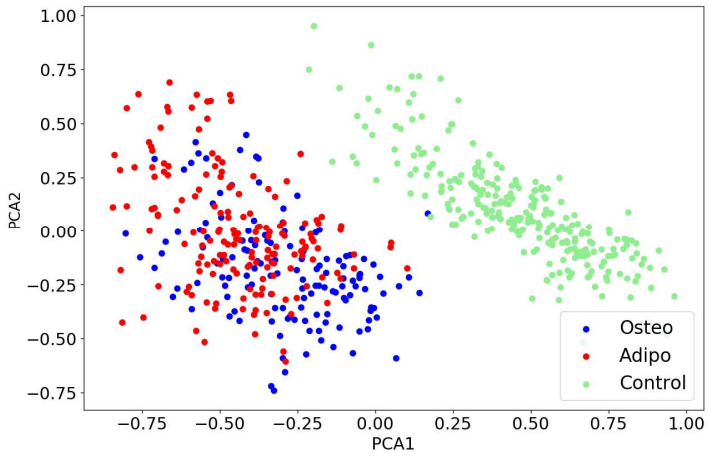

Figure 5.14 Exemplary two component PCA representation of multivariate data from adipogenic, osteogenic and control cells of data from day 10.0

Scree plots constructed from the Eigenvalues of the 19 principal components at each timepoint of the (AD, OD) datasets were created, Figure 5.15 shows exemplary plots for days 1 and 4 (additional scree plots in section 9.2.5). In most cases, PC1 was found to capture most of the variance in the data, however, PC2 also represented a relatively considerable variance at timepoints for days 3, 4 and 5.

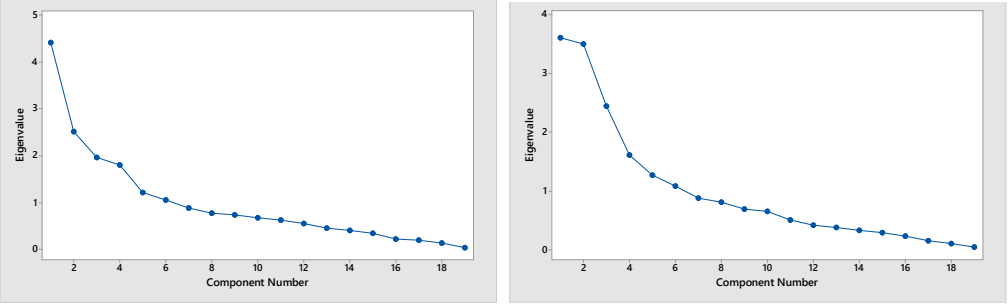

Figure 5.15 Exemplary scree plots for the (AD, OD) dataset for day 1 (A) and day 4 (B)

The coefficient of the dominant principal components (PC1 and PC2) were calculated and their longitudinal contributions assessed. In Table 5.4 and Table 5.5 the coefficients of PC1 and PC2 are presented as percentage contributions, respectively. Each cell is assigned a colour based on its value in relation to the maximum (bright red) and minimum (deep blue) value in the table. A positive value means that the feature is indicative of adipogenesis, while a negative value indicates osteogenic morphology as also shown in Figure 5.16. Form the values of coefficient it becomes apparent that the contribution for each feature to PC1

changes noticeably when only data from AD and OD lineages is compared. Interestingly, most features change their association to a lineage over time.

Table 5.4 Coefficients of PC1 represented as a percentage contribution to the overall PCA transformation of (AD, OD) dataset at each of the 9 timepoints

	Day 0.25	Day 0.50	Day 0.75	Day 1.00	Day 3.00	Day 4.00	Day 5.00	Day 7.00	Day 10.0
Cell area	6.4%	5.8%	1.8%	9.6%	-8.5%	8.9%	10.7%	8.7%	10.6%
Cell aspect ratio	-11.0%	-9.7%	-11.1%	-9.3%	9.1%	7.7%	-6.6%	5.1%	-3.7%
F-Actin	2.5%	4.2%	1.7%	6.2%	-6.1%	7.8%	8.7%	3.3%	6.2%
Fibre thickness	-1.9%	-0.6%	1.1%	1.7%	1.6%	0.1%	0.9%	-6.4%	-4.8%
Fibre thickness Var	4.9%	4.6%	-1.2%	7.8%	-6.3%	2.3%	6.9%	8.8%	8.6%
Fibre alignment	10.1%	8.7%	6.3%	9.4%	-8.1%	-3.6%	6.9%	0.9%	4.4%
Fibre curvature	-8.8%	-4.5%	-4.0%	-8.3%	7.4%	0.6%	-6.0%	-3.2%	-5.7%
LPFI	3.6%	3.2%	3.7%	1.3%	3.8%	-0.3%	-3.0%	-5.9%	-4.9%
Fibre spread var	2.3%	1.0%	-0.7%	1.4%	4.8%	2.2%	-3.9%	0.5%	-2.7%
Stellate factor	-1.8%	-4.5%	-8.4%	-1.5%	5.2%	7.0%	-3.7%	7.5%	0.0%
Fibre length	-8.1%	-8.3%	-10.4%	-6.8%	5.1%	10.7%	-1.7%	8.6%	5.7%
Fibre length var	0.9%	0.2%	-6.1%	2.2%	-2.6%	7.0%	3.4%	8.3%	7.7%
Fibre chirality	-6.6%	-7.5%	-8.2%	-7.1%	6.6%	8.8%	-6.1%	8.1%	-3.6%
Fibre chirality var	11.8%	10.0%	10.8%	10.5%	-9.7%	-6.2%	8.5%	-1.8%	5.3%
Nuclear brightness	-1.9%	-2.1%	0.6%	-2.3%	0.5%	0.5%	-2.4%	0.9%	0.6%
Chromatin cond	0.4%	3.8%	7.4%	-0.8%	-1.2%	-6.0%	-2.0%	-6.4%	-3.9%
Nuclear volume	5.4%	7.6%	5.6%	4.0%	-5.3%	-2.6%	6.6%	0.2%	6.6%
Poisson ratio	-4.4%	-6.5%	-7.6%	-0.4%	0.2%	9.6%	1.8%	10.2%	6.7%
Nuclear stiffness	7.2%	7.2%	3.4%	9.4%	-8.1%	8.1%	10.1%	5.2%	8.4%

Table 5.5 Coefficients of PC2 represented as a percentage contribution to the overall PCA transformation of (AD, OD) dataset at each of the 9 timepoints

	Day 0.25	Day 0.50	Day 0.75	Day 1.00	Day 3.00	Day 4.00	Day 5.00	Day 7.00	Day 10
Cell area	10.4%	-12.2%	13.8%	-8.3%	10.4%	-9.9%	6.6%	8.0%	-2.3%
Cell aspect ratio	4.2%	-3.1%	-1.9%	-6.6%	7.2%	7.9%	9.1%	-10.7%	-13.6%
F-Actin	11.0%	-11.3%	9.8%	-9.2%	7.2%	-9.7%	6.7%	6.0%	-1.3%
Fibre thickness	6.2%	-1.3%	0.4%	-5.6%	0.3%	-5.6%	4.0%	1.5%	-0.9%
Fibre thickness var	1.6%	-9.2%	12.1%	-4.8%	2.2%	-6.2%	1.8%	5.1%	-1.5%
Fibre alignment	-3.7%	-0.2%	6.7%	4.2%	-0.9%	-7.4%	-8.4%	8.4%	9.2%
Fibre curvature	2.2%	3.0%	-6.6%	-2.2%	-2.7%	6.2%	6.2%	-6.9%	-7.2%
LPFI	-6.9%	-1.3%	-2.6%	8.9%	-1.2%	2.9%	-7.1%	-2.6%	3.7%
Fibre spread var	-7.3%	-5.0%	-1.7%	10.0%	2.0%	2.4%	-5.0%	-5.5%	-2.2%
Stellate factor	-3.4%	-6.2%	0.4%	5.1%	6.9%	3.4%	0.0%	-4.7%	-7.3%
Fibre length	5.1%	-5.3%	3.0%	-6.4%	10.8%	2.2%	10.5%	-5.4%	-10.7%
Fibre length var	7.0%	-11.3%	8.5%	-5.1%	9.9%	-4.5%	6.1%	1.1%	-7.6%
Fibre chirality	2.3%	-6.1%	0.2%	-2.9%	6.2%	6.6%	5.4%	-6.1%	-8.7%
Fibre chirality var	-2.8%	2.7%	3.3%	4.4%	-3.6%	-9.2%	-8.3%	9.7%	11.8%
Nuclear brightness	-6.5%	-1.2%	3.7%	-1.4%	2.4%	-0.4%	0.9%	-4.3%	-1.9%
Chromatin cond	0.4%	2.3%	-4.3%	1.7%	-5.9%	-0.3%	0.1%	0.5%	1.9%
Nuclear volume	9.1%	1.4%	-1.5%	0.1%	-2.1%	-6.4%	2.6%	7.6%	-0.4%
Poisson ratio	-0.6%	-8.2%	7.5%	-7.2%	9.0%	0.2%	6.8%	0.1%	-4.2%
Nuclear stiffness	9.2%	-8.8%	11.8%	-5.9%	9.2%	-8.5%	4.3%	5.8%	-2.2%

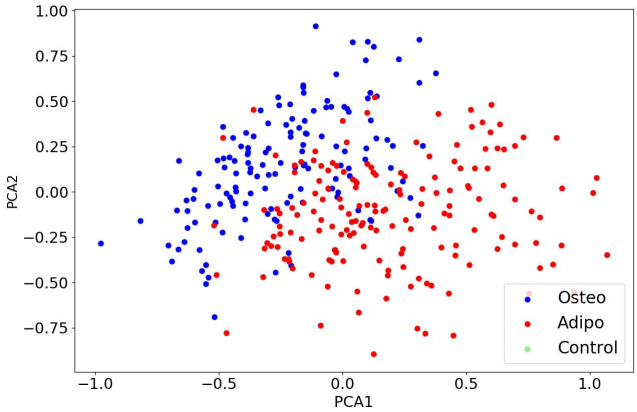

Figure 5.16 Exemplary two component PCA representation of multivariate data from adipogenic and osteogenic data from day 0.25

None of the 19 features were indicative of only 1 lineage over the duration of 10 days of differentiation. Therefore, we calculated the normalised total relative contribution of each feature towards both lineages. For example, the cell area is 7.33 times more indicative of adipogenesis, while fibre length was more predictive of osteogenesis in the early stages and of adipogenesis in the later timepoints. Values in Table 5.6 provide a relative indication of how much a feature is representative of either AD or OD. These values were calculated by summing up the positive and negative values across rows of Table 5.4 and then normalising the sums with the smallest values. Features such as nuclear brightness and chromatin condensation have a much smaller contribution in describing OD and AD cell morphology. Interestingly, although chromatin condensation is not a major determinant of AD from OD, it seems very influential when the control group is compared to differentiating cells (Table 5.3).

Table 5.6 Values providing relative indication of how much a morphometric feature is representative of either AD or OD.

	AD	**OD**
Cell area	19.8	-2.7
Cell aspect ratio	7.0	-16.4
F-Actin	12.9	-1.9
Fibre thickness	1.7	-4.3
Fibre thickness var	13.9	-2.4
Fibre alignment	14.8	-3.7
Fibre curvature	2.5	-12.9
LPFI	4.9	-4.5
Fibre spread var	3.8	-2.3
Stellate factor	6.3	-6.3
Fibre length	9.5	-11.2
Fibre length var	9.4	-2.7
Fibre chirality	7.5	-12.5
Fibre chirality var	18.1	-5.6
Nuclear brightness	1.0	-2.8
Chromatin cond	3.7	-6.5
Nuclear volume	11.5	-2.5

Poisson ratio	9.1	-6.0
Nuclear stiffness	18.8	-2.6

5.2.2.3 Feature correlation analysis

Table 5.7 shows the correlation analysis between features with a colour scale. Each cell is assigned a colour, where dark green represents the maximum positive correlation of 1, yellow is assigned to values close to 0 which corresponds to no correlation, and red represents the maximum negative correlation of -1. The analysis shows that only very few features exhibit a correlation of ± 0.4 or higher/lower. This indicates that the conducted LDA fit has unlikely been over-fitted to any set of features.

Table 5.7 Correlation analysis between morphometric features

	Cell area	Cell aspect ratio	F-Actin	Fibre thickness	Fibre thickness var	Fibre alignment	Fibre curvature	LPFI	Fibre spread var	Stellate factor	Fibre length	Fibre length var	Fibre chirality	Fibre chirality var	Nuclear brightness	Chromatin cond	Nuclear volume	Poisson ratio	Nuclear stiffness
Cell area	1																		
Cell aspect ratio	-0.2	1																	
F-Actin	0.5	-0.1	1																
Fibre thickness	-0.3	0.1	0.7	1															
Fibre thickness var	0.5	-0.2	0.3	-0.1	1														
Fibre alignment	0.3	-0.6	0.1	-0.2	0.4	1													
Fibre curvature	-0.3	0.5	-0.2	0.1	-0.2	-0.5	1												
LPFI	-0.1	-0.2	-0.1	0	-0.1	0.1	-0.1	1											
Fibre spread var	-0.1	-0.1	-0.1	-0	-0	0.2	-0.1	0.6	1										
Stellate factor	0	-0	-0.1	-0.1	-0	0.1	-0	0.1	0.2	1									
Fibre length	0.1	0.6	0.3	0.1	-0	-0.4	0.1	-0.2	-0.1	0	1								
Fibre length var	0.5	0.1	0.3	-0.1	0.3	0.1	-0.2	-0.1	0.1	0	0.3	1							
Fibre chirality	0	0.4	-0	-0.1	0	-0.3	0.1	-0	0	-0.1	0.3	0.1	1						
Fibre chirality var	0.3	-0.8	0.1	-0.1	0.3	0.6	-0.4	0.1	0.1	0	-0.5	-0	-0.3	1					
Nuclear brightness	-0	0	-0	0	-0	0	-0	0	0	0	-0	-0	-0	-0	1				
Chromatin cond	-0.1	-0.2	0.1	0.2	-0.1	0	-0	0.1	0	0	-0.1	-0.1	-0.2	0.1	-0	1			
Nuclear volume	0.5	-0.3	0.3	-0	0.2	0.2	-0.1	0	-0	0	-0.1	0.2	-0.2	0.3	-0.6	0.2	1		
Poisson ratio	-0.4	-0.2	-0.2	0.1	-0.2	0	0	0.2	0.1	0	-0.3	-0.3	-0.2	0.1	-0.3	0.2	0.2	1	
Nuclear stiffness	0.8	-0.3	0.4	-0.2	0.5	0.3	-0.2	-0.1	-0.1	0	-0	0.4	-0	0.3	-0.1	-0.1	0.2	0	1

Comparing the correlation analysis results to the influence each feature (Table 5.4) has on the principal components, it can be seen that many of the features with a correlation stronger than ± 0.3 also contributed heavily to the Eigenvalues of principal components 1 and 2. It is important to be aware of possibility that these features could be over represented in our LDA classification. This issue can be resolved by introducing more (uncorrelated) features to the classification. Moreover, further refinement of the feature quantification algorithms could also either eliminate or confirm these correlations.

5.2.2.4 Longitudinal classification of adipogenic and osteogenic differentiation

In the previous sections of this chapter, analysis was focused on distinguishing between the two different lineages. In the following section we will evaluate, how well the morphometric variance along a differentiation lineage is captured in our measurements.

Figure 5.17 A displays the LDA clustering of AD data labelled across 9 classes (days 0.25, 0.50, 0.75, 1, 3, 4, 5 and 7), while Figure 5.17 B only contains the LDA clustering of data from 3 well separated classes (i.e. days 0.25, 3 and 10). The correct prediction percentage (CPP) of the LDA fitting for all 9 classes was calculated to be around 47.03 %, which is much lower than any of the CPPs calculated between AD, OD and SC in section 5.2.2.1. However, the CPP of the LDA fit for 3 distant timepoints was almost double with around 83.04 %, on par with the CCP of (AD, OD) LDA fit for day 4 (Figure 5.12). The low CCP for all 9 classes suggests a need for introducing additional features which specifically capture the variance within the differentiation lineages over time. Another useful approach could also be to have separate sets of features for inter- and intra-lineage multivariate classification.

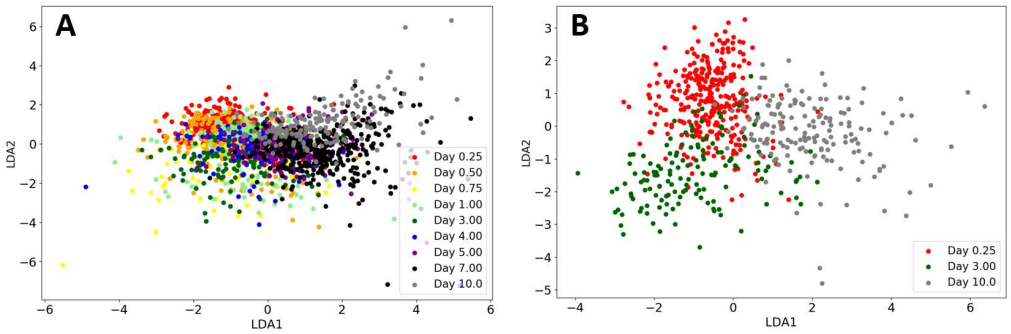

Figure 5.17 Two component LDA representation of multivariate data from adipogenically differentiated cells for up to 10 days (A) Class clustering of data labelled across 9 timepoints (days 0.25, 0.50, 0.75, 1, 3, 4, 5, 7 and 10) with a CPP of 0.4703 (B) Class clustering of data from 3 well distributed timepoints (days 0.25, 3 and 10) with a CPP of 0.8304

Figure 5.18 A shows the LDA clustering of OD data labelled across 9 classes (days 0.25, 0.50, 0.75, 1, 3, 4, 5, 7 and 10, while Figure 5.18 B only contains LDA clustering of data from 3 well separated classes of OD data (days 0.25, 3 and 10). The CPP from LDA fitting for all 9 classes was calculated to be around 39.99 %, which is even lower than the CPP of the corresponding LDA fitting of AD data. Moreover, the CPP of OD data from only 3 timepoints was also nearly double (69.45 %) than that from 9 classes. Considering the analysis from both sections 5.2.2.1 and 5.2.2.2, it was noticed that some of the features which contributed heavily in the classification of the (AD, OD) dataset, did not vary much for OD over the period of differentiation, such as cell area, nuclear stiffness, fibre thickness variability and fibre length variability.

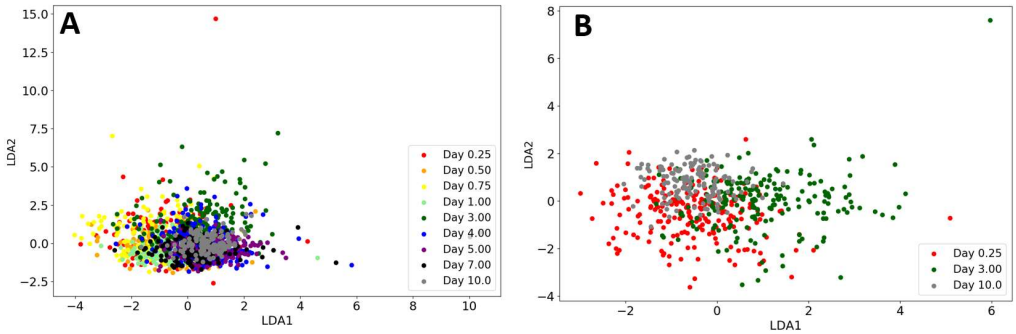

Figure 5.18 Two component LDA representation of multivariate data from osteogenically differentiated cells for up to 10 days (A) LDA clustering of data labelled across 9 classes (days 0.25, 0.50, 0.75, 1, 3, 4, 5, 7 and 10) with a CPP of 0.3999 (B) LDA clustering of data from 3 well distributed timepoints (days 0.25, 3 and 10) with a CPP of 0.6945

5.3 Summary

In this chapter the paths followed by each of the 19 features individually were evaluated, as well as any underlying biological process that might explain them. Some features followed trends which were obvious and easily definable (fibre alignment, fibre length variability), while others were subtler and often non-monotonic (F-actin, fibre thickness). Most of the features changed significantly from day 0 to 10. It was observed that measurements of most features were higher for AD in comparison to OD (i.e. AD (red) trendline is above the OD (blue) trendline), plausible explanations for this observation are discussed further in section 7.2.1.

A collective effect of the 19 features on the classification of the differentiation process was also investigated. An LDA classifier was used on (SC, AD, OD) and (AD, OD) data sets separately and their respective correct prediction percentages (CCP) were calculated. Both datasets showed a sustained increase in their CPP value over time, suggesting that cells from different groups became more morphologically distinct throughout differentiation. Following this, a breakdown influence of each feature on the class separation in (SC, AD, OD) and (AD, OD) datasets was investigated with Principal Component Analysis. The coefficient of the dominant principal components (i.e. PC1 and PC2) were compared longitudinally using colour scaling. In the analysis of the (AD, OD) dataset, positive and negative PC coefficient values reflected AD and OD association, respectively. It was observed that most features changed their associations to any lineage over time e.g. in the PC1 variance the fibre length coefficient contributed more towards adipogenesis at the early timepoints but switched towards osteogenesis in the later stages of the differentiation.

To rule out any over representation of any subset of features on the multivariate classification, a feature correlation analysis was performed. Calculations showed heavy correlation among features in only very few instances. However, when comparing the results

from the correlation analysis against the influence each feature has on the principal components, it was noticed that many of the features which showed a correlation stronger than ± 0.30 also contributed heavily to the variance in principal components 1 and 2. While it is of interest to explore the connection between highly correlated features, a possible over representation of these features in the LDA classification must be considered.

Lastly, LDA clustering of longitudinal data classes (days 0.25, 0.50, 0.75, 1, 3, 4, 5, 7 and 10) was performed for both AD and OD separately. CPP values for both AD and OD data sets were calculated, which suggested the need for further improvement of the feature quantification algorithms by the inclusion of additional features which could specifically capture the variance within the differentiation lineages (AD or OD) over time.

Chapter 6 | Effects of substrate stiffness on the morphometrics of cell differentiation

In vivo, cells sense their surroundings by inducing tension in their cytoskeletal network, which in turn applies contractile force on the substrate via integrin adhesions (D E Ingber, 2004). It is by the detection of change in this tension that relevant signalling cascades are triggered towards an appropriate cell response. Examination of culturing stem cells have revealed that cells, when grown on pulposus material (simulating brain tissue stiffness), differentiated to neurons; whereas cells adapted myogenic and osteogenic lineages when cultured on material of intermediate and higher stiffness, respectively (Engler et al., 2006). Similarly, Winer et al. (2009) showed that MSCs, when grown on substrate with moduli matching that of bone marrow tissue, were kept in a dormant state. A caveat to these observations is the fact that many cell niches have similar elastic properties, which makes it almost impossible to achieve multiple cell lineages with similar mechanical properties. This indicates the complexity of the processes regulating stem cell population and lineage determination, and hence calls for a deeper understanding of the relation between cell response and the stiffness of its environment (Watt & Hogan, 2000).

The elasticity of cell culture substrate is now considered to be integral in guiding stem cell fate (D E Ingber, 2004; Saha et al., 2008); and as mentioned in the previous chapter, a few studies have reported the effects mechanical cues can have on signalling cascades.

Unlike the majority of in vitro studies, most cells in their natural environment are attached to materials much softer than glass or plastic, and in many of those instances it is another cell of the similar type with stiffness modules between 0.01 to 10 kPa (Bao & Suresh, 2003; Wakatsuki, Kolodney, Zahalak, & Elson, 2000). This is well within the range for forces exerted by the cytoskeleton at the adhesion sites, to case deformation of its substrate, which the cells are unable to do on a glass or plastic substrate. Studying the stem cell's response to stiffness by reorganising its cytoskeletal network and more generally its overall shape, may give further insights into the mechanism underlying mechanotransduction (Yeung et al., 2005).

In Chapter 5, variations in morphometrics of differentiating stem cells was investigated over time. These experiments were conducted on glass coverslips with FBS coating, however, as mentioned above, cells in their natural environment almost never experience such high stiffness. Thus, in the following chapter, additional morphometric analysis to evaluate the cells' response to lower stiffness substrates will be presented.

6.1 Materials and methods

6.1.1 Experimental setup

PAA gel was polymerised on glass coverslips along with embedding fibronectin coating with 'Method B' as explained in section 3.3.1.2. Prior to cell seeding, gels were incubated with 10 % FBS in 24-well plates for 3 - 4 hours. Cells were detached from T25 flasks using Accutase solution, before full confluency was reached. Based on the cell count estimates, Accutase-cell suspension was portioned accordingly and added to xPan to achieve a final dilution of approximately 1500 cells/mL. 1 mL of this suspension was gently pipetted in each well. During this process the cell suspension was regularly stirred to prevent cells from settling down.

Once seeded, cells were allowed to settle and attach for about 24 h before being induced with differentiation media. At their specific timepoints (as indicated in Figure 6.1), coverslips were transferred to another multi-well plate, washed 3 times with (37 °C) sterile PBS and fixed with 10 min incubation in 3.7 % PFA.

Figure 6.1 Schematic of the configuration for experimental groups (adipogenic, osteogenic and control) at different timpoints

Coverslips were then washed with PBS and stored in a refrigerator submerged in PBS. Once all timepoints were completed and fixed, one coverslip from each timepoint and media was stained for actin and mounted on glass slides (thickness 1 mm). The mounting media contained DAPI to stain the nucleus. Imaging was carried out immediately after the staining process was completed to avoid photo-bleaching. Imaging was performed as described in detail in section 3.5.1.

6.1.2 Statistical analysis

This assessment was depended on sample size (n) and its z-scores of skewness and kurtosis. Table 6.1 entails skewness and kurtosis values of the population distribution along with their respective z-scores adapted from (Kim, 2013). Populations matching the listed criteria were treated as normally distributed for further statistical analysis.

Table 6.1 Skewness and kurtosis values of the population distribution with their respective z-scores (Kim, 2013)

Sample size	Criteria
n < 50	-1.96 < z-score < 1.96 (alpha of 0.05)
50 < n < 300	-3.29 < z-score < 3.29 (alpha of 0.05)
n > 300	Distribution was assessed qualitatively from their histograms and Q-Q plots, provided that absolute skewness and kurtosis values were smaller than 2 and 7, respectively

Furthermore, results were evaluated using the Shapiro-Wilks normality test. Shapiro-Wilks calculations did not always match with the assessed z-scores, in these cases visual inspection of the histograms and normal Q-Q plots were used to reach a decision. For hugely skewed data, outliers were assessed by thresholding data points to 3 times the Interquartile Range (IQR). Additionally, Levene's test was also performed on all the data to calculate the homogeneity of variance.

Analysis showed that data was log-normally distributed and therefore median values (with Q1 and Q3 as error bars) were plotted as line graphs with b-spline interpolation. 2-way ANOVA followed by TUKEY corrections on the logarithmic values of the dataset was also performed. The significance of differences was presented at 3 levels i.e. $p < 0.05$, $p < 0.01$ and $p < 0.001$, unless otherwise stated.

Another aim of this study was to assess the suitability of these morphometric features for machine learning characterisation. Dimensionality reduction techniques such as LDA and PCA were used to weigh what effect each feature might have on the classification of population.

6.2 Results

Table 6.2 provides the number of adipogenic and osteogenic cells for each timepoint. Descriptive statistics and population distribution analysis of each individual variable for adipogenic and osteogenic cells were carried out. Most of these variables exhibited a highly skewed distribution, and hence median values were used for the following plots.

Table 6.2 Cell numbers for adipogenic and osteogenic differentiation over different timepoints for cells grown on gel substrates with 10 kPa (AD) and 35 kPa (OD)

	AD	OD

Day 1	166	516
Day 2	82	239
Day 3	263	49
Day 4	182	451
Day 5	315	346
Day 7	80	21

Figure 6.2 to Figure 6.10 include plots for each of the 19 morphometric features in the same order as in Chapter 5. In this section, along with describing the underlying trends in OD and AD over time, measurements will also be compared with those discussed in chapter 5.

6.2.1 Univariate morphometric analysis

6.2.1.1 Cell level morphometric features

Cell area

Figure 6.2 displays changes in the spread area of AD and OD cells during differentiation. Pairwise ANOVA showed no significant difference in cell area of AD and OD at any time, whereas it was significantly higher ($p < 0.001$) by day 7 compared to the starting point (day 0). While undifferentiated cells exhibited a similar cell area on both, gels and glass, they were significantly ($p < 0.001$) less polar on gels (appendix 9.3.1).

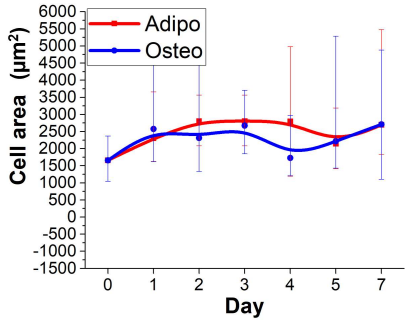

Figure 6.2 Cell area of adipogenic and osteogenic cells over a differentiation period of 7 days

Moreover, like on glass, the area of AD cells appeared to be increasing between days 5 to 7 ($p < 0.001$), but considering a standard deviation of 25922 with a median value of 36868, it could be an anomalous data point. Whereas, unlike on glass, OD cells appear to have gained cell area on gel substrates from day 4 onwards. This might be indicative of, but does not necessarily mean, that it would have continued to increase on par with AD. Nevertheless, these observation needs to be further investigated with higher number of observations. When compared to the absolute values of cell area, AD lineage on gel substrates showed a much bigger offset from their counterparts on glass. This lack of AD spreading might have

some connection with the observation that AD cells (on gels) appear to produce fat lipids much earlier than on glass i.e. between 7 - 10 days and 15 + days on gels and glass, respectively. This observation is in alignment with previous reports (discussed in section 2.5.5.4), which observed cells to differentiate faster towards AD lineage when forced into a small area i.e. high cell density, such as seeding on small adherable island substrates (Guilak et al., 2009).

Cell aspect ratio

Figure 6.3 shows the cell aspect ratio of adipogenic and osteogenic lineages over a differentiation period of 7 days. After remaining relatively consistent or the first 3 days, a decrease in the aspect ratio was observed, reaching very similar levels to what was reported for both cell lineages on glass (by day 7). Through the duration of the experiment, AD and OD cell aspect ratio followed a very synchronised path.

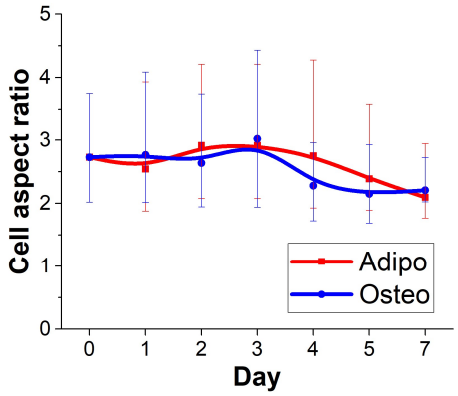

Figure 6.3 Cell aspect ratio of adipogenic and osteogenic cells over a differentiation period of 7 days

Amount of F-actin

Moreover, in Figure 6.4 a gradual increase in the amount of F-actin can be seen from the start, reaching its peak intensity by day 3 and then steadily coming down to the initial levels by day 5, moulding the trendline into a shape similar to that observed on glass (Figure 5.5).

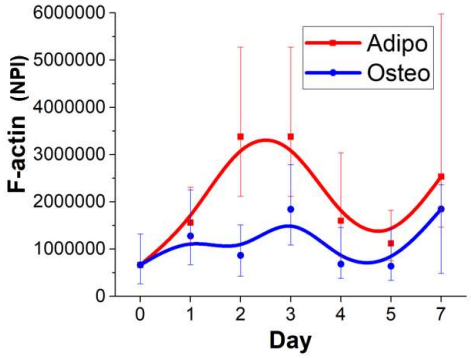

Figure 6.4 Amount of F-actin of adipogenic and osteogenic cells over a differentiation period of 7 days

Stellate factor

The stellate factor for adipogenesis and osteogenesis over a differentiation period of 7 days can be seen in Figure 6.5 Although both lineages appear to be decreasing over time, the analysis of variance showed no significant change in stellate factor between day 0 and 7 measurements.

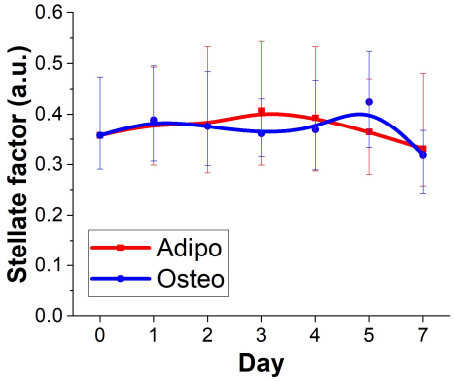

Figure 6.5 Stellate factor of adipogenic and osteogenic cells over a differentiation period of 7 days

6.2.1.2 Fibre level morphometric features

Fibre length and thickness

Similar to F-actin, fibre length and thickness (Figure 6.6) very much correspond to the trends followed by the same features on glass (Figure 5.7).

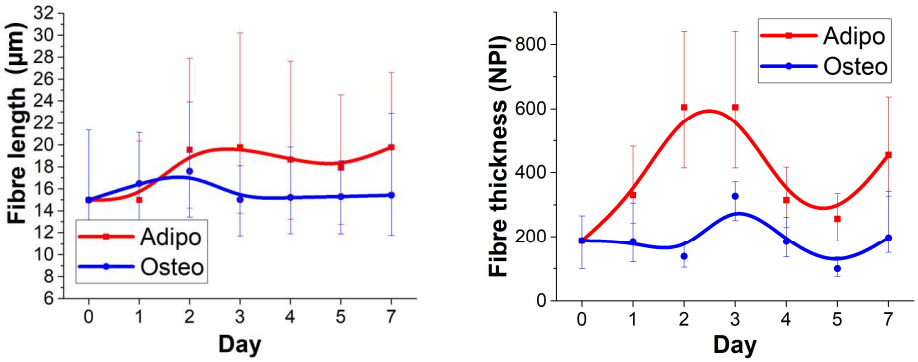

Figure 6.6 Fibre length and fibre thickness of adipogenic and osteogenic cells over a differentiation period of 7 days

Fibre orientation

In Figure 6.7, fibre orientation features, including fibre alignment, curvature, chirality and location of peak fibre intensity are plotted. These plots show some resemblance to their counter parts in chapter 5, e.g. fibre alignment and fibre curvature showed a general increase and slight decrease, respectively, whereas fibre chirality appeared to be steadily decreasing over time but only reaching a significant difference ($p < 0.01$) from the starting point by day 7. Location of peak fibre intensity, however, showed no noticeable trends.

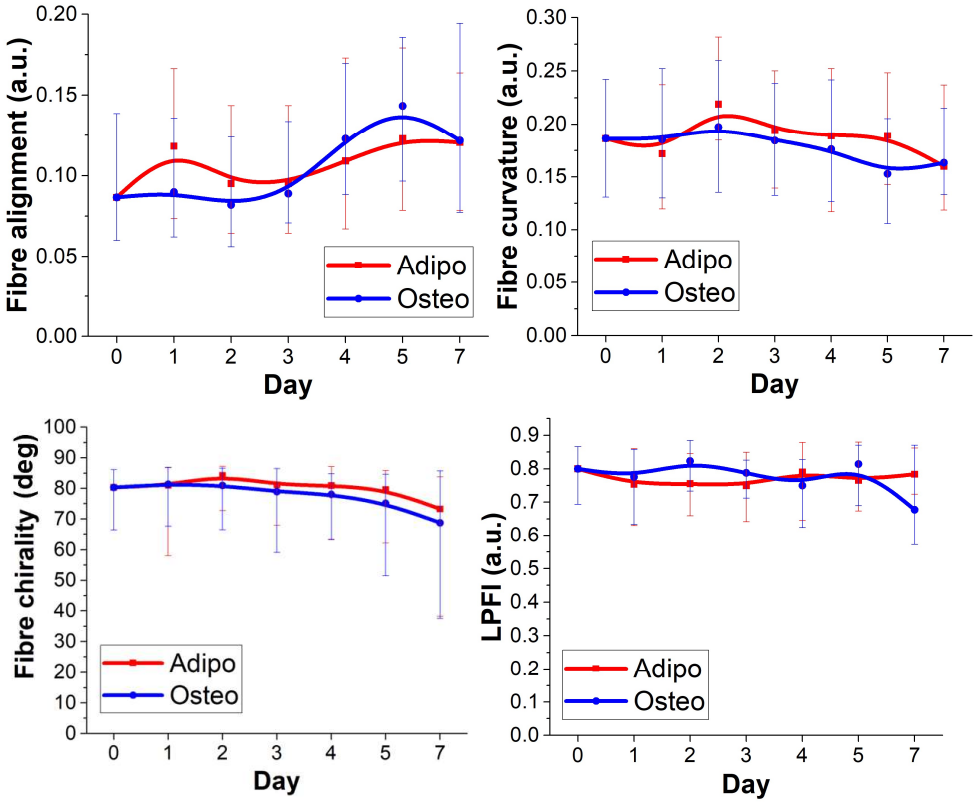

Figure 6.7 Fibre alignment, fibre curvature, fibre chirality and location of peak fibre instensity of adipogenic and osteogenic cells over a differentiation period of 7 days

6.2.1.3 Variance based features

Figure 6.8 displays variance-based features, including the variability of fibre length, thickness, chirality and spread. Except for fibre chirality variability, all other features in this category did not exhibit any significance variation ($p < 0.05$) from the starting point. However, AD and OD cells did appear to maintain significantly different fibre spread levels between day 1 and 5. Variance in fibre chirality had a significant ($p < 0.05$) increase from the starting point of the experiment by day 5.

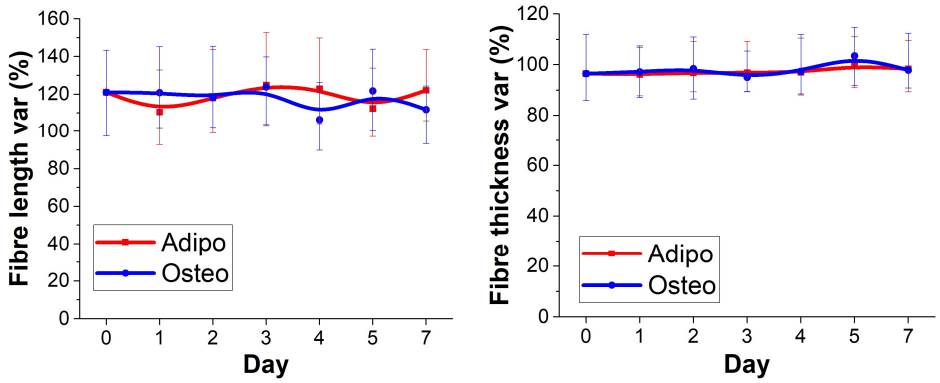

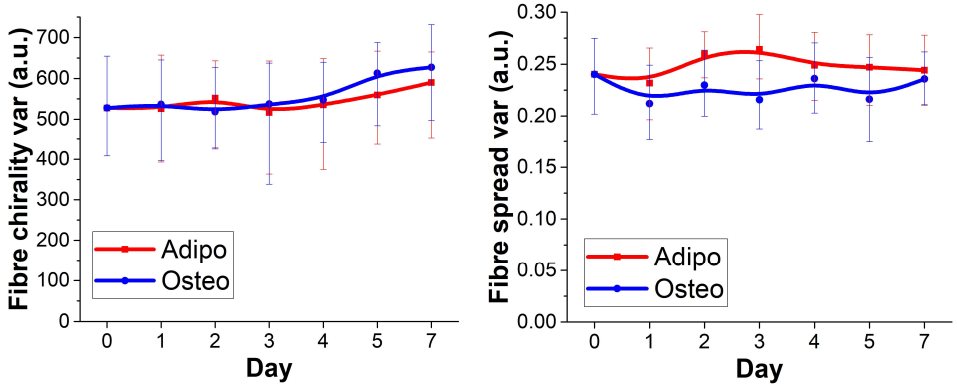

Figure 6.8 Variability of fibre length, fibre thickness, fibre chirality and fibre spread of adipogenic and osteogenic cells over a differentiation period of 7 days

6.2.1.4 Nuclear morphometrics

Nuclear morphometrics, including nuclear brightness, volume, stiffness and chromatin condensation can be found in Figure 6.9, as well as the Poisson ratio in Figure 6.10.

Similar to nuclear morphometrics of AD and OD cells on glass, the nuclear volume, stiffness and Poisson ratio showed the most variance among the 5 nuclear features over the 7 day differentiation period. The difference between AD and OD of these 3 nuclear features was significant within the first 48 h.

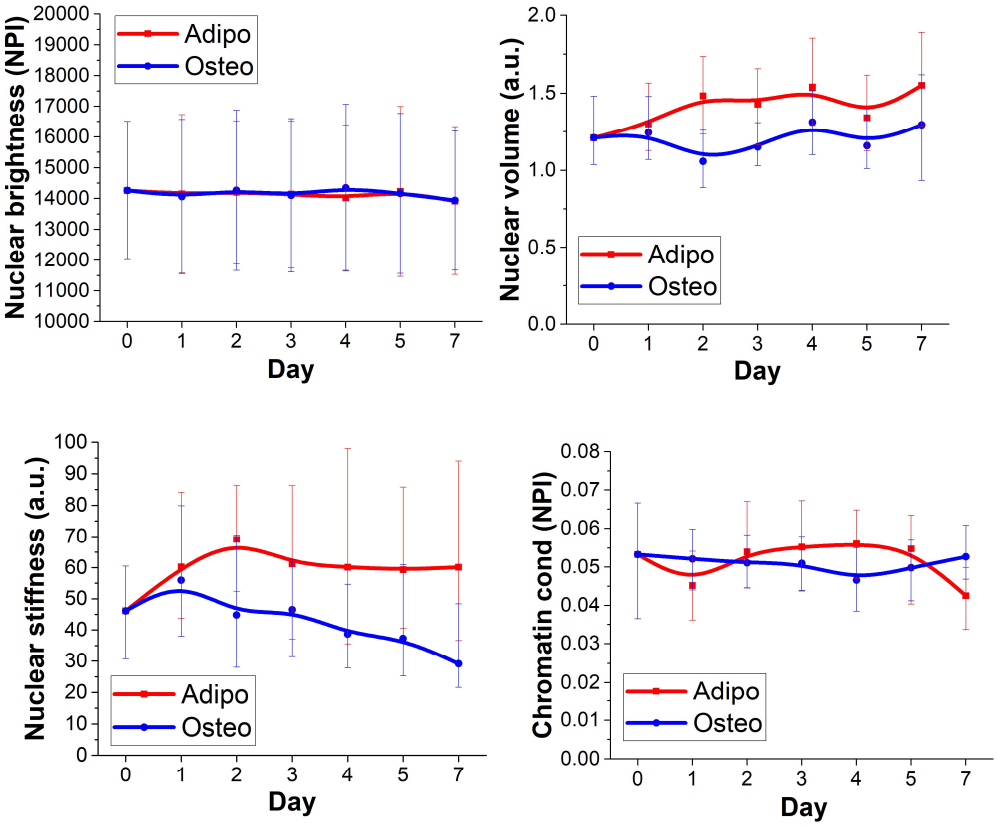

Figure 6.9 Nuclear brightness, nuclear volume, nuclear stiffness and chromatin condensation of adipogenic and osteogenic cells over a differentiation period of 7 days

It is worth mentioning, that our calculated (by extrapolation) Poisson ratio for both, the nuclei of cells differentiated on glass (Figure 5.11) and on gels (Figure 6.10) corroborated data reported by Pagliara et al. (2014). We also observed that nuclear auxetic properties appear to decrease as cells differentiate, suggesting that it might be a characteristic property of cell plasticity, which is likely to decrease during differentiation.

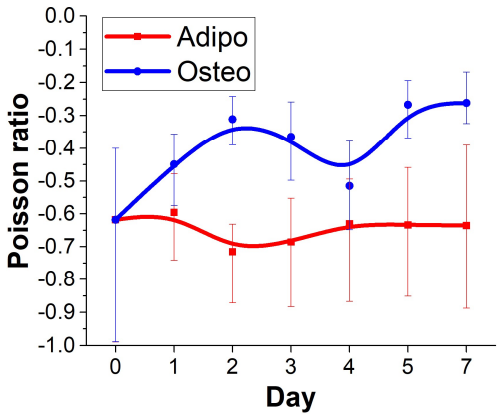

Figure 6.10 Poisson ratio of adipogenic and osteogenic cells over a differentiation period of 7 days

6.2.2 Multivariate assessment

6.2.2.1 Pairwise classification of adipogenic and osteogenic differentiation

Figure 6.11 shows the scatter plots of adipogenic, osteogenic and control cells on days 1, 3 and 7 after LDA fitting, accompanied with the 'correct prediction percentage' (CPP), which shows an overall improvement over time (more timepoints can be found in appendix 9.3.2).

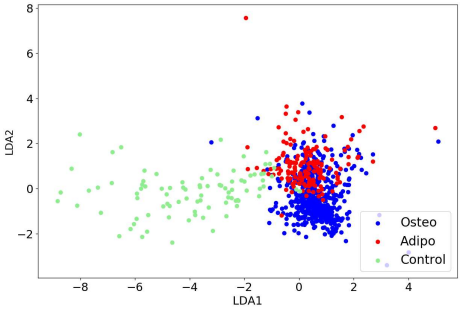

Day 1.00
CPP (SC, AD, OD): 77.4 %
CPP (AD, OD): 74.5 %

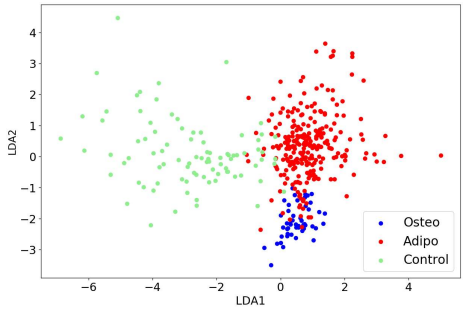

Day 3.00
CPP (SC, AD, OD): 91.5 %
CPP (AD, OD): 89.1 %

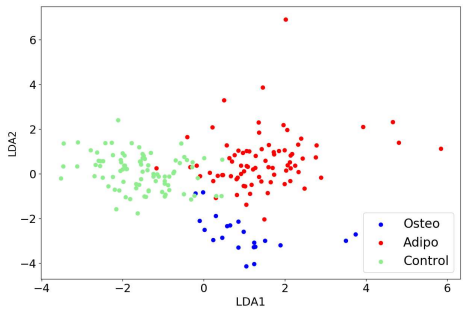

Day 7.0 - CPP (SC, AD, OD): 93.7 %, CPP (AD, OD): 88.1 %

Figure 6.11 Two component LDA fit representation of multivariate data from adipogenic, osteogenic and control cells (A) LDA clustering data from day 1 with a CPP of 0.774 (B) LDA clustering data from day 3 with a CPP of 0.915 (C) LDA clustering data from day 7 with a CPP of 0.937

Since the control group data points formed an almost completely segregated cluster from AD and OD, the CPP between AD and OD was also calculated separately to assess the effectiveness of intra-lineage classification on gels. Like the CPP of (SC, OD, AD) data, the CPP of (AD, OD) data also showed a general increase over the course of differentiation.

6.2.2.2 Feature analysis

From scree plots of the (SC, AD, OD) dataset (section 9.3.3), it was observed that most of the variance was represented by PC1 alone, whereas PC1 and PC2 together shared the variance in the (AD, OD) dataset (section 9.3.4). The coefficients of the principal components were calculated and their longitudinal contributions were tabulated as shown in Table 6.3 to Table 6.5. Each cell in these tables is assigned a colour based on where its value falls on the scale between the maximum (bright red) and the minimum (deep blue) values of each table. PC1 coefficients of the (SC, AD, OD) data switched from one extreme to the other at around the day 3 to 4 timepoint (Table 6.3). Whereas PC1 coefficients of the (AD, OD) data showed no noticeable trend (Table 6.4). On the other hand, PC2 coefficients of the (AD, OD) data also showed side switching at the day 3 to 4 mark (Table 6.5).

Table 6.3 Coefficients of PC1 represented as a percentage contribution to the overall PCA transformation of (SC, AD, OD) dataset at each of the 6 timepoints

	Day 1	Day 2	Day 3	Day 4	Day 5	Day 7
Cell area	8.5%	-8.5%	-8.1%	7.3%	8.7%	9.5%
Cell aspect ratio	-8.3%	7.0%	6.9%	-8.5%	-8.5%	-7.1%
F-actin	0.0%	3.3%	3.7%	1.1%	1.7%	-0.8%
Fibre thickness	-6.6%	6.8%	7.9%	-6.6%	-4.3%	-7.1%
Fibre thickness var	6.8%	-6.7%	-6.9%	5.8%	6.5%	7.1%
Fibre alignment	6.4%	-5.0%	-4.1%	6.7%	5.6%	3.6%
Fibre curvature	-8.7%	7.9%	7.4%	-9.2%	-9.5%	-8.4%
LPFI	5.5%	-5.7%	-6.7%	6.6%	5.5%	7.1%
Fibre spread var	-6.7%	8.0%	8.4%	-8.1%	-7.7%	-9.3%
Stellate factor	2.1%	1.2%	1.7%	0.9%	-1.5%	0.6%
Fibre length	-6.4%	5.8%	6.2%	-8.7%	-8.6%	-7.6%
Fibre length var	0.2%	-1.4%	0.7%	-1.0%	0.5%	2.6%

Fibre chirality	-8.0%	6.8%	6.7%	-7.2%	-7.4%	-6.4%
Fibre chirality var	8.5%	-7.0%	-6.8%	8.9%	8.9%	6.7%
Nuclear brightness	-1.9%	1.1%	0.8%	-0.6%	-0.8%	-0.8%
Chromatin cond	-2.0%	4.4%	3.1%	-1.6%	-2.2%	-1.5%
Nuclear volume	6.5%	-5.6%	-6.1%	5.5%	4.6%	6.6%
Poisson ratio	1.2%	-2.0%	-3.0%	1.4%	2.4%	2.9%
Nuclear stiffness	5.9%	-5.7%	-4.8%	4.2%	5.3%	4.5%

Table 6.4 Coefficients of PC1 represented as a percentage contribution to the overall PCA transformation of (AD, OD) dataset at each of the 6 timepoints

	Day 1	**Day 2**	**Day 3**	**Day 4**	**Day 5**	**Day 7**
Cell area	7.9%	7.4%	-7.2%	4.8%	-7.6%	7.5%
Cell aspect ratio	-8.1%	-8.9%	8.4%	-10.1%	9.6%	-8.5%
F-actin	3.8%	0.1%	-1.1%	2.0%	-3.3%	5.0%
Fibre thickness	-4.2%	-5.7%	6.0%	-5.6%	3.0%	-2.7%
Fibre thickness var	6.0%	7.4%	-7.2%	5.0%	-5.9%	5.5%
Fibre alignment	7.7%	7.5%	-8.3%	9.1%	-7.5%	6.8%
Fibre curvature	-9.3%	-9.6%	9.1%	-10.1%	10.1%	-9.2%
LPFI	4.2%	7.2%	-7.6%	6.5%	-5.2%	7.3%
Fibre spread var	-5.8%	-7.8%	7.1%	-7.6%	7.2%	-8.6%
Stellate factor	3.4%	-0.9%	0.4%	1.1%	1.5%	0.7%
Fibre length	-6.1%	-6.7%	6.3%	-9.8%	9.2%	-6.5%
Fibre length var	-0.8%	-0.7%	1.9%	-4.3%	1.4%	-3.0%
Fibre chirality	-8.0%	-6.8%	7.5%	-7.3%	7.6%	-6.9%
Fibre chirality var	8.9%	9.7%	-8.9%	10.2%	-10.1%	8.6%
Nuclear brightness	-2.8%	-1.9%	1.5%	-0.3%	0.7%	-1.6%
Chromatin cond	0.8%	1.2%	0.4%	-0.1%	0.9%	2.0%
Nuclear volume	5.7%	3.1%	-5.5%	3.9%	-3.1%	6.1%
Poisson ratio	0.0%	1.4%	-0.2%	0.2%	-1.5%	0.5%
Nuclear stiffness	6.5%	5.9%	-5.3%	2.2%	-4.7%	3.0%

Table 6.5 Coefficients of PC2 represented as a percentage contribution to the overall PCA transformation of (AD, OD) dataset at each of the 6 timepoints

	Day 1	Day 2	Day 3	Day 4	Day 5	Day 7
Cell area	-10.7%	-8.1%	-11.4%	14.0%	-12.9%	10.0%
Cell aspect ratio	-7.9%	-4.5%	-6.4%	5.2%	-6.8%	4.6%
F-actin	-13.1%	-12.7%	-13.2%	14.7%	-13.1%	12.0%
Fibre thickness	-6.1%	-9.2%	-7.1%	8.1%	-1.1%	8.0%
Fibre thickness var	-4.3%	-4.0%	-4.7%	3.5%	-6.0%	3.8%
Fibre alignment	3.2%	-0.3%	-0.7%	-1.4%	7.0%	-6.7%
Fibre curvature	-1.6%	0.4%	0.4%	-0.7%	-1.9%	2.2%
LPFI	3.2%	2.7%	2.5%	1.5%	0.1%	3.0%
Fibre spread var	-4.8%	-5.6%	-5.2%	-1.5%	0.9%	-2.0%
Stellate factor	-3.0%	-3.5%	-5.1%	6.2%	-4.0%	1.7%
Fibre length	-7.0%	-4.0%	-6.8%	4.1%	-5.7%	8.4%
Fibre length var	-11.5%	-7.5%	-11.7%	11.2%	-12.4%	10.4%
Fibre chirality	-0.2%	-0.1%	-0.5%	1.1%	-1.7%	3.0%
Fibre chirality var	4.0%	0.5%	1.6%	-0.5%	3.0%	-2.4%
Nuclear brightness	1.1%	5.3%	2.2%	-3.3%	2.9%	-5.5%
Chromatin cond	-1.4%	-3.2%	1.6%	1.3%	1.0%	-3.5%
Nuclear volume	-4.9%	-10.8%	-6.1%	10.4%	-8.3%	7.0%
Poisson ratio	-3.3%	7.1%	-1.8%	2.3%	-0.9%	2.6%
Nuclear stiffness	-8.8%	-10.5%	-10.9%	8.9%	-10.4%	3.5%

6.2.2.3 Feature correlation analysis

Table 6.6 shows the correlation analysis between features in a colour scale. Each cell is assigned a colour, where dark green represents the maximum positive correlation of 1, yellow is assigned to values close to 0 which corresponds to no correlation, and red represents the maximum negative correlation of -1. Similar to our conclusions of the feature correlation analysis in chapter 5, our analysis on the data from gel based experiments also showed very few features that had a correlation of ± 0.4 or higher/lower. This indicates that the conducted LDA fit has unlikely been over-fitted to any particular set of features.

Table 6.6 Correlation analysis between morphometric features

	Cell area	Cell aspect ratio	F-actin	Fibre thickness	Fibre thickness var	Fibre alignment	Fibre curvature	LPFI	Fibre spread var	Stellate factor	Fibre length	Fibre length var	Fibre chirality	Fibre chirality var	Nuclear brightness	Chromatin cond	Nuclear volume	Poisson ratio	Nuclear stiffness
Cell area	1.0																		
Cell aspect ratio	0.0	1.0																	
F-actin	0.6	0.1	1.0																
Fibre thickness	-0.1	0.2	0.5	1.0															
Fibre thickness var	0.4	-0.1	0.2	-0.1	1.0														
Fibre alignment	0.0	-0.5	0.0	0.0	0.1	1.0													
Fibre curvature	-0.3	0.4	-0.1	0.1	-0.2	-0.5	1.0												
LPFI	0.1	-0.2	0.0	-0.2	0.1	0.0	-0.1	1.0											
Fibre spread var	-0.3	0.3	-0.1	0.3	0.0	-0.1	0.2	-0.2	1.0										
Stellate factor	0.2	0.1	0.1	-0.1	0.1	0.2	-0.2	0.1	0.0	1.0									
Fibre length	-0.1	0.3	0.1	0.2	-0.2	-0.2	0.5	-0.2	0.4	0.1	1.0								
Fibre length var	0.4	0.3	0.3	0.0	0.1	-0.1	-0.1	0.0	0.1	0.3	0.3	1.0							
Fibre chirality	-0.2	0.4	-0.1	0.0	-0.1	-0.4	0.3	0.0	0.1	0.0	0.2	0.0	1.0						
Fibre chirality var	0.2	-0.6	0.1	-0.1	0.1	0.4	-0.4	0.2	-0.3	-0.1	-0.3	-0.1	-0.5	1.0					
Nuclear brightness	0.0	0.0	0.0	0.0	0.0	0.0	0.0	0.0	0.0	0.0	0.0	0.0	0.1	-0.1	1.0				
Chromatin cond	0.1	0.0	0.1	0.0	0.0	0.0	0.0	0.0	0.0	0.0	0.0	0.1	-0.1	0.0	0.0	1.0			
Nuclear volume	0.4	0.0	0.4	0.1	0.1	0.1	-0.1	0.0	-0.1	0.0	-0.1	0.1	-0.1	0.1	-0.6	0.0	1.0		
Poisson ratio	0.3	0.1	0.1	-0.1	0.1	0.0	0.0	0.1	-0.1	0.1	0.1	0.2	0.0	0.0	0.3	0.1	-0.1	1.0	
Nuclear stiffness	0.7	0.0	0.5	0.0	0.3	0.0	-0.2	0.0	-0.1	0.1	-0.1	0.3	-0.2	0.2	-0.1	0.1	0.1	-0.1	1.0

6.2.2.4 Longitudinal classification of adipogenic and osteogenic differentiation

Figure 6.12 A displays the LDA clustering of AD data labelled across 7 classes (days 0, 1, 2, 3, 4, 5 and 7), while Figure 6.12 B only contains the LDA clustering of data from 3 well separated classes (i.e. days 1, 3 and 7). The correct prediction percentage (CPP) of the LDA fitting for all 7 classes was calculated to be around 43.14 %, which is much lower than any of the CPPs calculated between AD, OD and SC in section 5.2.2.1, but unlike in section 5.2.2.4, where the CPP from the LDA fit for 3 distant timepoints nearly doubled, the CCP here only improved by around half to 67.52 %.

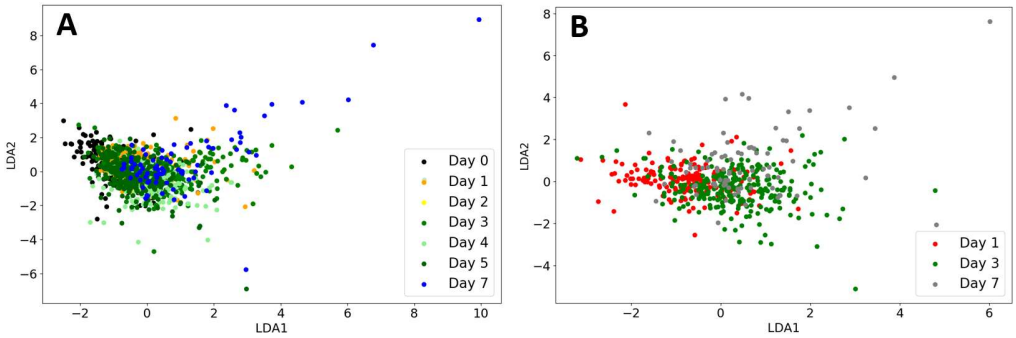

Figure 6.12 Two component LDA representation of multivariate data from adipogenically differentiated cells for up to 7 days (A) Class clustering of data labelled across 7 timepoints (days 0, 1, 2, 3, 4, 5 and 7) with a CPP of 0.4314 (B) Class clustering of data from 3 well distributed timepoints (days 1, 3 and 7) with a CPP of 0.6752

Figure 6.13 A shows the LDA clustering of OD data labelled across 7 classes (days 0, 1, 2, 3, 4, 5 and 7), while Figure 6.13 B only contains the LDA clustering of data from 3 well separated classes (i.e. days 1, 3 and 7). The CPP from the LDA fitting for all 7 classes was calculated to be around 60 %. Similar to that of AD, the CPP from 3 timepoints also increased by around half to 89.74 %.

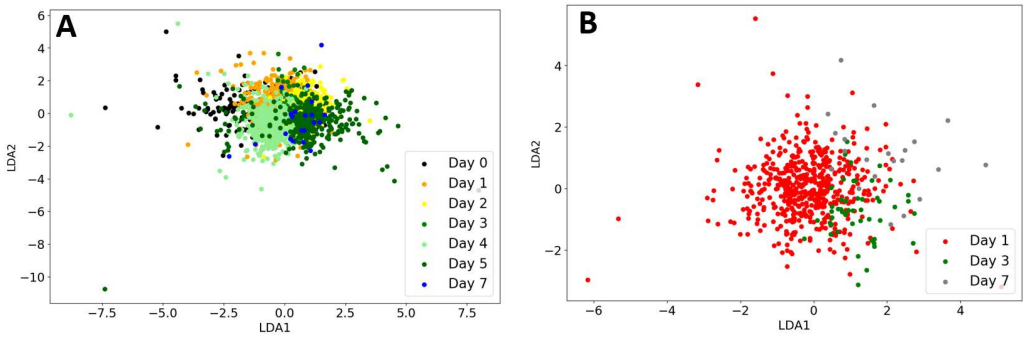

Figure 6.13 Two component LDA representation of multivariate data from osteogenically differentiated cells for up to 7 days (A) Class clustering of data labelled across 7 timepoints (days 0, 1, 2, 3, 4, 5 and 7) with a CPP of 0.6009 (B) Class clustering of data from 3 well distributed timepoints (days 1, 3 and 7) with a CPP of 0.8974

6.3 Summary

In this chapter, cells were differentiated on gel substrates of different stiffness (10 kPa for AD, 35 kPa for OD) and their morphometric features were measured, analysed and compared against the data from the differentiation experiment performed with glass substrates. Comparison of their temporal variation showed considerable resemblance in the trendlines of some features (F-actin, nuclear stiffness and fibre thickness), while others exhibited only general commonalities in the direction of change (cell area, cell aspect ratio, fibre curvature, Poisson ratio and fibre alignment). On the contrary, some features showed no noticeable temporal trends or variance at all (stellate factor, location of peak fibre intensity and fibre chirality).

Furthermore, the collective effect of all the features on the classification of the differentiation stages and lineages was also investigated. An LDA classifier was used on (SC, AD, OD) and (AD, OD) datasets separately and their respective correct prediction percentages (CCP) were calculated. A comparison between differentiation on gel and glass substrates highlighted less temporal variance on gels, especially for the AD lineage. Plausible explanations for this are further discussed in section 7.2.

Chapter 7 | Discussion and outlook

Stem cells have yet to contribute to their full potential in the field of regenerative medicine. Previously, it has been shown that stem cells differentiated in vitro were effective at repairing damaged tissue when injected at the treatment site(Zhang, Wernig, Duncan, Brüstle, & Thomson, 2001). This process had been further improved by introducing bio-scaffolding with traditional biochemical differentiation methods, with the aim to better prepare stem cells for later implantation by simulating the destination environment in vitro (Freed et al., 1994). However, further understanding of the process underlying cell differentiation is required to better manipulate their therapeutic potential.

Various methods have been developed by researchers to identify various characteristic properties of different cell lineages. However, most of these techniques are end-point assays and provide very little information about the changes occurring in the early stages of the differentiation process (Treiser et al., 2010). Moreover, most of these are population based assessments and do not consider the inherent heterogeneity of a typical cell population (Treiser et al., 2010).

This project aims to explore if the structural and geometrical specificity of the cytoskeletal components (actin in particular) encode any information regarding cell fate.

For this project we selected adipogenic (AD) and osteogenic (OD) differentiation lineages as these have been extensively studied over the past few decades. We then developed a novel approach to describe AD and OD cells by their cytoskeletal and nuclear morphology in terms of 19 distinct features. This set of parameters has a range of complexity, extending from one dimensional (e.g. fibre length and fibre thickness) to compound geometrical readings (e.g. fibre chirality and fibre alignment), while some extrapolate morphological and mechanical properties of the nucleus i.e. Poisson ratio and chromatin condensation. Measurements of these features were extracted by using a proprietary image analysis algorithm from fluorescent images of cells which were biochemically differentiated for up to 10 days on variant substrate stiffnesses (i.e. on glass in chapter 5, on 10 kPa and 35 kPa PAA gels in chapter 6).

The differentiation of hMSC was performed with cells cultured at low cell densities (500 - 750 cells/cm^2) to allow for single cell image acquisition. These cells were fixed at different timepoints, stained for F-actin (with phalloidin) and mounted on glass slides with mounting media containing DAPI.

Uni- and multivariate analysis were performed on the extracted features to assess their effectiveness for population classification. Analysis of individual features showed that some parameters changed markedly already in the early stages of differentiation. More interestingly we noted these changes to be non-linear and non-monotonic. Multivariate analysis showed that AD and OD morphology became progressively distinct over time. These analyses, in light with previously published literature on the subject has allowed us to more intricately hypothesise probable mechanisms involved with mechanotransduction which direct the lineage commitments.

7.1 Methods and optimisation

A variety of methods has been used throughout this project to achieve a reliable procedure for single cell imaging and their consequent feature analysis. Among those methods basic cell work and molecular biology techniques have been employed as well as computational and statistical analysis. While some of these methods were well established, like differentiation protocols and LDA classifier, others were specifically designed and adopted for this project. Certain inadequacies of these novel methods will be discussed in the following in order to position our findings in the correct context.

7.1.1 Experimental

In our literature survey, no studies were found in which single cell morphometric examination of the differentiation for more than 7 days had been attempted. This meant that experimental conditions were required to be optimised from bottom up. To allow for single cell imaging (for a minimum of 7 days), cells were required to be seeded at cell densities below 750 cells/cm^2, which is considerably lower than the recommended cell densities in established AD and OD protocols. Although the appearance of fat lipids and calcium can confirm a differentiation lineage, their absence by contrast does not allow any inferences. Histochemical tests confirmed that hMSCs do differentiate when seeded at such low cell densities, though later/slower than usual (confirmed only by day 15/20 instead of day 7/10 with higher cell densities). No conclusions could be made if cells at such low cell densities differentiate generally slower or start differentiating later in time, e.g. once they reach a high enough cell density. For further insights on this, suitable gene expression assays should be employed to confirm the progression of differentiation under our chosen experimental conditions.

Substrate stiffness was investigated with different PAA gels to contrast differentiation experiments carried out on glass. A gel stiffness as low as possible was desired (to mimic actual fat tissue), which unfortunately resulted in very small cells. As a compromise, a

stiffness of 10 kPa and 35 kPa was chosen for adipogenic and osteogenic cells, respectively. During our optimisation study we found that cells grown on 10 kPa gels were noticeably smaller than cells grown on 35 kPa gels or glass. As the features our algorithm measures are suitable for well spread cells, this size difference could lead to a lower accuracy in fibre detection for cells grown on 10 kPa gels, and consequently can affect the feature measurements. This issue could be address by fully differentiating AD and OD on both, 10 kPa and 35 kPa and compare the results. Moreover, it was observed that most gels (especially 10 kPa) had fewer than expected overall cell numbers, but a very high cell density on the edges of the coverslips (around the gel). Based on this, it could be hypothesised that there might be a negative migration gradient off the gel to a much stiffer glass substrate (as also reported by Hadden et al., 2017). One approach to address this issue could be to seed the cells on gels with a 30 mm diameter with a drop of cell suspension.

7.1.2 Data acquisition

An essential requirement for a reliable multivariate analysis is to have large amounts of data available. Without the use of high throughput microscopy, we were limited to how many images could be acquired in the available time. Moreover, time limitations also restricted the use of high resolution images, as this would have required much longer processing time.

Our analysis pipeline is currently optimised for images acquired at x20 magnification using an epi-fluorescence microscope but could be further adapted for high throughput live cell imaging in the future.

Another shortcoming during data acquisition was with measuring the mechanical properties of the gels, which was done by simple indentation. This technique measures gel stiffness on a macroscale, whereas cells may experience the stiffness very differently on a nanoscale as is described by (Trappmann et al., 2012).

7.1.3 Statistical analysis

Thorough population analysis was conducted to ensure the use of correct statistical analysis and representation; the normality of the populations was assessed in a semi quantitative approach. Although most of the populations were lognormally distributed, outlier's analysis showed that almost all of the populations had data points well outside 3 time the IQR mark (Kim, 2013). Cross correlation of aberrations in a population across all measured features might enable identification of the outlaying cells, which is likely to give further insights into the heterogeneous composition of a stem cell population. As mentioned before, because most populations were

lognormally distributed, all measured values were converted to log scale and analysed with parametric statistical techniques.

Furthermore, only the first two components of LDA and PCA were used for class clustering, while expanding the analysis to include the 3rd component of LDA and PCA could possibly further improve the CPP of the models. However, since the acquired data is high dimensional it might be advantageous to use non-linear classifiers instead e.g. SVM or Naïve Bayes.

7.2 Statistical analysis of morphometric features

In their natural environment, stem cells sense their surroundings by inducing tension in their cytoskeletal network, which in turn applies contractile force to the substrate via integrin adhesions (D E Ingber, 2004). It is by the detection of change in this tension that relevant signalling cascades are triggered towards an appropriate cell response. Like many other studies, we first studied the morphometric changes of cells differentiated on glass coverslips. We then repeated the same experiment with cells differentiated on 10 kPa (AD) and 35 kPa (OD) gel substrates with fibronectin coating and compared the results with the previous investigation; probable explanations for any observed differences were there drawn.

7.2.1 Univariate assessment

Comparison of the temporal variation in data from both studies showed considerable resemblance in the trendlines of some features (F-actin, nuclear stiffness and fibre thickness), while others exhibited only general commonalities in the direction of change (cell area, cell aspect ratio, fibre curvature, Poisson ratio and fibre alignment). On the contrary, some features showed no noticeable temporal trends or variance (stellate factor, location of peak fibre intensity and fibre chirality).

Comparing the data from experiments conducted on glass and PAA gels, it was noticed that less temporal variance was on gels than on glass, especially for AD lineage. This observation can be explained by the fact that adipogenic cells stayed considerably smaller when grown on gel substrate compared to their counterparts grown on glass, while osteogenic cells achieved a similar size regardless of their substrate. An explanation for this could be the difference in gel stiffness used for AD (10 kPa) and OD (35 kPa), which were chosen based on preliminary experiments and commonly reported stiffnesses in literature. Due to the softer substrate stiffness, adipogenic cells were limited in their ability to spread and grow bigger (Caliari & Burdick, 2016). Considering the limitations with image processing algorithms, smaller sized cells are measured with less accuracy resulting in lower variance compared to bigger sized cells.

7.2.2 Multivariate assessment

The analysis of PCA coefficients from both investigations showed that most features followed variant levels and directions of change over the period of differentiation. For example, the aspect ratio of the cell shape switched from being representative of OD variance in the beginning, towards AD in the later stages of differentiation (on glass – Table 5.4 and on gel – Table 6.5).

Treiser et al. (2010) studied morphometric features of stem cells differentiated over a period of 96 h and reported conclusive linear trends for both AD and OD. Though we observed similar trends during the early stages of the experiment, we realised that when monitored for a longer period of time (up to day 10) these trends went on to follow non-linear and non-monotonic paths. This indicates the necessity of carrying out differentiation studies for adequate time periods with a high resolution of timepoints to get a holistic and accurate view of the relation between cell morphology and the differentiation process.

Correct prediction percentages (CPP) from longitudinal LDA fits were lower than those achieved with cross-lineage LDA fits. One possible reason for this could be the fact that stem cell differentiation is an asynchronous process (Bongiorno et al., 2014), where cells may differentiate at varying speeds at different stages of the process. Since CPP is calculated by comparing the classification of cells (based on the LDA fit) against their original class labels, any cell differentiating significantly slower or faster than the average of the population is likely to be misclassified, which causes lowering of the CPP.

Another noteworthy distinction was found between the CPP from the longitudinal LDA fit of AD and OD data i.e. on glass AD had a higher CPP than OD, while it was the opposite on gels. As before, this can be explained by the difference in cell area for adipogenic cells grown on glass and gel substrates. As adipogenic cells remained considerably small due to their inability to spread on soft substrate, it might result in lower quality of image segmentation (i.e. fibre detection) (Eltzner et al., 2015). Lack of accuracy can make it harder for any linear classifier to effectively segregate classes, and hence can result in a lower CPP. While the CPP for AD (overall) was lower on gel substrate than on glass, the opposite was observed for OD (on gels). This observation can be attributed to the presence of fibronectin coating on gel substrates, which caused cells to spread more than on glass (section 9.1.1). This resulted in an improved segregation of timepoints for OD on gels, compared to the FBS coated glass.

7.2.3 Correlation

Correlation analysis was conducted to assess over representation of any subset of features on the multivariate classification. Calculations showed heavy correlations (> ± 0.6) among features only in very few instances. Moreover, when comparing the results from the correlation analysis against the influence each feature had on the principal components, it was noticed that many of the features which showed a correlation stronger than ± 0.3 also contributed heavily to the variances in principal components 1 and 2.

Nevertheless, certain correlations, such as between cell area and F-actin, were expected while others, such as the positive correlation of 0.7 between cell area and nuclear stiffness were intriguing findings. It can be hypothesised that larger cells require a sturdier cytoskeletal network, which in turn would exert more force on the nucleus. This additional force is likely to cause compression to the nucleus and increase compaction of chromatin organisation, as was also indicated by the accompanied reduction in Poisson ratio (Vishavkarma et al., 2014). Thus, it can be assumed that a more compressed nucleus might be stiffer in larger cells.

Another interesting correlation was found between cell aspect ratio, fibre alignment and fibre chirality variance. Undifferentiated cells are polar and have long fibres along the major axis, which means less angular variability. There may be high average chirality as most fibres will be making very large angles against the 'normal' drawn from the centre of the cell, while the variance among those angles would be low. With the progression of differentiation, cells become less polar and lose their fibre alignment, which could in turn allow fibres to arrange in more possible ways in relation to the cell centre.

7.3 Future work

In this project we developed a novel approach to perform single cell feature quantification of stem cells differentiating towards osteogenic and adipogenic lineages. For this, cell culture protocols were optimised, morphometric features characteristic of AD and OD developed, and detailed statistical analysis performed. However, some of these methodologies were found to have major limitations requiring further modification. Aside from overcoming these limitations and implementing improvements to our approach, further morphometric features should be investigated.

7.3.1 Multi-cytoskeleton analysis

Although the need for introducing additional morphometric features has been discussed, an attempt to fully utilise the already existing features is advisable. Various studies have reported connections between cell differentiation and the cell's cytoskeleton. In the case of adipogenic and osteogenic differentiation, actin has usually been the focus of attention, though some research has revealed a relation between other cytoskeletal networks and the differentiation process (Keeling et al., 2017; Shariftabrizi, Ahmadian, & Pazhang, 2012).

The mechanism by which acto-myosin stress fibres are involved in mechanically induced differentiation has previously been discussed (sections 2.2.2.5 and 2.4.1). Additionally, a correlation between F-actin and the myosin cytoskeleton has recently been reported by Keeling et al. (2017). Considering this, it can be reasoned that myosin could provide complementary information needed to understand the underlying process regulated by the acto-myosin machinery.

Actin based mechanotransduction mostly involves pathways triggered by tensile forces, however compression is another very common mechanical stimuli which cells experience in their natural environment (Peter Schumann et al., 2004). Compression can cause the cell nucleus to deform and consequently alter chromatin condensation. Vimentin has been shown to regulate the deformability of cells, which by extension implies that it plays an indirect role in the regulation of gene expression induced by mechanotransduction pathways (Sharma, Bolten, Wagner, & Hsieh, 2017). Furthermore, microtubules have been reported to not only go under substantial reorganisation but also have their synthesis rate reduced by almost 95 % during adipogenic differentiation (Spiegelman & Farmer, 1982; W. Yang et al., 2013). Most of these changes in the microtubule synthesis rate occur in the very early stages of differentiation and are thought to participate profoundly in the development of adipocytic morphology (Spiegelman & Farmer, 1982). A complete reconditioning of microtubule organisation also during osteogenic differentiation was reported by (Rodríguez, González, Ríos, & Cambiazo, 2004). Meka *et al.* (2017) observed that perturbation of the microtubules by nocodazole caused similar changes in cell morphology as would actin depolymerisation.

Thus, extracting tubulin and vimentin based morphometric features could likely help to better distinguish between different lineages and would allow for characterisation in the early stages of the process in greater detail.

7.3.2 Classification

In this project we mostly investigated the effectiveness of the extracted features individually and as aggregate using a LDA classifier. Previously, Treiser et al. (2010) used a SVM classifier

on very similar type of data, and also achieved high prediction accuracy i.e. above 80 %. However, based on the results from the Treiser et al. (2010) study and ours, it can be argued that linear classifiers, such as LDA and SVM appear to perform better with a lower number of classes (up to 3) but may require a non-linear kernel (alone or in ensemble with a linear kernel) to work with a higher number of classes.

7.3.3 Feature and experimental optimisation

Furthermore, features such as stellate factor and location of peak fibre intensity which showed very little to no trends might need further optimisation to capture any detected temporal variance. In addition to that, classification could also benefit from additional feature extraction. One such feature could be the identification/quantification of different types of actin fibres i.e. dorsal, ventral, arcs and perinuclear stress fibres (Figure 2.7), present at any given stage. This categorisation of stress fibres may be facilitated by also acquiring the locations and sizes of adhesion complexes.

Another promising approach for future work could be to determine a method and consequently morphometric features which can be employed in combination with live cell imaging to also acquire contextual information i.e. spreading phase, migration, and cell division

As was discussed in section 7.1.1, moving forward it is advisable to compare between lineages when both lineages have been differentiated on the same substrate stiffness, primarily to get better insights into cell behaviour on different mechanical environments but also to control system variation.

Chapter 8 | References

Alberts, B., Johnson, A., Lewis, J., Raff, M., Roberts, K., & Walter, P. (2008). *Molecular Biology of the Cell*. Garland Science.

Aldridge, A., Kouroupis, D., Churchman, S., English, A., Ingham, E., & Jones, E. (2013). Assay validation for the assessment of adipogenesis of multipotential stromal cells--a direct comparison of four different methods. *Cytotherapy*, *15*(1), 89–101.

Alexandrescu, V. A. (Ed.). (2016). *Wound Healing - New insights into Ancient Challenges*. InTech.

Alexandrova, A. Y., Arnold, K., Schaub, S., Vasiliev, J. M., Meister, J.-J., Bershadsky, A. D., & Verkhovsky, A. B. (2008). Comparative Dynamics of Retrograde Actin Flow and Focal Adhesions: Formation of Nascent Adhesions Triggers Transition from Fast to Slow Flow. *PLoS ONE*, *3*(9), e3234.

Anderson, H. C. (2003). Matrix vesicles and calcification. *Current rheumatology reports*, *5*, 222–226.

Angele, P., Yoo, J. U., Smith, C., Mansour, J., Jepsen, K. J., Nerlich, M., & Johnstone, B. (2003). Cyclic hydrostatic pressure enhances the chondrogenic phenotype of human mesenchymal progenitor cells differentiated in vitro. *Journal of orthopaedic research : official publication of the Orthopaedic Research Society*, *21*(3), 451–7.

Arnold, M., Cavalcanti-Adam, E. A., Glass, R., Blümmel, J., Eck, W., Kantlehner, M., … Spatz, J. P. (2004). Activation of Integrin Function by Nanopatterned Adhesive Interfaces. *ChemPhysChem*, *5*(3), 383–388.

Atilgan, E. X., Wirtz, D., & Sun, S. X. (2005). Morphology of the Lamellipodium and Organization of Actin Filaments at the Leading Edge of Crawling Cells.

Bao, G., & Suresh, S. (2003). Cell and molecular mechanics of biological materials. *Nature Materials*, *2*(11), 715–725.

Bastmeyer, M., & Stuermer, C. A. O. (1993). Behavior of fish retinal growth cones encountering chick caudal tectal membranes: A time-lapse study on growthcone collapse. *Journal of Neurobiology*, *24*(1), 37–50.

Bauer, P. J. (1981). Affinity and stoichiometry of calcium binding by arsenazo III. *Analytical Biochemistry*, *110*(1), 61–72.

Bessey, O. A., Lowry, O. H., & Brock, M. J. (1946). A method for the rapid determination of alkaline phosphatase with five cubic millimeters of serum. *J. Biol. Chem.*, *164*(1), 321–329.

Bongiorno, T., Kazlow, J., Mezencev, R., Griffiths, S., Olivares-Navarrete, R., McDonald, J. F., … Sulchek, T. (2014). Mechanical stiffness as an improved single-cell indicator of osteoblastic human mesenchymal stem cell differentiation. *Journal of Biomechanics*, *47*(9), 2197–2204.

Born, A.-K., Rottmar, M., Lischer, S., Pleskova, M., Bruinink, A., & Maniura-Weber, K. (2009). Correlating cell architecture with osteogenesis: first steps towards live single cell monitoring. *European cells & materials*, *18*, 49–60, 61–2;

Boucher, S. E. (2011). Simplified PCR assay for detecting early stages of multipotent

mesenchymal stromal cell differentiation. *Methods in molecular biology (Clifton, N.J.)*, *698*, 387–403.

Boucher, S., Lakshmipathy, U., & Vemuri, M. (2009). A simplified culture and polymerase chain reaction identification assay for quality control performance testing of stem cell media products. *Cytotherapy*, *11*(6), 761–767.

Bray, D. (2001). *Cell movements : from molecules to motility*. Garland Pub.

Bray, D., & White, J. (1988). Cortical flow in animal cells. *Science*, *239*(4842), 883–888.

Burridge, K., & Connell, L. (1983). Talin: A cytoskeletal component concentrated in adhesion plaques and other sites of actin-membrane interaction. *Cell Motility*, *3*(5), 405–417.

Burridge, K., & Guilluy, C. (2016). Focal adhesions, stress fibers and mechanical tension. *Experimental Cell Research*, *343*(1), 14–20.

Caliari, S. R., & Burdick, J. A. (2016). A practical guide to hydrogels for cell culture. *Nature Methods*, *13*(5), 405–414.

Campagnoli, C., Roberts, I. A., Kumar, S., Bennett, P. R., Bellantuono, I., & Fisk, N. M. (2001). Identification of mesenchymal stem/progenitor cells in human first-trimester fetal blood, liver, and bone marrow. *Blood*, *98*(8), 2396–402.

Chalut, K. J., & Paluch, E. K. (2016). The Actin Cortex: A Bridge between Cell Shape and Function. *Developmental Cell*, *38*, 571–573.

Chamberlain, G., Fox, J., Ashton, B., & Middleton, J. (2007). Concise Review: Mesenchymal Stem Cells: Their Phenotype, Differentiation Capacity, Immunological Features, and Potential for Homing. *Stem Cells*, *25*(11), 2739–2749.

Cheng, N.-C., Estes, B. T., Awad, H. A., & Guilak, F. (2009). Chondrogenic differentiation of adipose-derived adult stem cells by a porous scaffold derived from native articular cartilage extracellular matrix. *Tissue engineering. Part A*, *15*, 231–241.

Dahl, K. N., & Kalinowski, A. (2011). Nucleoskeleton mechanics at a glance. *Journal of Cell Science*, *124*(5), 675–678.

Dahl, K. N., Ribeiro, A. J. S., & Lammerding, J. (2008). Nuclear Shape, Mechanics, and Mechanotransduction. *Circulation Research*, *102*(11), 1307–1318.

Dalbay, M. T., Thorpe, S. D., Connelly, J. T., Chapple, J. P., & Knight, M. M. (2015). Adipogenic Differentiation of hMSCs is Mediated by Recruitment of IGF-1r Onto the Primary Cilium Associated With Cilia Elongation. *STEM CELLS*, *33*(6), 1952–1961.

Dechat, T., Pfleghaar, K., Sengupta, K., Shimi, T., Shumaker, D. K., Solimando, L., & Goldman, R. D. (2008). Nuclear lamins: major factors in the structural organization and function of the nucleus and chromatin. *Genes & Development*, *22*(7), 832–853.

Deguchi, S., Ohashi, T., & Sato, M. (2006). Tensile properties of single stress fibers isolated from cultured vascular smooth muscle cells. *Journal of Biomechanics*, *39*(14), 2603–2610.

del Rio, A., Perez-Jimenez, R., Liu, R., Roca-Cusachs, P., Fernandez, J. M., & Sheetz, M. P. (2009). Stretching Single Talin Rod Molecules Activates Vinculin Binding. *Science*, *323*(5914), 638–641.

Discher, D. E., Janmey, P., & Wang, Y.-L. (2005). Tissue cells feel and respond to the stiffness

of their substrate. *Science (New York, N.Y.)*, *310*, 1139–1143.

Eltzner, B., Wollnik, C., Gottschlich, C., Huckemann, S., & Rehfeldt, F. (2015). The Filament Sensor for Near Real-Time Detection of Cytoskeletal Fiber Structures. *PLOS ONE*, *10*(5), e0126346.

Engler, A. J., Sen, S., Sweeney, H. L., & Discher, D. E. (2006). Matrix Elasticity Directs Stem Cell Lineage Specification. *Cell*, *126*(4), 677–689.

English, A., Jones, E. A., Corscadden, D., Henshaw, K., Chapman, T., Emery, P., & McGonagle, D. (2007). A comparative assessment of cartilage and joint fat pad as a potential source of cells for autologous therapy development in knee osteoarthritis. *Rheumatology*, *46*(11), 1676–1683.

Farnier, C., Krief, S., Blache, M., Diot-Dupuy, F., Mory, G., Ferre, P., & Bazin, R. (2003). Adipocyte functions are modulated by cell size change: potential involvement of an integrin/ERK signalling pathway. *International Journal of Obesity*, *27*(10), 1178–1186.

Fink, T., Abildtrup, L., Fogd, K., Abdallah, B. M., Kassem, M., Ebbesen, P., & Zachar, V. (2004). Induction of Adipocyte-Like Phenotype in Human Mesenchymal Stem Cells by Hypoxia. *Stem Cells*, *22*(7), 1346–1355.

Fink, T., & Zachar, V. (2011). Adipogenic differentiation of human mesenchymal stem cells. *Methods in molecular biology (Clifton, N.J.)*, *698*, 243–51.

Fortier, L. A., & Travis, A. J. (2011). Stem cells in veterinary medicine. *Stem Cell Research & Therapy*, *2*(1), 9.

Freed, L. E., Vunjak-Novakovic, G., Biron, R. J., Eagles, D. B., Lesnoy, D. C., Barlow, S. K., & Langer, R. (1994). Biodegradable Polymer Scaffolds for Tissue Engineering. *Nature Biotechnology*, *12*(7), 689–693.

Fu, Y.-X., Gu, J.-H., Zhang, Y.-R., Tong, X.-S., Zhao, H.-Y., Yuan, Y., … Liu, Z.-P. (2013). Influence of osteoprotegerin on differentiation, activation, and apoptosis of Gaoyou duck embryo osteoclasts in vitro. *Poultry Science*, *92*(6), 1613–1620.

Gavara, N., & Chadwick, R. S. (2016). Relationship between cell stiffness and stress fiber amount, assessed by simultaneous atomic force microscopy and live-cell fluorescence imaging. *Biomechanics and Modeling in Mechanobiology*, *15*(3), 511–523.

Gefen, A., & Benayahu, D. (2014). *The mechanobiology of obesity and related diseases*.

Gerecht, S., Bettinger, C. J., Zhang, Z., Borenstein, J. T., Vunjak-Novakovic, G., & Langer, R. (2007). The effect of actin disrupting agents on contact guidance of human embryonic stem cells. *Biomaterials*, *28*, 4068–4077.

Giannone, G., Mège, R.-M., & Thoumine, O. (2009). Multi-level molecular clutches in motile cell processes. *Trends in Cell Biology*, *19*(9), 475–486.

Gillespie, P. G., & Walker, R. G. (2001). Molecular basis of mechanosensory transduction. *Nature*, *413*(6852), 194–202.

Gobaa, S., Hoehnel, S., & Lutolf, M. P. (2015). Substrate elasticity modulates the responsiveness of mesenchymal stem cells to commitment cues. *Integr. Biol. Integr. Biol*, *7*, 1135–1142.

Goetze, S., Mateos-Langerak, J., Gierman, H. J., de Leeuw, W., Giromus, O., Indemans, M. H. G., … van Driel, R. (2007). The Three-Dimensional Structure of Human Interphase

Chromosomes Is Related to the Transcriptome Map. *Molecular and Cellular Biology*, *27*(12), 4475–4487.

Gojo, S., Gojo, N., Takeda, Y., Mori, T., Abe, H., Kyo, S., … Umezawa, A. (2003). In vivo cardiovasculogenesis by direct injection of isolated adult mesenchymal stem cells. *Experimental Cell Research*, *288*, 51–59.

Gong, Z., & Niklason, L. E. (2008). Small-diameter human vessel wall engineered from bone marrow-derived mesenchymal stem cells (hMSCs). *The FASEB journal : official publication of the Federation of American Societies for Experimental Biology*, *22*, 1635–1648.

Gonzalez-Cruz, R. D., Fonseca, V. C., & Darling, E. M. (2012). Cellular mechanical properties reflect the differentiation potential of adipose-derived mesenchymal stem cells. *Proceedings of the National Academy of Sciences*, *109*(24), E1523–E1529.

Guilak, F., Cohen, D. M., Estes, B. T., Gimble, J. M., Liedtke, W., & Chen, C. S. (2009). Control of Stem Cell Fate by Physical Interactions with the Extracellular Matrix. *Cell Stem Cell*, *5*, 17–26.

Hadden, W. J., Young, J. L., Holle, A. W., McFetridge, M. L., Kim, D. Y., Wijesinghe, P., … Choi, Y. S. (2017). Stem cell migration and mechanotransduction on linear stiffness gradient hydrogels. *Proceedings of the National Academy of Sciences*, *114*(22), 5647–5652.

Hamill, O. P., & Martinac, B. (2001). Molecular Basis of Mechanotransduction in Living Cells. *Physiological Reviews*, *81*(2), 685–740.

Hamilton, D. W., Maul, T. M., & Vorp, D. A. (n.d.). Characterization of the response of bone marrow-derived progenitor cells to cyclic strain: implications for vascular tissue-engineering applications. *Tissue engineering*, *10*(3–4), 361–9.

Han, F., Gilbert, J. R., Harrison, G., Adams, C. S., Freeman, T., Tao, Z., … Hickok, N. J. (2007). Transforming growth factor-β1 regulates fibronectin isoform expression and splicing factor SRp40 expression during ATDC5 chondrogenic maturation. *Experimental Cell Research*, *313*(8), 1518–1532.

Havaki, S., Kouloukoussa, M., Amawi, K., Drosos, Y., Arvanitis, L. D., Goutas, N., … Marinos, E. (2007). Altered expression pattern of integrin alphavbeta3 correlates with actin cytoskeleton in primary cultures of human breast cancer. *Cancer Cell International*, *7*(1), 16.

Hofstetter, C. P., Schwarz, E. J., Hess, D., Widenfalk, J., El Manira, A., Prockop, D. J., & Olson, L. (2002). Marrow stromal cells form guiding strands in the injured spinal cord and promote recovery. *Proceedings of the National Academy of Sciences of the United States of America*, *99*, 2199–2204.

Holle, A. W., & Engler, A. J. (2011). More than a feeling: discovering, understanding, and influencing mechanosensing pathways. *Current Opinion in Biotechnology*, *22*(5), 648–654.

Holtzer, H., Abbott, J., Lash, J., & Holtzer, S. (1960). THE LOSS OF PHENOTYPIC TRAITS BY DIFFERENTIATED CELLS IN VITRO, I. DEDIFFERENTIATION OF CARTILAGE CELLS. *Proceedings of the National Academy of Sciences*, *46*(12), 1533–1542.

Hwang, J.-H., Byun, M. R., Kim, A. R., Kim, K. M., Cho, H. J., Lee, Y. H., … Hong, J.-H. (2015). Extracellular Matrix Stiffness Regulates Osteogenic Differentiation through MAPK

Activation. *PLOS ONE*, *10*(8), e0135519.

Ignotz, R. A., & Massagué, J. (1985). Type beta transforming growth factor controls the adipogenic differentiation of 3T3 fibroblasts. *Proceedings of the National Academy of Sciences*, *82*(24).

in `t Anker, P. S., Scherjon, S. A., Kleijburg-van der Keur, C., Noort, W. A., Claas, F. H. J., Willemze, R., … Kanhai, H. H. H. (2003). Amniotic fluid as a novel source of mesenchymal stem cells for therapeutic transplantation. *Blood*, *102*(4), 1548–1549.

Ingber, D. E. (2003). Mechanobiology and diseases of mechanotransduction. *Annals of medicine*, *35*, 564–577.

Ingber, D. E. (2004). The mechanochemical basis of cell and tissue regulation. *Mechanics & chemistry of biosystems : MCB*, *1*(1), 53–68.

Jaiswal, R. K., Jaiswal, N., Bruder, S. P., Mbalaviele, G., Marshak, D. R., & Pittenger, M. F. (2000). Adult human mesenchymal stem cell differentiation to the osteogenic or adipogenic lineage is regulated by mitogen-activated protein kinase. *The Journal of biological chemistry*, *275*(13), 9645–52.

Javazon, E. H., Beggs, K. J., & Flake, A. W. (2004). Mesenchymal stem cells: paradoxes of passaging. *Experimental hematology*, *32*(5), 414–25.

Jorgensen, P., Edgington, N. P., Schneider, B. L., Rupes, I., Tyers, M., & Futcher, B. (2007). The Size of the Nucleus Increases as Yeast Cells Grow. *Molecular Biology of the Cell*, *18*(9), 3523–3532.

Jurado, C., Haserick, J. R., & Lee, J. (2004). Slipping or Gripping? Fluorescent Speckle Microscopy in Fish Keratocytes Reveals Two Different Mechanisms for Generating a Retrograde Flow of Actin. *Molecular Biology of the Cell*, *16*(2), 507–518.

Kabsch, W., & Holmes, K. C. (1995). The actin fold. *FASEB journal : official publication of the Federation of American Societies for Experimental Biology*, *9*(2), 167–74.

Keeling, M. C., Flores, L. R., Dodhy, A. H., Murray, E. R., & Gavara, N. (2017). Actomyosin and vimentin cytoskeletal networks regulate nuclear shape, mechanics and chromatin organization. *Scientific Reports*, *7*(1), 5219.

Kilian, K. A., Bugarija, B., Lahn, B. T., & Mrksich, M. (2010). Geometric cues for directing the differentiation of mesenchymal stem cells. *Proceedings of the National Academy of Sciences of the United States of America*, *107*(11), 4872–7.

Kim, H.-Y. (2013). Statistical notes for clinical researchers: assessing normal distribution (2) using skewness and kurtosis. *Restorative dentistry & endodontics*, *38*(1), 52–4.

Knippenberg, M., Helder, M. N., Doulabi, B. Z., Semeins, C. M., Wuisman, P. I. J. M., & Klein-Nulend, J. (2005). Adipose tissue-derived mesenchymal stem cells acquire bone cell-like responsiveness to fluid shear stress on osteogenic stimulation. *Tissue engineering*, *11*(11–12), 1780–8.

Kopen, G. C., Prockop, D. J., & Phinney, D. G. (1999). Marrow stromal cells migrate throughout forebrain and cerebellum, and they differentiate into astrocytes after injection into neonatal mouse brains. *Proceedings of the National Academy of Sciences of the United States of America*, *96*, 10711–10716.

Kouzarides, T. (2007). Chromatin Modifications and Their Function. *Cell*, *128*(4), 693–705.

Krause, U., Seckinger, A., & Gregory, C. A. (2011). Assays of osteogenic differentiation by cultured human mesenchymal stem cells. *Methods in molecular biology (Clifton, N.J.)*, *698*, 215–30.

Kwon, Y.-N., Kim, W. K., Lee, S.-H., Kim, K., Kim, E. Y., Ha, T. H., … Bae, K.-H. (2011). Monitoring of adipogenic differentiation at the single-cell level using atomic force microscopic analysis. *Journal of Spectroscopy*, *26*(6), 329–335.

Lanza, R. (2009). *Essentials of stem cell biology*. Academic Press.

Leary, N. O., Pembroke, A., & Duggan, P. F. (1992). Single stable reagent (Arsenazo III) for optically robust measurement of calcium in serum and plasma. *Clinical chemistry*, *38*, 904–908.

Lee, W.-C. C., Maul, T. M., Vorp, D. A., Rubin, J. P., & Marra, K. G. (2007). Effects of uniaxial cyclic strain on adipose-derived stem cell morphology, proliferation, and differentiation. *Biomechanics and modeling in mechanobiology*, *6*, 265–273.

Li, L., & Xie, T. (2005). STEM CELL NICHE: Structure and Function. *Annual Review of Cell and Developmental Biology*, *21*(1), 605–631.

Liou, Y.-R., Torng, W., Kao, Y.-C., Sung, K.-B., Lee, C.-H., & Kuo, P.-L. (2014). Substrate Stiffness Regulates Filopodial Activities in Lung Cancer Cells. *PLoS ONE*, *9*(2), e89767.

Lu, L., Oswald, S. J., Ngu, H., & Yin, F. C. P. (2008). Mechanical properties of actin stress fibers in living cells. *Biophysical Journal*, *95*(12), 6060–6071.

Luger, K., Dechassa, M. L., & Tremethick, D. J. (2012). New insights into nucleosome and chromatin structure: an ordered state or a disordered affair? *Nature Reviews Molecular Cell Biology*, *13*(7), 436–447.

Lv, H., Li, L., Sun, M., Zhang, Y., Chen, L., Rong, Y., & Li, Y. (2015). Mechanism of regulation of stem cell differentiation by matrix stiffness. *Stem Cell Research & Therapy*, *6*(1), 103.

Maciel, B. B., Rebelatto, C. L. K., Brofman, P. R. S., Brito, H. F. V, Patricio, L. F. L., Cruz, M. A., & Locatelli-Dittrich, R. (2014). Morphology and morphometry of feline bone marrow-derived mesenchymal stem cells in culture 1. *Pesquisa Veterinária Brasileira*, *34*(3411).

Mackay, A. M., Beck, S. C., Murphy, J. M., Barry, F. P., Chichester, C. O., & Pittenger, M. F. (1998). Chondrogenic differentiation of cultured human mesenchymal stem cells from marrow. *Tissue engineering*, *4*, 415–428.

Maeshima, K., Iino, H., Hihara, S., & Imamoto, N. (2011). Nuclear size, nuclear pore number and cell cycle. *Nucleus*, *2*(2), 113–118.

Mallavarapu, A., & Mitchison, T. (1999). Regulated actin cytoskeleton assembly at filopodium tips controls their extension and retraction. *Journal of Cell Biology*, *146*(5), 1097–1106.

Manasek, F. J., Burnside, M. B., & Waterman, R. E. (1972). Myocardial cell shape change as a mechanism of embryonic heart looping. *Developmental Biology*, *29*(4), 349–371.

Martins, R. P., Finan, J. D., Farshid, G., & Lee, D. A. (2012). Mechanical Regulation of Nuclear Structure and Function. *Annual Review of Biomedical Engineering*, *14*(1), 431–455.

Martins, R. P., Ostermeier, G. C., & Krawetz, S. A. (2004). Nuclear Matrix Interactions at the

Human Protamine Domain. *Journal of Biological Chemistry*, *279*(50), 51862–51868.

Mathieu, P. S., & Loboa, E. G. (2012). Cytoskeletal and focal adhesion influences on mesenchymal stem cell shape, mechanical properties, and differentiation down osteogenic, adipogenic, and chondrogenic pathways. *Tissue engineering. Part B, Reviews*, *18*(6), 436–44.

Mattila, P. K., & Lappalainen, P. (2008). Filopodia: molecular architecture and cellular functions. *Nature Reviews Molecular Cell Biology*, *9*(6), 446–454.

Mazumder, A., & Shivashankar, G. V. (2007). Gold-Nanoparticle-Assisted Laser Perturbation of Chromatin Assembly Reveals Unusual Aspects of Nuclear Architecture within Living Cells. *Biophysical Journal*, *93*(6), 2209–2216.

McBeath, R., Pirone, D. M., Nelson, C. M., Bhadriraju, K., & Chen, C. S. (2004). Cell shape, cytoskeletal tension, and RhoA regulate stem cell lineage commitment. *Developmental cell*, *6*(4), 483–95.

McBride, S. H., & Knothe Tate, M. L. (2008). Modulation of stem cell shape and fate A: the role of density and seeding protocol on nucleus shape and gene expression. *Tissue engineering. Part A*, *14*, 1561–1572.

Meka, S. R. K., Chacko, L. A., Ravi, A., Chatterjee, K., & Ananthanarayanan, V. (2017). Role of Microtubules in Osteogenic Differentiation of Mesenchymal Stem Cells on 3D Nanofibrous Scaffolds. *ACS Biomaterials Science & Engineering*, *3*(4), 551–559.

Meyers, J., Craig, J., & Odde, D. J. (2006). Potential for control of signaling pathways via cell size and shape. *Current biology : CB*, *16*, 1685–1693.

Mobasheri, A., Kalamegam, G., Musumeci, G., & Batt, M. E. (2014). Chondrocyte and mesenchymal stem cell-based therapies for cartilage repair in osteoarthritis and related orthopaedic conditions. *Maturitas*, *78*(3), 188–198.

Mori, G., Brunetti, G., Oranger, A., Carbone, C., Ballini, A., Muzio, L. Lo, … Grano, M. (2011). Dental pulp stem cells: osteogenic differentiation and gene expression. *Annals of the New York Academy of Sciences*, *1237*(1), 47–52.

Morrison, S. J., & Spradling, A. C. (2008). Stem Cells and Niches: Mechanisms That Promote Stem Cell Maintenance throughout Life. *Cell*, *132*(4), 598–611.

Mullins, R. D., Heuser, J. A., & Pollard, T. D. (1998). The interaction of Arp2/3 complex with actin: nucleation, high affinity pointed end capping, and formation of branching networks of filaments. *Proceedings of the National Academy of Sciences of the United States of America*, *95*(11), 6181–6.

Nakahara, H., Dennis, J. E., Bruder, S. P., Haynesworth, S. E., Lennon, D. P., & Caplan, A. I. (1991). In vitro differentiation of bone and hypertrophic cartilage from periosteal-derived cells. *Experimental cell research*, *195*(2), 492–503.

Neves, S. R., Tsokas, P., Sarkar, A., Grace, E. A., Rangamani, P., Taubenfeld, S. M., … Iyengar, R. (2008). Cell Shape and Negative Links in Regulatory Motifs Together Control Spatial Information Flow in Signaling Networks. *Cell*, *133*, 666–680.

Newman, P., & Watt, F. M. (1988). Influence of cytochalasin D-induced changes in cell shape on proteoglycan synthesis by cultured articular chondrocytes. *Experimental cell research*, *178*, 199–210.

O'Connor, C., Adams, J., & Fairman, J. (2014). *Cell Biology for Seminars*. Nature Education.

O'Connor, C. M., & Adams, J. U. (2010). *Essentials of cell biology*.

Pagliara, S., Franze, K., McClain, C. R., Wylde, G. W., Fisher, C. L., Franklin, R. J. M., … Chalut, K. J. (2014). Auxetic nuclei in embryonic stem cells exiting pluripotency. *Nature Materials*, *13*(6), 638–644.

Pajerowski, J. D., Dahl, K. N., Zhong, F. L., Sammak, P. J., & Discher, D. E. (2007). Physical plasticity of the nucleus in stem cell differentiation. *Proceedings of the National Academy of Sciences*, *104*(40), 15619–15624.

Parhami, F., Jackson, S. M., Tintut, Y., Le, V., Balucan, J. P., Territo, M., & Demer, L. L. (1999). Atherogenic Diet and Minimally Oxidized Low Density Lipoprotein Inhibit Osteogenic and Promote Adipogenic Differentiation of Marrow Stromal Cells. *Journal of Bone and Mineral Research*, *14*(12), 2067–2078.

Park, J. S., Chu, J. S. F., Cheng, C., Chen, F., Chen, D., & Li, S. (2004). Differential effects of equiaxial and uniaxial strain on mesenchymal stem cells. *Biotechnology and Bioengineering*, *88*, 359–368.

Pellegrin, S., Mellor, H., Barry, P., Andrews, P., & Jester, J. V. (2007). Actin stress fibres. *Journal of cell science*, *120*(Pt 20), 3491–9.

Peter Schumann, D., Angele, M., Kinner, B., Englert, C., Hente, R., Füchtmeier, B., … Kujat, R. (2004). *Biorheology. Biorheology* (Vol. 41). Pergamon Press.

Pittenger, M. F. (1999). Multilineage Potential of Adult Human Mesenchymal Stem Cells. *Science*, *284*(5411), 143–147.

Ponti, A., Machacek, M., Gupton, S. L., Waterman-Storer, C. M., & Danuser, G. (2004). Two Distinct Actin Networks Drive the Protrusion of Migrating Cells. *Science*, *305*(5691), 1782–1786.

Poole, A. R., Matsui, Y., Hinek, A., & Lee, E. R. (1989). Cartilage macromolecules and the calcification of cartilage matrix. *The Anatomical record*, *224*(2), 167–79.

Potian, J. A., Aviv, H., Ponzio, N. M., Harrison, J. S., & Rameshwar, P. (2003). Veto-like activity of mesenchymal stem cells: functional discrimination between cellular responses to alloantigens and recall antigens. *Journal of immunology (Baltimore, Md. : 1950)*, *171*(7), 3426–34.

Qian, S.-W., Li, X., Zhang, Y.-Y., Huang, H.-Y., Liu, Y., Sun, X., & Tang, Q.-Q. (2010). Characterization of adipocyte differentiation from human mesenchymal stem cells in bone marrow. *BMC Developmental Biology*, *10*(1), 47.

Recknor, J. B., Sakaguchi, D. S., & Mallapragada, S. K. (2006). Directed growth and selective differentiation of neural progenitor cells on micropatterned polymer substrates. *Biomaterials*, *27*, 4098–4108.

Reece, J. B., Urry, L. A., Cain, M. L., Wasserman, S. A., Minorsky, P. V., & Jackson, R. B. (2013). *Campbell biology*.

Reyes, M., Lund, T., Lenvik, T., Aguiar, D., Koodie, L., & Verfaillie, C. M. (2001). Purification and ex vivo expansion of postnatal human marrow mesodermal progenitor cells. *Blood*, *98*, 2615–2625.

Ridley, A. J. (2011). Life at the Leading Edge. *Cell*, *145*(7), 1012–1022.

Rodríguez, J. P., González, M., Ríos, S., & Cambiazo, V. (2004). Cytoskeletal organization of

human mesenchymal stem cells (MSC) changes during their osteogenic differentiation. *Journal of cellular biochemistry*, *93*(4), 721–31.

Saha, K., Keung, A. J., Irwin, E. F., Li, Y., Little, L., Schaffer, D. V, & Healy, K. E. (2008). Substrate modulus directs neural stem cell behavior. *Biophysical journal*, *95*, 4426–4438.

Schäpe, J., Praußе, S., Radmacher, M., & Stick, R. (2009). Influence of Lamin A on the Mechanical Properties of Amphibian Oocyte Nuclei Measured by Atomic Force Microscopy. *Biophysical Journal*, *96*(10), 4319–4325.

Schardin, M., Cremer, T., Hager, H. D., & Lang, M. (1985). Specific staining of human chromosomes in Chinese hamster x man hybrid cell lines demonstrates interphase chromosome territories. *Human genetics*, *71*(4), 281–7.

Schofield, R. (1978). The relationship between the spleen colony-forming cell and the haemopoietic stem cell. *Blood cells*, *4*(1–2), 7–25.

Schuldt, A. (2005). Spire: a new nucleator for actin. *Nature Cell Biology*, *7*(2), 107–107.

Sekiya, I., Larson, B. L., Vuoristo, J. T., Cui, J.-G., & Prockop, D. J. (2003). Adipogenic Differentiation of Human Adult Stem Cells From Bone Marrow Stroma (MSCs). *Journal of Bone and Mineral Research*, *19*(2), 256–264.

Sen, B., Xie, Z., Case, N., Ma, M., Rubin, C., & Rubin, J. (2008). Mechanical strain inhibits adipogenesis in mesenchymal stem cells by stimulating a durable beta-catenin signal. *Endocrinology*, *149*, 6065–6075.

Shariftabrizi, A., Ahmadian, S., & Pazhang, Y. (2012). Dynamics of γ-tubulin cytoskeleton in HL-60 leukemia cells undergoing differentiation and apoptosis by all-trans retinoic acid. *Molecular Medicine Reports*, *5*(2), 545–551.

Sharma, P., Bolten, Z. T., Wagner, D. R., & Hsieh, A. H. (2017). Deformability of Human Mesenchymal Stem Cells Is Dependent on Vimentin Intermediate Filaments. *Annals of Biomedical Engineering*, *45*(5), 1365–1374.

Sheterline, P., & Sparrow, J. C. (1994). Actin. *Protein profile*, *1*(1), 1–121.

Shih, Y.-R. V, Tseng, K.-F., Lai, H.-Y., Lin, C.-H., & Lee, O. K. (2011). Matrix stiffness regulation of integrin-mediated mechanotransduction during osteogenic differentiation of human mesenchymal stem cells. *Journal of Bone and Mineral Research*, *26*(4), 730–738.

Simmons, C. A., Matlis, S., Thornton, A. J., Chen, S., Wang, C. Y., & Mooney, D. J. (2003). Cyclic strain enhances matrix mineralization by adult human mesenchymal stem cells via the extracellular signal-regulated kinase (ERK1/2) signaling pathway. *Journal of Biomechanics*, *36*, 1087–1096.

Slack, J. M. (2000). Stem cells in epithelial tissues. *Science (New York, N.Y.)*, *287*(5457), 1431–3.

Small, J. V., Herzog, M., Häner, M., & Abei, U. (1994). Visualization of actin filaments in keratocyte lamellipodia: Negative staining compared with freeze-drying. *Journal of Structural Biology*, *113*(2), 135–141.

Sonowal, H., Kumar, A., Bhattacharyya, J., Gogoi, P., & Jaganathan, B. (2013). Inhibition of actin polymerization decreases osteogeneic differentiation of mesenchymal stem cells through p38 MAPK pathway. *Journal of Biomedical Science*, *20*(1), 71.

Spiegelman, B. M., & Farmer, S. R. (1982). Decreases in tubulin and actin gene expression prior to morphological differentiation of 3T3 Adipocytes. *Cell*, *29*(1), 53–60.

Spivakov, M., & Fisher, A. G. (2007). Epigenetic signatures of stem-cell identity. *Nature Reviews Genetics*, *8*(4), 263–271.

Spradling, A., Drummond-Barbosa, D., & Kai, T. (2001). Stem cells find their niche. *Nature*, *414*(6859), 98–104.

Strambio-De-Castillia, C., Niepel, M., & Rout, M. P. (2010). The nuclear pore complex: bridging nuclear transport and gene regulation. *Nature Reviews Molecular Cell Biology*, *11*(7), 490–501.

Stricker, J., Falzone, T., & Gardel, M. L. (2010). Mechanics of the F-actin cytoskeleton. *Journal of Biomechanics*, *43*(1), 9–14.

Svitkina, T. M., Verkhovsky, A. B., McQuade, K. M., & Borisy, G. G. (1997). Analysis of the actin-myosin II system in fish epidermal keratocytes: mechanism of cell body translocation. *The Journal of cell biology*, *139*(2), 397–415.

Tee, Y. H., Shemesh, T., Thiagarajan, V., Hariadi, R. F., Anderson, K. L., Page, C., … Bershadsky, A. D. (2015). Cellular chirality arising from the self-organization of the actin cytoskeleton. *Nature Cell Biology*, *17*(4), 445–457.

Terraciano, V., Hwang, N., Moroni, L., Park, H. Bin, Zhang, Z., Mizrahi, J., … Elisseeff, J. (2007). Differential response of adult and embryonic mesenchymal progenitor cells to mechanical compression in hydrogels. *Stem cells (Dayton, Ohio)*, *25*(11), 2730–8.

Thomas, G. P., & El Haj, A. J. (1996). Bone marrow stromal cells are load responsive in vitro. *Calcified Tissue International*, *58*, 101–108.

Trappmann, B., Gautrot, J. E., Connelly, J. T., Strange, D. G. T., Li, Y., Oyen, M. L., … Huck, W. T. S. (2012). Extracellular-matrix tethering regulates stem-cell fate. *Nature Materials*, *11*(7), 642–649.

Treiser, M. D., Yang, E. H., Gordonov, S., Cohen, D. M., Androulakis, I. P., Kohn, J., … Moghe, P. V. (2010). Cytoskeleton-based forecasting of stem cell lineage fates. *Proceedings of the National Academy of Sciences of the United States of America*, *107*(2), 610–5.

Tuan, R. S., Boland, G., & Tuli, R. (2003). Adult mesenchymal stem cells and cell-based tissue engineering. *Arthritis research & therapy*, *5*(1), 32–45.

Tumbar, T., & Fuchs, E. (2009). Chapter 22 – Epithelial Hair Follicle Stem Cells. In *Essentials of Stem Cell Biology* (pp. 189–197).

van der Kooy, D., & Weiss, S. (2000). Why stem cells? *Science (New York, N.Y.)*, *287*(5457), 1439–41.

Vemuri, M. C., Chase, L. G., & Rao, M. S. (2011). *Mesenchymal Stem Cell Assays and Applications*. Humana Press.

Versaevel, M., Grevesse, T., & Gabriele, S. (2012). Spatial coordination between cell and nuclear shape within micropatterned endothelial cells. *Nature Communications*, *3*(1), 671.

Vishavkarma, R., Raghavan, S., Kuyyamudi, C., Majumder, A., Dhawan, J., & Pullarkat, P. A. (2014). Role of actin filaments in correlating nuclear shape and cell spreading. *PloS one*, *9*(9), e107895.

Vogel, V. (2006). MECHANOTRANSDUCTION INVOLVING MULTIMODULAR PROTEINS: Converting Force into Biochemical Signals. *Annual Review of Biophysics and Biomolecular Structure*, *35*(1), 459–488.

Volpi, E. V, Chevret, E., Jones, T., Vatcheva, R., Williamson, J., Beck, S., … Sheer, D. (2000). Large-scale chromatin organization of the major histocompatibility complex and other regions of human chromosome 6 and its response to interferon in interphase nuclei. *Journal of cell science*, *113 (Pt 9)*, 1565–76.

Wakatsuki, T., Kolodney, M. S., Zahalak, G. I., & Elson, E. L. (2000). Cell mechanics studied by a reconstituted model tissue. *Biophysical journal*, *79*(5), 2353–68.

Wakitani, S., Saito, T., & Caplan, A. I. (1995). Myogenic cells derived from rat bone marrow mesenchymal stem cells exposed to 5-azacytidine. *Muscle & nerve*, *18*, 1417–1426.

Wang, N., Tytell, J. D., & Ingber, D. E. (2009). Mechanotransduction at a distance: mechanically coupling the extracellular matrix with the nucleus. *Nature Reviews Molecular Cell Biology*, *10*(1), 75–82.

Watt, F. M., & Hogan, B. L. (2000). Out of Eden: stem cells and their niches. *Science (New York, N.Y.)*, *287*, 1427–1430.

Webster, M., Witkin, K. L., & Cohen-Fix, O. (2009). Sizing up the nucleus: nuclear shape, size and nuclear-envelope assembly. *Journal of Cell Science*, *122*(10), 1477–1486.

Weickert, J. (1999). Coherence-Enhancing Diffusion Filtering. *International Journal of Computer Vision*, *31*(2/3), 111–127.

Winer, J. P., Janmey, P. A., McCormick, M. E., & Funaki, M. (2009). Bone marrow-derived human mesenchymal stem cells become quiescent on soft substrates but remain responsive to chemical or mechanical stimuli. *Tissue engineering. Part A*, *15*, 147–154.

Woodbury, D., Schwarz, E. J., Prockop, D. J., & Black, I. B. (2000). Adult rat and human bone marrow stromal cells differentiate into neurons. *Journal of neuroscience research*, *61*, 364–370.

Wu, C.-Y., Rolfe, P. A., Gifford, D. K., & Fink, G. R. (2010). Control of Transcription by Cell Size. *PLoS Biology*, *8*(11), e1000523.

Yang, C., & Svitkina, T. (2011). Visualizing branched actin filaments in lamellipodia by electron tomography. *Nature Cell Biology*, *13*(9), 1012–1013.

Yang, W., Guo, X., Thein, S., Xu, F., Sugii, S., Baas, P. W., … Han, W. (2013). Regulation of adipogenesis by cytoskeleton remodelling is facilitated by acetyltransferase MEC-17-dependent acetylation of α-tubulin. *Biochemical Journal*, *449*(3), 605–612.

Yang, Y., Beqaj, S., Kemp, P., Ariel, I., & Schuger, L. (2000). Stretch-induced alternative splicing of serum response factor promotes bronchial myogenesis and is defective in lung hypoplasia. *The Journal of clinical investigation*, *106*(11), 1321–30.

Yeung, T., Georges, P. C., Flanagan, L. A., Marg, B., Ortiz, M., Funaki, M., … Janmey, P. A. (2005). Effects of substrate stiffness on cell morphology, cytoskeletal structure, and adhesion. *Cell Motility and the Cytoskeleton*, *60*(1), 24–34.

Yim, E. K. F., Pang, S. W., & Leong, K. W. (2007). Synthetic nanostructures inducing differentiation of human mesenchymal stem cells into neuronal lineage. *Experimental Cell Research*, *313*, 1820–1829.

Yoshikawa, T., Peel, S. A., Gladstone, J. R., & Davies, J. E. (1997). Biochemical analysis of the response in rat bone marrow cell cultures to mechanical stimulation. *Biomed Mater Eng*, *7*, 369–377.

Yourek, G., Hussain, M. A., & Mao, J. J. (2007). Cytoskeletal Changes of Mesenchymal Stem Cells During Differentiation. *ASAIO Journal*, *53*(2), 219–228.

Yu, H., Tay, C. Y., Leong, W. S., Tan, S. C. W., Liao, K., & Tan, L. P. (2010). Mechanical behavior of human mesenchymal stem cells during adipogenic and osteogenic differentiation. *Biochemical and Biophysical Research Communications*, *393*(1), 150–155.

Zanetti, N. C., & Solursh, M. (1984). Induction of chondrogenesis in limb mesenchymal cultures by disruption of the actin cytoskeleton. *The Journal of cell biology*, *99*, 115–123.

Zemel, A., Rehfeldt, F., Brown, A. E. X., Discher, D. E., & Safran, S. A. (2010). Optimal matrix rigidity for stress-fibre polarization in stem cells. *Nature Physics*, *6*(6), 468–473.

Zhang, S.-C., Wernig, M., Duncan, I. D., Brüstle, O., & Thomson, J. A. (2001). In vitro differentiation of transplantable neural precursors from human embryonic stem cells. *Nature Biotechnology*, *19*(12), 1129–1133.

Zhao, H., Gu, J., Dai, N., Gao, Q., Wang, D., Song, R., … Liu, Z. (2016). Osteoprotegerin exposure at different stages of osteoclastogenesis differentially affects osteoclast formation and function. *Cytotechnology*, *68*(4), 1325–35.

Zuk, P. A., Zhu, M., Ashjian, P., De Ugarte, D. A., Huang, J. I., Mizuno, H., … Hedrick, M. H. (2002). Human Adipose Tissue Is a Source of Multipotent Stem Cells. *Molecular Biology of the Cell*, *13*(12), 4279–4295.

Chapter 9 | Appendix

9.1 Chapter 4 appendix

9.1.1 Systemic variation study

Control studies have been carried out comparing two different cell donors, as well as substrate stiffness and coating. For this, cells from two different donors have been grown on PAA gels with a stiffness of 35 kPa coated with fibronectin as well as on glass coated with FBS or fibronectin.

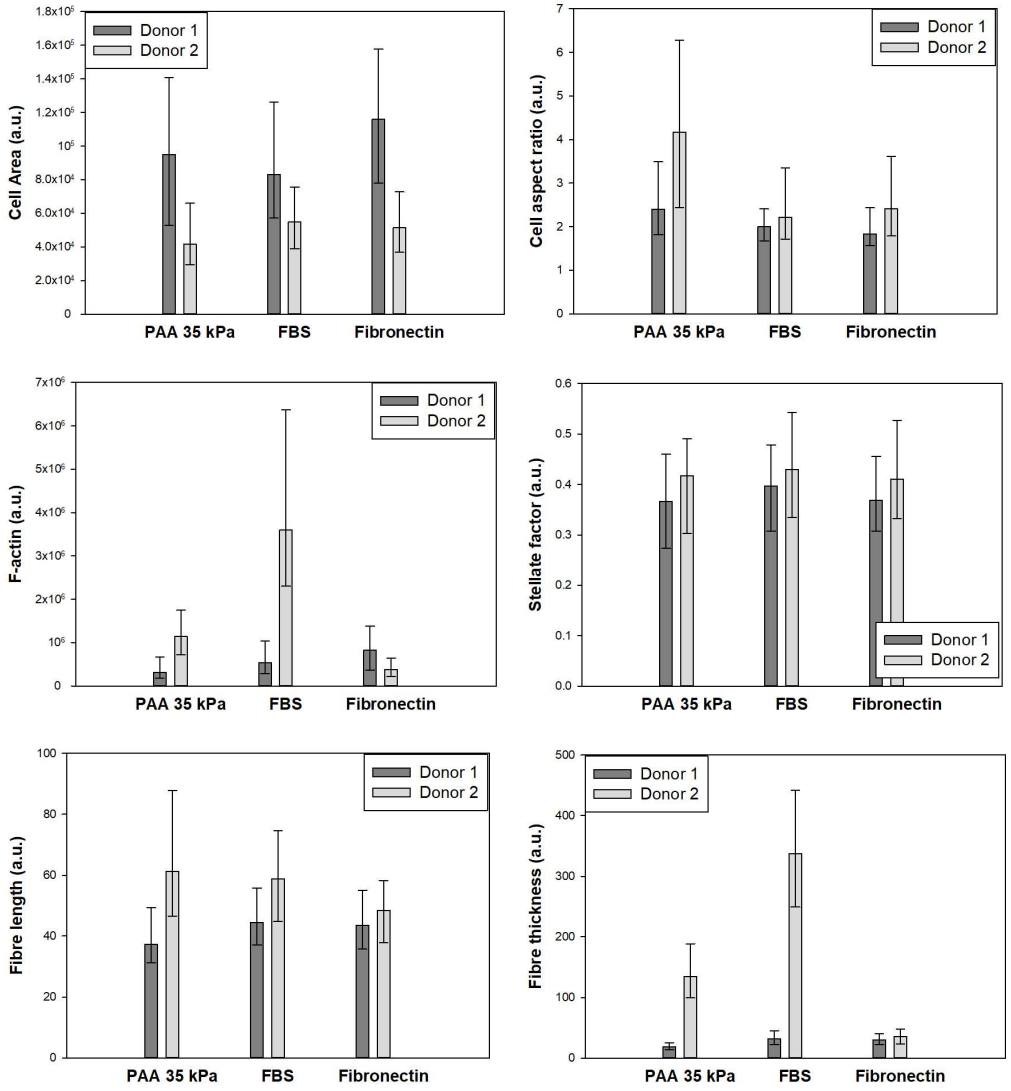

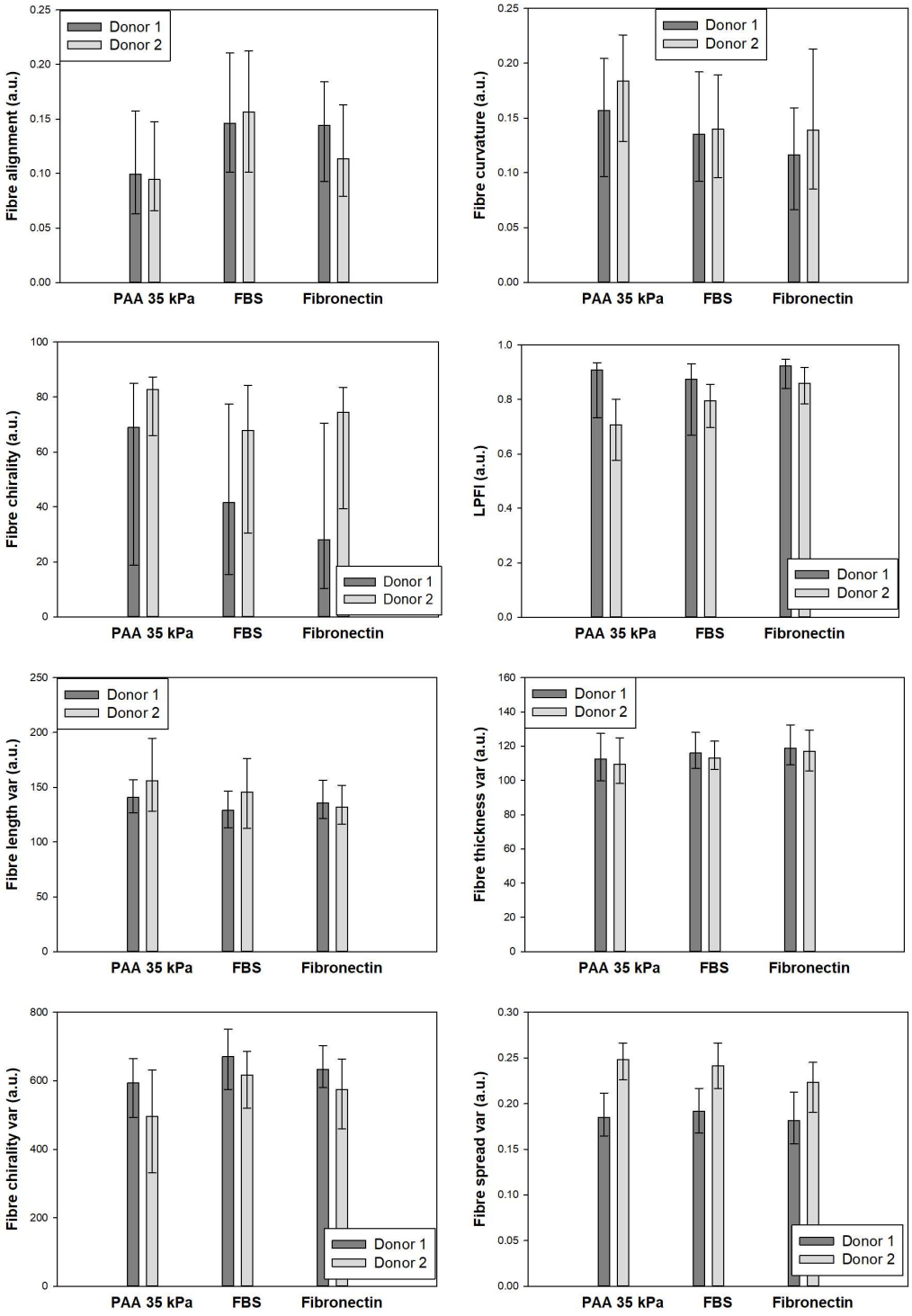
Fibre alignment (a.u.)
Fibre curvature (a.u.)
Fibre chirality (a.u.)
LPFI (a.u.)
Fibre length var (a.u.)
Fibre thickness var (a.u.)
Fibre chirality var (a.u.)
Fibre spread var (a.u.)
Donor 1
Donor 2
PAA 35 kPa
FBS
Fibronectin

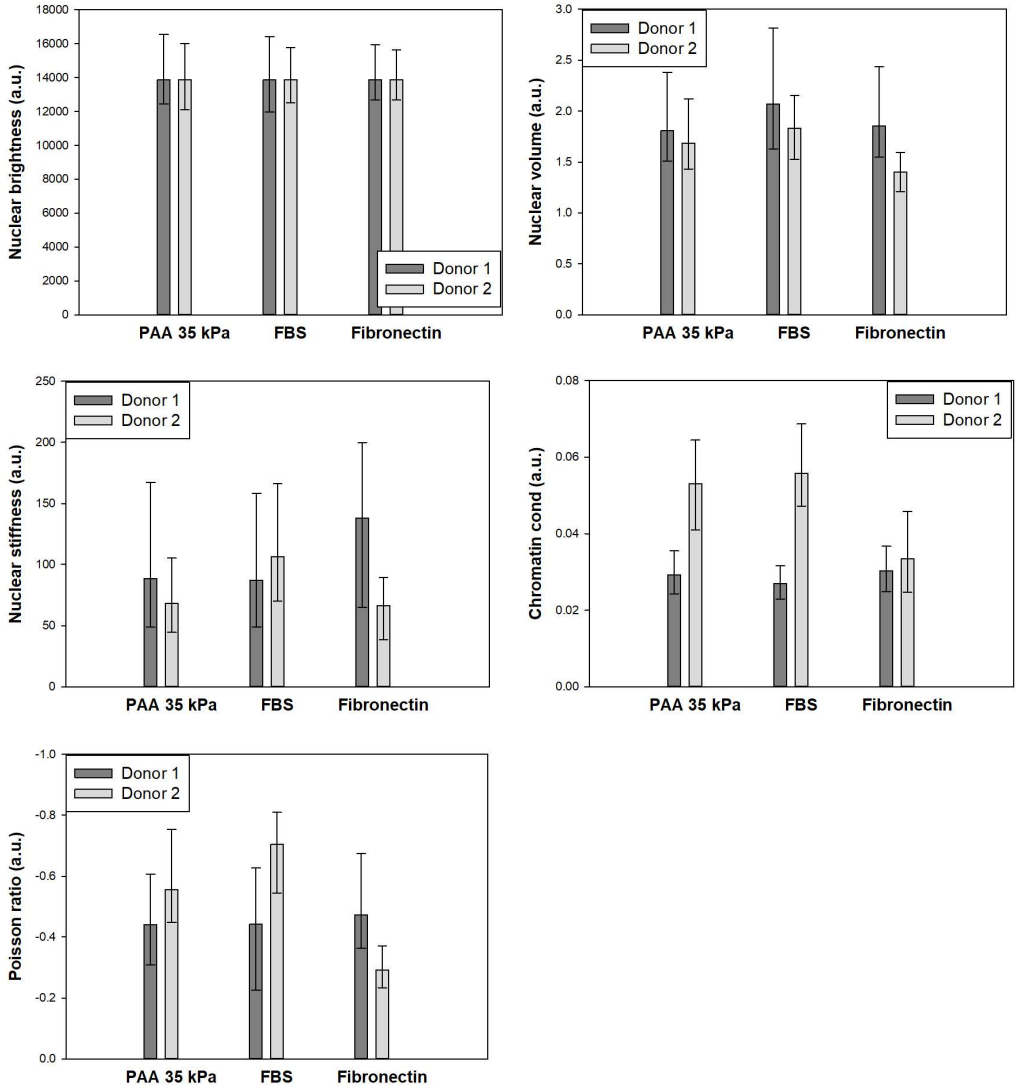

9.1.2 Substrate based variance

9.1.2.1 MANOVA

Effect		Value	F	Hypothesis df	Error df	Sig.
Intercept	Pillai's Trace	.998	6252.925	19.000	257.000	.000
	Wilks' Lambda	.002	6252.925	19.000	257.000	.000
	Hotelling's Trace	462.279	6252.925	19.000	257.000	.000
	Roy's Largest Root	462.279	6252.925	19.000	257.000	.000

9.1.2.2 ANOVA

Dependent Variable	Type III Sum of Squares	df	Mean Square	F	Sig.
Cell area	73422763892.174	2	36711381946.087	8.275	.000
Cell aspect ratio	18.652	2	9.326	9.993	.000
F-actin	18908394389111.030	2	9454197194555.516	13.644	.000

Fibre thickness	14015.843	2	7007.922	21.465	.000
Fibre thickness var	4529.325	2	2264.663	7.189	.001
Fibre alignment	.092	2	.046	11.562	.000
Fibre curvature	.056	2	.028	6.729	.001
LPFI	.463	2	.231	8.975	.000
Fibre spread var	.005	2	.003	1.606	.203
Stellate factor	.028	2	.014	.889	.412
Fibre length	1114.155	2	557.078	1.594	.205
Fibre length var	5549.944	2	2774.972	3.200	.042
Fibre chirality	12548.141	2	6274.070	6.331	.002
Fibre chirality var	362983.259	2	181491.630	12.522	.000
Nuclear brightness	244509.098	2	122254.549	.018	.982
Chromatin cond	.001	2	.000	2.936	.055
Nuclear volume	3.786	2	1.893	3.094	.047
Poisson ratio	.119	2	.059	.888	.413
Nuclear stiffness	385870.276	2	192935.138	6.191	.002

9.1.3 Donor based variance

9.1.3.1 ANOVA

Dependent Variable	Type III Sum of Squares	df	Mean Square	F	Sig.
Cell area	85231744139.796	1	85231744139.796	44.627	.000
Cell aspect ratio	30.054	1	30.054	12.931	.000
F-actin	827866833030068.800	1	827866833030068.800	138.309	.000
Fibre thickness	6724381.631	1	6724381.631	388.694	.000
Fibre thickness var	989.309	1	989.309	4.111	.044
Fibre alignment	7.988E-6	1	7.988E-6	.002	.967
Fibre curvature	.001	1	.001	.304	.582
LPFI	.009	1	.009	.360	.549
Fibre spread var	.154	1	.154	94.574	.000
Stellate factor	.187	1	.187	8.446	.004
Fibre length	17516.154	1	17516.154	28.255	.000
Fibre length var	19974.539	1	19974.539	13.021	.000
Fibre chirality	12229.297	1	12229.297	13.538	.000
Fibre chirality var	322575.541	1	322575.541	19.464	.000
Nuclear brightness	908148.640	1	908148.640	.151	.698
Chromatin cond	.062	1	.062	127.328	.000
Nuclear volume	10.466	1	10.466	23.911	.000
Poisson ratio	4.589	1	4.589	52.115	.000
Nuclear stiffness	18503.958	1	18503.958	1.888	.170

9.1.3.2 MANOVA

Effect		Value	F	Hypothesis df	Error df	Sig.
Intercept	Pillai's Trace	.997	5587.924	19.000	273.000	.000
	Wilks' Lambda	.003	5587.924	19.000	273.000	.000
	Hotelling's Trace	388.903	5587.924	19.000	273.000	.000
	Roy's Largest Root	388.903	5587.924	19.000	273.000	.000

9.1.4 Variance of experimental repeats

9.1.4.1 Day 3

Adipogenic cells

Effect		Value	F	Hypothesis df	Error df	Sig.
Intercept	Pillai's Trace	.998	4239.650	19.000	127.000	.000
	Wilks' Lambda	.002	4239.650	19.000	127.000	.000
	Hotelling's Trace	634.278	4239.650	19.000	127.000	.000
	Roy's Largest Root	634.278	4239.650	19.000	127.000	.000

Dependent Variable	Type III Sum of Squares	df	Mean Square	F	Sig.
Cell area	12576144490.640	1	12576144490.640	22.235	.000
Cell aspect ratio	3.087	1	3.087	4.018	.047
F-actin	14863702152846.438	1	14863702152846.438	4.187	.043
Fibre thickness	353524.015	1	353524.015	77.510	.000
Fibre thickness var	17564.839	1	17564.839	82.521	.000
Fibre alignment	.108	1	.108	37.305	.000
Fibre curvature	.007	1	.007	3.574	.061
LPFI	.241	1	.241	1.667	.199
Fibre spread var	.118	1	.118	2.005	.159
Stellate factor	.612	1	.612	32.430	.000
Fibre length	5504.440	1	5504.440	13.393	.000
Fibre length var	26288.670	1	26288.670	62.249	.000
Fibre chirality	50.788	1	50.788	.126	.723
Fibre chirality var	18716.941	1	18716.941	1.408	.237
Nuclear brightness	1296336.483	1	1296336.483	.220	.640
Chromatin cond	.002	1	.002	4.400	.038
Nuclear volume	.094	1	.094	1.151	.285
Poisson ratio	.070	1	.070	1.800	.182
Nuclear stiffness	36363.311	1	36363.311	44.512	.000

Osteogenic cells

Effect		Value	F	Hypothesis df	Error df	Sig.
Intercept	Pillai's Trace	.998	3778.507	19.000	176.000	.000
	Wilks' Lambda	.002	3778.507	19.000	176.000	.000
	Hotelling's Trace	407.907	3778.507	19.000	176.000	.000
	Roy's Largest Root	407.907	3778.507	19.000	176.000	.000

Dependent Variable	Type III Sum of Squares	df	Mean Square	F	Sig.
Cell area	15617100348.827	2	7808550174.413	12.501	.000
Cell aspect ratio	79.141	2	39.571	16.457	.000
F-actin	69633421191084.060	2	34816710595542.030	16.659	.000
Fibre thickness	1466351.473	2	733175.736	58.086	.000
Fibre thickness var	1095.643	2	547.822	1.468	.233
Fibre alignment	.052	2	.026	5.708	.004
Fibre curvature	.008	2	.004	2.239	.109
LPFI	6.070	2	3.035	15.235	.000
Fibre spread var	1.853	2	.927	13.432	.000
Stellate factor	1.669	2	.835	40.022	.000
Fibre length	30248.345	2	15124.173	22.644	.000
Fibre length var	5049.985	2	2524.992	5.061	.007
Fibre chirality	48165.214	2	24082.607	53.510	.000
Fibre chirality var	289384.976	2	144692.488	8.017	.000
Nuclear brightness	16408925.180	2	8204462.590	1.238	.292
Chromatin cond	.049	2	.025	22.744	.000
Nuclear volume	2.287	2	1.144	7.875	.001
Poisson ratio	4.184	2	2.092	61.385	.000
Nuclear stiffness	8971.021	2	4485.510	5.958	.003

9.1.4.2 Day 7

Adipogenic cells

Effect		Value	F	Hypothesis df	Error df	Sig.
Intercept	Pillai's Trace	.998	11009.917	19.000	339.000	.000
	Wilks' Lambda	.002	11009.917	19.000	339.000	.000
	Hotelling's Trace	617.075	11009.917	19.000	339.000	.000
	Roy's Largest Root	617.075	11009.917	19.000	339.000	.000

Dependent Variable	Type III Sum of Squares	df	Mean Square	F	Sig.
Cell area	202482072821.200	2	101241036410.600	49.517	.000
Cell aspect ratio	57.009	2	28.505	20.884	.000

F-actin	46524511603952.440	2	23262255801976.220	38.028	.000
Fibre thickness	282456.442	2	141228.221	152.059	.000
Fibre thickness var	74715.203	2	37357.601	147.006	.000
Fibre alignment	.073	2	.036	11.353	.000
Fibre curvature	.036	2	.018	19.653	.000
LPFI	4.389	2	2.194	16.116	.000
Fibre spread var	.360	2	.180	3.956	.020
Stellate factor	2.909	2	1.454	61.682	.000
Fibre length	56144.102	2	28072.051	62.808	.000
Fibre length var	47341.819	2	23670.910	40.788	.000
Fibre chirality	147805.742	2	73902.871	130.836	.000
Fibre chirality var	194416.869	2	97208.435	7.529	.001
Nuclear brightness	5715263.552	2	2857631.776	.514	.599
Chromatin cond	.032	2	.016	42.001	.000
Nuclear volume	1.975	2	.988	4.545	.011
Poisson ratio	8.568	2	4.284	180.657	.000
Nuclear stiffness	80962.194	2	40481.097	11.141	.000

Osteogenic cells

Effect		Value	F	Hypothesis df	Error df	Sig.
Intercept	Pillai's Trace	.998	2751.487[b]	19.000	107.000	.000
	Wilks' Lambda	.002	2751.487[b]	19.000	107.000	.000
	Hotelling's Trace	488.582	2751.487[b]	19.000	107.000	.000
	Roy's Largest Root	488.582	2751.487[b]	19.000	107.000	.000

Dependent Variable	Type III Sum of Squares	df	Mean Square	F	Sig.
Cell area	12013110494.493	1	12013110494.493	23.445	.000
Cell aspect ratio	18.728	1	18.728	23.745	.000
F-actin	1163432774732.723	1	1163432774732.723	7.762	.006
Fibre thickness	88585.058	1	88585.058	130.846	.000
Fibre thickness var	2558.155	1	2558.155	12.578	.001
Fibre alignment	.033	1	.033	7.743	.006
Fibre curvature	.001	1	.001	.938	.335
LPFI	6.278	1	6.278	34.102	.000
Fibre spread var	.229	1	.229	4.861	.029
Stellate factor	.504	1	.504	31.120	.000
Fibre length	10592.209	1	10592.209	47.796	.000
Fibre length var	3515.222	1	3515.222	6.299	.013

Fibre chirality	37851.496	1	37851.496	48.654	.000
Fibre chirality var	89008.108	1	89008.108	7.174	.008
Nuclear brightness	2317440.501	1	2317440.501	.339	.562
Chromatin cond	.082	1	.082	53.549	.000
Nuclear volume	6.847	1	6.847	42.373	.000
Poisson ratio	6.370	1	6.370	161.953	.000
Nuclear stiffness	3122.935	1	3122.935	4.115	.045

9.2 Chapter 5 appendix

9.2.1 Descriptive statistics for adipogenic cells

Cell area

	N	Skewness			Kurtosis			Shapiro-Wilk	
	Statistic	Statistic	Std. Error	Z value	Statistic	Std. Error	Z value	Statistic	Sig.
Day_0.00	119	0.664	0.222	2.991	-0.119	0.44	-0.270	0.958	0.003
Day_0.25	312	0.726	0.138	5.261	0.309	0.275	1.124	0.943	0
Day_0.50	262	0.668	0.15	4.453	0.154	0.3	0.513	0.866	0
Day_0.75	101	0.139	0.24	0.579	0.009	0.476	0.019	0.985	0.298
Day_1.00	211	0.468	0.167	2.802	0.268	0.333	0.805	0.989	0.563
Day_3.00	147	0.428	0.2	2.140	-0.949	0.397	-2.390	0.907	0
Day_4.00	130	0.036	0.212	0.170	-0.14	0.422	-0.332	0.984	0.278
Day_5.00	216	0.374	0.166	2.253	-0.341	0.33	-1.033	0.966	0.011
Day_7.00	360	-0.099	0.129	-0.767	-0.609	0.256	-2.379	0.992	0.792
Day_10.0	167	-0.165	0.188	-0.878	-0.728	0.374	-1.946	0.975	0.054

Cell aspect ratio

	N	Skewness			Kurtosis			Shapiro-Wilk	
	Statistic	Statistic	Std. Error	Z value	Statistic	Std. Error	Z value	Statistic	Sig.
Day_0.00	119	-0.155	0.222	-0.698	-0.644	0.44	-1.464	0.984	0.282
Day_0.25	312	0.046	0.138	0.333	-0.831	0.275	-3.022	0.972	0.032
Day_0.50	262	0.137	0.15	0.913	-0.889	0.3	-2.963	0.959	0.003
Day_0.75	101	0.7	0.24	2.917	0.498	0.476	1.046	0.959	0.003
Day_1.00	211	-0.021	0.167	-0.126	-0.834	0.333	-2.504	0.971	0.026
Day_3.00	147	0.648	0.2	3.240	1.06	0.397	2.670	0.975	0.056
Day_4.00	130	0.693	0.212	3.269	-0.306	0.422	-0.725	0.921	0
Day_5.00	216	0.733	0.166	4.416	0.105	0.33	0.318	0.954	0.002
Day_7.00	360	0.904	0.129	7.008	0.473	0.256	1.848	0.827	0
Day_10.0	167	0.502	0.188	2.670	-0.46	0.374	-1.230	0.957	0.002

F-actin

	N	Skewness			Kurtosis			Shapiro-Wilk	
	Statistic	Statistic	Std. Error	Z value	Statistic	Std. Error	Z value	Statistic	Sig.
Day_0.00	119	0.474	0.222	2.135	0.365	0.44	0.830	0.982	0.196

Day_0.25	312	0.183	0.138	1.326	-0.38	0.275	-1.382	0.973	0.035
Day_0.50	262	-0.151	0.15	-1.007	0.399	0.3	1.330	0.991	0.713
Day_0.75	101	0.943	0.24	3.929	1.835	0.476	3.855	0.948	0.001
Day_1.00	211	0.363	0.167	2.174	-0.4	0.333	-1.201	0.954	0.001
Day_3.00	147	0.383	0.2	1.915	0.124	0.397	0.312	0.946	0
Day_4.00	130	0.267	0.212	1.259	-0.003	0.422	-0.007	0.983	0.205
Day_5.00	216	0.469	0.166	2.825	-0.098	0.33	-0.297	0.988	0.491
Day_7.00	360	-0.038	0.129	-0.295	0.475	0.256	1.855	0.917	0
Day_10.0	167	0.514	0.188	2.734	-0.083	0.374	-0.222	0.985	0.327

Fibre thickness

	N	Skewness			Kurtosis			Shapiro-Wilk	
	Statistic	Statistic	Std. Error	Z value	Statistic	Std. Error	Z value	Statistic	Sig.
Day_0.00	119	-0.014	0.222	-0.063	-0.295	0.44	-0.670	0.994	0.939
Day_0.25	312	0.082	0.138	0.594	-0.375	0.275	-1.364	0.992	0.813
Day_0.50	262	-0.033	0.15	-0.220	0.065	0.3	0.217	0.967	0.013
Day_0.75	101	0.623	0.24	2.596	-0.714	0.476	-1.500	0.927	0
Day_1.00	211	0.303	0.167	1.814	-0.507	0.333	-1.523	0.972	0.031
Day_3.00	147	-0.636	0.2	-3.180	0.223	0.397	0.562	0.963	0.006
Day_4.00	130	0.134	0.212	0.632	1.926	0.422	4.564	0.974	0.044
Day_5.00	216	0.644	0.166	3.880	0.799	0.33	2.421	0.95	0.001
Day_7.00	360	-0.064	0.129	-0.496	-0.806	0.256	-3.148	0.839	0
Day_10.0	167	-1.085	0.188	-5.771	2.769	0.374	7.404	0.954	0.001

Fibre thickness variability

	N	Skewness			Kurtosis			Shapiro-Wilk	
	Statistic	Statistic	Std. Error	Z value	Statistic	Std. Error	Z value	Statistic	Sig.
Day_0.00	119	0.199	0.222	0.896	0.322	0.44	0.732	0.985	0.314
Day_0.25	312	0.549	0.138	3.978	0.245	0.275	0.891	0.965	0.008
Day_0.50	262	0.68	0.15	4.533	0.837	0.3	2.790	0.964	0.008
Day_0.75	101	-0.236	0.24	-0.983	-0.087	0.476	-0.183	0.992	0.851
Day_1.00	211	0.453	0.167	2.713	0.089	0.333	0.267	0.953	0.001
Day_3.00	147	0.363	0.2	1.815	0.307	0.397	0.773	0.979	0.1
Day_4.00	130	-0.11	0.212	-0.519	-0.403	0.422	-0.955	0.986	0.366
Day_5.00	216	0.545	0.166	3.283	0.217	0.33	0.658	0.982	0.174
Day_7.00	360	-0.201	0.129	-1.558	-0.312	0.256	-1.219	0.995	0.974
Day_10.0	167	0.111	0.188	0.590	0.135	0.374	0.361	0.993	0.875

Fibre alignment

	N	Skewness			Kurtosis			Shapiro-Wilk	
	Statistic	Statistic	Std. Error	Z value	Statistic	Std. Error	Z value	Statistic	Sig.
Day_0.00	119	-0.124	0.222	-0.559	0.099	0.44	0.225	0.995	0.972

Day_0.25	312	-0.377	0.138	-2.732	-0.527	0.275	-1.916	0.951	0.001
Day_0.50	262	-0.398	0.15	-2.653	-0.715	0.3	-2.383	0.967	0.012
Day_0.75	101	-0.908	0.24	-3.783	1.756	0.476	3.689	0.956	0.002
Day_1.00	211	-0.301	0.167	-1.802	-0.553	0.333	-1.661	0.978	0.095
Day_3.00	147	-0.48	0.2	-2.400	-0.128	0.397	-0.322	0.989	0.547
Day_4.00	130	-0.301	0.212	-1.420	-0.878	0.422	-2.081	0.969	0.018
Day_5.00	216	-0.433	0.166	-2.608	-0.126	0.33	-0.382	0.957	0.002
Day_7.00	360	-0.772	0.129	-5.984	0.544	0.256	2.125	0.978	0.084
Day_10.0	167	-0.54	0.188	-2.872	-0.217	0.374	-0.580	0.975	0.048

Fibre curvature

	N	Skewness			Kurtosis			Shapiro-Wilk	
	Statistic	Statistic	Std. Error	Z value	Statistic	Std. Error	Z value	Statistic	Sig.
Day_0.00	119	-0.276	0.222	-1.243	-0.243	0.44	-0.552	0.991	0.737
Day_0.25	312	-0.385	0.138	-2.790	0.539	0.275	1.960	0.973	0.039
Day_0.50	262	-0.374	0.15	-2.493	0.868	0.3	2.893	0.954	0.002
Day_0.75	101	-0.619	0.24	-2.579	-0.179	0.476	-0.376	0.962	0.005
Day_1.00	211	-0.149	0.167	-0.892	0.234	0.333	0.703	0.991	0.717
Day_3.00	147	0.051	0.2	0.255	-0.604	0.397	-1.521	0.976	0.06
Day_4.00	130	-0.288	0.212	-1.358	0.208	0.422	0.493	0.984	0.28
Day_5.00	216	-0.029	0.166	-0.175	-0.204	0.33	-0.618	0.984	0.255
Day_7.00	360	-0.359	0.129	-2.783	0.403	0.256	1.574	0.954	0.001
Day_10.0	167	-0.082	0.188	-0.436	-0.051	0.374	-0.136	0.99	0.681

Location of peak fibre intensity

	N	Skewness			Kurtosis			Shapiro-Wilk	
	Statistic	Statistic	Std. Error	Z value	Statistic	Std. Error	Z value	Statistic	Sig.
Day_0.00	119	0.534	0.222	2.407	1.116	0.440	2.535	0.980	0.127
Day_0.25	312	-1.939	0.138	-14.046	8.968	0.275	32.589	0.860	0.000
Day_0.50	261	-1.675	0.151	-11.109	5.988	0.300	19.932	0.894	0.000
Day_0.75	101	-0.871	0.240	-3.627	5.867	0.476	12.324	0.900	0.000
Day_1.00	211	-0.813	0.167	-4.857	9.516	0.333	28.544	0.912	0.000
Day_3.00	147	0.474	0.200	2.368	0.355	0.397	0.893	0.983	0.204
Day_4.00	130	-1.026	0.212	-4.830	3.513	0.422	8.330	0.977	0.075
Day_5.00	216	-6.985	0.166	-42.200	75.188	0.330	228.134	0.981	0.161
Day_7.00	312	-0.869	0.138	-6.293	4.904	0.275	17.820	0.975	0.047
Day_10.0	167	-0.579	0.188	-3.083	1.246	0.374	3.336	0.970	0.021

Fibre spread variability

	N	Skewness			Kurtosis			Shapiro-Wilk	
	Statistic	Statistic	Std. Error	Z value	Statistic	Std. Error	Z value	Statistic	Sig.
Day_0.00	119	-0.412	0.222	-1.856	0.773	0.44	1.757	0.98	0.127

Day_0.25	312	-2.128	0.138	-15.420	9.73	0.275	35.382	0.924	0
Day_0.50	261	-1.838	0.151	-12.172	7.682	0.3	25.607	0.842	0
Day_0.75	101	-0.869	0.24	-3.621	2.141	0.476	4.498	0.958	0.003
Day_1.00	211	-1.279	0.167	-7.659	3.57	0.333	10.721	0.945	0
Day_3.00	147	-0.484	0.2	-2.420	0.833	0.397	2.098	0.988	0.486
Day_4.00	130	-2.372	0.212	-11.189	13.967	0.422	33.097	0.987	0.456
Day_5.00	216	-7.524	0.166	-45.325	86.232	0.33	261.309	0.989	0.564
Day_7.00	360	-0.251	0.129	-1.946	0.485	0.256	1.895	0.958	0.003
Day_10.0	167	-0.085	0.188	-0.452	-0.409	0.374	-1.094	0.99	0.672

Stellate factor

	N	Skewness			Kurtosis			Shapiro-Wilk	
	Statistic	Statistic	Std. Error	Z value	Statistic	Std. Error	Z value	Statistic	Sig.
Day_0.00	119	-0.753	0.222	-3.392	0.591	0.44	1.343	0.969	0.019
Day_0.25	312	-0.568	0.138	-4.116	0.997	0.275	3.625	0.984	0.258
Day_0.50	262	-0.747	0.15	-4.980	0.427	0.3	1.423	0.971	0.027
Day_0.75	101	-0.481	0.24	-2.004	0.277	0.476	0.582	0.977	0.069
Day_1.00	211	-0.248	0.167	-1.485	0.15	0.333	0.450	0.992	0.798
Day_3.00	147	-0.453	0.2	-2.265	1.189	0.397	2.995	0.968	0.015
Day_4.00	130	-0.01	0.212	-0.047	0.044	0.422	0.104	0.993	0.91
Day_5.00	216	-0.223	0.166	-1.343	-0.207	0.33	-0.627	0.983	0.212
Day_7.00	360	-0.003	0.129	-0.023	-0.455	0.256	-1.777	0.947	0
Day_10.0	167	-0.154	0.188	-0.819	-0.16	0.374	-0.428	0.991	0.743

Fibre length

	N	Skewness			Kurtosis			Shapiro-Wilk	
	Statistic	Statistic	Std. Error	Z value	Statistic	Std. Error	Z value	Statistic	Sig.
Day_0.00	119	0.597	0.222	2.689	0.415	0.44	0.943	0.974	0.044
Day_0.25	312	0.536	0.138	3.884	0.519	0.275	1.887	0.968	0.015
Day_0.50	262	0.118	0.15	0.787	0.182	0.3	0.607	0.979	0.101
Day_0.75	101	0.23	0.24	0.958	0.288	0.476	0.605	0.988	0.509
Day_1.00	211	0.329	0.167	1.970	0.279	0.333	0.838	0.991	0.74
Day_3.00	147	0.366	0.2	1.830	0.126	0.397	0.317	0.988	0.496
Day_4.00	130	0.135	0.212	0.637	-0.681	0.422	-1.614	0.982	0.173
Day_5.00	216	0.029	0.166	0.175	-0.288	0.33	-0.873	0.989	0.607
Day_7.00	360	0.031	0.129	0.240	-0.56	0.256	-2.188	0.919	0
Day_10.0	167	-0.083	0.188	-0.441	-0.222	0.374	-0.594	0.993	0.862

Fibre length variability

	N	Skewness			Kurtosis			Shapiro-Wilk	
	Statistic	Statistic	Std. Error	Z value	Statistic	Std. Error	Z value	Statistic	Sig.
Day_0.00	119	-0.809	0.222	-3.644	1.724	0.44	3.918	0.956	0.002
Day_0.25	312	-0.061	0.138	-0.442	-0.101	0.275	-0.367	0.986	0.377
Day_0.50	262	-0.004	0.15	-0.027	-0.101	0.3	-0.337	0.981	0.154
Day_0.75	101	-0.441	0.24	-1.838	1.168	0.476	2.454	0.975	0.055
Day_1.00	211	-0.295	0.167	-1.766	0.829	0.333	2.489	0.979	0.113
Day_3.00	147	0.11	0.2	0.550	-0.523	0.397	-1.317	0.987	0.415
Day_4.00	130	0.001	0.212	0.005	2.013	0.422	4.770	0.966	0.01
Day_5.00	216	0.014	0.166	0.084	-0.392	0.33	-1.188	0.985	0.315
Day_7.00	360	-0.068	0.129	-0.527	0.054	0.256	0.211	0.973	0.033
Day_10.0	167	-0.234	0.188	-1.245	0.964	0.374	2.578	0.992	0.83

Nuclear brightness

	N	Skewness			Kurtosis			Shapiro-Wilk	
	Statistic	Statistic	Std. Error	Z value	Statistic	Std. Error	Z value	Statistic	Sig.
Day_0.00	119	0.174	0.222	0.784	-0.98	0.44	-2.227	0.968	0.016
Day_0.25	312	0.085	0.138	0.616	-0.943	0.275	-3.429	0.964	0.007
Day_0.50	262	0.184	0.15	1.227	-0.811	0.3	-2.703	0.966	0.011
Day_0.75	101	0.112	0.24	0.467	-1.109	0.476	-2.330	0.959	0.003
Day_1.00	211	0.071	0.167	0.425	-0.912	0.333	-2.739	0.985	0.306
Day_3.00	147	-0.123	0.2	-0.615	-0.73	0.397	-1.839	0.97	0.023
Day_4.00	130	0.14	0.212	0.660	-0.864	0.422	-2.047	0.972	0.029
Day_5.00	216	0.132	0.166	0.795	-0.709	0.33	-2.148	0.976	0.06
Day_7.00	360	0.094	0.129	0.729	-0.769	0.256	-3.004	0.977	0.076
Day_10.0	167	0.176	0.188	0.936	-0.747	0.374	-1.997	0.975	0.052

Nuclear volume

	N	Skewness			Kurtosis			Shapiro-Wilk	
	Statistic	Statistic	Std. Error	Z value	Statistic	Std. Error	Z value	Statistic	Sig.
Day_0.00	119	0.011	0.222	0.050	-0.684	0.440	-1.554	0.989	0.548
Day_0.25	312	0.138	0.138	0.999	-0.191	0.275	-0.694	0.993	0.857
Day_0.50	262	0.570	0.150	3.790	0.027	0.300	0.091	0.968	0.016
Day_0.75	101	0.034	0.240	0.144	-0.160	0.476	-0.336	0.992	0.836
Day_1.00	211	0.488	0.167	2.914	-0.320	0.333	-0.959	0.965	0.010
Day_3.00	147	-0.195	0.200	-0.973	0.158	0.397	0.397	0.986	0.339
Day_4.00	130	0.598	0.212	2.816	1.812	0.422	4.296	0.950	0.001
Day_5.00	216	0.409	0.166	2.470	0.880	0.330	2.671	0.986	0.368
Day_7.00	360	0.005	0.129	0.043	0.406	0.256	1.583	0.992	0.848

Day_10.0	167	0.399	0.188	2.126	0.157	0.374	0.421	0.982	0.173

Nuclear stiffness

	N	Skewness			Kurtosis			Shapiro-Wilk	
	Statistic	Statistic	Std. Error	Z value	Statistic	Std. Error	Z value	Statistic	Sig.
Day_0.00	119	-0.052	0.222	-0.234	2.309	0.44	5.248	0.948	0.001
Day_0.25	312	0.449	0.138	3.254	-0.334	0.275	-1.215	0.964	0.008
Day_0.50	262	0.212	0.15	1.413	-0.368	0.3	-1.227	0.952	0.001
Day_0.75	101	-0.199	0.24	-0.829	0.018	0.476	0.038	0.993	0.876
Day_1.00	211	0.187	0.167	1.120	0.265	0.333	0.796	0.983	0.235
Day_3.00	147	0.369	0.2	1.845	-0.673	0.397	-1.695	0.945	0
Day_4.00	130	-0.605	0.212	-2.854	2.48	0.422	5.877	0.94	0
Day_5.00	216	0.131	0.166	0.789	-0.081	0.33	-0.245	0.987	0.442
Day_7.00	360	-0.013	0.129	-0.101	1.229	0.256	4.801	0.99	0.696
Day_10.0	167	-0.137	0.188	-0.729	-0.003	0.374	-0.008	0.985	0.318

Chromatin condensation

	N	Skewness			Kurtosis			Shapiro-Wilk	
	Statistic	Statistic	Std. Error	Z value	Statistic	Std. Error	Z value	Statistic	Sig.
Day_0.00	115	-0.535	0.226	-2.367	0.411	0.447	0.919	0.983	0.247
Day_0.25	312	-0.854	0.138	-6.188	1.435	0.275	5.218	0.936	0
Day_0.50	262	-0.821	0.15	-5.473	0.395	0.3	1.317	0.91	0
Day_0.75	101	0.213	0.24	0.888	-0.571	0.476	-1.200	0.975	0.063
Day_1.00	210	-0.59	0.168	-3.512	-0.418	0.334	-1.251	0.964	0.011
Day_3.00	147	-0.557	0.2	-2.785	-0.082	0.397	-0.207	0.948	0.001
Day_4.00	130	-0.87	0.212	-4.104	3.516	0.422	8.332	0.976	0.085
Day_5.00	215	-0.756	0.166	-4.554	1.51	0.33	4.576	0.969	0.025
Day_7.00	360	-1.636	0.129	-12.682	5.132	0.256	20.047	0.989	0.655
Day_10.0	167	-0.604	0.188	-3.213	0.363	0.374	0.971	0.951	0.001

Poisson ratio

	N	Skewness			Kurtosis			Shapiro-Wilk	
	Statistic	Statistic	Std. Error	Z value	Statistic	Std. Error	Z value	Statistic	Sig.
Day_0.00	119	-0.245	0.222	-1.104	-0.254	0.44	-0.577	0.985	0.345
Day_0.25	310	-1.164	0.138	-8.435	2.231	0.276	8.083	0.882	0
Day_0.50	262	0.422	0.15	2.813	0.809	0.3	2.697	0.964	0.008
Day_0.75	101	0.024	0.24	0.100	0.003	0.476	0.006	0.995	0.977
Day_1.00	210	-0.932	0.168	-5.548	3.081	0.334	9.225	0.981	0.168
Day_3.00	147	-0.691	0.2	-3.455	3.222	0.397	8.116	0.961	0.005

Day_4.00	130	-1.021	0.212	-4.816	3.091	0.422	7.325	0.924	0
Day_5.00	215	-0.664	0.166	-4.000	0.589	0.33	1.785	0.985	0.333
Day_7.00	359	-2.138	0.129	-16.574	13.201	0.257	51.366	0.936	0
Day_10.0	165	-0.451	0.189	-2.386	1.012	0.376	2.691	0.957	0.003

9.2.2 Descriptive statistics for osteogenic cells

Cell area

	N	Skewness			Kurtosis			Shapiro-Wilk	
	Statistic	Statistic	Std. Error	Z value	Statistic	Std. Error	Z value	Statistic	Sig.
Day_0.00	119	0.664	0.222	2.993	-0.119	0.440	-0.271	0.958	0.003
Day_0.25	312	0.726	0.138	5.264	0.309	0.275	1.121	0.943	0.000
Day_0.50	262	0.668	0.150	4.436	0.154	0.300	0.514	0.866	0.000
Day_0.75	101	0.139	0.240	0.581	0.009	0.476	0.019	0.985	0.298
Day_1.00	211	0.468	0.167	2.796	0.268	0.333	0.803	0.989	0.563
Day_3.00	147	0.428	0.200	2.138	-0.949	0.397	-2.388	0.907	0.000
Day_4.00	130	0.036	0.212	0.171	-0.140	0.422	-0.332	0.984	0.278
Day_5.00	216	0.374	0.166	2.258	-0.341	0.330	-1.033	0.966	0.011
Day_7.00	360	-0.099	0.129	-0.767	-0.609	0.256	-2.376	0.992	0.792
Day_10.0	167	-0.165	0.188	-0.877	-0.728	0.374	-1.947	0.975	0.054

Cell aspect ratio

	N	Skewness			Kurtosis			Shapiro-Wilk	
	Statistic	Statistic	Std. Error	Z value	Statistic	Std. Error	Z value	Statistic	Sig.
Day_0.00	119	-0.155	0.222	-0.698	-0.644	0.440	-1.463	0.984	0.167
Day_0.25	213	0.247	0.167	1.483	-0.894	0.332	-2.695	0.968	0.006
Day_0.50	265	0.394	0.150	2.630	-0.313	0.298	-1.051	0.961	0.001
Day_0.75	183	0.409	0.180	2.275	-0.613	0.357	-1.715	0.956	0.001
Day_1.00	175	0.171	0.184	0.934	-0.655	0.365	-1.795	0.990	0.527
Day_3.00	197	0.446	0.173	2.573	-0.438	0.345	-1.271	0.959	0.001
Day_4.00	266	0.219	0.149	1.466	-0.228	0.298	-0.765	0.972	0.014
Day_5.00	187	0.368	0.178	2.071	-0.308	0.354	-0.871	0.971	0.012
Day_7.00	127	0.651	0.215	3.029	0.380	0.427	0.891	0.964	0.003
Day_10.0	141	0.570	0.204	2.793	-0.432	0.406	-1.065	0.955	0.001

F-actin

	N	Skewness			Kurtosis			Shapiro-Wilk	
	Statistic	Statistic	Std. Error	Z value	Statistic	Std. Error	Z value	Statistic	Sig.
Day_0.00	119	0.474	0.222	2.136	0.365	0.440	0.829	0.979	0.060
Day_0.25	213	0.368	0.167	2.209	-0.219	0.332	-0.661	0.976	0.033
Day_0.50	265	-0.151	0.150	-1.009	1.321	0.298	4.431	0.983	0.144
Day_0.75	183	-0.465	0.180	-2.591	-0.535	0.357	-1.497	0.984	0.181

Day_1.00	175	0.404	0.184	2.201	-0.314	0.365	-0.859	0.985	0.229
Day_3.00	197	-0.299	0.173	-1.726	-0.066	0.345	-0.192	0.994	0.865
Day_4.00	266	0.794	0.149	5.314	1.689	0.298	5.674	0.978	0.047
Day_5.00	187	-0.247	0.178	-1.393	0.938	0.354	2.653	0.940	0.000
Day_7.00	127	0.090	0.215	0.419	-0.342	0.427	-0.802	0.989	0.464
Day_10.0	141	0.387	0.204	1.897	-0.026	0.406	-0.064	0.987	0.285

Fibre thickness

	N	Skewness			Kurtosis			Shapiro-Wilk	
	Statistic	Statistic	Std. Error	Z value	Statistic	Std. Error	Z value	Statistic	Sig.
Day_0.00	119	-0.014	0.222	-0.062	-0.295	0.440	-0.671	0.996	0.987
Day_0.25	213	0.368	0.167	2.207	-0.521	0.332	-1.569	0.947	0.000
Day_0.50	265	-0.857	0.150	-5.730	1.004	0.298	3.369	0.958	0.001
Day_0.75	183	-0.297	0.180	-1.652	-0.746	0.357	-2.089	0.971	0.012
Day_1.00	175	0.498	0.184	2.713	-0.077	0.365	-0.212	0.983	0.137
Day_3.00	197	-0.833	0.173	-4.811	0.068	0.345	0.198	0.991	0.640
Day_4.00	266	0.481	0.149	3.224	0.257	0.298	0.863	0.981	0.093
Day_5.00	187	-0.117	0.178	-0.660	-0.689	0.354	-1.949	0.949	0.000
Day_7.00	127	-0.057	0.215	-0.264	-1.096	0.427	-2.570	0.968	0.006
Day_10.0	141	0.198	0.204	0.969	-0.668	0.406	-1.648	0.965	0.004

Fibre thickness variability

	N	Skewness			Kurtosis			Shapiro-Wilk	
	Statistic	Statistic	Std. Error	Z value	Statistic	Std. Error	Z value	Statistic	Sig.
Day_0.00	119	0.199	0.222	0.898	0.322	0.440	0.732	0.989	0.489
Day_0.25	213	0.097	0.167	0.583	-0.084	0.332	-0.253	0.989	0.425
Day_0.50	265	0.406	0.150	2.713	1.113	0.298	3.733	0.975	0.026
Day_0.75	183	0.336	0.180	1.873	-0.476	0.357	-1.333	0.975	0.027
Day_1.00	175	0.738	0.184	4.018	0.625	0.365	1.712	0.948	0.000
Day_3.00	197	0.292	0.173	1.684	0.694	0.345	2.014	0.979	0.059
Day_4.00	266	0.694	0.149	4.648	0.333	0.298	1.120	0.955	0.001
Day_5.00	187	1.038	0.178	5.844	2.387	0.354	6.751	0.985	0.199
Day_7.00	127	0.306	0.215	1.424	-0.244	0.427	-0.572	0.981	0.087
Day_10.0	141	0.835	0.204	4.089	1.545	0.406	3.809	0.976	0.032

Fibre alignment

	N	Skewness			Kurtosis			Shapiro-Wilk	
	Statistic	Statistic	Std. Error	Z value	Statistic	Std. Error	Z value	Statistic	Sig.
Day_0.00	119	-0.124	0.222	-0.561	0.099	0.440	0.225	0.995	0.930

Day_0.25	213	-0.711	0.167	-4.264	0.458	0.332	1.379	0.972	0.013
Day_0.50	265	-0.250	0.150	-1.669	-0.018	0.298	-0.061	0.988	0.405
Day_0.75	183	-0.390	0.180	-2.171	0.127	0.357	0.355	0.980	0.070
Day_1.00	175	0.057	0.184	0.311	-0.513	0.365	-1.405	0.985	0.195
Day_3.00	197	-0.273	0.173	-1.575	-0.385	0.345	-1.118	0.981	0.093
Day_4.00	266	-0.159	0.149	-1.068	-0.693	0.298	-2.328	0.989	0.417
Day_5.00	187	-0.388	0.178	-2.183	-0.258	0.354	-0.731	0.988	0.358
Day_7.00	127	-0.302	0.215	-1.407	-0.545	0.427	-1.278	0.980	0.081
Day_10.0	141	-0.404	0.204	-1.977	-0.332	0.406	-0.819	0.977	0.035

Fibre curvature

	N	Skewness			Kurtosis			Shapiro-Wilk	
	Statistic	Statistic	Std. Error	Z value	Statistic	Std. Error	Z value	Statistic	Sig.
Day_0.00	119	-0.276	0.222	-1.245	-0.243	0.440	-0.552	0.987	0.333
Day_0.25	213	-0.272	0.167	-1.634	0.817	0.332	2.462	0.985	0.216
Day_0.50	265	-0.283	0.150	-1.894	0.412	0.298	1.381	0.977	0.040
Day_0.75	183	-0.245	0.180	-1.365	-0.329	0.357	-0.920	0.984	0.183
Day_1.00	175	-0.853	0.184	-4.644	1.198	0.365	3.282	0.964	0.003
Day_3.00	197	-0.632	0.173	-3.650	1.137	0.345	3.299	0.985	0.211
Day_4.00	266	-0.267	0.149	-1.785	0.240	0.298	0.806	0.989	0.485
Day_5.00	187	-0.624	0.178	-3.510	0.241	0.354	0.681	0.957	0.001
Day_7.00	127	-0.164	0.215	-0.765	-0.582	0.427	-1.364	0.987	0.303
Day_10.0	141	-0.218	0.204	-1.069	-0.078	0.406	-0.193	0.990	0.578

Location of peak fibre intensity

	N	Skewness			Kurtosis			Shapiro-Wilk	
	Statistic	Statistic	Std. Error	Z value	Statistic	Std. Error	Z value	Statistic	Sig.
Day_0.00	119	0.463	0.222	2.086	1.018	0.440	2.313	0.982	0.106
Day_0.25	213	-3.056	0.167	-18.333	16.223	0.332	48.887	0.860	0.000
Day_0.50	264	-1.250	0.150	-8.338	3.774	0.299	12.633	0.875	0.000
Day_0.75	180	-5.651	0.181	-31.206	38.172	0.360	105.964	0.944	0.000
Day_1.00	175	-1.807	0.184	-9.839	5.372	0.365	14.710	0.836	0.000
Day_3.00	197	-1.628	0.173	-9.396	4.177	0.345	12.118	0.938	0.000
Day_4.00	266	-0.647	0.149	-4.333	1.761	0.298	5.916	0.949	0.000
Day_5.00	187	0.470	0.178	2.645	0.683	0.354	1.933	0.981	0.095
Day_7.00	127	0.551	0.215	2.563	0.528	0.427	1.239	0.980	0.071
Day_10.0	141	-0.138	0.204	-0.677	-0.474	0.406	-1.168	0.989	0.443

Fibre spread variability

	N	Skewness			Kurtosis			Shapiro-Wilk	
	Statistic	Statistic	Std. Error	Z value	Statistic	Std. Error	Z value	Statistic	Sig.
Day_0.00	119	-0.272	0.222	-1.226	0.523	0.440	1.188	0.992	0.745
Day_0.25	213	-1.591	0.167	-9.545	4.183	0.332	12.607	0.890	0.000
Day_0.50	265	-1.730	0.150	-11.559	8.543	0.298	28.651	0.923	0.000
Day_0.75	183	-2.451	0.180	-13.645	9.490	0.357	26.557	0.981	0.097
Day_1.00	174	-2.954	0.184	-16.042	16.871	0.366	46.067	0.761	0.000
Day_3.00	197	-0.266	0.173	-1.537	0.207	0.345	0.601	0.988	0.389
Day_4.00	266	-0.751	0.149	-5.029	1.816	0.298	6.103	0.943	0.000
Day_5.00	187	-0.218	0.178	-1.225	0.255	0.354	0.720	0.990	0.550
Day_7.00	127	0.413	0.215	1.921	0.183	0.427	0.429	0.985	0.225
Day_10.0	141	-0.424	0.204	-2.075	-0.112	0.406	-0.277	0.981	0.097

Stellate factor

	N	Skewness			Kurtosis			Shapiro-Wilk	
	Statistic	Statistic	Std. Error	Z value	Statistic	Std. Error	Z value	Statistic	Sig.
Day_0.00	119	-0.753	0.222	-3.396	0.591	0.440	1.342	0.960	0.001
Day_0.25	213	-0.444	0.167	-2.667	-0.049	0.332	-0.148	0.978	0.049
Day_0.50	265	-0.235	0.150	-1.574	-0.120	0.298	-0.403	0.994	0.914
Day_0.75	183	-0.093	0.180	-0.516	-0.536	0.357	-1.500	0.991	0.594
Day_1.00	175	-0.330	0.184	-1.799	0.727	0.365	1.991	0.979	0.057
Day_3.00	197	-0.197	0.173	-1.138	-0.610	0.345	-1.769	0.978	0.046
Day_4.00	197	-0.245	0.173	-1.416	0.176	0.345	0.511	0.991	0.589
Day_5.00	256	-0.301	0.152	-1.976	0.020	0.303	0.065	0.983	0.132
Day_7.00	127	0.128	0.215	0.595	-0.403	0.427	-0.946	0.990	0.525
Day_10.0	141	0.082	0.204	0.403	-0.133	0.406	-0.328	0.992	0.699

Fibre length

	N	Skewness			Kurtosis			Shapiro-Wilk	
	Statistic	Statistic	Std. Error	Z value	Statistic	Std. Error	Z value	Statistic	Sig.
Day_0.00	119	0.597	0.222	2.693	0.415	0.440	0.942	0.975	0.026
Day_0.25	213	0.231	0.167	1.387	-0.254	0.332	-0.766	0.984	0.178
Day_0.50	265	0.252	0.150	1.685	0.061	0.298	0.204	0.990	0.500
Day_0.75	183	0.399	0.180	2.220	-0.177	0.357	-0.495	0.968	0.007
Day_1.00	175	-0.140	0.184	-0.761	0.053	0.365	0.146	0.990	0.529
Day_3.00	197	0.280	0.173	1.618	0.195	0.345	0.566	0.978	0.048
Day_4.00	197	0.011	0.173	0.061	0.306	0.345	0.888	0.990	0.522
Day_5.00	187	0.100	0.178	0.563	-0.132	0.354	-0.374	0.986	0.248
Day_7.00	127	0.128	0.215	0.595	-0.403	0.427	-0.946	0.990	0.525

Day_10.0	141	0.387	0.204	1.897	0.014	0.406	0.035	0.983	0.142

Fibre length variability

	N	Skewness			Kurtosis			Shapiro-Wilk	
	Statistic	Statistic	Std. Error	Z value	Statistic	Std. Error	Z value	Statistic	Sig.
Day_0.00	119	0.597	0.222	2.693	0.415	0.440	0.942	0.975	0.026
Day_0.25	213	0.231	0.167	1.387	-0.254	0.332	-0.766	0.984	0.178
Day_0.50	265	0.252	0.150	1.685	0.061	0.298	0.204	0.990	0.500
Day_0.75	183	0.399	0.180	2.220	-0.177	0.357	-0.495	0.968	0.007
Day_1.00	175	-0.140	0.184	-0.761	0.053	0.365	0.146	0.990	0.529
Day_3.00	197	0.280	0.173	1.618	0.195	0.345	0.566	0.978	0.048
Day_4.00	197	0.011	0.173	0.061	0.306	0.345	0.888	0.990	0.522
Day_5.00	187	0.100	0.178	0.563	-0.132	0.354	-0.374	0.986	0.248
Day_7.00	127	0.128	0.215	0.595	-0.403	0.427	-0.946	0.990	0.525
Day_10.0	141	0.387	0.204	1.897	0.014	0.406	0.035	0.983	0.142

Nuclear brightness

	N	Skewness			Kurtosis			Shapiro-Wilk	
	Statistic	Statistic	Std. Error	Z value	Statistic	Std. Error	Z value	Statistic	Sig.
Day_0.00	119	0.174	0.222	0.785	-0.980	0.440	-2.226	0.966	0.004
Day_0.25	213	0.275	0.167	1.650	-0.695	0.332	-2.094	0.967	0.005
Day_0.50	265	0.127	0.150	0.849	-0.750	0.298	-2.515	0.972	0.015
Day_0.75	183	0.217	0.180	1.206	-0.681	0.357	-1.904	0.976	0.033
Day_1.00	175	0.199	0.184	1.085	-0.632	0.365	-1.731	0.981	0.099
Day_3.00	197	0.089	0.173	0.511	-0.923	0.345	-2.677	0.976	0.035
Day_4.00	266	0.134	0.149	0.898	-0.870	0.298	-2.922	0.979	0.056
Day_5.00	187	0.046	0.178	0.261	-1.009	0.354	-2.852	0.963	0.002
Day_7.00	127	0.081	0.215	0.378	-0.865	0.427	-2.027	0.971	0.012
Day_10.0	141	0.180	0.204	0.881	-0.327	0.406	-0.807	0.983	0.141

Nuclear volume

	N	Skewness			Kurtosis			Shapiro-Wilk	
	Statistic	Statistic	Std. Error	Z value	Statistic	Std. Error	Z value	Statistic	Sig.
Day_0.00	119	0.011	0.222	0.050	-0.684	0.440	-1.554	0.988	0.390
Day_0.25	213	-0.307	0.167	-1.842	-0.320	0.332	-0.965	0.981	0.089
Day_0.50	265	0.227	0.150	1.514	-0.150	0.298	-0.502	0.986	0.233
Day_0.75	183	0.143	0.180	0.799	-0.524	0.357	-1.466	0.994	0.866
Day_1.00	175	-0.110	0.184	-0.602	-0.089	0.365	-0.244	0.988	0.386
Day_3.00	197	0.164	0.173	0.946	0.114	0.345	0.330	0.993	0.810

Day_4.00	266	0.505	0.149	3.383	1.417	0.298	4.761	0.969	0.008
Day_5.00	187	-0.156	0.178	-0.876	-0.464	0.354	-1.312	0.988	0.403
Day_7.00	127	-0.128	0.215	-0.594	0.166	0.427	0.390	0.993	0.782
Day_10.0	141	0.044	0.204	0.214	-0.582	0.406	-1.436	0.988	0.378

Nuclear stiffness

	N	Skewness			Kurtosis			Shapiro-Wilk	
	Statistic	Statistic	Std. Error	Z value	Statistic	Std. Error	Z value	Statistic	Sig.
Day_0.00	119	-0.052	0.222	-0.234	2.309	0.440	5.246	0.955	0.001
Day_0.25	213	-0.073	0.167	-0.436	0.895	0.332	2.698	0.984	0.165
Day_0.50	265	0.258	0.150	1.724	-0.612	0.298	-2.051	0.984	0.165
Day_0.75	183	0.304	0.180	1.691	-0.407	0.357	-1.140	0.977	0.042
Day_1.00	175	-0.139	0.184	-0.758	-0.286	0.365	-0.784	0.993	0.787
Day_3.00	197	-0.044	0.173	-0.253	0.950	0.345	2.756	0.985	0.232
Day_4.00	266	0.191	0.149	1.279	2.729	0.298	9.169	0.969	0.008
Day_5.00	187	0.230	0.178	1.296	0.174	0.354	0.493	0.987	0.329
Day_7.00	127	-0.280	0.215	-1.302	-0.169	0.427	-0.397	0.988	0.379
Day_10.0	141	0.334	0.204	1.638	-0.131	0.406	-0.322	0.986	0.262

Chromatin condensation

	N	Skewness			Kurtosis			Shapiro-Wilk	
	Statistic	Statistic	Std. Error	Z value	Statistic	Std. Error	Z value	Statistic	Sig.
Day_0.00	118	-2.678	0.223	-12.024	10.953	0.442	24.788	0.775	0.000
Day_0.25	213	-0.844	0.167	-5.064	0.182	0.332	0.549	0.901	0.000
Day_0.50	265	-0.914	0.150	-6.111	1.321	0.298	4.431	0.881	0.000
Day_0.75	183	0.099	0.180	0.549	-0.753	0.357	-2.108	0.980	0.069
Day_1.00	175	-0.787	0.184	-4.285	1.925	0.365	5.270	0.918	0.000
Day_3.00	197	-0.001	0.173	-0.005	1.538	0.345	4.463	0.984	0.174
Day_4.00	266	-0.441	0.149	-2.954	0.919	0.298	3.088	0.984	0.193
Day_5.00	187	-0.729	0.178	-4.100	1.926	0.354	5.447	0.940	0.000
Day_7.00	127	0.275	0.215	1.279	0.471	0.427	1.105	0.983	0.156
Day_10.0	141	-5.827	0.204	-28.542	52.076	0.406	128.411	0.958	0.001

Poisson ratio

	N	Skewness			Kurtosis			Shapiro-Wilk	
	Statistic	Statistic	Std. Error	Z value	Statistic	Std. Error	Z value	Statistic	Sig.
Day_0.00	119	-0.245	0.222	-1.103	-0.254	0.440	-0.578	0.989	0.453
Day_0.25	212	-1.199	0.167	-7.179	2.633	0.333	7.917	0.912	0.000
Day_0.50	264	-0.944	0.150	-6.295	3.535	0.299	11.833	0.927	0.000

Day_0.75	182	-1.085	0.180	-6.025	2.791	0.358	7.788	0.978	0.054
Day_1.00	175	-0.643	0.184	-3.504	1.193	0.365	3.266	0.957	0.001
Day_3.00	195	-0.564	0.174	-3.240	1.062	0.346	3.064	0.983	0.135
Day_4.00	265	-0.195	0.150	-1.301	0.510	0.298	1.710	0.992	0.703
Day_5.00	187	-0.906	0.178	-5.097	1.830	0.354	5.175	0.948	0.000
Day_7.00	127	-0.737	0.215	-3.431	0.272	0.427	0.638	0.935	0.000
Day_10.0	141	-0.248	0.204	-1.213	1.347	0.406	3.321	0.984	0.161

9.2.3 LDA scatter plots

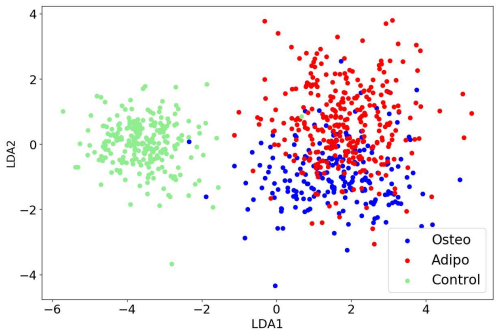

Day 0.25
CPP (SC, AD, OD): 85.5 %
CPP (AD, OD): 78.5 %

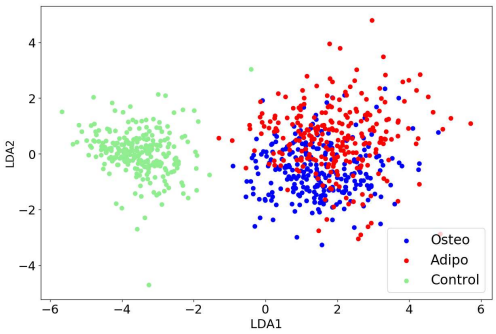

Day 0.50
CPP (SC, AD, OD): 81.8 %
CPP (AD, OD): 73.0 %

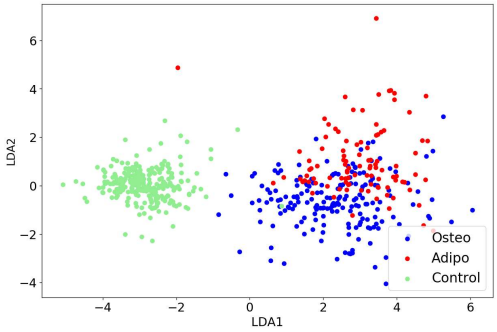

Day 0.75
CPP (SC, AD, OD): 87.3 %
CPP (AD, OD): 76.1 %

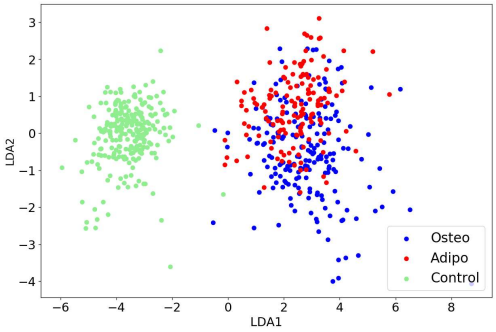

Day 3.00
CPP (SC, AD, OD): 83.3 %
CPP (AD, OD): 70.9 %

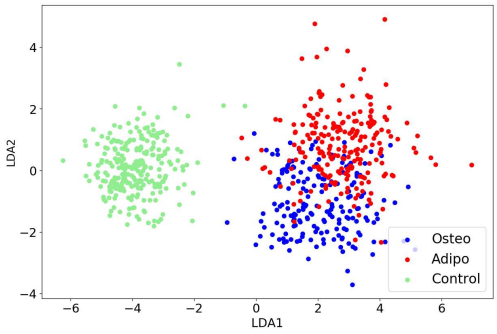

Day 5.00
CPP (SC, AD, OD): 88.9 %
CPP (AD, OD): 81.9 %

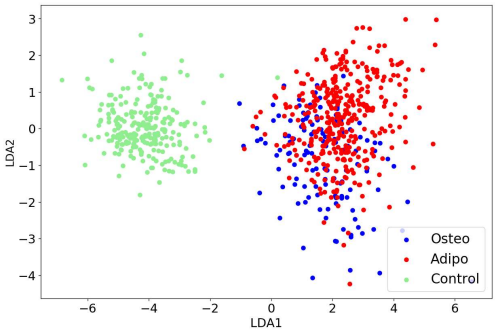

Day 7.00
CPP (SC, AD, OD): 85.7 %
CPP (AD, OD): 78.2 %

9.2.4 Scree plots for (SC, AD, OD) datasets

Scree plots constructed from the Eigenvalues of 19 principal components at each timepoint of (SC, AD, OD) datasets. The y-axis contains the Eigenvalue score of each component and the x-axis contains the principal components name arranged in the order of decreasing contribution in the total variance of PCA transformed data.

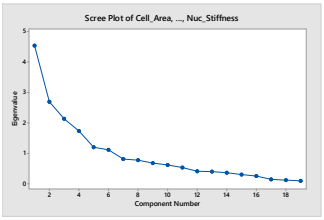

Day 0.25

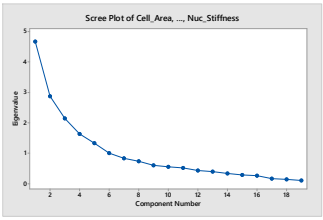

Day 0.50

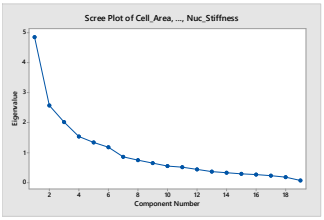

Day 0.75

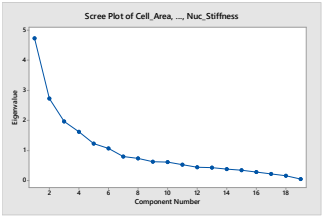

Day 1

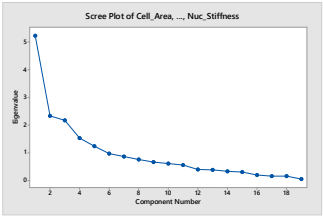

Day 3

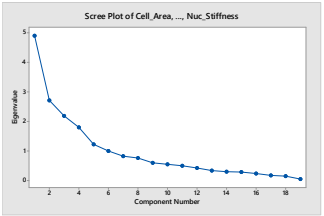

Day 4

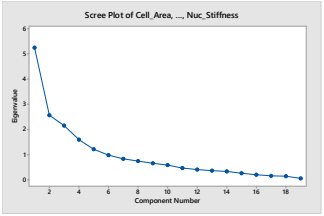

Day 5

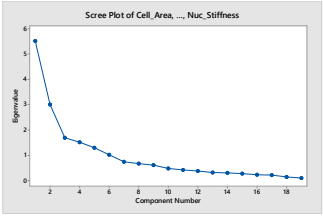

Day 7

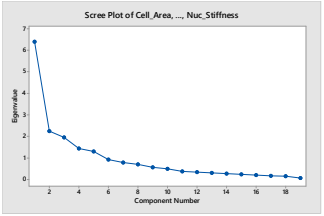

Day 10

9.2.5 Scree plots for (AD, OD) datasets

Scree plots constructed from the Eigenvalues of 19 principal components at each time-point of (AD, OD) datasets. The y-axis contains the Eigenvalue score of each component and the x-axis contains the principal components name arranged in the order of decreasing contribution in the total variance of PCA transformed data.

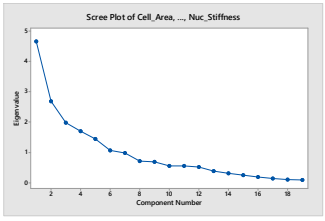

Day 0.25

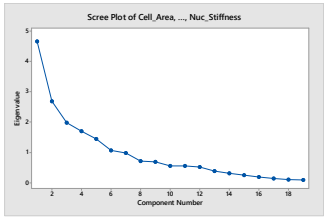

Day 0.50

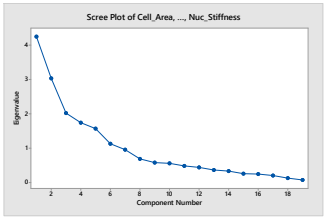

Day 0.75

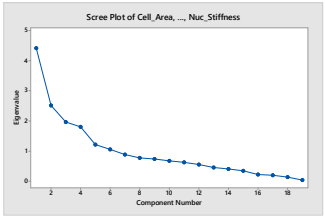

Day 1

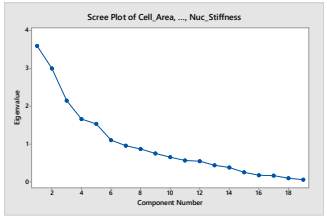

Day 3

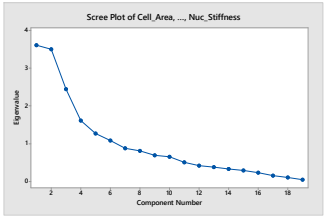

Day 4

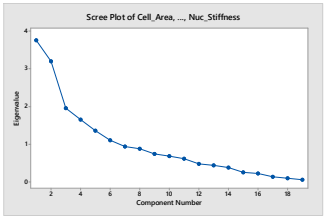

Day 5

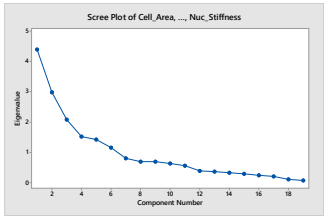

Day 7

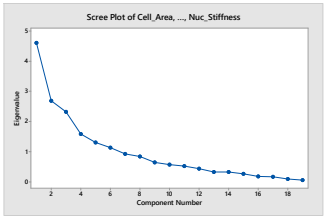

Day 10

9.3 Chapter 6 appendix

9.3.1 ANOVA of cell aspect ratio

ANOVA of cell aspect ratio at timepoint day 0 for gel versus glass substrate

	Sum of Squares	df	Mean Square	F	Sig.
Between Groups	202.967	1	202.967	29.464	.000
Within Groups	3030.957	440	6.889		
Total	3233.924	441			

9.3.2 LDA scatter plots

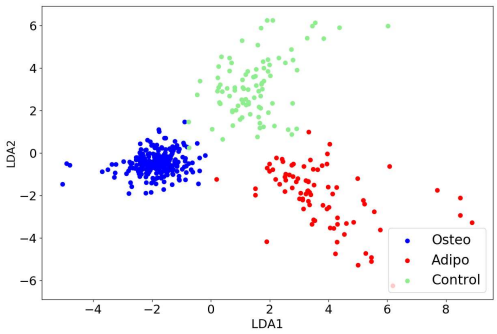

Day 2
CPP (SC, AD, OD): 98.5 %
CPP (AD, OD): 98.1 %

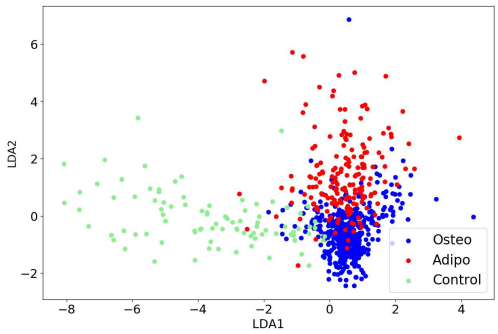

Day 4
CPP (SC, AD, OD): 85.0 %
CPP (AD, OD): 82.9 %

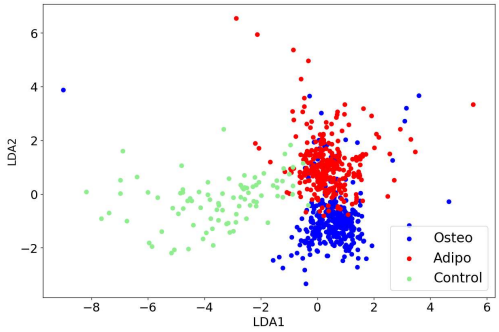

Day 5
CPP (SC, AD, OD): 87.7 %
CPP (AD, OD): 86.1 %

9.3.3 Scree plots for (SC, AD, OD) datasets

Scree plots constructed from the Eigenvalues of 19 principal components at each timepoint of (SC, AD, OD) datasets. The y-axis contains the Eigenvalue score of each component and the x-axis contains the principal components name arranged in the order of decreasing contribution in the total variance of PCA transformed data.

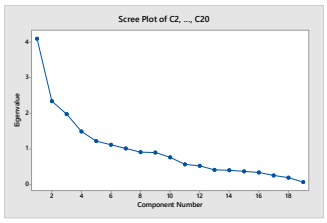

Day 1

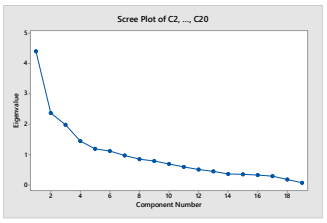

Day 2

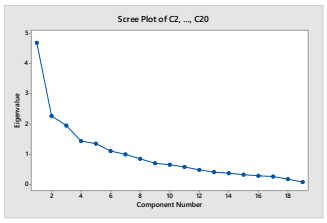

Day 3

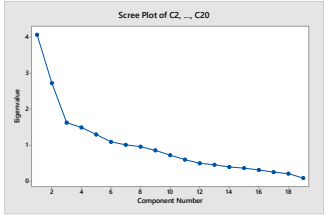

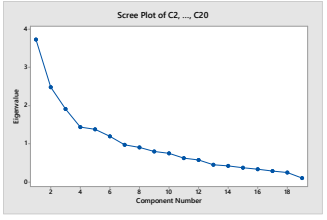

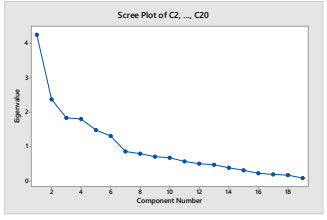

Day 4 Day 5 Day 7

9.3.4 Scree plots for (AD, OD) datasets

Scree plots constructed from the Eigenvalues of 19 principal components at each time-point of (AD, OD) datasets. The y-axis contains the Eigenvalue score of each component and the x-axis contains the principal components name arranged in the order of decreasing contribution in the total variance of PCA transformed data.

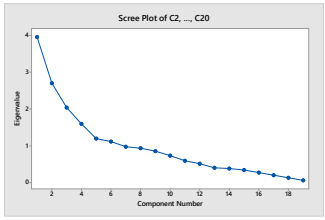

Day 1

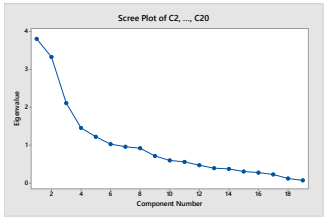

Day 2

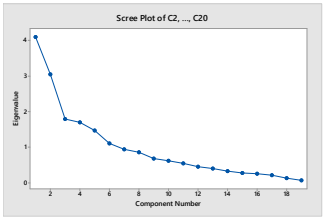

Day 3

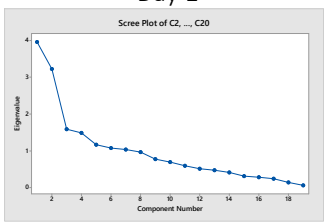

Day 4

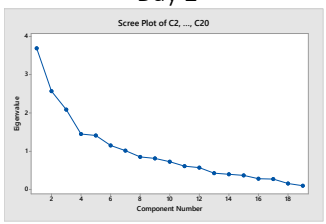

Day 5

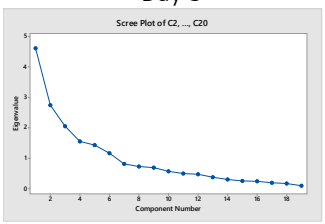

Day 7

9.4 Python script for LDA and PCA

```
from IPython import get_ipython
get_ipython().magic('reset -sf')

import matplotlib.pyplot as plt
import pandas as pd
from sklearn.decomposition import PCA as sklearnPCA
from sklearn.discriminant_analysis import LinearDiscriminantAnalysis as LDA
from sklearn.datasets.samples_generator import make_blobs
from pandas.tools.plotting import parallel_coordinates
from xlrd import open_workbook
import csv
import numpy as np
from sklearn import datasets
from sklearn.decomposition import PCA
from sklearn.discriminant_analysis import QuadraticDiscriminantAnalysis as QDA
from sklearn.metrics import confusion_matrix, classification_report, precision_score
```

```
df = pd.read_csv('File name.csv')
df = df.dropna()
df.columns = ['Class', 'p1', 'p2', 'p3', 'p4', 'p5', 'p6', 'p7',
         'p8', 'p9', 'p10', 'p11',
         'p12', 'p13', 'p14', 'p15', 'p16', 'p17', 'p18', 'p19']

y = df['Class']          # Split off classifications
X = df.ix[:, 'p1':]      # Split off features
X_norm = (X - X.min())/(X.max() - X.min())

lda = LDA(n_components=2) #2-dimensional LDA
lda_transformed = pd.DataFrame(lda.fit_transform(X_norm, y))

# Plot all scatter of between AD, OD and SC data points
plt.figure(figsize=(12, 8), dpi=120)
plt.scatter(lda_transformed[y==1][0], lda_transformed[y==1][1], label='Osteo', c='blue')
plt.scatter(lda_transformed[y==2][0], lda_transformed[y==2][1], label='Adipo', c='red')
plt.scatter(lda_transformed[y==3][0], lda_transformed[y==3][1], label='Control', c='lightgreen')

# Plot all scatter of longitudinal data points from the experiment in chapter 6
plt.scatter(lda_transformed[y==0][0], lda_transformed[y==0][1], label='Day 0', c='Black')
plt.scatter(lda_transformed[y==1][0], lda_transformed[y==1][1], label='Day 1', c='orange')
plt.scatter(lda_transformed[y==2][0], lda_transformed[y==2][1], label='Day 2', c='yellow')
plt.scatter(lda_transformed[y==3][0], lda_transformed[y==3][1], label='Day 3', c='Green')
plt.scatter(lda_transformed[y==4][0], lda_transformed[y==4][1], label='Day 4', c='lightgreen')
plt.scatter(lda_transformed[y==5][0], lda_transformed[y==5][1], label='Day 5', c='darkgreen')
plt.scatter(lda_transformed[y==6][0], lda_transformed[y==6][1], label='Day 7', c='blue')

# Display legend and show plot
plt.xticks(fontsize=18, rotation=0)
plt.yticks(fontsize=18, rotation=0)
plt.legend(loc=4, prop={'size': 20})
plt.xlabel('LDA1', fontsize=18)
plt.ylabel('LDA2', fontsize=16)

plt.show()

# to calculate CPP of the model with an without SC data

prob = lda.predict(X_norm)
y=y.values
a = np.count_nonzero(prob==y)
b = np.prod(y.shape)
correct = float(a) / float(b)
c = np.prod(y.shape) - np.count_nonzero(y)
correct2 = float(a - c) / float(b - c)
```

```
print(correct)              # gives CPP with SC data
print(correct2)             # gives CPP without SC data


pca = sklearnPCA(n_components=2) #2-dimensional PCA
pca_transformed = pd.DataFrame(pca.fit_transform(X_norm))

# Plot all scatter of between AD, OD and SC data points
plt.figure(figsize=(12, 8), dpi=120)
plt.scatter(pca_transformed[y==1][0], pca_transformed[y==1][1], label='Osteo', c='blue')
plt.scatter(pca_transformed[y==2][0], pca_transformed[y==2][1], label='Adipo', c='red')
plt.scatter(pca_transformed[y==0][0], pca_transformed[y==0][1], label='Control', c='lightgreen')

# Plot all scatter of longitudinal data points from the experiment in chapter 6
plt.scatter(pca_transformed[y==0][0], pca_transformed[y==0][1], label='Day 0', c='Black')
plt.scatter(pca_transformed[y==1][0], pca_transformed[y==1][1], label='Day 1', c='red')
plt.scatter(pca_transformed[y==2][0], pca_transformed[y==2][1], label='Day 2', c='orange')
plt.scatter(pca_transformed[y==3][0], pca_transformed[y==3][1], label='Day 3', c='yellow')
plt.scatter(pca_transformed[y==4][0], pca_transformed[y==4][1], label='Day 4', c='lightgreen')
plt.scatter(pca_transformed[y==5][0], pca_transformed[y==5][1], label='Day 5', c='darkgreen')
plt.scatter(pca_transformed[y==6][0], pca_transformed[y==6][1], label='Day 7', c='blue')
plt.xticks(fontsize=18, rotation=0)
plt.yticks(fontsize=18, rotation=0)
plt.legend(loc=4, prop={'size': 20})
plt.xlabel('PCA1', fontsize=18)
plt.ylabel('PCA2', fontsize=16)
plt.show()
```